

# Flexible and Conformal Antennas and Applications

Lead Guest Editor: Maggie Y. Chen

Guest Editors: Félix A. Miranda, Xing Lan, and Xuejun Lu





---

# **Flexible and Conformal Antennas and Applications**

International Journal of Antennas and Propagation

---

## **Flexible and Conformal Antennas and Applications**

Lead Guest Editor: Maggie Y. Chen

Guest Editors: Félix A. Miranda, Xing Lan, and Xuejun Lu



---

Copyright © 2018 Hindawi. All rights reserved.

This is a special issue published in "International Journal of Antennas and Propagation." All articles are open access articles distributed under the Creative Commons Attribution License, which permits unrestricted use, distribution, and reproduction in any medium, provided the original work is properly cited.

## Editorial Board

- Ana Alejos, Spain  
Mohammad Ali, USA  
Jaume Anguera, Spain  
Rodolfo Araneo, Italy  
Alexei Ashikhmin, USA  
Herve Aubert, France  
Paolo Baccarelli, Italy  
Xiulong Bao, Ireland  
Toni Björninen, Finland  
Stefania Bonafoni, Italy  
Paolo Burghignoli, Italy  
Shah Nawaz Burokur, France  
Giuseppe Castaldi, Italy  
Luca Catarinucci, Italy  
Felipe Catedra, Spain  
Marta Cavagnaro, Italy  
Shih Yuan Chen, Taiwan  
Yu Jian Cheng, China  
Renato Cicchetti, Italy  
Riccardo Colella, Italy  
Laura Corchia, Italy  
Lorenzo Crocco, Italy  
Claudio Curcio, Italy  
Francesco D'Agostino, Italy  
María Elena de Cos Gómez, Spain  
Tayeb A. Denidni, Canada  
Giuseppe Di Massa, Italy
- Michele D'Urso, Italy  
Francisco Falcone, Spain  
Miguel Ferrando Bataller, Spain  
Flaminio Ferrara, Italy  
Vincenzo Galdi, Italy  
Claudio Gennarelli, Italy  
Farid Ghanem, Algeria  
Sotirios K. Goudos, Greece  
Rocco Guerriero, Italy  
Kerim Guney, Turkey  
Song Guo, Japan  
Tamer S. Ibrahim, USA  
M. Ramlee Kamarudin, UK  
Slawomir Koziel, Iceland  
Luis Landesa, Spain  
Ding-Bing Lin, Taiwan  
Angelo Liseno, Italy  
Pierfrancesco Lombardo, Italy  
Lorenzo Luini, Italy  
Atsushi Mase, Japan  
Diego Masotti, Italy  
Ch. F. Mecklenbräuker, Austria  
A. Toaha Mobashsher, Australia  
Ananda S. Mohan, Australia  
J.-M. Molina-Garcia-Pardo, Spain  
Giuseppina Monti, Italy  
Giorgio Montisci, Italy
- Andrea Francesco Morabito, Italy  
N. Nasimuddin, Singapore  
Mourad Nedil, Canada  
Symeon Nikolaou, Cyprus  
Giacomo Oliveri, Italy  
Mauro Parise, Italy  
Ikmo Park, Republic of Korea  
Josep Parrón, Spain  
Matteo Pastorino, Italy  
Xianming Qing, Singapore  
Ahmad Safaai-Jazi, USA  
Safieddin Safavi-Naeini, Canada  
Magdalena Salazar-Palma, Spain  
Stefano Selleri, Italy  
Raffaele Solimene, Italy  
Gino Sorbello, Italy  
Seong-Youp Suh, USA  
Sheng Sun, Hong Kong  
Larbi Talbi, Canada  
Luciano Tarricone, Italy  
Parveen Wahid, USA  
Chien-Jen Wang, Taiwan  
Wen-Qin Wang, China  
Mustapha C E Yagoub, Canada  
Shiwen Yang, China  
Yuan Yao, China

# Contents

## **Flexible and Conformal Antennas and Applications**

Maggie Y. Chen , Félix A. Miranda, Xing Lan, and Xuejun Lu  
Editorial (2 pages), Article ID 6367571, Volume 2018 (2018)

## **Material Selection and Fabrication Processes for Flexible Conformal Antennas**

Mahmuda Akter Monne , Xing Lan, and Maggie Yihong Chen   
Review Article (14 pages), Article ID 9815631, Volume 2018 (2018)

## **Design of Low-Complexity Hybrid Precoder and Inkjet-Printed Antenna Array for Massive MIMO Downlink Systems**

Subitha D  and Mathana J M  
Research Article (8 pages), Article ID 4315128, Volume 2018 (2018)

## **Inkjet-Printed Flexible MEMS Switches for Phased-Array Antennas**

Mahmuda Akter Monne, Xing Lan, Chunbo Zhang, and Maggie Yihong Chen   
Research Article (10 pages), Article ID 4517848, Volume 2018 (2018)

## **Miniaturized Printed Inverted-F Antenna for Internet of Things: A Design on PCB with a Meandering Line and Shorting Strip**

Cheuk Yin Cheung, Joseph S. M. Yuen, and Steve W. Y. Mung   
Research Article (5 pages), Article ID 5172960, Volume 2018 (2018)

## **Accurate 3D Mapping Algorithm for Flexible Antennas**

Saed Asaly, Boaz Ben-Moshe , and Nir Shvalb   
Research Article (12 pages), Article ID 3748623, Volume 2018 (2018)

## **A Ring-Focus Antenna with Splash Plate in Ka-Band**

Laiding Zhao , Xiaodong Bai, Rui Li, and Jidong Xie  
Research Article (8 pages), Article ID 9790143, Volume 2018 (2018)

## **Low-Cost Printed Flexible Antenna by Using an Office Printer for Conformal Applications**

Kashif Nisar Paracha, Sharul Kamal Abdul Rahim, Hassan Tariq Chattha , Saqer Saleh Aljaafreh, Sabih ur Rehman , and Yew Chiong Lo  
Research Article (7 pages), Article ID 3241581, Volume 2018 (2018)

## **Printable Materials for the Realization of High Performance RF Components: Challenges and Opportunities**

Eva S. Rosker, Rajinder Sandhu, Jimmy Hester, Mark S. Goorsky, and Jesse Tice   
Review Article (19 pages), Article ID 9359528, Volume 2018 (2018)

## **Design, Fabrication, and Testing of Active Skin Antenna with 3D Printing Array Framework**

Jinzhu Zhou, Haitao Li, Le Kang, Baofu Tang, Jin Huang, and Zhiheng Cai  
Research Article (15 pages), Article ID 7516323, Volume 2017 (2018)

## Editorial

# Flexible and Conformal Antennas and Applications

Maggie Y. Chen <sup>1</sup>, Félix A. Miranda,<sup>2</sup> Xing Lan,<sup>3</sup> and Xuejun Lu<sup>4</sup>

<sup>1</sup>Ingram School of Engineering, Texas State University, San Marcos, TX 78666, USA

<sup>2</sup>NASA Glenn Research Center, Cleveland, OH 44135, USA

<sup>3</sup>NG Next, Northrop Grumman Corporation, Redondo Beach, CA 90278, USA

<sup>4</sup>Department of Electrical and Computer Engineering, University of Massachusetts, Lowell, MA 01854, USA

Correspondence should be addressed to Maggie Y. Chen; [maggie.chen@txstate.edu](mailto:maggie.chen@txstate.edu)

Received 14 March 2018; Accepted 14 March 2018; Published 6 June 2018

Copyright © 2018 Maggie Y. Chen et al. This is an open access article distributed under the Creative Commons Attribution License, which permits unrestricted use, distribution, and reproduction in any medium, provided the original work is properly cited.

There are numerous ongoing research efforts in flexible antenna technology since these antennas can enable communications in curved surfaces not suitable for traditional rigid antennas, as well as exhibiting wide adaptability, low mass density, small volume, lightweight, and low cost. A considerable effort is being carried out on the novel antenna configurations exhibiting agile operating frequencies, tunable bandwidth, switchable polarization, and reconfigurable radiation pattern. Due to the significant research efforts and fast development in the field, International Journal of Antennas and Propagation set out to publish a special issue devoted to the topic of Flexible and Conformal Antennas and Applications. The result is a collection of ten outstanding articles submitted by investigators representing seven countries across Asia, Europe, and North America.

For additive manufacturing and direct write printing, material selection and manufacturing process are critical to the antenna and radio frequency (RF) components' overall electrical and mechanical performance. M. A. Monne et al. from Texas State University, in "Material Selection and Fabrication Processes for Flexible Conformal Antennas," discuss extensively the major fabrication techniques and associated materials used for the fabrication of flexible conformal antennas, including 3D printing technology, wearable textile technology, substrate-integrated waveguide technology, and membrane technology. The application of each type of fabrication technique is analyzed through experimental results, which further underlines the importance of material selection and the various fabrication processes. E. S. Rosker et al. from Northrop Grumman Corporation and UCLA, in

"Printable Materials for the Realization of High Performance RF Components: Challenges and Opportunities," thoroughly discuss the attributes and challenges of additive manufacturing and direct writing techniques for the development of a variety of RF components including antennas, filters, and transmission lines. In this very comprehensive paper, the authors discuss printing methods, ink formulation, and post-processing approaches necessary to attain RF components and devices with performance comparable to those developed using conventional techniques and address future areas of research where further work is needed to optimize the performance and exploit the full potential of printed RF components.

Various types of flexible antennas were designed and reported. J. Zhou et al. from Xidian University, in "Design, Fabrication, and Testing of Active Skin Antenna with 3D Printing Array Framework," report the design, fabrication, and testing of a novel active skin antenna which consists of an encapsulation shell, antenna skin, and RF and beam control circuits. An active skin antenna prototype with 32 microstrip antenna elements was fabricated using a hybrid manufacturing method. 3D printing technology was applied to fabricate the array framework, and the different layers were bonded to form the final antenna skin by using traditional composite processes. The proposed design and fabrication technique is suitable for the development of a conformal load-bearing antenna or smart skin antenna installed in the structural surface of aircraft, warships, and armored vehicles. L. Zhao et al. from Nanjing University of Posts and Telecommunications, in "A Ring-Focus Antenna with Splash Plate in

Ka-Band,” report a ring-focus antenna fed by a splash plate for Ka-band communications. In this paper, the authors introduce a new theory for the splash-plate feed design. Their simulation also shows a very good agreement with the measurement data. The measured efficiency satisfies the requirement for Ka-band communications. K. N. Paracha et al. from Universiti Teknologi Malaysia, in “Low-Cost Printed Flexible Antenna by Using an Office Printer for Conformal Applications,” report a coplanar waveguide- (CPW-) fed Z-shaped planar antenna printed using an ink-jet printer on a flexible polyethylene terephthalate (PET) substrate. The radiation efficiency of 62% was achieved at 2.45 GHz. The performance of the printed antenna under various bending conditions is also tested for conformal applications for the future 5G network. C. Y. Cheung et al. from Hong Kong have demonstrated a printed inverted-F antenna (PIFA) in the paper titled “Miniaturized Printed Inverted-F Antenna for Internet of Things: A Design on PCB with a Meandering Line and Shorting Strip.” This antenna employs a smart meandering line and shorting strip design technique to further reduce the overall size, profile, and cost and increase the antenna’s various electrical performances. This technique can be adapted and widely applied to various Internet of Things (IoT) and numerous other wireless applications due to its merits.

Flexible high-speed digital switching, amplifiers, and digital beamforming networks are critical to realize flexible phased-array antenna. M. A. Monne et al. from Texas State University, in “Inkjet-Printed Flexible MEMS Switches for Phased-Array Antennas,” report a fully ink-jet-printed flexible MEMS switch for phased-array antennas. The physical structure of the printed MEMS switch consists of an anchor with a clamp-clamp beam, a sacrificial layer, and bottom transmission lines. 5 mil Kapton® polyimide film is used as a flexible substrate material. Layer-by-layer fabrication process and material evaluation are illustrated. The MEMS switch has a low actuation voltage of 1.2 V, current capacity of 0.2195 mA, a current on-off ratio of 2195:1, and an RF insertion loss of 5 dB up to 13.5 GHz. Printed MEMS switch technology is a promising candidate for flexible and reconfigurable phased-array antennas and other RF and microwave frequency applications.

Numerical simulation of an antenna system can be used as guidance towards flexible antenna development. S. Asaly et al. from Ariel University, in “Accurate 3D Mapping Algorithm for Flexible Antennas,” report a new accurate 3D flexible antenna surface mapping technology using a small-sized monocular camera and known patterns on the antenna surface. This method demonstrated up to 0.1-millimeter antenna mapping accuracy from 1 m distance. The method provides an effective tool for accurate 3D mapping of a flexible antenna surface. D. Subitha and J. M. Mathana from Anna University, in “Design of Low-Complexity Hybrid Precoder and Inkjet-Printed Antenna Array for Massive MIMO Downlink Systems,” propose two design methodologies to reduce the complexity of massive multiple input multiple output (MIMO) systems. The first one is the design of a low-complexity hybrid precoder based on zero-forcing (ZF) precoding algorithm and Neumann series approximation.

The second one is the design of a flexible, environment friendly, simple 128-element Z-shaped coplanar waveguide (CPW) monopole array at the frequency of 2.4 GHz. The performance of the proposed designs are evaluated in terms of probability of error in the hybrid precoding algorithm and radiation characteristics like gain, directivity, and return loss for the printed antenna design.

Uniformly, these authors highlight both the promise and the challenges faced by this emerging field of antenna development. In summary, this special issue provides a snapshot of the current development of flexible and conformal antennas across the globe. Hopefully, this publication will provide a benchmark for future development of innovative, high-performance, low-cost, rapid deployable, and flexible antennas for various applications.

*Maggie Y. Chen*  
*Félix A. Miranda*  
*Xing Lan*  
*Xuejun Lu*

## Review Article

# Material Selection and Fabrication Processes for Flexible Conformal Antennas

Mahmuda Akter Monne <sup>1</sup>, Xing Lan,<sup>2</sup> and Maggie Yihong Chen <sup>1,3</sup>

<sup>1</sup>Material Science Engineering and Commercialization Program, Texas State University, San Marcos, TX 78666, USA

<sup>2</sup>One Space Park, Northrop Grumman, Redondo Beach, CA 90278, USA

<sup>3</sup>Ingram School of Engineering, Texas State University, San Marcos, TX 78666, USA

Correspondence should be addressed to Maggie Yihong Chen; [maggie.chen@txstate.edu](mailto:maggie.chen@txstate.edu)

Received 26 October 2017; Revised 28 December 2017; Accepted 13 February 2018; Published 20 May 2018

Academic Editor: Symeon Nikolaou

Copyright © 2018 Mahmuda Akter Monne et al. This is an open access article distributed under the Creative Commons Attribution License, which permits unrestricted use, distribution, and reproduction in any medium, provided the original work is properly cited.

Flexible antennas offer many advantages for communication, radar, RF identification, and energy harvesting applications. A review on the material selection and fabrication process of flexible antennas is presented since these aspects are critical to the antenna's overall electrical and mechanical performance. A number of different material and fabrication techniques are reviewed in detail for different types of antennas. In addition, experimental results are also discussed for these antennas, which further underlines the importance of material selection and the various fabrication processes.

## 1. Introduction

In recent years, a great deal of interest has arisen in both industry and academia for flexible electronics. In fact, this research area now occupies the top of the research pyramid of many national research agencies. The revenue of flexible electronics is estimated to be 3 billion USD in 2017 and projected to be over 300 billion USD in 2028 according to the latest market analysis report [1].

Moreover, flexible electronics is becoming an appealing candidate for the next generation of consumer electronics due to light weight, low cost of manufacturing, ease of fabrication, and the availability of inexpensive flexible substrates (i.e., papers, textiles, and plastics) [2]. Flexible electronic systems also incorporate flexible antennas to provide additional room for system trade-off space and design flexibility.

For example, a flexible antenna can be integrated onto a light weight, conformal, and flexible platform [3]. This kind of flexible antenna meets the requirement of different communication tasks using different antenna technologies (i.e., robotic devices or on human clothes, mandate a small size, light weight, and low power antenna system) [3]. On the other hand, because of the low profile of the flexible antenna

design, coverage of the local network will be short (~10 m) to medium range (~5 km–10 km) [4, 5].

A flexible substrate should be highly deformable and mechanically robust and must exhibit high tolerance levels of bending repeatability to comply with flexible technologies and integrated components [6]. Also, solvent resistivity, low cost (allowing large area, mass production), and moisture resistance can be additional requirements for substrate selection. There were various kinds of substrates utilized by researches, for example, steel [7], fabric [8], fluidic [9], paper [10], as well as synthesized materials. Among these, two most widely researched flexible substrate candidates are plastic and stainless steel [7]. Steel is not particularly deformable and heavier than plastic; therefore, it is unsuitable for many applications, particularly in wearable and display applications. Antennas were printed on 4 mm felt fabric textile [8], which is developed for wearable and conformal applications. However, it is hard to maintain the shape of fabric substrates during applications, as well as prone to environmental degradations. Paper substrate leads to potential electronic devices at low cost, which are also disposable and fully recyclable. A single-band antenna was printed and demonstrated on a 46 mm × 30 mm paper substrate [10]. However, the high loss

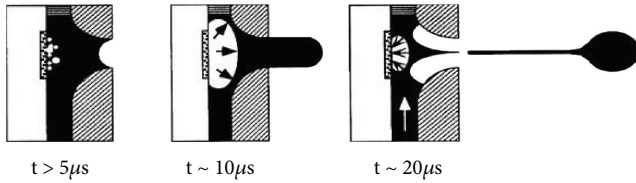


FIGURE 1: Drop formation by a thermal inkjet printer [36].

factor leads to reduced antenna efficiency due to either conduction losses, dielectric losses, or impedance mismatch [11]. On the other hand, plastic substrates are lighter and deformable alternatives with many suitable variants. With the DuPont brand Kapton polyimide film, the maximum fabrication temperature can be as high as 400°C. Kapton also has low loss factor over a wide frequency range, high tensile strength, and dielectric strength [12].

There are four major types of flexible antennas, namely 3D-printed flexible antennas, passive and active wearable textile antennas, substrate-integrated waveguide antennas, and membrane-based antennas. Their fabrication process, performance, and application are discussed in detail in the following sections.

## 2. 3D-Printed Flexible Antennas

This section reviews the currently available 3D printing technologies for the fabrication of flexible antennas. It also includes a method overview, advantages, and drawbacks of each technique, including inkjet printing, aerosol jet printing, and screen printing.

### 2.1. 3D Inkjet Printing Technique

**2.1.1. Conductive and Insulating Materials.** Conductive materials for printed and flexible antennas include various conductive inks and pastes which provide critical performance characteristics of a printed pattern. The choices of conductive material ink include the metallic solution of silver, gold, copper, and nickel nanoparticles, conductive polymers, carbon nanotubes, and graphene [13]. Also, each of these conductive materials offers different advantages to the final conductive system.

Conductive nanoparticle ink is based on conductive nanoparticles or nanoflakes dispensed in a liquid solvent usually in colloidal form [14–25]. A commercial silver ink (NovaCentrix, JSB-40G) in aqueous dispersion has 40% solid silver nanoflakes by weight with average particle size of 60–80 nm. It also has a viscosity (8–12 cP) which is suitable for inkjet print head. Viscosity of the ink can be increased by loading more nanoflakes, but it significantly increases the clogging rate. Curing the substrate after printing is an important step to evaporate the solvent so that only conductive material remains. Sintering could be in any form such as thermal curing, UV, or photonic curing. Sintering process like extended time of thermal curing or high-power UV or photonic curing can appreciably improve the conductivity of the printed patterns.

Another type of solution-based ink is silver metalorganic nanoparticle ink [26]. Jahn et al., Pabst et al., Calvert, and

Zhang et al. investigated silver printing from an aqueous transition metal complex-  $[\text{AgO}_2\text{C}(\text{CH}_2\text{OCH}_2)_3\text{H}]$  based metalorganic dispersion ink [27–30]. They achieved metallic silver-printed pattern conductivity as high as  $2.7 \times 10^7 \text{ S m}^{-1}$ . To achieve a layer-by-layer silver film growth using metalorganic dispersion ink, a sequential reactive inkjet (RI) process must be employed [27]. Reactive silver ink ( $\text{AgC}_2\text{H}_3\text{O}_2$ ) (Sigma-Aldrich) is introduced to deploy the RI process. The RI process involves an initial printed metalorganic ink, followed by a secondary printed reactive ink. Interlayer adhesion can be improved by different surface treatments like oxygen plasma treatment.

Insulating materials are used for the dielectric layer during the fabrication of multilayer interconnects. There are few choices of dielectric material for printing technology that have excellent mechanical and thermal stability, chemical resistance, and electrical properties (e.g., high electrical breakdown field). Various forms of polymers can be suitable candidates for interlayer dielectrics and flexible devices. As an example, a form of polyimide, made from its precursor poly(amic acid) 18% of volume weight diluted with a little more than 80% of volume weight of 1-methyl-2-pyrrolidone (NMP) upon heating and other chemical treatments, can be used as ink [31]. It is reported that polyketone resin dissolved in a solvent mixture of 50% ethyl lactate and 50%  $\alpha$ -terpineol can be used as a suitable insulator, exhibiting a high electrical breakdown voltage of 17.5 MV/m [32]. Silicone elastomer is a two-part prepolymer liquid, which can be printed out as well [33]. In [33], it shows that the spin-on-glass can also be diluted to have the viscosity and solid content suitable for printing.

**2.1.2. Operation of Inkjet Printer.** Inkjet printers can be divided into two basic groups based on their operation procedure: continuous and drop-on-demand [34]. In continuous inkjet printers, the ink is first pumped through a nozzle forming a liquid jet. Secondly, the formed liquid jet is deflected by electrostatic plates to the paper or to a reservoir for recirculation.

Today, most inkjet printers are based on the drop formation process, which is called drop-on-demand (DOD) [34, 35]. The drop-on-demand method provides smaller drops and higher placement accuracy compared to the continuous inkjet printers. In this method, the pulse that creates the ink drop can be generated either thermally or piezoelectrically. As seen in Figure 1, in a thermal inkjet printer, a heated plate causes a vapor bubble, which pushes the ink out through the nozzle. The total ejection time is a few microseconds, and the temperature of the plate can rise by about 300°C during the ejection.

Figure 2(a) shows the schematic of a shear-mode piezoelectric print head. In this type of print head, an electric field applied to a piezoceramic actuator element causes shear action deformation which is used to eject the ink through the nozzle [37]. The print head design shown in Figure 2(b) is called the bend-mode design. In this design, ink rejection is caused by the piezoceramic plates bonded to a diaphragm to form an array of bilaminar electromechanical transducers.

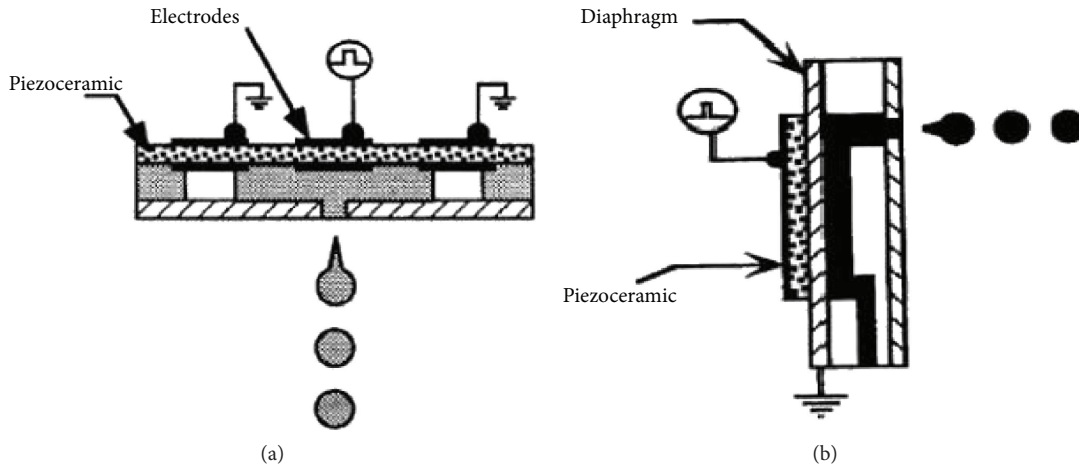


FIGURE 2: Design of a (a) shear-mode and (b) bend-mode piezoelectric inkjet print head [36].

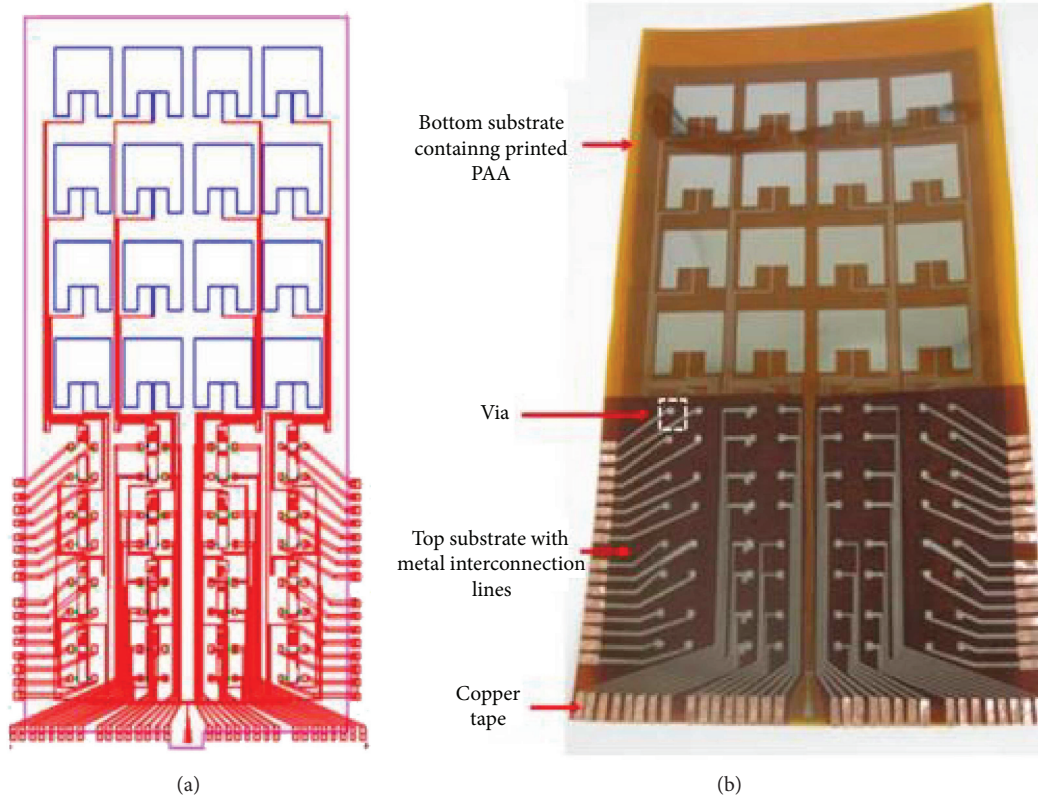


FIGURE 3: (a) Schematic layout of a 4 by 4 PAA subsystem with a multilayer interconnection scheme. (b) Photograph of the fully printed PAA system [39].

The print heads in a Tektronix's Phaser 300 and 350 and Epson's Color Stylus 400, 600, and 800 inkjet printers are of the bend-mode piezoceramic type [36]. The Fujifilm Dimatix Materials Printer is the most widely used inkjet printer for fabrication [38]. Since the printing is usually performed at room temperature ( $25^{\circ}\text{C}$ ), this inkjet printer is capable of printing on a variety of substrates, including low temperature plastics. Additionally, during deposition, surface topology is also not an issue due to its contactless printing technique. This printing technique can also fill the contacts of multilayer interconnection without any obstacle. It is also

possible to print multiple layers of different materials on top of each other.

**2.1.3. Inkjet-Printed Antennas.** Figure 3 shows the inkjet-printed  $4 \times 4$  phased-array antenna (PAA) fabricated by Subbaraman et al. [39]. The entire PAA was inkjet printed using Fujifilm Dimatix Material Printer (DMP-2831), including the silver-based patch antenna elements and carbon nanotube (CNT) field-effect transistors (FETs) in the phase-shifting network. The DC control circuits for the CNT FETs were printed on a separate Kapton substrate, and multilayer

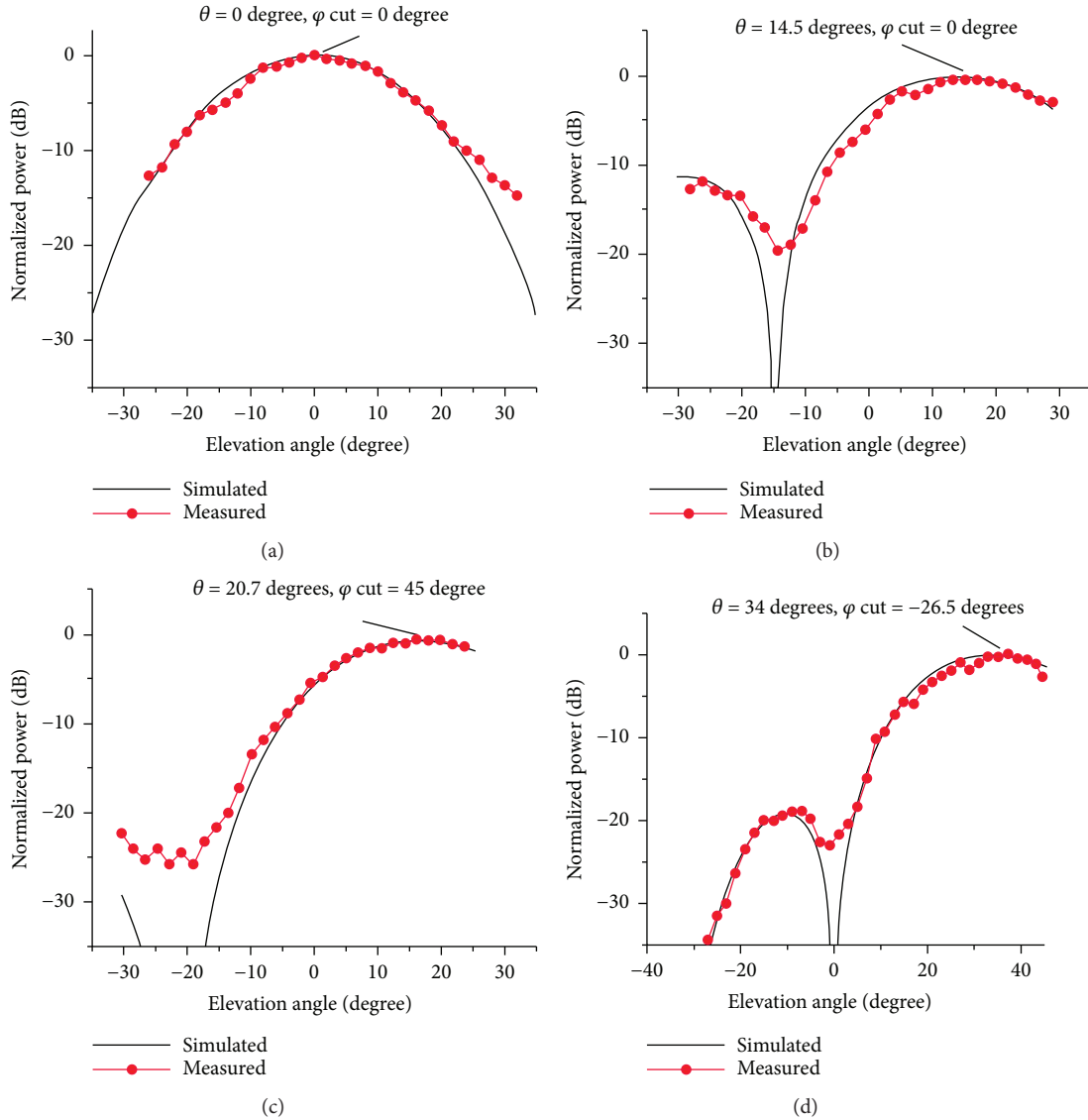


FIGURE 4: Measured and simulated far-field radiation patterns of the printed PAA system at 5 GHz steering at (a)  $\theta = 0$ ,  $\varphi = 0$ ; (b)  $\theta = 14.5$ ,  $\varphi = 0$ ; (c)  $\theta = 20.7$ ,  $\varphi = -45$ ; and (d)  $\theta = 34$ ,  $\varphi = -26.5$  [39].

interconnects were realized through lamination and vias. The antenna was designed to work at 5 GHz for Mars communication sponsored by NASA Glenn Research Center. Figure 4 compares the measured and simulated far-field radiation patterns at four different steering angles at 5 GHz [39]. Without counting the loss of the transmission line, the gain of the fully printed PAA was as high as 14.6 dBi with an efficiency of 58%.

Compared to traditional antenna design, this lightweight, flexible, and conformal PAA is a promising candidate for on Mars communication, flexible portable wireless systems, as well as other airborne communication systems. Inkjet printing provides resolution down to 15 microns, which is important for high frequency applications. Furthermore, as shown in the above example, CNT FETs are printed together with the antenna patch to provide steering capability. The CNT FET is a four-layer (source/drain, channel, dielectric, and gate) 3D device with a channel size of 80 microns, which

could not be realized with other flexible antenna technologies. Even though the viscosity of inkjet printable materials is limited to 8 to 12 cP, there are plenty of materials in the market that are within the range.

The following section describes another fabrication technique named aerosol jet printing technique. This printing technique not only provides resolution down to 5 microns but also is able to process materials with the viscosity from 1 to 1000 cP, which provides a wide choice of materials.

**2.2. 3D Aerosol Jet Printing Technique.** Aerosol jet printing, also known as maskless mesoscale material deposition or M3D [40], is another material deposition technique for printed electronics. Figure 5 shows the aerosol jet printing process. It begins with the atomization of ink by heating it up to 80°C [40]. Aerosol jet produces droplets of one to two micrometers in diameter. Finally, the atomized droplets are entrained in a gas stream and delivered to the print head.

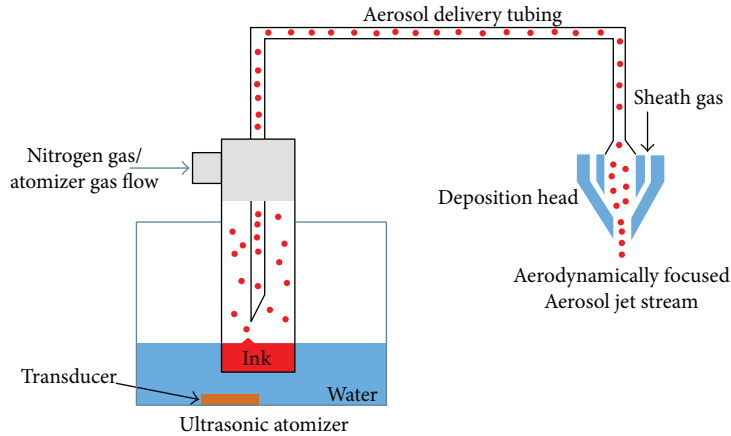


FIGURE 5: Aerosol jet printing operation process [41].

TABLE 1: Compatible materials for aerosol jet printing [43].

Conductive metals	Nanoparticle Ag, Au, Pt, Pd, ...
Conductive polymers	PEDOT, carbon nanotubes (CNTs)
Semiconductors	P3HT, PQT, CNTs, ...
Resistors	Carbon, metal oxide, ...
Dielectric	Epoxy, acrylic, PMMA, polyamide, PTFE, ...

An annular clean gas flow is also introduced around the aerosol stream, to pivot the droplets into a collimated beam of material. A converging nozzle is the exit path of the combined gas flow; it compresses the gas stream to a diameter as small as  $10\ \mu\text{m}$  [41].

Pre-designed electrical components are printed by moving the print head conjugated with a mechanically movable stop/start shutter. The minimum printing resolution of an Optomec Aerosol Jet printer (AJ 300) is  $5\ \mu\text{m}$ – $10\ \mu\text{m}$  [40–42], with single-layer thicknesses from tens of nanometers to  $>10\ \mu\text{m}$  [41]. For the application of millimeter size features and surface coating, a wide nozzle print head allows efficient printing. It should be noted that all the fabrication by this technique occurs without the use of any vacuum or pressure chambers at room temperature. Generally, very little splatter or overspray from the droplets occurs despite the high velocity of the printing process [42].

Literature review shows that a wide range of materials have been successfully deposited with the aerosol jet process which includes diluted thick film pastes, thermosetting polymers such as UV-curable epoxies, solvent-based polymers like polyurethane and polyimide, and biologic materials [43].

**2.2.1. Material Compatibility.** The aerosol jet can process a wide range of materials required for the manufacturing of printed electronic materials, such as conductors, semiconductors, resistors, and dielectrics/insulators [44]. Table 1 shows the combinations of materials printed layerwise to create differing functionality [43].

**2.2.2. Aerosol Jet-Printed Antenna.** Figure 6 shows the first printed near-field antenna by Optomec fabricated by an

aerosol jet printer for near-field communication (NFC) [43]. According to the report from Optomec, it is found that the field strength of the printed antenna is 40% lower than other traditional antennas, but it meets ISO 14443 standard for operating at 13.56 MHz in close proximity with a reader antenna [43]. Additionally, the performance was also improved later through additional power input or a lower resistance coil [43].

The intended application for this antenna was mainly for NFC, which was used in portable device such as a smartphone, to establish communication by bringing them within 4 cm (1.6 in) of each other. It also can be used in contactless payment systems, similar to those used in credit cards and electronic ticket smartcards, and allows mobile payment systems. Furthermore, this antenna can be used for social networking and sharing contacts, photos, videos, or files.

Aerosol jet printing provides resolution down to 5 microns, which is by far the most accurate fabrication technology. It is also widely adopted to print micron-size active components. It is also capable to process materials with the viscosity from 1 to 1000 cP, which provides a wide choice of materials.

The following section describes screen printing techniques for the fabrication of conformal antenna, which is one of the most cost-effective and simplest fabrication techniques used by manufacturers.

**2.3. Antenna Fabrication by Screen Printing.** Screen printing is based on a twisted screen with different thicknesses and thread densities. A rubber-edge blade is driven down forcing the screen into contact, producing a printed pattern with the glued substrate [45]. This process forces the ink to be ejected into the exposed areas of the screen as well on the substrate, and thus, the desired pattern is formed. The most common materials used in this technology are polyester and stainless steel. Figure 7 shows the screen printing process and fabricated flexible antenna, reported in [45].

Several RFIDs and flexible transparent antennas have been prototyped successfully using screen printing [46–48]. Figure 7(b) shows a successful fabrication of a flexible

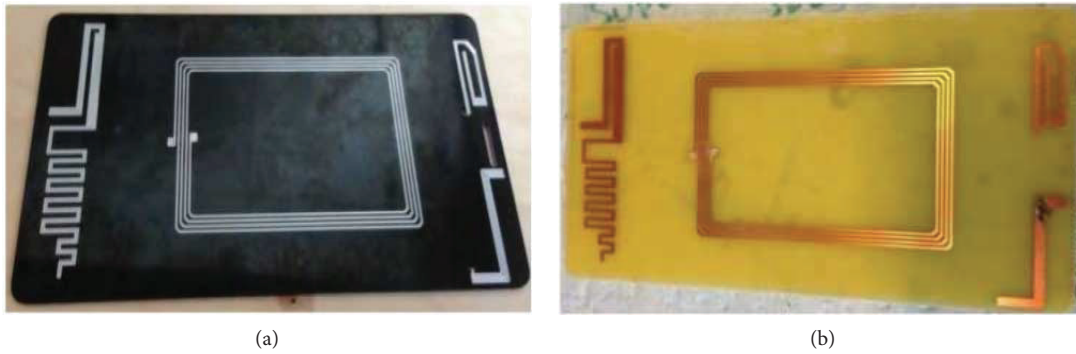


FIGURE 6: Aerosol jet-printed near-field antenna by Optomec for near-field communication. (a) Printed with silver nanoparticle ink. (b) Printed with Cu nanoparticle ink [43].

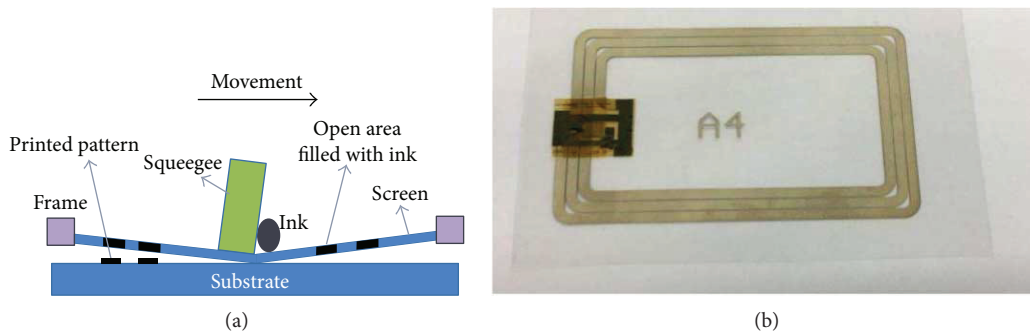


FIGURE 7: (a) Screen printing process [6]. (b) Screen-printed flexible antenna [45].

antenna for an interrogator application. The antenna demonstrated in this system was screen-printed by Quad Industries, utilizing printing inks developed by Agfa [45].

There are disadvantages associated with this technique, which includes the limited control over the thickness, number of passes, and resolution of the printed patterns. Layer consistency is also a challenge because of the change of ink viscosity and surface energy of the substrate due to the artifacts left by thermal curing of solvent-based inks [48].

In summary, 3D aerosol and inkjet printing are promising technologies that could be used to fabricate accurate antenna geometries with resolution down to 5–10 microns and active components such as switches and amplifiers. It could even be used to directly print on fabrics for wearable antennas.

### 3. Wearable Textile Antennas

Due to the recent miniaturization of wireless devices, the utilization of wearable textiles in antenna segment has been seen on the rise. A wearable antenna is a part of the clothing used for communication purposes, which also includes tracking and navigation, mobile computing, and public safety. It can also be used in telemedicine application.

*3.1. Passive Wearable Antennas.* One of the first proposals on wearable antennas appeared in 2001 [49]. The Salonen et al. proposed a GPS antenna with circular polarization where they have experimented five different synthetic

fabric materials as dielectric substrates in 2004 [50]. Copper tape was used to make the conductive parts. The dielectric synthetic materials were from: Vellux® (5 mm thick fabric), synthetic felt (4 mm thick, nonwoven), Delinova 200® (made of polyamide Cordura® fibres laminated with Gore-Tex membrane and having a thickness of 0.5 mm), fleece (a very soft polyester fabric with 4 mm thickness), and upholstery fabric [50, 51]. The relative permittivity of the five fabrics was also measured, and the values ranged between 1.1 and 1.7 [50, 51]. Among all five studied fabrics, polyamide fibre (Cordura) was the most promising and interesting fabric for the development of a flexible antenna [51]. This material also has a property of constant thickness and high resistance, which allows this material to have more stable geometric dimensions for the antenna application.

Salonen et al. [52] presented a planar inverted-F antenna (PIFA), built on a flexible substrate for dual-band operation. Basically, it was intended to be placed on a shirt sleeve and operated at 900 MHz and 2.4 GHz [52]. The antenna showed good performance at upper band frequency (2.4 GHz) even with a human body present, but lower band frequency (900 MHz) radiation was not achieved [52].

Figure 8 shows the placement of wearable antenna on a human body [53] and fabricated textile patch antenna [54]. The material was a woven conductive fabric with a thickness of 0.125 mm and 0.05  $\Omega$ /square surface resistance [53]. The material selection for a wearable antenna is a critical step to be robust and suitable for certain applications.

In [55], an aramid woven fabric which is flame resistant and suitable for integration into fire fighter garments



FIGURE 8: (a) Wearability of the antenna [53]. (b) Fabricated textile patch antennas. From left to right: applying copper tape, woven copper thread, and conductive spray [54].



FIGURE 9: Embroidered spiral antenna. (a) Top view. (b) Zoomed-in view [60].

is reported. A highly conductive nylon fabric was used as the conductor. It has three metalized layers (Ni/Cu/Ag) which provide high conductivity with the sheet resistance of  $0.03 \Omega/\text{square}$ . Moreover, it also can provide flexibility and protection against corrosion.

Spiral antennas are one the most popular antennas because of their large bandwidth and low-profile properties. Various research papers have been published on the fabrication process of wearable spiral antennas [56–59]. The idea of embroidered spiral antennas is comparatively new. Investigations are still ongoing [57–59]. The density of the embroidered threads has been significantly elevated with the largest one reported in [58]. Figure 9 shows the embroidered spiral antenna. The antenna was fed by a  $50 \Omega$  flexible coaxial cable.

Due to the large size and weight of the specific anthropomorphic mannequin (SAM) phantom, there is inherent difficulty in measuring the wearable spiral antenna with the conventional far-field measurement technique [60]. A novel cylindrical near-field measurement methodology was adopted to get the simulation results in Figures 10(a) and 10(b). The distance reported was 2 mm between the antenna and a human body during testing. All the separations have [S11] generally lower than  $-5 \text{ dB}$  for almost the

entire frequency range above 0.5 GHz. The antenna is curved on the  $y$ -axis with  $30^\circ$ ,  $40^\circ$ , and  $50^\circ$  curvature angles, respectively.

For the past few years, research has been going on to find out the effect of sewing types on the performance of different types of embroidered antennas. Three different sewing types have been studied in [61]. For a meandered sleeve monopole antenna, the sewing direction of spiral stitch was always along the direction of meandered line, so the antenna with spiral stitch has shown better performance. For a disc antenna, the sewing pattern of concentric circle stitch is similar to the current distribution of disc antenna. Therefore, it has demonstrated better performance. Based on this discussion, it can be concluded that the best RF performances can be obtained when the sewing direction is same as the current direction. Thus, different sewing types should be chosen for different antenna designs.

Additionally, [62] has presented the use of embroidered nonuniform mesh patch antennas which reported to maintain good antenna gain and efficiency for significantly reduced special conducting threads usage. It is found that the NMPAs have similar current and electric field distribution as a solid patch antenna at the  $\text{TM}_{01}$  mode. Furthermore, it is worth noting that the actual length of the embroidered

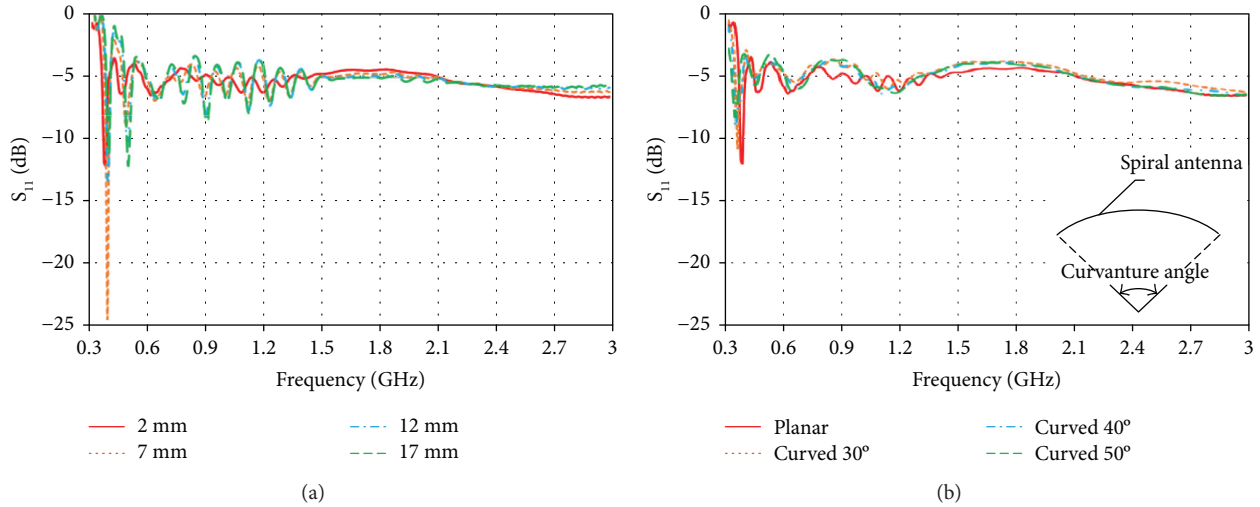


FIGURE 10: Simulated  $|S_{11}|$  of the spiral antenna on the SAM phantom. (a) Planar spiral antenna at various distances from SAM phantom. (b) Different curvatures of the spiral antenna on the SAM phantom [60].

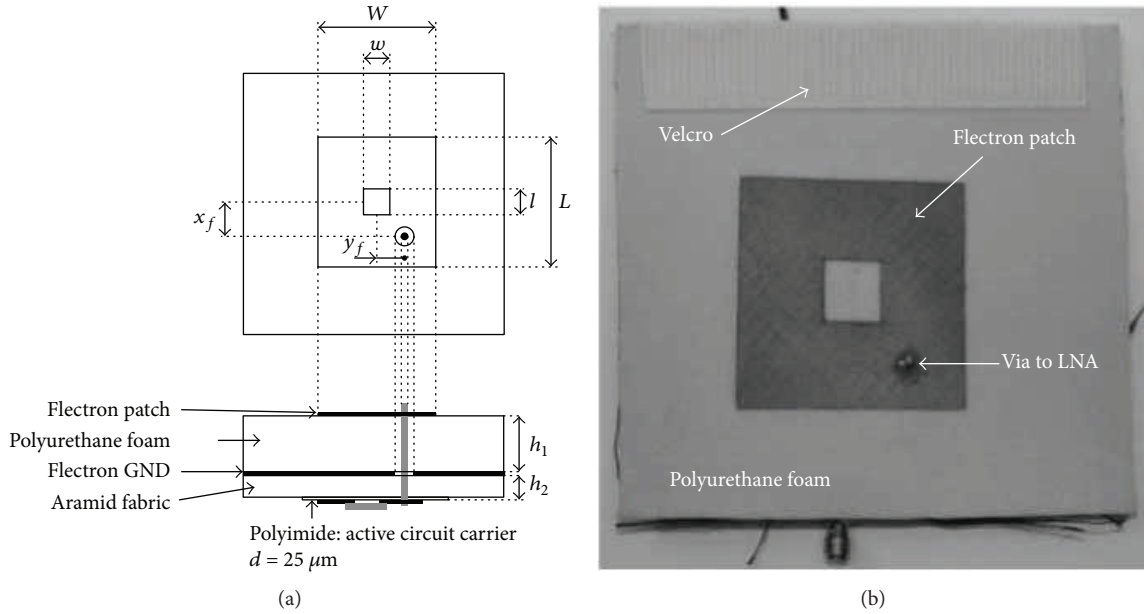


FIGURE 11: (a) Geometry of the active receiving wearable antenna. (b) Top view of the active receiving antenna [63].

stitches is longer than the exterior dimensions of the embroidered patch; thus, the resonant frequency of an embroidered antenna is lower than the copper equivalent due to the extended electrical length.

This paper also shown that fully textile embroidered 5 GHz NMPA had 60% antenna efficiency with only 20% of the conductor coverage which is a highly satisfying outcome in terms of cost, flexibility, and antenna performance. Therefore, it will benefit potential wearable antenna applications since the cost of manufacturing and materials can be reduced.

3.2. Active Wearable Antennas. The first active wearable textile antenna was designed in 2010. This was an active

receiving textile antenna in 2.45 GHz ISM band and was addressed for the use in personal area networks [63]. The antenna was designed by integrating a low-noise amplifier on hybrid textile substrate and connecting it directly underneath a wearable patch antenna, as shown in Figure 11 [63]. Furthermore, the antenna gain was reported to be 5 dBi and a noise figure of about 1.3 dB.

After the fabrication of the first active textile antenna, the research moved towards application sector. A high degree of robustness, reliability, and autonomy is required for a wireless and wearable monitoring system without adding too much weight. In 2013 [64], active textile antenna was designed and fabricated for three different applications such as sensing, localization, and communication applications.

After the fabrication of the full textile antenna, the fabricated area was further reused by placing active electronic elements underneath the antenna patch. Finally, the fabrication process was ended by adding an energy harvester directly on top of the antenna patch.

An active wearable antenna was also reported in [65] for the global positioning system (GPS) and satellite phone application. This article discussed about the design procedure of a combined GPS and iridium active antenna. During the construction of the square patch antenna, a flexible foam and fabric substrates were used. Then, the conductors were etched on thin copper-on-polyimide films. Later, a compact low-noise amplifier chip was integrated underneath the feed substrate. Finally, after simulation, they reported that the active antenna exhibited a gain higher than 25 dBi and a 3 dB axial ratio bandwidth exceeding 183 MHz in free-space conditions.

A novel autonomous wearable coordinated wireless sensor node network was developed in [66], where each flexible textile node was used for synchronous measurements and transmitting the data to a base station. On-body node-to-node communication was exploited for synchronize measurements. Finally, multiple autonomous nodes were used to share sensor data between these nodes. The extensive application area of this flexible node system includes the various rescue missions of workers and law enforcement officers, as well as the military and civilians.

**3.3. Fabrication Challenges.** The fabrication of the embroidered wearable antenna is a challenging process. The tension of the threads causes warping of the substrate and the antenna. Also, when a wearable textile antenna is worn on the human body, long term electromagnetic radiation poses potential health risks. Minimization of specific absorption rate is therefore a challenge for wearable patch antennas.

Additionally, patch antenna is usually low profile and easy to fabricate; thus, patch antenna is a good candidate as wearable antenna. The use of textile materials as substrates reduces surface wave losses and enhances the overall bandwidth.

**3.4. Effect of Relative Humidity on Wearable Antennas.** The influence of environmental relative humidity on textile antennas is investigated in [67]. All antenna prototypes were conditioned in a climatic test cabinet under the range of relative humidity from 10% to 90%. For each relative humidity, the return loss characteristic was measured. Figure 12 displays the shifting and broadening of the return loss characteristic for a cotton-based antenna which is designed to operate at 2.45 GHz.

From the figure above, it can be concluded that the influence of relative humidity depends on both electromagnetic properties of the substrate material and relative permittivity. Also, the loss tangent increases with increasing relative humidity of the environment in which the antennas operate. This is a result of a change in electrical permittivity and loss tangent of the substrate material, influenced by the presence of moist.

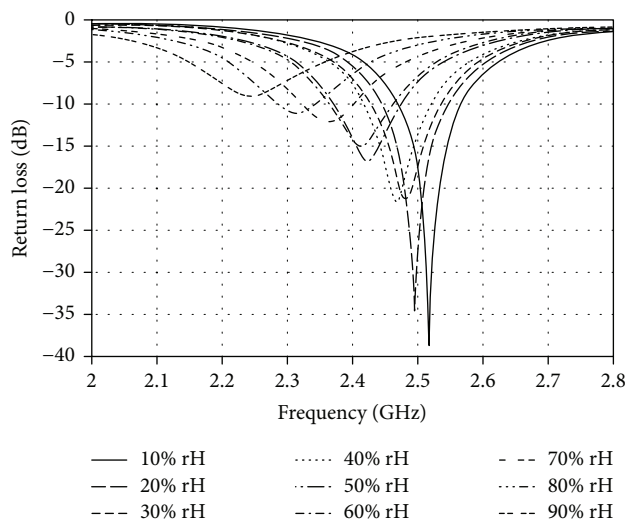


FIGURE 12: The effect of relative humidity on return loss [67].

### 3.5. Impact of Recurrent Washing on Wearable Antennas.

In [68], Björninen et al. reported the impact of recurrent washing on wearable antennas. They studied the impact of recurrent washing on the performance of UHF RFID tags based on an electrotile antenna. It is reported that prior washing the fully functional electrotile tags showed a high attainable read range of 5.5 m, then after washing the tags 7 times in a household washing machine in a 40°C program cycle with detergent reduced the read range to 2.8 m. Thereafter, up to 10 wash repetitions, the performance remained constant.

So, it can be concluded that the recurrent washing of wearable antenna has a negative impact on the performance of the antenna.

In summary, the textile antenna is a promising approach for wearable applications. However, it is limited by choices of suitable fabric and resolution of the antenna geometry. Back radiation, humidity, and washing could be big challenges for practical applications. It is also limited to passive antennas, since active components with micrometer feature size could not be woven into fabrics.

## 4. Substrate-Integrated Waveguide Antennas

Since substrate-integrated waveguide antenna on paper, plastic, and textile is an emerging and promising research area, this session is dedicated to this topic. This topic covers paper-based substrate-integrated waveguide (SIW) components, plastic SIW components and antennas, and wearable textile SIW antennas.

**4.1. Paper-Based SIW Components.** The implementation of SIW structures on paper substrate using inkjet printing was first presented in [69]. Figure 13 shows the SIW interconnects and components that have been fabricated and tested on a multilayer low-cost and eco-friendly paper substrate [69].

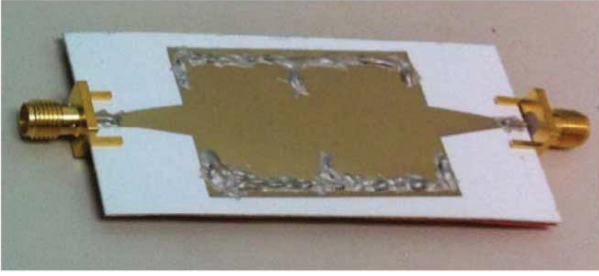


FIGURE 13: Implementation of a paper-based SIW filter [69].

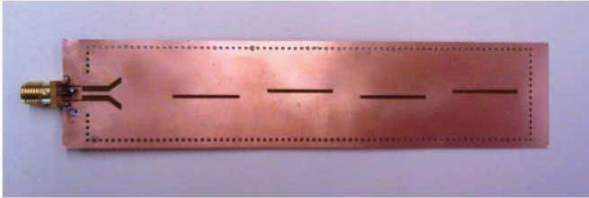


FIGURE 14: Implementation of SIW antenna on plastic substrate [70].

The operating frequency for the paper-based SIW filter was reported from 3 to 10 GHz. It is clearly seen that the achievable performance of paper-based SIW components is still menial to components based on commonly used dielectric material. But, this implementation of SIW structures on paper substrate represents the groundwork for future wireless systems and wearable devices.

**4.2. Plastic SIW Components and Antennas.** Electronic technologies are being converting from rigid to flexible due to low technology cost, available materials, and mechanically flexible substrates. Polyethylene terephthalate (PET) substrate has become an important candidate substrate material for the development of future flexible devices as well as conformal and wearable wireless antenna systems. Figure 14 shows the fabricated SIW antenna on plastic PET substrate. The operating frequency was reported at 5 GHz frequency band [70].

Further performance of the plastic-based flexible antennas was verified after bending. Although the PET substrates have quite a high loss and the performance of the components cannot attain the results as of commonly used dielectric materials, the achieved results represent a fundamental step towards the implementation of cost-effective wireless terminals, which can be eventually integrated with other systems such as energy-harvesting systems, to obtain autonomous nodes for future wireless sensor networks.

**4.3. Wearable Textile SIW Antennas.** Figure 15 illustrates a novel wearable SIW antenna which was fabricated entirely from textile-based materials. The structure consists of a cavity-backed slot antenna which operates in the 2.45 GHz industrial, scientific, and medical band, for short-range communication between rescue workers [71].

During the fabrication process, two conductive fabrics were glued on top of the textile substrate to assemble the

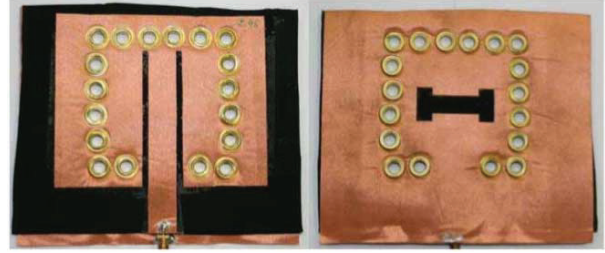


FIGURE 15: Cavity-backed SIW antenna on textile [71].

SIW textile antenna. The structure was then cut through to implement the via holes. Finally, the eyelets were fixed in the holes. The performance of the antenna was measured in terms of the input matching and radiation pattern. The prototype SIW antenna performance was reported to be comparatively good. Additionally, the measurements were also performed on the antenna after bending and integration into clothing which indicated the high-performance system to be suitable for on-body communication.

Finally, a compact and highly integrated wearable textile SIW antenna system was presented in [72]. This compact system was integrated on two flexible solar cells, a flexible power management system, and a microenergy cell. It is reported that the energy harvesting and power management hardware have negligible influence on the performance of the wearable textile antenna, which proves that the selected topology is suitable for a complex-integrated platform and the system could combine the energy scavenged from artificial light in an indoor environment.

In summary, SIW technology offers a simple and cost-effective fabrication process for paper, plastic, and textile substrates. The structure allows easy integration of passive and active components onto the antenna, realizing complete systems on a textile carrier well suited for on-body use.

## 5. Membrane-Based Phased-Array Antenna

In addition to being costly, the conventional phased-array antenna technologies are not a suitable match for future space-based synthetic aperture radar (SAR) applications due to their large mass and stow volume (mass density of 8–15 kg/m<sup>3</sup> for antenna, electronics, and structure). As a result, supporting this huge payload antenna for existing launch vehicles is not practical. However, using flexible electronics and antennas could dramatically reduce the weight (mass density of 2 kg/m<sup>3</sup>), stow volume, and associated cost of space-based SAR [73].

In [73], the architecture of the active membrane phased array is reported as in Figure 16. The active membrane phased array is composed of 2 layers, with radiating patches on one layer and their ground plane on the second layer. The membrane is reported as a 50 μm thick Pyralux® AP™ (DuPont's copper-clad all-polyimide flexible circuit material) with 9 μm copper layers. The T/R electronics are coupled to the patches via slot feeds. The antenna feed details are discussed in [74]. The T/R module, which is independently assembled and attached to the membrane

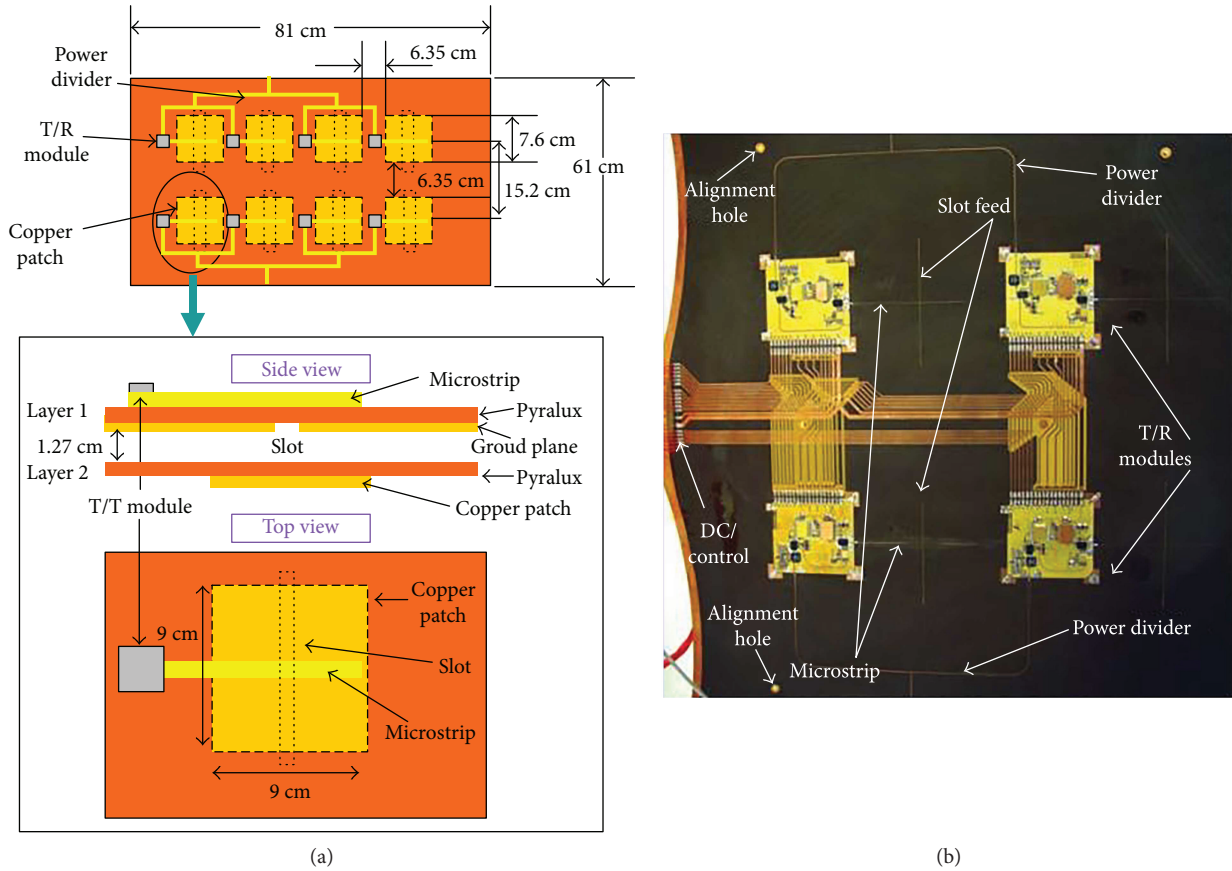


FIGURE 16: Membrane antenna architecture. (a)  $2 \times 4$  element array. Unit cell top and side views. (b) A close-up of the membrane array showing four of the T/R modules of the array [73].

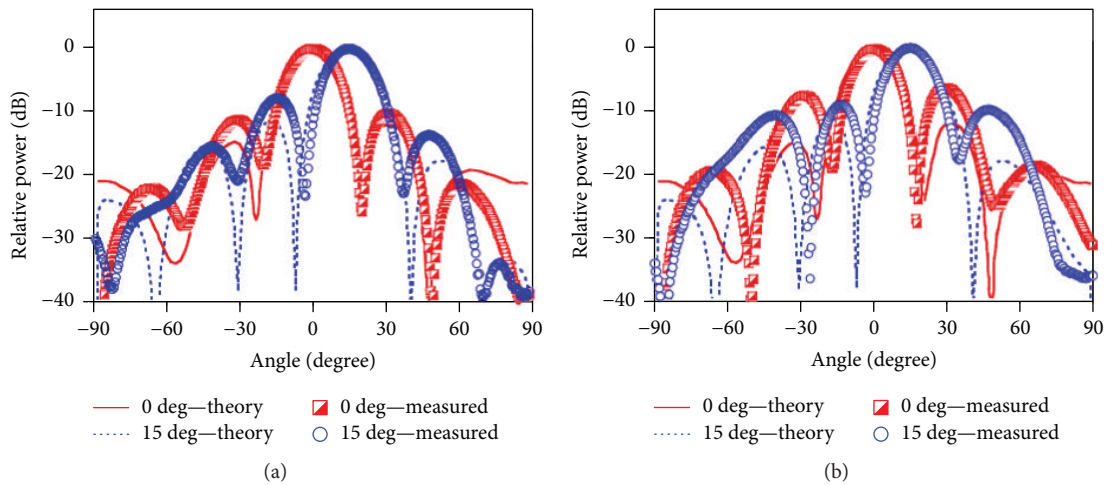


FIGURE 17: (a) Measured and theoretical receive antenna patterns for  $0^\circ$  and  $15^\circ$  steering angles. (b) Measured and theoretical transmit antenna patterns for  $0^\circ$  and  $15^\circ$  steering angles [73].

array, is a hybrid multilayer module on a flexible Pyralux AP substrate.

The measured and theoretical patterns for  $0^\circ$  and  $15^\circ$  steering angles in receive and transmit modes, respectively, are shown in Figure 17 [73]. The cross-polarization patterns

are better than  $-30$  dB for all cases [73]. The main beam is steered to its expected scan angle for all cases.

The membrane antenna is based on copper-clad substrate, which is a subtraction process. In order words, antenna patterns and interconnect lines are produced

using a traditional etching method. The achievable resolution of antenna geometry and interconnect lines limits the application of the technology to simple patterns and low RF frequencies. Furthermore, the subtraction process is not compatible with flexible T/R modules to achieve true flexible active antennas.

## 6. Conclusion

In this review, we have identified and discussed the major fabrication techniques and associated materials used for the fabrication of flexible conformal antennas, including 3D printing technology, wearable textile technology, substrate-integrated waveguide technology, and membrane technology. The membrane antenna is based on copper-clad substrate, which needs to be processed using a traditional etching method. The achievable resolution of antenna geometry and interconnect lines limits the application of the technology to simple patterns and low RF frequencies. The subtraction process is not compatible with true flexible active antennas. The textile antenna is a promising approach for wearable applications due to a comfort level. Active wearable textile antennas were developed incorporating a low-noise amplifier, solar cells, and so on. However, it is limited by choices of suitable fabric and resolution of the antenna geometry. Back radiation, humidity, and washing could be big challenges for practical applications. SIW technology offers a simple and cost-effective fabrication process for paper, plastic, and textile substrates. The structure allows easy integration of passive and active components onto the antenna, realizing complete systems on a textile carrier well suited for on-body use. 3D aerosol and inkjet printing are promising technologies that could be used to fabricate accurate antenna geometries with resolution down to 5–10 microns and active components such as switches and amplifiers. 3D printing makes true flexible active antennas possible. It could even be used to directly print on fabrics for wearable antennas. Attaching 3D-printed flexible and elastic antennas onto fabrics could be another feasible approach for wearable antennas. However, printable nanomaterials are limited for the 3D printing process. The textile, SIW, and membrane antennas cost less to start with, since there is no need for the 3D printers. However, for large volume roll-to-roll fabrication, the cost of the above approaches is similar.

A lot of work has yet to be done to increase the performance of these antennas. To make progress in the development of various conformally flexible antennas, significant amounts of multidisciplinary collaborative efforts are expected, including material, manufacture, engineering, and integration. These efforts will eventually lead to numerous innovative, high-performance, low-cost, rapid deployable, and flexible antennas for various applications in the near future.

## Conflicts of Interest

The authors declare that they have no conflicts of interest.

## Acknowledgments

The authors would like to thank Jack Maceachern for his careful proofreading of this paper.

## References

- [1] J. Hu, "Overview of flexible electronics from ITRI's viewpoint," in *2010 28th VLSI Test Symposium (VTS)*, pp. 84–84, Santa Cruz, CA, USA, April 2010.
- [2] A. Nathan and B. R. Chalamala, "Special issue on flexible electronics technology, part 1: systems and applications," *Proceedings of the IEEE*, vol. 93, no. 7, pp. 1235–1238, 2005.
- [3] D. T. Pham, H. Subbaraman, M. Y. Chen, X. Xu, and R. T. Chen, "Light weight and conformal 2-bit,  $1 \times 4$  phased-array antenna with CNT-TFT-based phase shifter on a flexible substrate," *IEEE Transactions on Antennas and Propagation*, vol. 59, no. 12, pp. 4553–4558, 2011.
- [4] L. Zheng, M. B. Nejad, S. Rodriguez, L. Zhang, C. Chen, and H. Tenhunen, "System-on-flexible-substrates: electronics for future smart-intelligent world," in *2006 HDP'06 Conference on High Density Microsystem Design and Packaging and Component Failure Analysis*, pp. 29–36, Shanghai, China, June 2006.
- [5] R. J. Mailloux, *Phased Array Antenna Handbook-Second Edition*, Artech House, London, 2005.
- [6] H. R. Khaleel, H. M. Al-Rizzo, and A. I. Abbosh, *Design, Fabrication, and Testing of Flexible Antennas-Handbook*, Intech Open Limited, London, 2013.
- [7] A. Nathan, A. Ahnood, M. T. Cole et al., "Flexible electronics: the next ubiquitous platform," *Proceedings of the IEEE*, vol. 100, no. Special Centennial Issue, pp. 1486–1517, 2012.
- [8] S. Zhang, "Design advances of embroidered fabric antennas," Loughborough University, 2014, <https://dspace.lboro.ac.uk/dspace-jspui/handle/2134/>.
- [9] M. Kubo, X. Li, C. Kim et al., "Stretchable microfluidic radio-frequency antennas," *Advanced Materials*, vol. 22, no. 25, pp. 2749–2752, 2010.
- [10] D. E. Anagnostou, A. A. Gheethan, A. K. Amert, and K. W. Whites, "A direct-write printed antenna on paper-based organic substrate for flexible displays and WLAN applications," *Journal of Display Technology*, vol. 6, no. 11, pp. 558–564, 2010.
- [11] 2016, <http://www.antenna-theory.com>, <http://www.antenna-theory.com/basics/efficiency.php>.
- [12] S. Zafri, *Experimental Investigation of Dielectric Strength of Polymer Film*, University of Windsor, Ontario, Canada, 2001, <https://www.collectionscanada.gc.ca/obj/s4/f2/dsk3/ftp04/MQ62224.pdf>.
- [13] "Selecting conductive materials for manufacturing inks (metallics, nanoparticles and graphene provide unique properties that are key to driving performance and growth)," 2015, <http://www.printedelectronicsnow.com>, Printed Electronics.
- [14] 2018, <http://www.novacentrix.com>, <https://www.novacentrix.com/products/metalon-inks/inkjet>.
- [15] S. B. Fuller, E. J. Wilhelm, and J. M. Jacobson, "Ink-jet printed nanoparticle microelectromechanical systems," *Journal of Microelectromechanical Systems*, vol. 11, no. 1, pp. 54–60, 2002.
- [16] D. Wallace, D. Hayes, T. Chen et al., "Ink-jet as a MEMS manufacturing tool," in *2007 First International Conference on Integration and Commercialization of Micro and Nanosystems*, pp. 1161–1168, Sanya, Hainan, China, January 2007.

- [17] C.-H. Tien, C.-H. Hung, and T.-H. Yu, "Microlens arrays by direct-writing inkjet print for LCD backlighting applications," *Journal of Display Technology*, vol. 5, no. 5, pp. 147–151, 2009.
- [18] T. Sekitani, M. Takamiya, Y. Noguchi et al., "A large-area wireless power-transmission sheet using printed organic transistors and plastic MEMS switches," *Nature Materials*, vol. 6, no. 6, pp. 413–417, 2007.
- [19] J. Lessing, A. C. Glavan, S. B. Walker, C. Keplinger, J. A. Lewis, and G. M. Whitesides, "Inkjet printing of conductive inks with high lateral resolution on omniphobic "R<sup>F</sup> paper" for paper-based electronics and MEMS," *Advanced Materials*, vol. 26, no. 27, pp. 4677–4682, 2014.
- [20] A. A. Bessonov and M. N. Kirikova, "Flexible and printable sensors," *Nanotechnologies in Russia*, vol. 10, no. 3-4, pp. 165–180, 2015.
- [21] R. J. Houben, *Equipment for Printing of High Viscosity Liquids and Molten Metals*, University of Twente, Enschede, Netherlands, 2012.
- [22] B. K. Gale, M. A. Eddings, S. O. Sundberg, A. Hatch, J. Kim, and T. Ho, *Comprehensive Microsystems - Low-Cost MEMS Technologies*, Elsevier, London, 2008.
- [23] J. Courbat, Y. Kim, D. Briand, and N. De Rooij, "Inkjet printing on paper for the realization of humidity and temperature sensors," in *2011 16th International Solid-State Sensors, Actuators and Microsystems Conference (TRANSDUCERS)*, pp. 1356–1359, Beijing, China, June 2011.
- [24] T. Kawase, H. Siringhaus, R. H. Friend, and T. Shimoda, "Inkjet printed via-hole interconnections and resistors for all-polymer transistor circuits," *Advanced Materials*, vol. 13, no. 21, pp. 1601–1605, 2001.
- [25] S. H. Ko, J. Chung, N. Hotz, K. H. Nam, and C. P. Grigoropoulos, "Metal nanoparticle direct inkjet printing for low-temperature 3D micro metal structure fabrication," *Journal of Micromechanics and Microengineering*, vol. 20, no. 12, article 125010, 2010.
- [26] K. Black, J. Singh, D. Mehta, S. Sung, C. J. Sutcliffe, and P. R. Chalker, "Silver ink formulations for sinter-free printing of conductive films," *Scientific Reports*, vol. 6, no. 1, article 20814, 2016.
- [27] S. F. Jahn, T. Blaudeck, R. R. Baumann et al., "Inkjet printing of conductive silver patterns by using the first aqueous particle-free MOD ink without additional stabilizing ligands," *Chemistry of Materials*, vol. 22, no. 10, pp. 3067–3071, 2010.
- [28] O. Pabst, J. Perelaer, E. Beckert, U. S. Schubert, R. Eberhardt, and A. Tünnermann, "All inkjet-printed piezoelectric polymer actuators: characterization and applications for micropumps in lab-on-a-chip systems," *Organic Electronics*, vol. 14, no. 12, pp. 3423–3429, 2013.
- [29] P. Calvert, "Inkjet printing for materials and devices," *Chemistry of Materials*, vol. 13, no. 10, pp. 3299–3305, 2001.
- [30] Z. Zhang, X. Zhang, Z. Xin, M. Deng, Y. Wen, and Y. Song, "Synthesis of monodisperse silver nanoparticles for ink-jet printed flexible electronics," *Nanotechnology*, vol. 22, no. 42, article 425601, 2011.
- [31] F. Zhang, C. Tuck, R. Hague et al., "Inkjet printing of polyimide insulators for the 3D printing of dielectric materials for microelectronic applications," *Journal of Applied Polymer Science*, vol. 133, no. 18, 2016.
- [32] G.-K. Lau and M. Shrestha, "Ink-jet printing of micro-electromechanical systems (MEMS)," *Micromachines*, vol. 8, no. 6, p. 194, 2017.
- [33] H. F. Schlaak, M. Jungmann, M. Matysek, and P. Lotz, "Novel multilayer electrostatic solid-state actuators with elastic dielectric," in *Proceedings Volume 5759, Smart Structures and Materials 2005: Electroactive Polymer Actuators and Devices (EAPAD)*, pp. 121–133, San Diego, CA, USA, May 2005.
- [34] D. T. K. Pham, "Carbon nanotube thin film transistor on flexible substrate and its applications as switches in a phase shifter for a flexible phased-array antenna," University of Texas, Austin, 2010, <https://repositories.lib.utexas.edu>.
- [35] N. D. Sankur, *Flexible Electronics: Materials and Device Fabrication*, Virginia Polytechnic Institute and State University, 2005, <https://theses.lib.vt.edu>.
- [36] H. P. Le, "Progress and trends in ink-jet printing technology," *Journal of Imaging Science and Technology*, vol. 42, no. 1, pp. 49–62, 1998.
- [37] J. Brünahl, *Physics of Piezoelectric Shear Mode Inkjet Actuators*, Royal Institute of Technology, 2003, <http://www.diva-portal.org/smash/get/diva2:9351/FULLTEXT01.Pdf>.
- [38] W. Su, B. S. Cook, Y. Fang, and M. M. Tentzeris, "Fully inkjet-printed microfluidics: a solution to low-cost rapid three-dimensional microfluidics fabrication with numerous electrical and sensing applications," *Scientific Reports*, vol. 6, no. 1, 2016.
- [39] H. Subbaraman, D. T. Pham, X. Xu et al., "Inkjet-printed two-dimensional phased-array antenna on a flexible substrate," *IEEE Antennas and Wireless Propagation Letters*, vol. 12, pp. 170–173, 2013.
- [40] M. Hedges and A. B. Marin, "3D aerosol jet® printing-adding electronics functionality to RP/RM," in *DDMC 2012 Conference*, pp. 1–5, Berlin, 2012.
- [41] S. Agarwala, G. L. Goh, and W. Y. Yeong, "Optimizing aerosol jet printing process of silver ink for printed electronics," *IOP Conference Series: Materials Science and Engineering*, vol. 191, article 012027, 2017.
- [42] R. Eckstein, "Aerosol jet printed electronic devices and systems," 2017, <https://www.optomec.com/printed-electronics/aerosol-jet-technology/>.
- [43] "Direct printing of 3D antenna and sensors for mobile device applications and the internet of things," 2017, <https://www.optomec.com/printed-electronics/aerosol-jet-core-applications/internet-of-things/>, <http://www.Optomec.com>.
- [44] T. Blumenthal, V. Fratello, G. Nino, and K. Ritala, *Aerosol Jet® Printing onto 3D and Flexible Substrates*, Quest Integrated Inc., Kent, WA, USA, 2017.
- [45] I. G. Elinoff, "Introducing a screen printed, flexible antenna for RFID devices," 2017, [https://www.electronicproducts.com/Semiconductors/Applications/Introducing\\_a\\_screen\\_printed\\_flexible\\_antenna\\_for\\_RFID\\_devices.aspx](https://www.electronicproducts.com/Semiconductors/Applications/Introducing_a_screen_printed_flexible_antenna_for_RFID_devices.aspx).
- [46] R. Valmiro, H. Kitaguti, and S. E. Barbin, "A silk-screen printed RFID tag antenna," in *2015 Asia-Pacific Microwave Conference (APMC)*, Nanjing, China, December 2015.
- [47] A. Moschos, T. Syrovoy, L. Syrova, and G. Kaltsas, "A screen-printed flexible flow sensor," *Measurement Science and Technology*, vol. 28, no. 5, article 055105, 2017.
- [48] PCI, "Dynamic surface tension and surface energy in ink formulations and substrates," 2001, <https://www.pcimac.com/articles/85879-dynamic-surface-tension-and-surface-energy-in-ink-formulations-and-substrates>, <http://www.pcimac.com>.
- [49] B. Gupta, S. Sankaralingam, and S. Dhar, "Development of wearable and implantable antennas in the last decade: a

- review,” in *2010 10th Mediterranean Microwave Symposium*, pp. 251–267, Guzelyurt, Cyprus, August 2010.
- [50] P. Salonen, Y. Rahmat-Samii, M. Schaffrath, and M. Kivikoski, “Effect of textile materials on wearable antenna performance: a case study of GPS antennas,” in *2004 IEEE Antennas and Propagation Society International Symposium*, vol. 1, pp. 459–462, Monterey, CA, USA, June 2004.
- [51] R. Salvado, C. Loss, R. Gonçalves, and P. Pinho, “Textile materials for the design of wearable antennas: a survey,” *Sensors*, vol. 12, no. 11, pp. 15841–15857, 2012.
- [52] P. Salonen, L. Sydanheimo, and M. Keskilammi, “A small planar inverted-F antenna for wearable applications,” in *1999. Digest of Papers. The Third International Symposium on Wearable Computers*, San Francisco, CA, USA, October 1999.
- [53] M. Tanaka and J. Jang, “Wearable microstrip antenna,” *IEEE Antennas and Propagation Society International Symposium*, vol. 2, pp. 704–707, 2003.
- [54] J. G. Santos, A. Alomainy, and Y. Hao, “Textile antennas for on-body communications: techniques and properties,” in *The Second European Conference on Antennas and Propagation, EuCAP 2007*, pp. 1–4, Edinburgh, UK, 2007.
- [55] C. Hertleer, L. Van Langenhove, H. Rogier, and L. Vallozzi, “A textile antenna for fire fighter garments,” 2015, <https://www.researchgate.net/publication/268414746>.
- [56] H. Abufanas, R. J. Hadi, C. Sandhagen, and A. Bangert, “New approach for design and verification of a wideband Archimedean spiral antenna for radiometric measurement in biomedical applications,” in *2015 German Microwave Conference (GeMiC)*, pp. 127–130, Nuremberg, Germany, March 2015.
- [57] A. Kiourti, J. Zhong, and J. L. Volakis, “Conformal spiral antenna based on conductive textile threads for load bearing applications,” in *International Workshop on Antenna Technology: Small Antennas, Innovative Structures and Application*, pp. 1–21, Orlando, FL, USA, 2016.
- [58] B. Ivšić, A. Galoić, and D. Bonefačić, “Embroidered textile logarithmic spiral antenna and its energy efficiency,” in *2015 57th International Symposium ELMAR (ELMAR)*, pp. 157–160, Zadar, Croatia, September 2015.
- [59] Z. Wang, L. Z. Lee, and J. L. Volakis, “A 10 : 1 bandwidth textile-based conformal spiral antenna with integrated planar balun,” in *2013 IEEE Antennas and Propagation Society International Symposium (APSURSI)*, pp. 220–221, Orlando, FL, USA, July 2013.
- [60] S. Zhang, A. Paraskevopoulos, C. Luxey, J. Pinto, and W. Whittow, “Broad-band embroidered spiral antenna for off-body communications,” *IET Microwaves, Antennas & Propagation*, vol. 10, no. 13, pp. 1395–1401, 2016.
- [61] Y. P. Huang, “Effect of sewing types on flexible embroidery antennas in UHF band,” in *2013 European Microwave Conference (EuMC)*, pp. 88–91, Nuremberg, Germany, October 2013.
- [62] S. Zhang, W. Whittow, R. Seager, A. Chauraya, and J. (Y.). C. Vardaxoglou, “Non-uniform mesh for embroidered microstrip antennas,” *IET Microwaves, Antennas & Propagation*, vol. 11, no. 8, pp. 1086–1091, 2017.
- [63] F. Declercq and H. Rogier, “Active integrated wearable textile antenna with optimized noise characteristics,” *IEEE Transactions on Antennas and Propagation*, vol. 58, no. 9, pp. 3050–3054, 2010.
- [64] H. Rogier, S. Agneessens, A. Dierck et al., “Active textile antennas in professional garments for sensing, localisation and communication,” in *2013 European Microwave Conference (EuMC)*, pp. 850–853, Nuremberg, Germany, 2013.
- [65] A. Dierck, H. Rogier, and F. Declercq, “A wearable active antenna for global positioning system and satellite phone,” *IEEE Transactions on Antennas and Propagation*, vol. 61, no. 2, pp. 532–538, 2013.
- [66] P. Vanveerdeghem, P. van Torre, C. Stevens, J. Knockaert, and H. Rogier, “Synchronous wearable wireless body sensor network composed of autonomous textile nodes,” *Sensors*, vol. 14, no. 10, pp. 18583–18610, 2014.
- [67] C. Hertleer, A. van Laere, H. Rogier, and L. van Langenhove, “Influence of relative humidity on textile antenna performance,” *Textile Research Journal*, vol. 80, no. 2, pp. 177–183, 2009.
- [68] T. Björninen, J. Virkki, L. Sydänheimo, and L. Ukkonen, “Impact of recurrent washing on the performance of electro-textile UHF RFID tags,” in *2014 IEEE RFID Technology and Applications Conference (RFID-TA)*, pp. 251–255, Tampere, Finland, September 2014.
- [69] R. Moro, M. Bozzi, S. Kim, and M. Tentzeris, “Novel inkjet-printed substrate integrated waveguide (SIW) structures on low-cost materials for wearable applications,” in *2012 42nd European Microwave Conference (EuMC)*, pp. 72–75, Amsterdam, Netherlands, November 2012.
- [70] R. Moro, A. Collado, S. Via, A. Georgiadis, and M. Bozzi, “Plastic-based substrate integrated waveguide (SIW) components and antennas,” in *2012 42nd European Microwave Conference (EuMC)*, pp. 1007–1010, Amsterdam, Netherlands, November 2012.
- [71] R. Moro, S. Agneessens, H. Rogier, and M. Bozzi, “Wearable textile antenna in substrate integrated waveguide technology,” *Electronics Letters*, vol. 48, no. 16, pp. 985–987, 2012.
- [72] S. Lemey and H. Rogier, “Substrate integrated waveguide textile antennas as energy harvesting platforms,” in *2015 International Workshop on Antenna Technology (iWAT)*, pp. 23–26, Seoul, South Korea, March 2015.
- [73] A. Moussessian, L. Del Castillo, J. Huang et al., “An active membrane phased array radar,” in *2005 IEEE MTT-S International Microwave Symposium Digest*, p. 4, Long Beach, CA, USA, June 2005.
- [74] J. Huang and A. Moussessian, “Thin-membrane aperture-coupled L-band patch antenna,” in *2004. IEEE Antennas and Propagation Society International Symposium*, pp. 2388–2391, Monterey, CA, USA, June 2004.

## Research Article

# Design of Low-Complexity Hybrid Precoder and Inkjet-Printed Antenna Array for Massive MIMO Downlink Systems

Subitha D  and Mathana J M

*S.A. Engineering College, Anna University, Department of Electronics and Communication Engineering, Chennai, India*

Correspondence should be addressed to Subitha D; [subithab@saec.ac.in](mailto:subithab@saec.ac.in)

Received 25 August 2017; Revised 15 January 2018; Accepted 31 January 2018; Published 24 April 2018

Academic Editor: Maggie Y. Chen

Copyright © 2018 Subitha D and Mathana J M. This is an open access article distributed under the Creative Commons Attribution License, which permits unrestricted use, distribution, and reproduction in any medium, provided the original work is properly cited.

The dramatically growing mobile communication industry necessitates the demand for the speedy and error-free connectivity at considerably low cost for the billions of users. This is made possible only through the technological advancements that replace the current 4G wireless systems by 5G. Massive MIMO is the key technology used in 5G that offers spectral efficiency of up to 3 times and throughput of up to 10 times the current 4G. The additional antennas used in massive MIMO systems help in many ways but lack in complexity. Hence, in this paper, we propose two design methodologies to reduce the complexity of massive MIMO systems. The first one is the design of low-complexity hybrid precoder based on Zero-Forcing (ZF) precoding algorithm and Neumann series approximation. The second one is the design of flexible, environment friendly, simple 128-element antenna array at the frequency of 2.4 GHz using inkjet printing technology. The substrate used for printing is the “glossy paper” with dielectric constant of 2.31, and the ink used is silver nanoparticle ink with conductivity of 35,700,000 s/m. The element used for the formation of array is the z-shaped coplanar waveguide (CPW) monopole antenna. The performance of the proposed designs is evaluated in terms of probability of error for the hybrid precoding algorithm and radiation characteristics like gain, directivity, and return loss for the printed antenna design.

## 1. Introduction

The future of wireless networks is in the hands of technologies that provide good quality, intense security, and improved reliability. The most promising 5G wireless standards are expected to satisfy all the above requirements by providing higher data rate, low latency between radio links, and minimal power consumption than the existing network. Though the above-mentioned performance targets do not need to be met simultaneously, they provide the basis for the Gbits/s user experience for 5G networks [1–3].

The large-scale (massive) MIMO is one of the promising technologies that can meet the above performance targets in which a central node (base station) with antennas in the order of 100's serves multiple users (mobile terminals) with single or small number of antennas [4–7]. When the number of base station (BS) antennas  $M$  grows very large or tends to infinity, the effects of noise and fast fading present in the channel vanish [8]. Increasing  $M$  also makes the diagonal elements of the Gram matrix ( $\mathbf{G} = \mathbf{H}\mathbf{H}^H$ ) more dominant for

the given channel matrix  $\mathbf{H}$ . This implies that the channels of the independent users become orthogonal which completely eliminates the interuser interference. But for practical systems with  $M \ll \infty$ , the Inter-user interference can be mitigated by applying precoding techniques at the transmitter side. But the major problem associated with this system is its complexity due to the large dimensional matrices that changes frequently at the rate proportional to the channel's Doppler spread. Hence, in this paper, we propose two design approaches to simplify the complexity issue: the first one is the low-complexity hybrid precoding algorithm and the second one is the design of antenna array using simple and cheap inkjet printing technology.

The first part of this paper is the design of low-complexity hybrid precoding algorithm for massive MIMO systems. Among various precoding algorithms available, the hybrid precoding has gained more attention in the recent times due to its complexity and cost trade-offs [9]. The drawback of pure digital precoding is the requirement of dedicated RF modules for each of the BS antennas. Since the array size of

the massive MIMO system is typically large, digital precoding becomes more complex in terms of area, cost, and power limitations. But the hybrid precoder architecture shown in Figure 1 groups the transmitting antenna elements into a number of subarray modules [10]. Hence, separate RF chains are assigned for each subarray module rather than individual antenna element which reduces the cost of the system considerably. Hybrid precoder combines a low-dimensional baseband precoder (digital) with a high-dimensional RF precoder (analog). The digital precoder controls the signal supplied to the RF precoder by the complex weight matrix  $\mathbf{W}_D$ , and the complex analog weight matrix  $\mathbf{W}_A$  of the RF precoder controls the phase shift network of the antenna array. More extensive research works have been carried out on developing hybrid precoding algorithms in [9–12]. All these works devise various hybrid algorithms for massive antenna systems based on computationally intensive block diagonalization and eigenvalue decomposition methods. Though plenty of works evolved to reduce the complexity of these methods, their implementation in hardware is not feasible as they deal with lot of division operations. Since the hardware like FPGAs are more friendly with MAC (multiply and accumulate) operations, we propose here a hardware friendly zero forcing (ZF) algorithm-based [13] hybrid precoder. Though ZF algorithm is simple, the matrix inversion associated with this algorithm is highly expensive as the number of user antennas increases. Thus, the complexity of the ZF algorithm is greatly reduced by replacing large-scale matrix inversion by low-complexity Neumann series-based approximation [14].

The second part of the work introduces a simple, low-cost, environment friendly antenna design for massive MIMO systems using inkjet printing technology [15]. The performance of the design is verified using CST MWS tool. The ink used for printing is silver nanoparticle ink, and substrate used for printing is the flexible 2D “glossy paper.”

The rest of this paper is organized as follows. Section 2 describes the low-complexity hybrid precoding algorithm and its performance characteristics simulated using MATLAB. Then, the antenna design using inkjet printing technology and its performance using CST MWS is discussed in Section 3.

## 2. Low-Complexity Hybrid Precoder Design

**2.1. System Description.** Consider the downlink massive MIMO system where a base station (BS) with  $M$  transmit antennas communicates with  $K$  mobile users equipped with single receiving antenna. The modulated data vector  $\mathbf{m}$  intended for  $K$  users is represented as

$$\mathbf{m} = [m_1 \quad m_2 \quad \dots \quad m_K]^T \in \mathbb{C}^{K \times 1}. \quad (1)$$

This modulated data vector is first processed by  $N \times K$  digital precoder  $\mathbf{W}_D$  followed by  $N$  number of RF chains. Here, we critically assume that the proposed precoder architecture requires at least  $K$  number of RF chains

( $N=K$ ) to enable multistream data transmission of  $K$  users. The output of the digital precoder is carried over by the respective RF chains and converted into analog domain. Next, they are processed by  $M \times N$  RF precoder  $\mathbf{W}_A$  that controls the phase angle of the phase shifters connected to each of the antenna elements. Thus, the  $M \times 1$  precoded data vector is expressed as [16]

$$\mathbf{s} = \mathbf{W}\mathbf{m} = \mathbf{W}_A\mathbf{W}_D\mathbf{m}, \quad (2)$$

where  $\mathbf{s} = [s_1 \quad s_2 \quad \dots \quad s_M]^T \in \mathbb{C}^{M \times 1}$ . In (2), the data vector  $\mathbf{m}$  is transformed into the symbol vector  $\mathbf{s}$  by means of the linear precoder matrix  $\mathbf{W}$ . Here, the weight matrix  $\mathbf{W}$  of size  $M \times K$  is split into two as  $\mathbf{W}_D$  and  $\mathbf{W}_A$ . This precoded data vector  $\mathbf{s}$  is then transmitted over the MIMO channel  $\mathbf{H}$  that yields

$$\mathbf{y} = \mathbf{H}\mathbf{s} + \mathbf{n}, \quad (3)$$

where  $\mathbf{y} \in \mathbb{C}^{K \times 1}$  is the data vector received by  $K$  single antenna users,  $\mathbf{n}$  is the white Gaussian noise of unit variance, zero mean, and  $\mathbf{H} = [\mathbf{H}_1^T \quad \mathbf{H}_2^T \quad \dots \quad \mathbf{H}_K^T]^T \in \mathbb{C}^{K \times M}$  where  $\mathbf{H}_k \in \mathbb{C}^{1 \times M}$  is the channel gain of the  $k$ th user with single antenna. If each user is equipped with  $N_U$  number of antennas rather than single, the channel gain of each user is given by  $\mathbf{H}_k \in \mathbb{C}^{N_U \times M}$ . Thus, the received signal at the  $k$ th user terminal is given by [17]

$$\mathbf{y}_k = \mathbf{H}_k\mathbf{W}_k\mathbf{m}_k + \sum_{i=1, i \neq k}^K \mathbf{H}_i\mathbf{W}_i\mathbf{m}_i + \mathbf{n}. \quad (4)$$

The first term in above expression is the desired signal of the intended user, the second term is the interference from other users, and the last term  $\mathbf{n}$  is the noise added by the channel. As massive MIMO significantly reduces the effects of channel noise and fast fading effects, the interference due to other users (interuser interference) need to be taken care. Zero forcing (ZF) is one technique of linear precoding in which the precoding matrix is the optimal solution obtained by forcing the interuser interference in each of the user terminals to zero. In (4), by forcing the second term that denotes the interuser interference to zero, we obtain the solution for  $\mathbf{W}$  as given below [17].

$$\mathbf{W} = \mathbf{H}^H (\mathbf{H}\mathbf{H}^H)^{-1}. \quad (5)$$

The above equation can now be represented using Gram matrix  $\mathbf{G}$  as

$$\mathbf{W} = \mathbf{H}^H \mathbf{G}^{-1}, \quad (6)$$

where Gram matrix  $\mathbf{G} = \mathbf{H}\mathbf{H}^H \in \mathbb{C}^{K \times K}$  and substituting the above equation of  $\mathbf{W}$  in (2) we get the precoded data vector

$$\mathbf{s} = \mathbf{H}^H \mathbf{G}^{-1} \mathbf{m}. \quad (7)$$

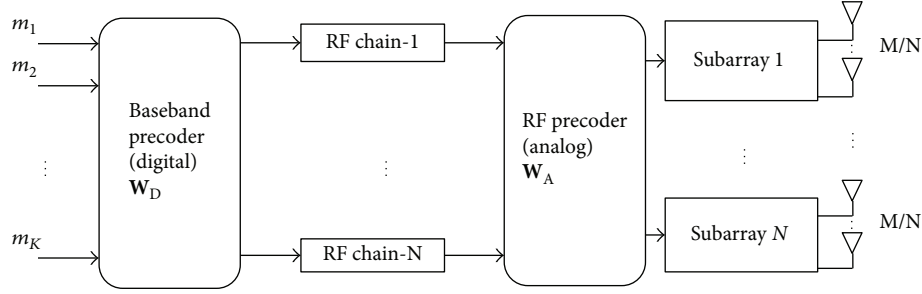


FIGURE 1: Block diagram of the hybrid precoder structure.

To obtain the precoded data vector  $\mathbf{s}$  given in (7), the steps involved in the ZF precoder are Gram matrix computation  $\mathbf{G}$ , inversion of Gram matrix  $\mathbf{G}^{-1}$ , multiplication of  $\mathbf{G}^{-1}$  with  $\mathbf{m}$  and  $\mathbf{H}^H$ . While implementing the above structure in hardware, the Gram matrix computation module and multiplication module requires less complex tasks since they need only multiplier modules that can easily be implemented in hardware MAC units. But the inverse computation module requires division operation that is highly infeasible in hardware. Hence, finding  $\mathbf{G}^{-1}$  is computationally challenging, especially, when the dimension of the matrix is quite high [8]. Thus, we aim to reduce the complexity of the ZF precoding algorithm by replacing direct inversion by simple mathematical approximations such as Neumann series.

**2.2. Low-Complexity Hybrid Precoding Algorithm.** According to [14],  $\mathbf{G}^{-1}$  in (7) is approximated using Neumann series as

$$\mathbf{G}^{-1} \approx \sum_{n=0}^L (\mathbf{I} - \mathbf{Z}^{-1}\mathbf{G})^n \mathbf{Z}^{-1}, \quad (8)$$

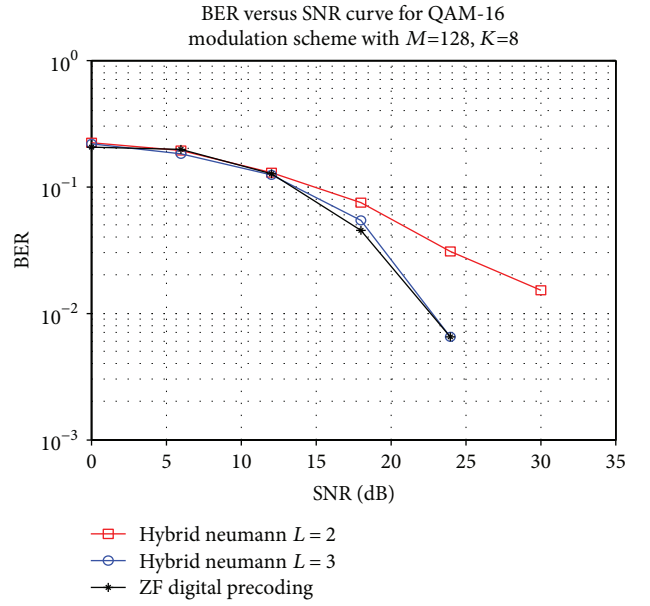
where  $\mathbf{I}$  is the identity matrix of size  $K$  and matrix  $\mathbf{Z}$  is an initial approximation of  $\mathbf{G}$ , mostly it is chosen as the diagonal matrix containing the diagonal elements of  $\mathbf{G}$  and hence much easier to invert. Computing (8) requires  $L-1$  matrix multiplications where  $L$  is the order of the polynomial. Here, (8) reaches equality as  $L$  tends to infinity and the convergence rate is initiated by the correct selection of  $\mathbf{Z}$ . Using the above stated approximation, the RF precoder matrix  $\mathbf{W}_A$  is obtained first with the knowledge of channel matrix  $\mathbf{H}$  as given below

$$\mathbf{W}_A = \mathbf{H}^H \mathbf{G}^{-1} \approx \mathbf{H}^H \sum_{n=0}^L (\mathbf{I} - \mathbf{Z}^{-1}\mathbf{G})^n \mathbf{Z}^{-1}. \quad (9)$$

Once the RF precoder  $\mathbf{W}_A$  is found, we can readily find the digital precoding matrix  $\mathbf{W}_D$  from the ZF algorithm given in (5) as

$$\mathbf{W}_D = \mathbf{H}_d^H (\mathbf{H}_d \mathbf{H}_d^H)^{-1}, \quad (10)$$

where  $\mathbf{H}_d$  is the effective channel gain of the digital precoder by assuming fixed analog precoder. Hence, the effective

FIGURE 2: BER performance of hybrid precoding in urban micro cell scenario for  $128 \times 8$  massive MIMO system.

channel including the analog precoder  $\mathbf{W}_A$  is given as  $\mathbf{H}_d = \mathbf{H}\mathbf{W}_A$ . Then, substituting in (10) yields

$$\mathbf{W}_D = (\mathbf{H}\mathbf{W}_A)^H (\mathbf{H}\mathbf{W}_A (\mathbf{H}\mathbf{W}_A)^H)^{-1}. \quad (11)$$

As we know that  $(\mathbf{H}\mathbf{W}_A)^H = \mathbf{W}_A^H \mathbf{H}^H$  (conjugate transpose property) the above equation becomes

$$\mathbf{W}_D = \mathbf{W}_A^H \mathbf{H}^H (\mathbf{H}\mathbf{W}_A \mathbf{W}_A^H \mathbf{H}^H)^{-1}. \quad (12)$$

The inversion operation in (12) is also approximated using Neumann approximation. Finally, the RF and digital precoders can be designed using the relations (10) and (12), respectively, for the hybrid precoder architecture.

The proposed algorithm which is based on ZF algorithm can also be extended for the downlink system with users equipped with  $N_U$  number of antennas instead of single antenna [17]. This yields the complex channel matrix of size  $KN_U \times M$  which in turn expands the corresponding precoder matrix size by an amount of  $N_U$ . Hence, the demand for the low-complexity algorithms is higher as the size of the matrix grows.

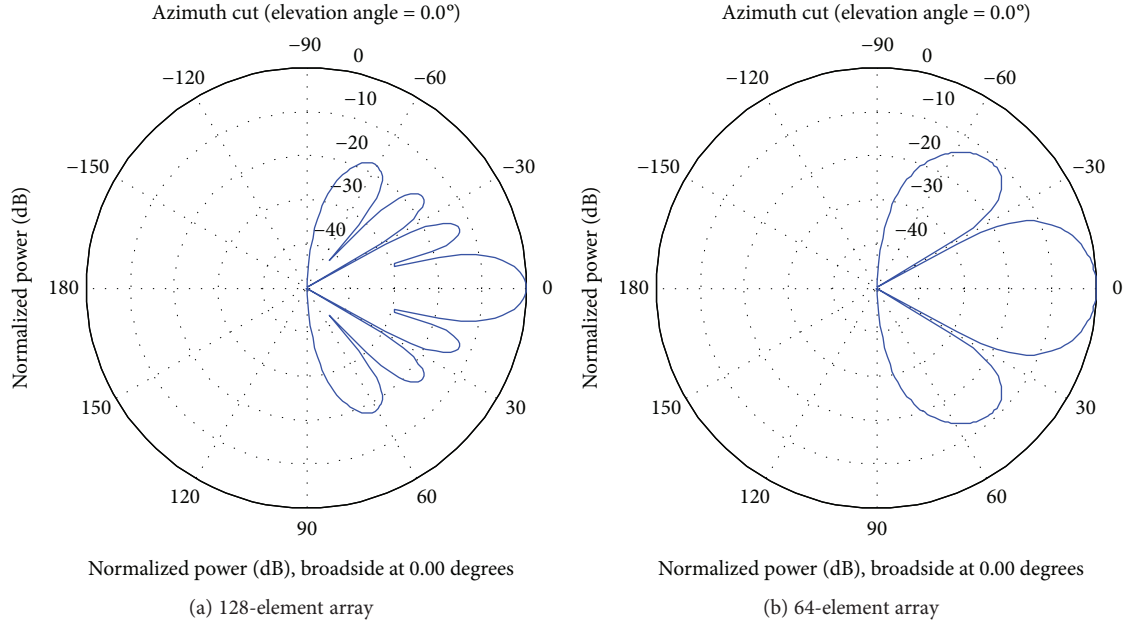


FIGURE 3: Radiation pattern of the antenna array with 16 subarrays in rectangular geometry.

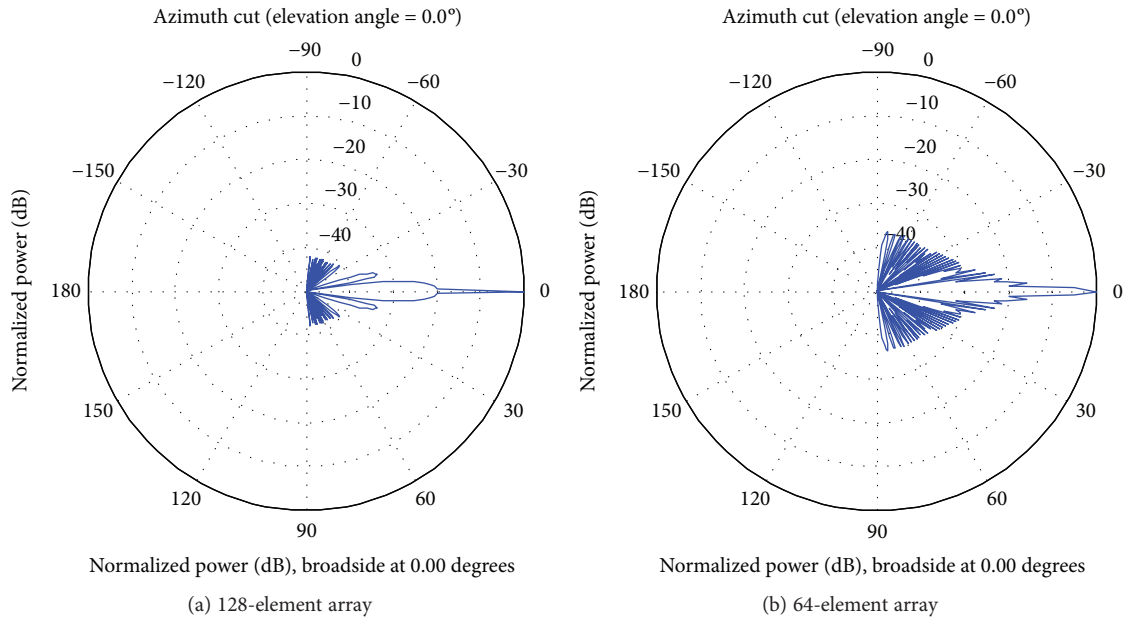


FIGURE 4: Radiation pattern of the ULA with 16 subarrays.

**2.3. Simulation Results.** This subsection illustrates the BER performance of the proposed Neumann series-based hybrid precoding algorithm, and comparisons are made with direct inversion-based digital precoding. The performance is evaluated for a massive MIMO downlink system with BS equipped with  $M=128$  uniform linear antenna array with antenna spacing of  $d=\lambda/2$  serving  $K=8$  mobile users. The above system requires the knowledge of downlink channel matrix  $\mathbf{H}$  of size  $K \times M$  for the computation of precoding matrices  $\mathbf{W}_A$  and  $\mathbf{W}_D$ . This complex channel matrix is simulated using WINNER phase-II [18] model.

TABLE 1: Properties of ink and substrate used for printing.

Ink properties	
Viscosity	2.3 mPa·sec
Surface tension	35 mN/m
Conductivity	35,700,000 S/m
"Glossy paper" substrate properties	
Relative permittivity	4.01
Loss tangent	0.07
Dielectric constant	2.31
Thickness	0.1 mm

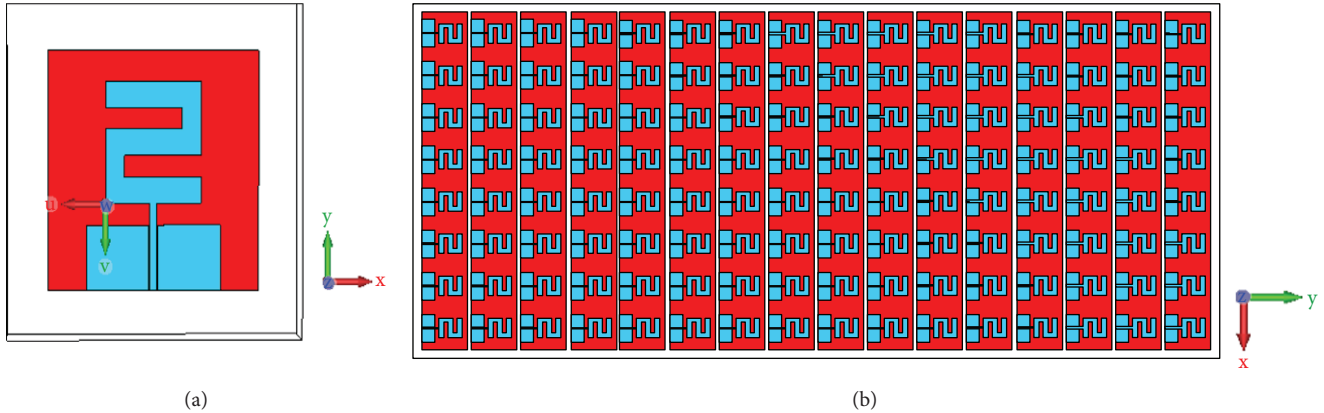


FIGURE 5: (a) Single Z-shaped CPW monopole antenna. (b) Array of 128 Z-shaped CPW monopole elements.

The simulations are carried out for a propagation scenario of urban micro cell where both BS and MSs are surrounded by uniform distribution of scatterers located in an elliptical region covering the entire street accommodating both BS and mobile stations (MS). The coverage area of BS is chosen as 500 meters with the antenna heights well below the surrounding buildings. Data sequences are generated randomly and mapped using 16-QAM to obtain  $\mathbf{m}$ . The modulated symbols are multiplied with  $\mathbf{W}_A$  and  $\mathbf{W}_D$  to get  $\mathbf{s}$ . Then,  $\mathbf{s}$  is transmitted through the channel where it is added with zero mean, unit variance Gaussian noise to obtain  $\mathbf{y}$ . The error performance is calculated for the system described above, and Figure 2 shows the performance of Neumann-based hybrid precoding for order  $L=1$  and 2. The simulation results clearly exhibit that the error performance reaches the optimal value of ZF precoding (direct inversion based) as  $L$  increases.

### 3. Massive MIMO Antenna Design

**3.1. Background Knowledge of Antenna Array.** Considering the points discussed above to facilitate the hybrid precoder architecture for massive MIMO system, it is required to divide the antenna elements into subarray modules. Each of these subarray modules is fed by dedicated RF chains, thus reducing the number of RF chains required by individual antenna element. The geometry of array and the number of subarray elements have a major impact on the radiation characteristics of the system. For massive MIMO systems to support multiuser transmission, multiple beams are needed to focus on each user. The results simulated in MATLAB shown below depicts the radiation pattern of 64 and 128 antenna arrays with 16 subarray modules where each subarray comprises 4 and 8 elements, respectively. From the results, it is evident that the rectangular array provides multi-beam radiation characteristics with the number of beams almost equal to the number of elements in the subarray. The higher the number of elements in the subarray, the larger is the number of beams. Thus, the array geometry and number of subarray elements clearly decide on the radiation pattern of the massive antenna array. From Figures 3 and 4, it is clear that the uniform linear array (ULA)

geometry of subarrays produces many ripples with no considerable main beams, as in the case of rectangular geometry, which produces multiple beams with reasonable gain. Hence, to support multibeam transmission of 5G wireless applications, rectangular geometry of subarrays is preferred over linear pattern.

**3.2. Printed Antenna Array Design-Simulation Results.** Next, we focus on the design of 128-element massive antenna array in a more effective, flexible way using inkjet printing technology. The operating frequency of the proposed design is 2.4 GHz as this lies in the frequency range used for the typical mobile radio communication worldwide. The substrate used for printing is the cheap, readily available, environmental friendly material “glossy paper.” The major advantage of this material is its flexibility to various applications. The ink used for printing is the conductive silver nanoparticle ink having conductivity of 35,700,000 S/m. The properties of the ink and paper substrate are given in Table 1.

Figure 5(a) shows the design Z-shaped monopole element with the dimensions given in [15], and Figure 5(b) depicts the 128-element massive array. This arrangement is having 16 subarrays with each subarray integrated with 8 Z-shaped elements. The subarray spacing of the proposed design is 10 mm. Figures 6(a) and 6(b) plot the return loss characteristics over the frequency range of 2–6 GHz for the antenna array and single element, respectively. It is seen that the  $S_{1,1}$  value is considerably less than 14 dB over the frequency range of interest in both plots. The notch at 2.4 GHz is clearly visible in both plots. The graphs shown in Figures 7(a) and 7(b) are the 2D model of the gain radiation pattern at  $\phi=0$  and 90 degrees, respectively. Figures 8(a) and 8(b) depict 3D model of gain and directivity pattern. From all these, it is clear that the proposed design exhibits a reasonably high gain of around 27.3 dB at the frequency of 2.4 GHz with the beamwidth of 7.5 degrees at  $\phi=0$  degrees. This proposed design outperforms the recent microstrip massive antenna array design printed on LTCC substrate whose gain is just 7 dB [19]. Thus, the proposed inkjet-printed antenna array produces nearly 20 dB gain improvement over the previous work.

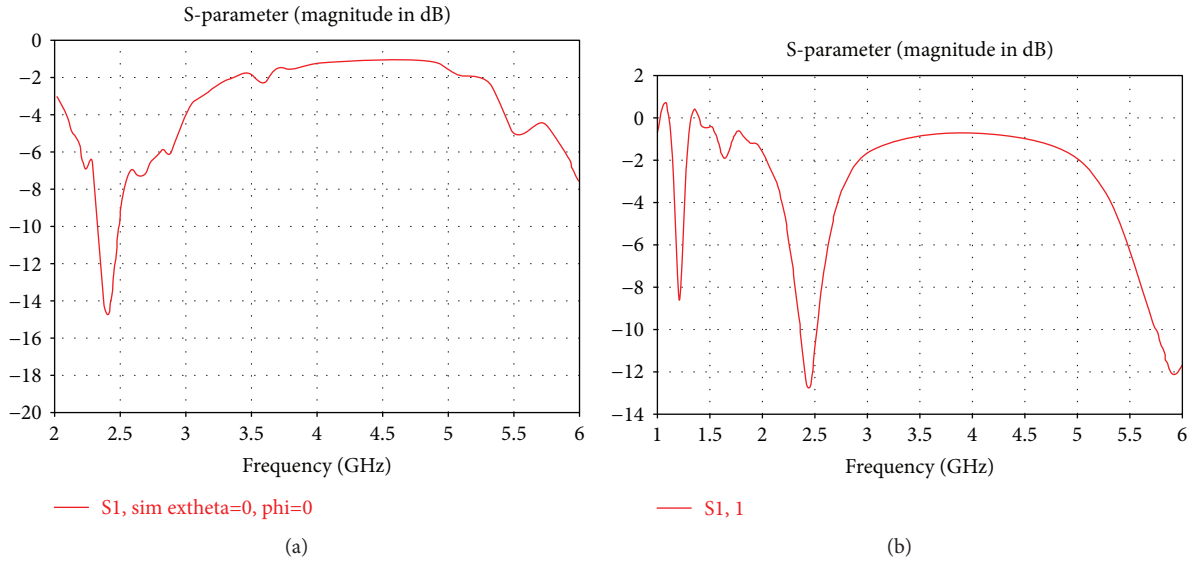


FIGURE 6: (a) S-parameter graph of 128-element array. (b) S-parameter graph of single Z-shaped element.

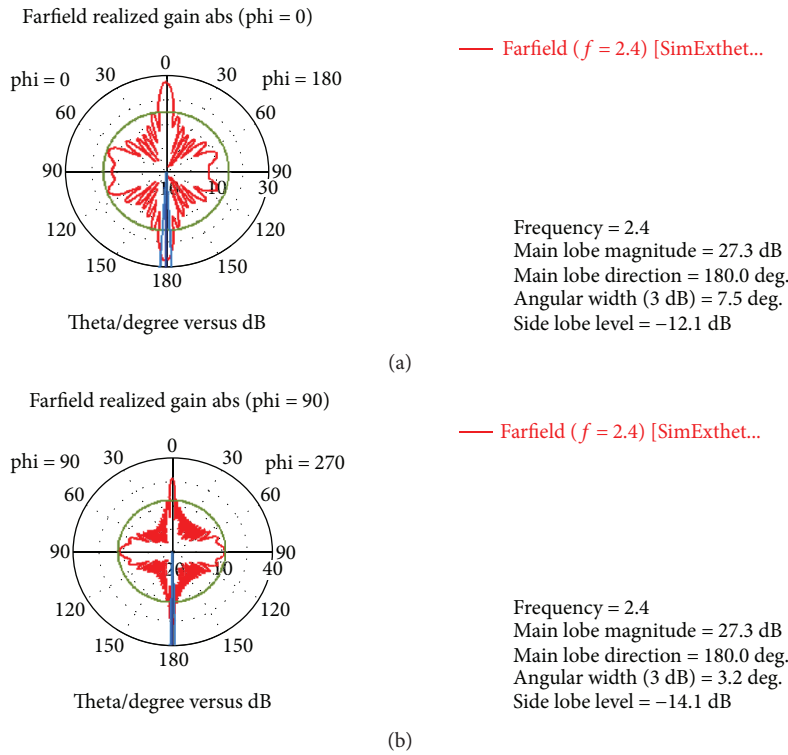


FIGURE 7: (a) 2D model of gain radiation pattern of the 128-antenna array at phi=0 deg. (b) 2D model of gain radiation pattern of the 128-antenna array at phi=90 deg.

### 4. Conclusion

In this paper, we have proposed a low-complexity hybrid precoder and a 2D printed antenna array for 5G wireless applications. The complexity of hybrid precoder based on ZF algorithm incurred by direct inversion of large size matrix is greatly reduced by Neumann series approximation. The

error performance of this proposed hybrid algorithm is comparable with the fully digital precoding algorithm with reduced complexity. Also, the 128-element antenna array designed using inkjet printing technology shows an excellent gain of 27.34 dB at the frequency of 2.4 GHz with the return loss of -15 dB. The proposed antenna array, integrated by 16 subarray modules each comprising 8 Z-shaped CPW

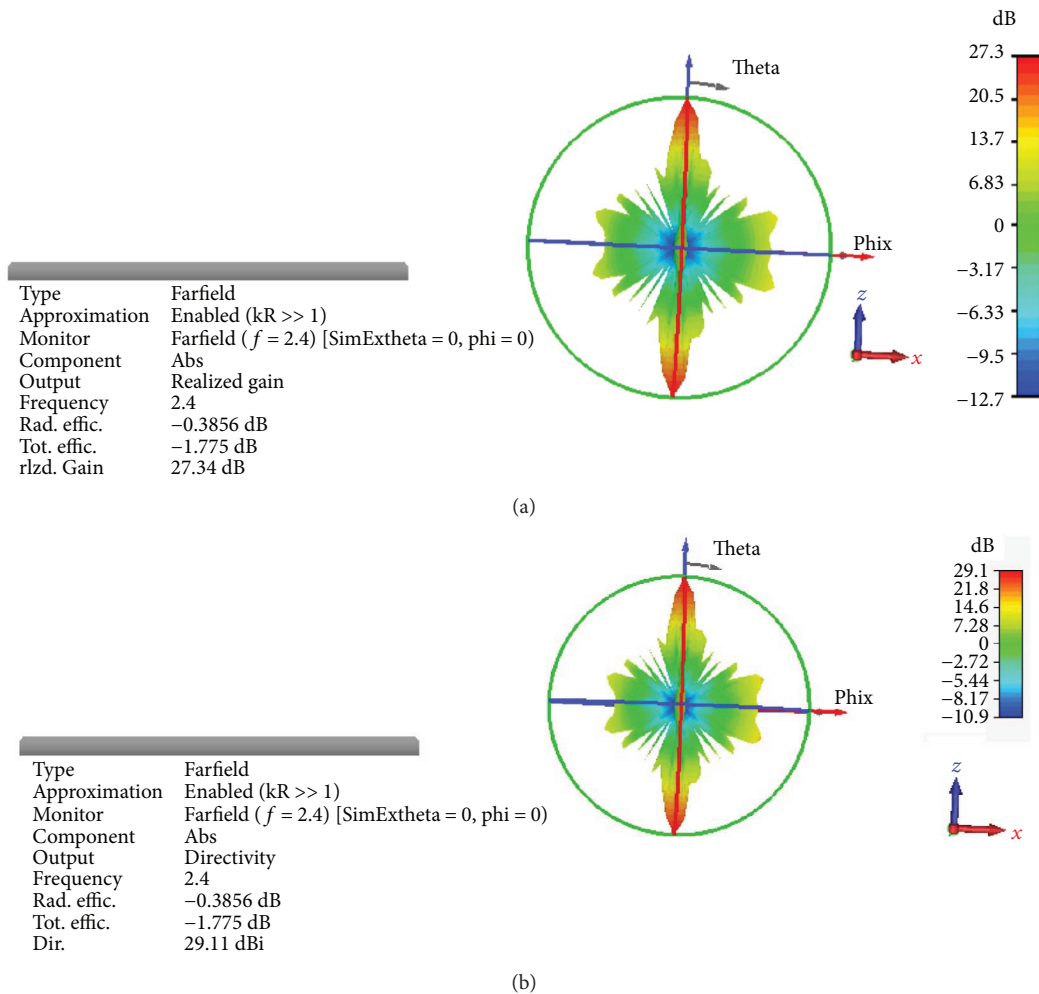


FIGURE 8: (a) 3D model of the radiation pattern of the gain. (b) 3D model of the radiation pattern of the directivity.

monopole elements, generates multibeam radiation pattern to facilitate the multiuser transmission of 5G networks. This confirms that the proposed 2D flexible printed antenna array is feasible for future 5G applications.

## Conflicts of Interest

The authors declare that they have no conflicts of interest.

## References

- [1] Huawei Technologies Co., Ltd, *New Air Interface and Radio Access Virtualization*, White Paper, 2015.
- [2] METIS Project, <https://www.metis2020.com/>.
- [3] 5G Forum, <http://www.5gforum.org/>.
- [4] E. Larsson, O. Edfors, F. Tufvesson, and T. Marzetta, "Massive MIMO for next generation wireless systems," *IEEE Communications Magazine*, vol. 52, no. 2, pp. 186–195, 2014.
- [5] T. L. Marzetta, "Noncooperative cellular wireless with unlimited numbers of base station antennas," *IEEE Transactions on Wireless Communications*, vol. 9, no. 11, pp. 3590–3600, 2010.
- [6] H. Huh, G. Caire, H. C. Papadopoulos, and S. A. Ramprasad, "Achieving "massive MIMO" spectral efficiency with a not-so-large number of antennas," *IEEE Transactions on Wireless Communications*, vol. 11, no. 9, pp. 3226–3239, 2012.
- [7] F. Rusek, D. Persson, B. K. Lau, E. G. Larsson, T. L. Marzetta, and F. Tufvesson, "Scaling up MIMO: opportunities and challenges with very large arrays," *IEEE Signal Processing Magazine*, vol. 30, no. 1, pp. 40–60, 2013.
- [8] L. Lu, G. Y. Li, A. Lee Swindlehurst, A. Ashikhmin, and R. Zhang, "An overview of massive MIMO: benefits and challenges," *IEEE Journal of Selected Topics in Signal Processing*, vol. 8, no. 5, pp. 742–758, 2014.
- [9] F. Sotrohi and W. Yu, "Hybrid digital and analog beamforming design for large-scale antenna arrays," *IEEE Journal of Selected Topics in Signal Processing*, vol. 10, no. 3, pp. 501–513, 2016.
- [10] S. Park, A. Alkhateeb, and R. W. Heath, "Dynamic subarrays for hybrid precoding in wideband mmWave MIMO systems," *IEEE Transactions on Wireless Communications*, vol. 16, no. 5, pp. 2907–2920, 2017.
- [11] M. Kim and Y. H. Lee, "MSE-based hybrid RF/baseband processing for millimeter-wave communication systems in MIMO interference channels," *IEEE Transactions on Vehicular Technology*, vol. 64, no. 6, pp. 2714–2720, 2015.

- [12] W. Ni and X. Dong, "Hybrid block diagonalization for massive multiuser MIMO systems," *IEEE Transactions on Communications*, vol. 64, no. 1, pp. 201–211, 2016.
- [13] X. Gao, O. Edfors, F. Rusek, and F. Tufvesson, "Linear precoding performance in measured very-large MIMO channels," in *2011 IEEE Vehicular Technology Conference (VTC Fall)*, San Francisco, CA, USA, September 2011.
- [14] H. Prabhu, J. Rodrigues, O. Edfors, and F. Rusek, "Approximative matrix inverse computations for very-large MIMO and applications to linear pre-coding systems," in *2013 IEEE Wireless Communications and Networking Conference (WCNC)*, pp. 2710–2715, Shanghai, China, April 2013.
- [15] A. M. Mansour, N. Shehata, B. M. Hamza, and R. M. Rizk, "Efficient design of flexible and low cost paper-based inkjet printed antenna," *International Journal of Antennas and Propagation*, vol. 2015, Article ID 845042, 6 pages, 2015.
- [16] A. Alkhateeb, G. Leus, and R. W. Heath, "Limited feedback hybrid precoding for multi-user millimeter wave systems," *IEEE Transactions on Wireless Communications*, vol. 14, no. 11, pp. 6481–6494, 2015.
- [17] R. C. de Lamare, "Massive MIMO systems: signal processing challenges and research trends," in *Centre for Telecommunications Studies (CETUC)*, Pontifical Catholic University of Rio de Janeiro, 2013.
- [18] L. Hentila, P. Kyosti, M. Kaske, M. Narandzic, and M. Alatosava, *MATLAB Implementation of the WINNER Phase II Channel Model Ver 1.1*, 2007.
- [19] C.-N. Hu, D.-C. Chang, C.-H. Yu, T.-W. Hsaio, and D.-P. Lin, "Millimeter-wave microstrip antenna array design and an adaptive algorithm for future 5G wireless communication systems," *International Journal of Antennas and Propagation*, vol. 2016, Article ID 7202143, 10 pages, 2016.

## Research Article

# Inkjet-Printed Flexible MEMS Switches for Phased-Array Antennas

Mahmuda Akter Monne,<sup>1</sup> Xing Lan,<sup>2</sup> Chunbo Zhang,<sup>2</sup> and Maggie Yihong Chen <sup>1</sup>

<sup>1</sup>Ingram School of Engineering, Texas State University, San Marcos, TX 78666, USA

<sup>2</sup>One Space Park, Northrop Grumman, Redondo Beach, CA 90278, USA

Correspondence should be addressed to Maggie Yihong Chen; [maggie.chen@txstate.edu](mailto:maggie.chen@txstate.edu)

Received 30 December 2017; Accepted 8 February 2018; Published 28 March 2018

Academic Editor: Herve Aubert

Copyright © 2018 Mahmuda Akter Monne et al. This is an open access article distributed under the Creative Commons Attribution License, which permits unrestricted use, distribution, and reproduction in any medium, provided the original work is properly cited.

This paper presents a fully inkjet-printed flexible MEMS switch for phased-array antennas. The physical structure of the printed MEMS switch consists of an anchor with a clamp-clamp beam, a sacrificial layer, and bottom transmission lines. 5-mil Kapton® polyimide film is used as a flexible substrate material. Two different types of conductive ink PEDOT:PSS from Sigma Aldrich and silver nanoparticle ink from NovaCentrix are used for the fabrication of different printed layers. Layer-by-layer fabrication process and material evaluation are illustrated. Layer characterization is done with respect to critical thickness and resistance using 2D/3D material analysis. Fujifilm Dimatix Material Printer (DMP-2800) is used for fabrication, and KLA-Tencor (P-7) profiler is used for 2D and 3D analysis of each layer. The MEMS switch has a low actuation voltage of 1.2 V, current capacity of 0.2195 mA, a current on-off ratio of 2195:1, and an RF insertion loss of 5 dB up to 13.5 GHz. Printed MEMS switch technology is a promising candidate for flexible and reconfigurable phased-array antennas and other radio frequency (RF) and microwave frequency applications.

## 1. Introduction

Digital beamforming phased-array antennas (PAAs) with distributed control and processing electronics offer numerous advantages for radio frequency (RF) communications, such as electronically controllable beamforming and steering, high average transmitted power and efficiency, flexible subarraying to provide multiple communication links simultaneously, reconfigurable high-gain patterns, and increased reliability through reconfiguring redundant array elements. Low-cost, high-gain, lightweight, and conformal active PAA on flexible substrates is of particular interest in space communication networks. However, the major deterrent to developing such systems is the difficulty in integrating antenna and electronic circuits on the flexible surface, especially the switch-controlled phase shifters and amplifiers. Previously, a prototype of active PAA is designed using carbon nanotubes (CNT) as the active material in the digital switching device [1]. However, the printed flexible CNT

transistor switch is limited to 5 GHz [2]. Graphene transistor potentially has higher working frequency. However, the current on-off ratio is limited to 38 due to the intrinsic zero-bandgap property [3, 4]. A MEMS switch theoretically has unlimited bandwidth and on-off ratio due to the mechanical property. However, there is no report about high-performance fully printed flexible MEMS switch.

The attractiveness of printing technology is due to its greatly simplified fabrication process. In this process, it is possible to achieve multilayered microstructures and thin-film devices in a simple and cost-effective way [5–7]. The most widely used printing techniques are inkjet, aerosol jet, screen printing [8], flexographic printing, and gravure printing [8]. The sheet-based inkjet printing technique has been gaining attention because of its unique features, such as simplicity of fabrication, compatibility with different substrates, feasibility of noncontact, low-temperature processing, and low cost. Aerosol jet printing offers one of the best printing resolutions with good flexibility, but the

TABLE 1: Commercially available polymers for printed electronics.

Name	Specifications	Properties/current limits
Riston® (DuPont)	Dry film	A “general purpose” dry film for acid and alkaline etch up to 15 $\mu\text{m}$
Kapton (DuPont)	Dry film	A “general purpose” dry film for printing with all types of nanoparticle ink (Ag, Au, and CNT)
NovaCentrix Novela® (NOVELA Advance Microsystem)	One-sided dry film	Substrate thickness: 10–25 $\mu\text{m}$ Minimum track width and spacing: 10 $\mu\text{m}$ Minimum dielectric layer thickness: 1.8 $\mu\text{m}$

tool and its setup are more expensive than the comparatively low-cost inkjet printing.

Furthermore, inkjet printers can be divided into two basic process groups: continuous and drop-on-demand [9, 10]. In continuous inkjet printers, the ink is first pumped through a nozzle forming a liquid jet. Next, the formed liquid jet is deflected by electrostatic plates to the paper or to a reservoir for recirculation. Today, most inkjet printers are based on a drop formation process, which is called drop-on-demand (DOD) [9, 11]. The drop-on-demand method provides smaller drops and higher placement accuracy compared to the continuous inkjet printers. In this study, drop-on-demand inkjet printing is used [12]. The pulse that creates the ink drop can be generated either thermally or piezoelectrically. In our work, a Fujifilm Dimatix piezoelectric type inkjet printer is used.

Currently, a large variety of MEMS devices such as sensors, actuators, and switches are available [13–15]. These devices, however, are mostly developed and fabricated by cleanroom micromachining technology, which is complicated in its processing steps and expensive to develop. The subtractive nature of the micromachining also incurs material waste and is not environmentally friendly [16, 17]. So far, there are very few research articles found from literature on printed MEMS devices. MEM relay is one of them, which was published in February 2016 [18]. However, the fabrication process of the mentioned article was not fully based on printing technology. Instead, the fabrication process was a combination of inkjet printing technique and another thin film deposition (spin coating) and etching technique. Only the electrodes of the MEM relay were fabricated using inkjet printing technique, while other layers like gate insulator and sacrificial layers were fabricated by spin coating and chemical etching (preparation of via holes). In the same article, they reported several measurements with respect to pull-in voltage (7.2 V), turn on delay (8  $\mu\text{s}$ ), on-off ratio ( $10^8$ ), and on state resistance (3.7  $\Omega$ ). It is to be noted that from the literature review, other than this article, there are no fully printed MEMS switch reported.

In this work, we explore the design, fabrication, and characterization of the fully 3D inkjet-printed flexible MEMS switches where all the layers like electrodes, sacrificial layer, cantilever, and anchor were fabricated using inkjet printing technology. The MEMS switch is a key component of phase shifter and can be printed together with antenna elements to develop a fully printed active phased-array antenna system.

TABLE 2: Typical properties of PEDOT [22].

Properties	Parameters
Visual appearance	Dark blue liquid
Solid content	0.8 wt%
Viscosity	7–12 cP
Surface tension	31–34 mN/m
pH	1.5–3.0
Surface resistance	110 $\Omega/\text{sq}$ .
Shelf life	6 months

## 2. Material Evaluation for Inkjet Printing of MEMS Switches

Polymeric material is used in most flexible electronics and/or organic electronic applications. A polymeric solid is made of many repeating molecules called monomers. Polymers can exhibit various mechanical, electrical, and optical properties depending on the synthesis conditions and chemical properties. The electrical conductivity of insulating polymers is about  $10^{-18}$  S/m whereas that of doped *trans*-polyacetylene is  $10^7$  S/m [19]. Some polymers such as poly(*cis*-1,4-isoprene) and poly(chloromethylstyrene) are sensitive to high-energy radiation. If the polymer is exposed to ultraviolet light, the chemical properties, such as solubility, of the polymer in the exposed area change. Photolithography is a very well-known process in electronics that uses this principle. To understand the electronic properties of polymers, it can be considered that each monomer has its electron orbitals in a certain electronic state [19]. Table 1 shows some commercially available substrate polymers. A Kapton film (HN type) of thickness 125  $\mu\text{m}$  from DuPont was used as a substrate in this research. As per manufacturer specifications, Kapton film can be used at temperatures as low as  $-269^\circ\text{C}$  and as high as  $400^\circ\text{C}$  [20]. Kapton film is chosen as the substrate for this work due to its flexibility, high temperature operability ( $400^\circ\text{C}$ ), and low elastic coefficient. As acid etching is one of the important steps during device fabrication, it is also important to choose a substrate whose performance is not degraded by acid.

To print either in a large scale, such as a functional circuit, or in a very small scale, such as a nanometer-sized device, will require careful thought and engineering for the printing parameter settings. Unfortunately, these two opposing dimension extremes do appear in a single MEMS device that we designed, as both large-scale transmission lines and small-scale device details are present. To prevent

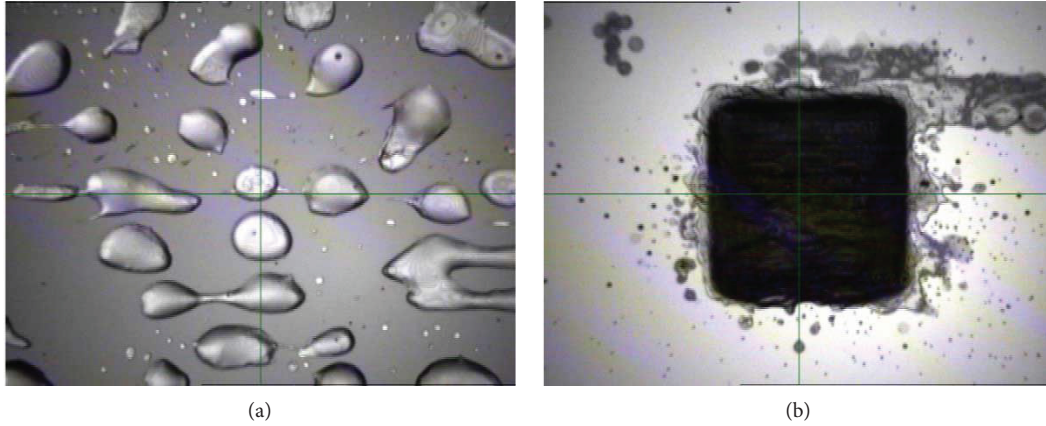


FIGURE 1: Surface treatment effect on PEDOT printing: (a) without surface treatment and (b) with surface treatment (5 mm × 5 mm pattern).

TABLE 3: Set parameters during the printing of each type of material.

Material ink	Nozzle voltage (V)	Drop spacing ( $\mu\text{m}$ )	Angle between print head and cartridge (degree)	Meniscus point	Platen temperature ( $^{\circ}\text{C}$ )	Cartridge temperature ( $^{\circ}\text{C}$ )
PEDOT	30	25	5.6	4.0	38	26
Ag	26	35	8.2	4.5	48	28

the deviation in operation of the nozzles of Fujifilm Dimatix, testing of each of the 16 nozzles is necessary before any printing operation. It was found from a review of the literature and our experimental work, for small pattern or feature printing, that the usage of a single nozzle provides more consistent results than using multiple nozzles.

Two types of conductive inks were used throughout the research: PEDOT (poly(3,4-ethylenedioxythiophene)-poly (styrene sulfonate)) high-conductivity grade from Sigma-Aldrich was used for transmission line and clamp-clamp beam fabrication. Metalon silver ink (JSB-40G) from NovaCentrix was used for the sacrificial layer. The viscosity of the silver ink is about 8–10 cP with surface tension 28–32 dyne/cm [21]. On the other hand, PEDOT is a water-based ink. Deposition of PEDOT on top of Kapton is difficult as it is a water-based ink and the surface of the substrate is hydrophobic. Therefore, the surface of the Kapton substrate needs special treatment and a modified printing environment to promote adhesion for printing with PEDOT ink.

It is also observed that, by setting a minimum distance between the cartridge nozzles and substrate and a lower waveform triggering voltage of around 20–26 V, it was possible to achieve very small printed structure sizes during ink deposition. Furthermore, it was seen that using only one nozzle at a time during printing resulted in quality outputs.

**2.1. PEDOT Ink Evaluation.** PEDOT is used to fabricate two of the most important portions of the printed MEMS switch, namely, transmission lines and clamp-clamp beam. The reason behind choosing PEDOT for these two parts is its acid-resistant property. It is a polymer-type ink not reactive to acid which is required for the MEMS fabrication. Also,

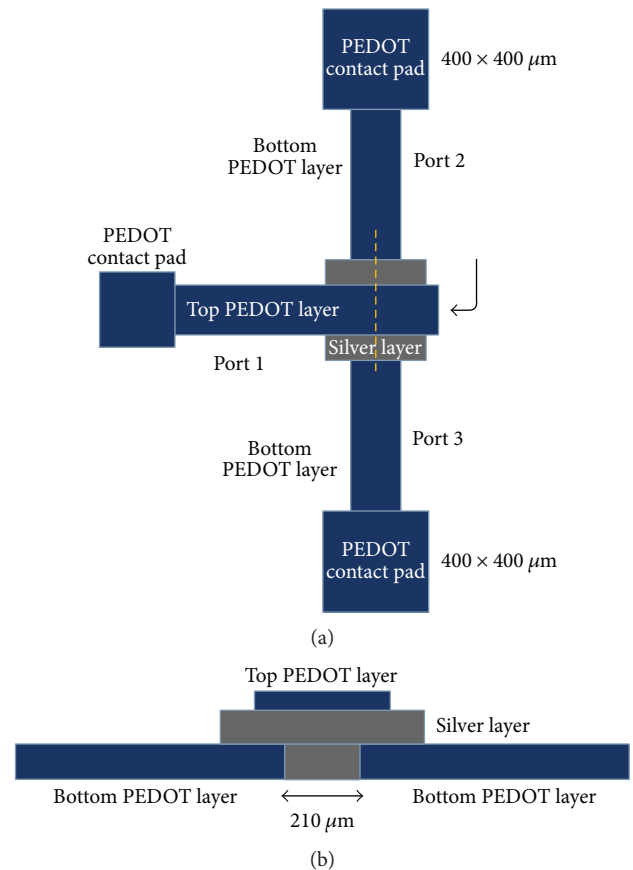


FIGURE 2: Schematic (a) top view and (b) cross-sectional view of the designed MEMS switch along the dashed line plane.

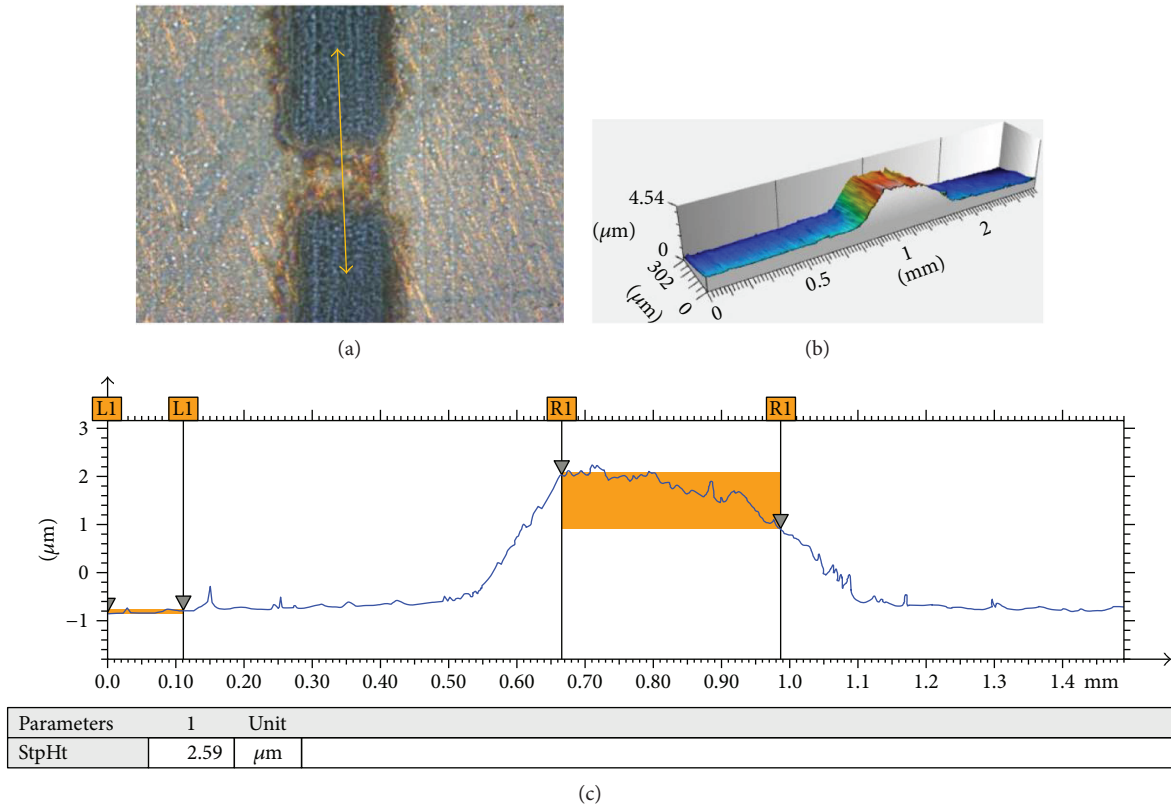


FIGURE 3: (a) First printed PEDOT layer on Kapton substrate. (b) APEX 3D thickness analysis. (c) Thickness measurement by KLA-Tencor.

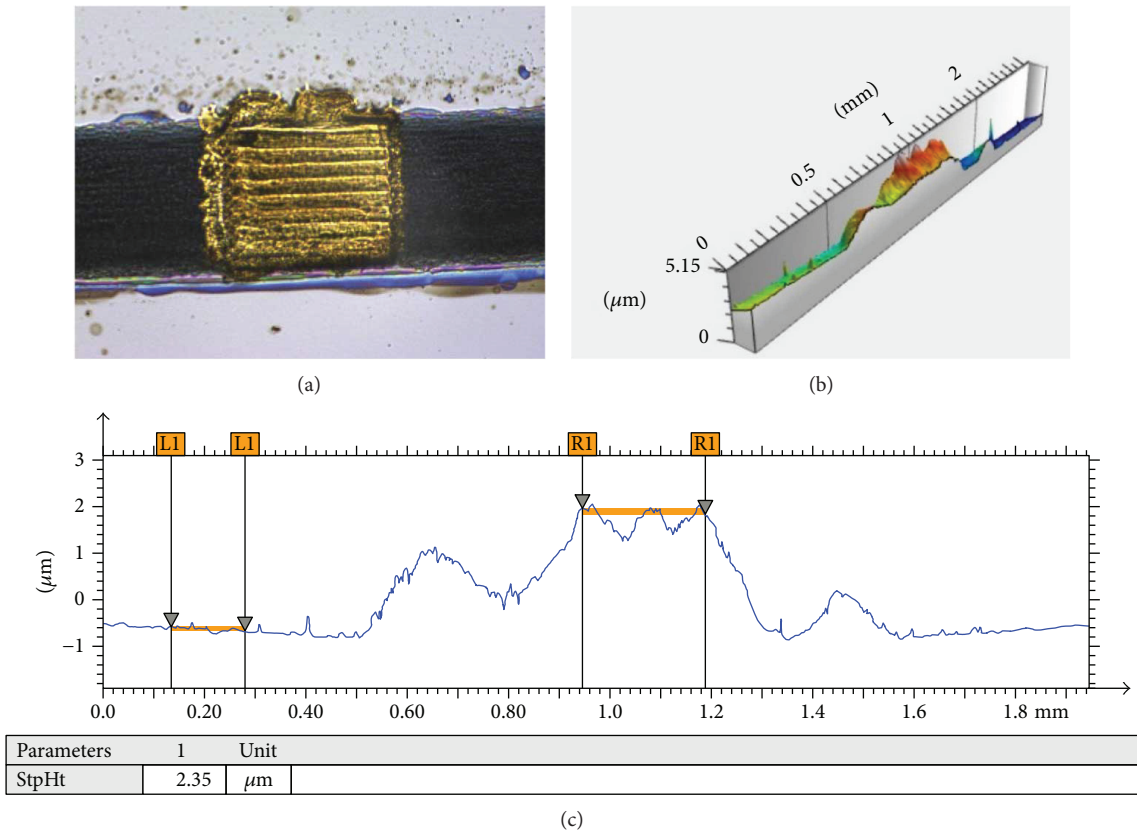


FIGURE 4: (a) Printed sacrificial layer on top of PEDOT. (b) APEX 3D analysis. (c) 2D analysis of the layer for thickness measurement.

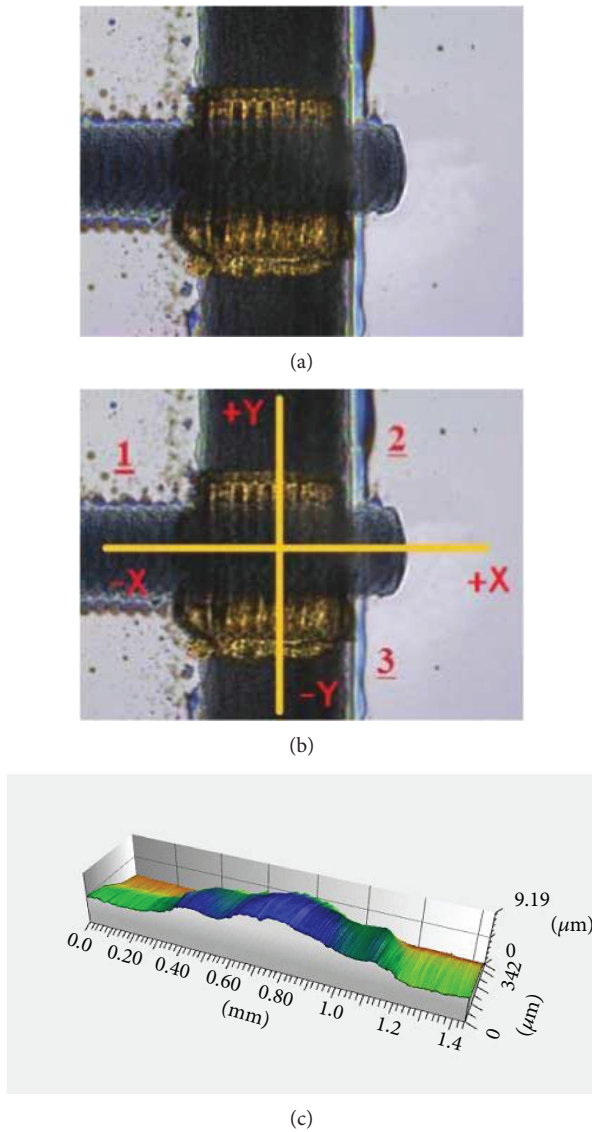


FIGURE 5: (a) Complete three-layer device. (b) Three terminals labeled for further data measurement. (c) 3D view of the printed layers to check uniformity (scanning was taken along the direction of  $-Y$  to  $+Y$ ).

TABLE 4: Measured resistance before etching.

Terminal points	Resistances ( $\Omega$ )
1-2	387~430
1-3	300~330
2-3	700~1000

PEDOT has relatively low viscosity which makes it suitable for inkjet printers. Table 2 shows the typical properties of PEDOT [22].

PEDOT is stored between  $4^{\circ}\text{C}$  and  $25^{\circ}\text{C}$  in a vacuum freezer. As mentioned earlier, to achieve good printing results with PEDOT, surface treatment of the substrate is needed. Figure 1 shows the printing of PEDOT without

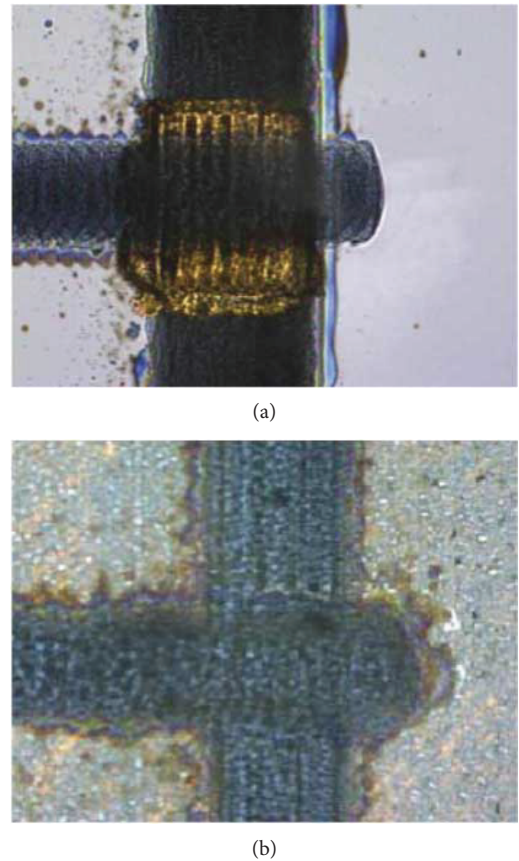


FIGURE 6: (a) Complete device before etching. (b) Complete device after etching.

TABLE 5: Measured resistance after membrane release.

Terminal points	Resistances ( $M\Omega$ )
1-2	0.2~0.3
1-3	0.15~0.2
2-3	0.45~0.5

and with surface treatment. A significantly better pattern printing is achieved after surface treatment by oxygen plasma cleaning at 100 watts for 5 minutes. It should be noted that oxygen plasma treatment increased the adhesion to the substrate surface. For PEDOT printing, the firing voltage setting for the print head is between 20 and 25 V, with firing frequency at 5 kHz and cartridge temperature of  $24^{\circ}\text{C}$ . The platen temperature was held at  $38^{\circ}\text{C}$  during printing. Table 3 shows the set parameters of the Fujifilm Dimatix Material Printer during deposition.

**2.2. Silver Ink Evaluation.** In the prototype MEMS device fabrication, silver layer is used as a sacrificial layer which will be removed after the device fabrication. Metalon silver ink is highly conductive at standard curing temperatures ( $120^{\circ}\text{C}$  for 10 min. and  $220^{\circ}\text{C}$  for 30 min.). After a standard curing process, a 1 cm by 1 cm silver patch gives  $1.22\ \Omega$

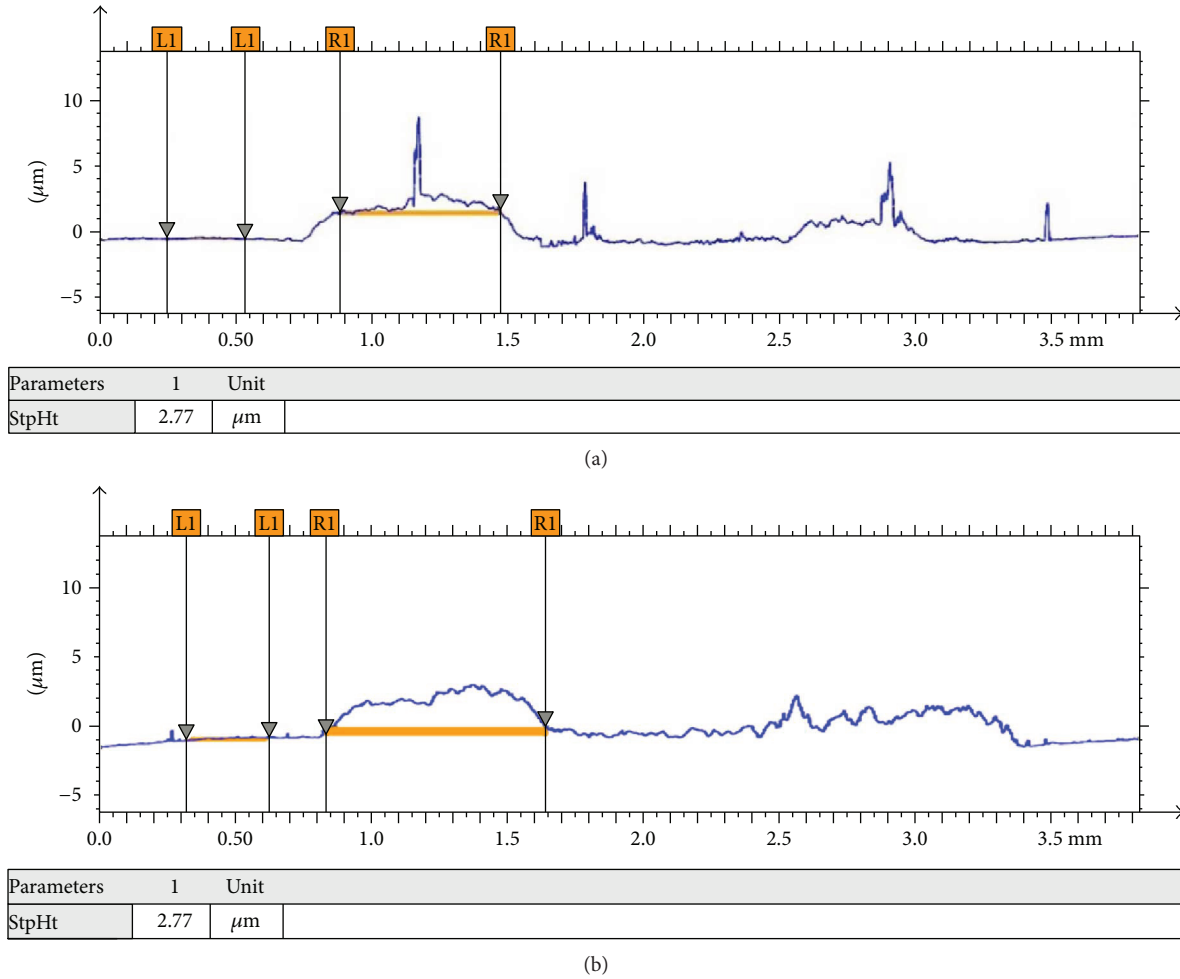


FIGURE 7: Thickness comparison: (a) before etching and (b) after etching.

resistance with a thickness of  $0.75\ \mu\text{m}$  for a printing parameter of 30 to  $35\ \mu\text{m}$  drop spacing.

### 3. Design and Fabrication of MEMS Switch

Figure 2 shows the schematic top view and cross-sectional view of the designed MEMS switch. According to the design, the two transmission lines have a separation of  $210\ \mu\text{m}$ , and the length and width of clamp-clamp beam are  $1400\ \mu\text{m}$  and  $260\ \mu\text{m}$ , respectively. Three contact points are also printed at the three terminals of the switch. Two ends of the transmission line contacts have dimensions of  $400\ \mu\text{m}$  by  $400\ \mu\text{m}$  and the beam end contact has a dimension of  $290\ \mu\text{m}$  by  $290\ \mu\text{m}$ . The dimensions of clamp-clamp contact point are less than that of the other two to achieve a minimum weight.

**3.1. Analysis of the Bottom Transmission Line Layer.** Figure 3(a) shows the image of the first printed layer of the device, which is the transmission line consisting of deposited PEDOT polymer ink. The image was taken by KLA-Tencor process camera. This transmission line has an average thickness of  $2.59\ \mu\text{m}$ . Figure 3(b) is the uniformity analysis in 3D, and Figure 3(c) shows the 2D thickness measurement. This

step needs a total of 20 layers of printed PEDOT to achieve the designed critical thickness.

From Figure 3(a), it appears that the two transmission lines are shorted by a slight amount of contact. The reason for this is the spreading of ink during printing. But the amount of PEDOT is quite small, and the amount of spreading is not significant enough to short the path. The measured resistances between the two transmission lines were found to be infinite which proved that the two transmission lines were not shorted. Additionally, the end-to-end resistance of a single PEDOT transmission line is measured to be between 1.1 and  $2.0\ \text{k}\Omega$ .

**3.2. Analysis of the Silver Sacrificial Layer.** Figure 4(a) shows the second printed layer which is the Ag sacrificial layer of the device. The average thickness of this layer is about  $2.35\ \mu\text{m}$ . Figure 4(b) shows the uniformity of deposited Ag metallic ink by APEX 3D analysis, and Figure 4(c) shows the 2D thickness measurement. The Ag sacrificial layer is needed with a total of three printed layers to achieve the required critical thickness.

**3.3. Membrane Releasing of Printed MEMS Switch.** Figure 5(a) shows a complete three-layer printed device.

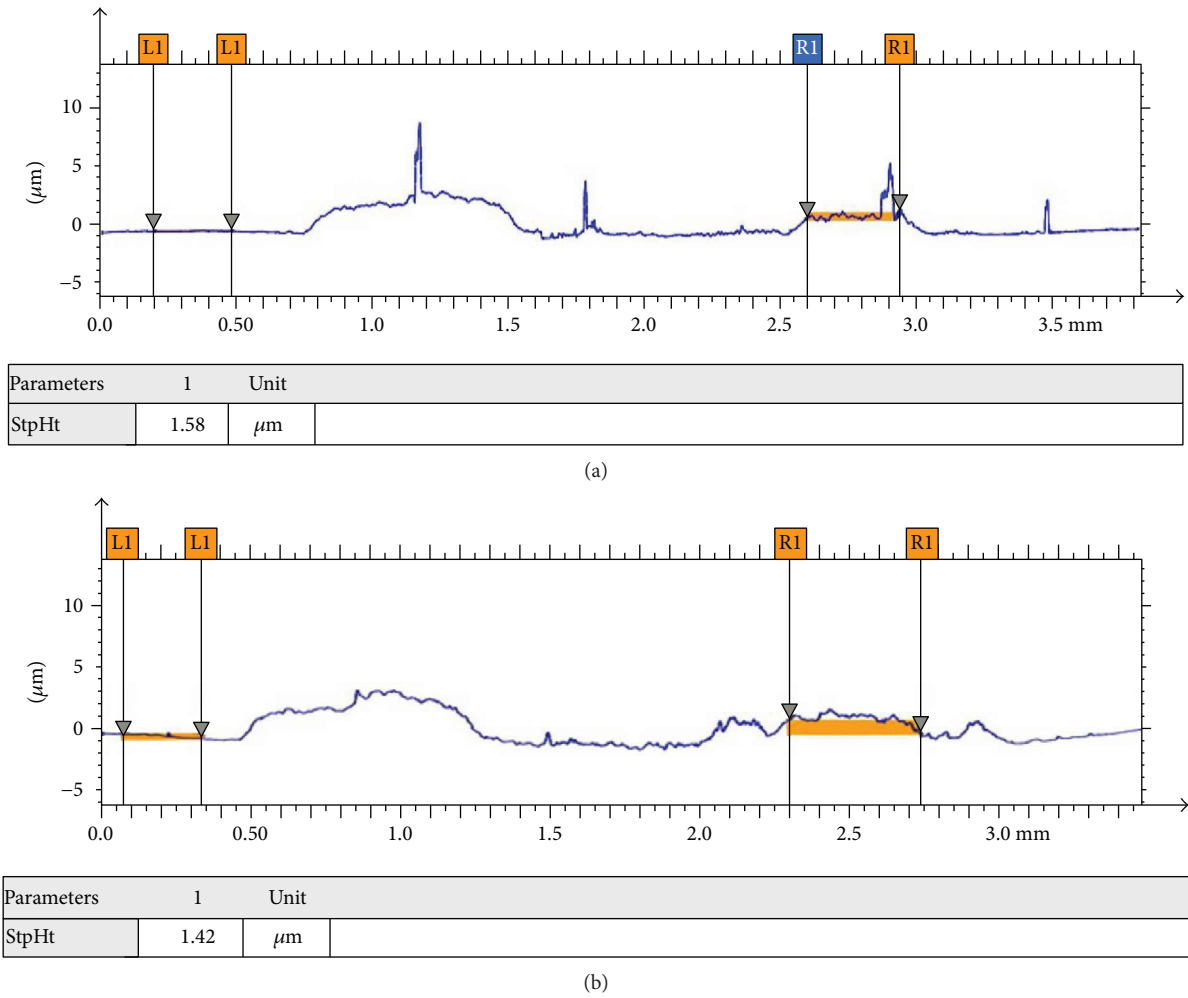


FIGURE 8: Thickness comparison in anchor region (a) before etching and (b) after etching.

Figure 5(b) shows the pointed terminals as 1, 2, and 3. In this image, the clamp-clamp beam, transmission line 1, and transmission line 2 terminals are labeled as 1, 2, and 3, respectively. Figure 5(c) shows the uniformity of printed layers by APEX 3D analysis. The purpose of thickness analysis is to maintain the critical thickness of each layer of the device. Next, the thickness of the sacrificial layer is used to calculate the approximate pull-down/actuation voltage. KLA-Tencor scanning has been taken in either the  $-Y$  to  $+Y$  direction (Figure 4) or the  $-X$  to  $+X$  direction (Figure 5).

Table 4 is the measured resistance between any two of the three terminals of the fabricated switch. It should be noted that Ag is a highly conductive material ink. Before the removal of sacrificial Ag layer, it is shorting the three terminals of the switch. From Table 4, the smaller resistances indicate the shorted path among these three terminals due to the Ag sacrificial layer.

An acid solution is used for etching the Ag sacrificial layer and releasing the membrane. Figures 6(a) and 6(b) show the complete MEMS switch before and after etching. It took about 15 minutes to completely release the

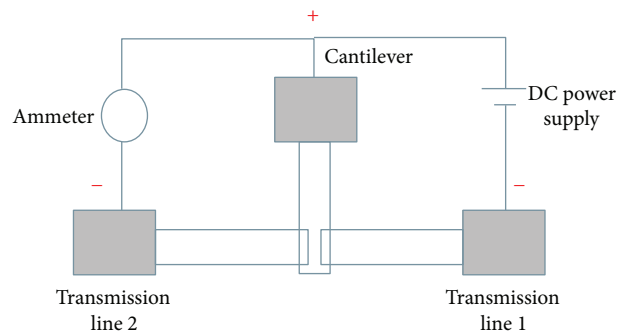


FIGURE 9: Circuit configuration for DC testing.

membrane. It is also evident from Figure 6(b) that the Ag sacrificial layer is completely etched off. End-to-end terminal resistance is measured, which will indicate whether the membrane is completely released or not.

Table 5 shows the resistances between any two of the three terminals of the MEMS switch after etching the Ag sacrificial layer. According to the original design, after the removal of the sacrificial layer, there should not be any

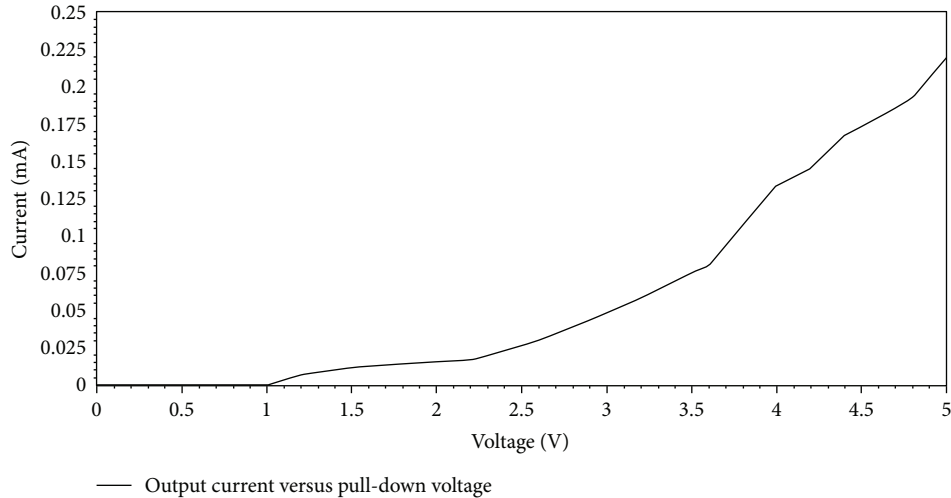


FIGURE 10: Input voltage versus output current.

physical contact among three terminals. So, theoretically, the resistances between the terminals should be very high after removing the sacrificial layer. High resistance values between any two terminals in Table 5 prove that the membrane has been released successfully. Another way to prove a successful membrane release is to compare the thickness measurement before and after etching.

**3.4. Thickness Comparison before and after Membrane Release.** Figure 7 shows the thickness comparison before and after etching. Scanning was taken along the  $-X$  to  $+X$  direction (Figure 7(b)). It is seen in Figure 7(a) that the thickness of the sacrificial layer region was  $2.77 \mu\text{m}$  before etching, and Figure 7(b) shows that the thickness measurement of the same region after etching is  $2.76 \mu\text{m}$ . The measured profile of the post release air gap in Figure 5 is further proof that the release has been done successfully. Although the clamp-clamp beam dropped down a little bit about  $0.01 \mu\text{m}$ , there is still quite a large air gap between the beam and transmission lines as the measured resistance is very high in between any two terminals.

Additionally, Figure 8 shows the comparison of 2D thicknesses in the anchor region. These two thicknesses are also almost the same for before and after etching, which proves that the clamp-clamp was still hanging with some air gap in between the clamp-clamp beam and transmission lines.

#### 4. DC and RF Characterization of the Printed MEMS Switch

Two different connection schemes are used to analyze the DC performance analysis of the switch. Figure 9 shows the schematic diagram of connection. The input voltage is applied between the clamp-clamp beam and transmission line 1, and output signal is taken using an ammeter in between the clamp-clamp beam and transmission line 2. The application for this MEMS switch requires that the input signal is applied on one side of the transmission line and the output is collected from the other side when the

switch is turned on. The input signal was applied by an external power supply (model: GPS-3303), and the output was measured by the ammeter option of a multimeter (model: HP 34401 A).

By using the power supply, applied voltage is increased gradually from 0 V to 5 V which is incremented by 0.2 V. It is seen that there were very small current (0.0001 mA) or no current output till 1.0 V. Just after crossing the 1.0 V, the device starts conducting with 0.0068 mA output current. During the start of current conduction, the recorded voltage was 1.2 V. Therefore, the actuation voltage for the printed MEMS switch is 1.2 V.

Figure 10 presents the plotted data for input voltage versus output current for connection type 1. It is evident from the plot that it has three different regions, which are 0–1.2 V, 1.2–4.8 V, and beyond 4.8 V. The first region is 0–1.1 V where the switch is not turned on; the second is 1.2–4.8 V which is the active region for the switch; and finally, after 4.8 V, the switch saturates.

After completely pulling down the clamp-clamp beam, we removed the ammeter between the cantilever and transmission line 2. RF signal from vector network analyzer is applied to transmission line 1 through the RF probe. The output from transmission line 2 is evaluated through the S21 parameter measurement using a vector network analyzer up to 13.5 GHz. The maximum insertion loss is about 5 dB. The insertion loss could be further reduced by optimizing the conductivity of the transmission line.

To put the inkjet-printed MEMS switch in perspective with other microswitches, Table 6 summarized the experimental results of an electrostatically actuated MEMS switch.

#### 5. Conclusion

This research work demonstrates a major milestone toward the fabrication of a 3D inkjet-printed flexible MEMS switch. The MEMS switch consists of three different layers with different sizes. A detailed analysis of each layer and

TABLE 6: An upfront summary of the performance of the printed MEMS switch.

Actuation scheme	Electrostatic
Actuation voltage	1.2 V
R (clamp-clamp beam-transmission line), connected by sacrificial layer	280~400 $\Omega$
R (clamp-clamp beam-transmission line), after removal of sacrificial layer	2.5~3.0 M $\Omega$
R (transmission line-transmission line), connected by sacrificial layer	380~450 $\Omega$
R (transmission line-transmission line), after removal of sacrificial layer	0.40~0.55 M $\Omega$
Current capacity	0.0001~0.2195 mA
Current on-off ratio	2195 : 1
RF insertion loss measured up to 13.5 GHz	5 dB

characterization are also illustrated in this paper. The MEMS switch has a low actuation voltage of 1.2 V, current capacity of 0.2195 mA, a current on-off ratio of 2195 : 1, and an RF insertion loss of 5 dB up to 13.5 GHz. The performance of the MEMS switch could be further improved through the optimization of material selection and fabrication process. We believe that these results have paved the way for the development of next-generation high-performance, lightweight, mechanically flexible, and low-activation voltage RF MEMS switches for numerous phased-array antenna systems and other commercial and military communication applications.

## Conflicts of Interest

The authors declare that they have no conflicts of interest.

## Acknowledgments

This research was supported by NASA STTR Phase II under Contract no. NNX15CC34C and Northrop Grumman Grant no. 2206730. The authors would like to thank Jack Maceachern for his careful proofreading of this paper.

## References

- [1] M. Y. Chen, D. Pham, H. Subbaraman, L. Xuejun, and R. T. Chen, "Conformal ink-jet printed C-band phased-array antenna incorporating carbon nanotube field-effect transistor based reconfigurable true-time delay lines," *IEEE Transactions on Microwave Theory and Techniques*, vol. 60, no. 1, pp. 179–184, 2012.
- [2] J. Vaillancourt, H. Zhang, P. Vasinajindakaw et al., "All ink-jet printed carbon nanotube (CNT) thin-film transistor on a polyimide substrate with an ultra-high operating frequency of over 5 GHz," *Applied Physics Letters*, vol. 93, no. 24, article 243301, 2008.
- [3] Z. Wang, A. F. Cook, X. Yang, Z. Liu, Y. Qingkai, and M. Y. Chen, "Graphene-based flexible field effect transistor with inkjet printed silver electrodes," *Current Nanoscience*, vol. 9, no. 5, pp. 635–637, 2013.
- [4] M. A. Monne, E. Eureka, Z. Wang, and M. Y. Chen, "Inkjet printed graphene-based field-effect transistors on flexible substrate," in *Proceedings of SPIE*, vol. 10349 of *Low-Dimensional Materials and Devices*, pp. 1034905-1–1034905-6, San Diego, CA, USA, 2017.
- [5] D. T. Pham, H. Subbaraman, M. Y. Chen, X. Xu, and R. T. Chen, "Self-aligned carbon nanotube thin-film transistors on flexible substrates with novel source–drain contact and multi-layer metal interconnection," *IEEE Transactions on Nanotechnology*, vol. 11, no. 1, pp. 44–50, 2012.
- [6] S. Gamerith, A. Klug, H. Scheiber, U. Scherf, E. Moderegger, and E. J. List, "Direct ink-jet printing of Ag–Cu nanoparticle and Ag-precursor based electrodes for OFET applications," *Advanced Functional Materials*, vol. 17, no. 16, pp. 3111–3118, 2007.
- [7] T. Dürkop, S. Getty, E. Cobas, and M. Fuhrer, "Extraordinary mobility in semiconducting carbon nanotubes," *Nano Letters*, vol. 4, no. 1, pp. 35–39, 2004.
- [8] S. Khan and L. Lorenzelli, "Technologies for printing sensors and electronics over large flexible substrates: a review," *IEEE Sensors Journal*, vol. 15, no. 6, pp. 3164–3185, 2015.
- [9] H. P. Le and Le Technologies Inc., "Progress and trends in ink-jet printing technology," *Journal of Imaging Science and Technology*, vol. 42, pp. 49–62, 1998.
- [10] H. Wijshoff, "The dynamics of the piezo inkjet printhead operation," *Physics Reports*, vol. 491, no. 4-5, pp. 77–177, 2010.
- [11] N. D. Sankir, *Flexible Electronics: Materials and Device Fabrication*, Virginia Polytechnic Institute and State University, Blacksburg, VA, USA, 2005.
- [12] W. Van Hoeve, S. Gekle, J. H. Snoejer, M. Versluis, M. P. Brenner, and D. Lohse, "Breakup of diminutive Rayleigh jets," *Physics of Fluids*, vol. 22, no. 12, article 122003, 2010.
- [13] V. R. Marinov, Y. A. Atanasov, A. Khan et al., "Direct-write vapor sensors on FR4 plastic substrates," *IEEE Sensors Journal*, vol. 7, no. 6, pp. 937–944, 2007.
- [14] V. Mulloni, F. Giacomozzi, and B. Margesin, "Controlling stress and stress gradient during the release process in gold suspended micro-structures," *Sensors and Actuators A: Physical*, vol. 162, no. 1, pp. 93–99, 2010.
- [15] D. Neculoiu, F. Giacomozzi, L. Bary et al., "Compact lumped elements micromachined band-pass filters with discrete switching for 1.8/5.2 GHz applications," in *2006 International Semiconductor Conference*, pp. 107–110, Sinaia, Romania, 2006.
- [16] X. Rottenberg, H. Jansen, P. Fiorini, W. De Raedt, and H. Tilmans, "Novel RF-MEMS capacitive switching structures," in *2002 32nd European Microwave Conference*, pp. 1–4, Milan, Italy, 2002.
- [17] H. S. Nalwa, *Handbook of Nanostructured Materials and Nanotechnology*, vol. 5, Academic Press, San Diego, CA, USA, 1999.
- [18] S. Chung, M. A. Karim, H. J. Kwon, W. Scheideler, and V. Subramanian, "A high-speed inkjet-printed microelectromechanical relay with a mechanically enhanced double-clamped channel-beam," *Journal of Microelectromechanical Systems*, vol. 26, no. 1, pp. 95–101, 2016.
- [19] J. Mort and G. Pfister, *Electronic Properties of Polymers*, John Wiley & Sons, Hoboken, NJ, USA, 1982.
- [20] Dupont, "Dupont™ Kapton® HN Polyimide Film," 2016, <http://www.dupont.com/content/dam/dupont/products-and>

services/membranes-and-films/polyimide-films/documents/  
DEC-Kapton-HN-datasheet.pdf.

- [21] Novacentrix, “Metalon® conductive inks for printed electronics,” <https://www.novacentrix.com/sites/default/files/pdf/Metalon%20JS-B40G.PDF>.
- [22] S. Aldrich, “Jetting instructions for Orgacon™ IJ-1005,” March 2012, [https://www.sigmaaldrich.com/content/dam/sigma-aldrich/docs/Sigma/Product\\_Information\\_Sheet/1/739316pis.pdf](https://www.sigmaaldrich.com/content/dam/sigma-aldrich/docs/Sigma/Product_Information_Sheet/1/739316pis.pdf).

## Research Article

# Miniaturized Printed Inverted-F Antenna for Internet of Things: A Design on PCB with a Meandering Line and Shorting Strip

Cheuk Yin Cheung,<sup>1</sup> Joseph S. M. Yuen,<sup>2</sup> and Steve W. Y. Mung <sup>2</sup>

<sup>1</sup>The Hong Kong University of Science and Technology, Hong Kong

<sup>2</sup>Innovation Technology Company Limited, Hong Kong

Correspondence should be addressed to Steve W. Y. Mung; [mungwaiyin@hotmail.com](mailto:mungwaiyin@hotmail.com)

Received 29 July 2017; Revised 21 December 2017; Accepted 24 January 2018; Published 26 March 2018

Academic Editor: Xing Lan

Copyright © 2018 Cheuk Yin Cheung et al. This is an open access article distributed under the Creative Commons Attribution License, which permits unrestricted use, distribution, and reproduction in any medium, provided the original work is properly cited.

This paper focuses on a printed inverted-F antenna (PIFA) with meandering line and meandering shorting strip under 2.4 GHz industrial, scientific, and medical (ISM) band for Internet of things (IoT) applications. Bluetooth Low Energy (BLE) technology is one of potential platforms and technologies for IoT applications under ISM band. Printed circuit board (PCB) antenna commonly used in commercial and medical applications because of its small size, low profile, and low cost compared to low temperature cofired ceramic (LTCC) technology. The proposed structure of PIFA is implemented on PCB to gain all these advantages. Replacing conventional PCB line in PIFA by the meandering line and meandering shorting strip improves the efficiency of the PIFA as well as the bandwidth. As a case study, design and measurement results of the proposed PIFA are presented.

## 1. Introduction

Internet of things (IoT) is a concept that applies current network technology to improve different industries and environment for a higher quality of life in society. IoT is a worldwide network that provides a platform allowing big data transfer and connection between people and things. In a smart city, the wireless connections between sensors and users provide real-time monitoring [1, 2]. Big data is received by sensors, which can be used for solving parking problem [3] and traffic congestion [3] and controlling the quality of air and water [4]. For example, in medical application, data is shared with patients and medical professionals through IoT; therefore, consulting efficiency is enhanced as well as lowering the medical cost [5]. These several applications provide a successful improvement in our society. There are three main layers in the IoT architecture, sensing, network, and application [6]. In the network layer, wireless parts including an antenna and RF front-end circuits are the main challenges for IoT development [7, 8]. There are different wireless solutions, in which Bluetooth Low Energy (BLE) [9] and Zigbee [10] are highly potential suitable platforms for IoT

applications. These wireless technologies are operated under 2.4 GHz industrial, scientific, and medical (ISM) band. Nowadays, minimizing the size of the wireless part especially the antenna is still the main challenging research area.

There are many existing size-reduced solutions, and one of the common types is low temperature cofired ceramic (LTCC) antenna [11, 12]. They have different sizes and lengths among these LTCC antennas such as length with 7 mm, 5 mm, and 3 mm. In Figure 1(a), it shows an incident E-field propagates to a vertical dipole of length  $L = 0.5\lambda_1$ , where  $\lambda_1$  is the wavelength used. If the current distribution of the dipole is uniform, the actual current distribution is nearly sinusoidal. If the same dipole is used at a longer wavelength,  $\lambda_2$ , so the length is only  $L = 0.1\lambda_2$  long. The current tapers almost linearly from the central feed point to zero at the ends in a triangular distribution in Figure 1(b). Assuming dipole with uniform current distribution, the radiation resistance  $R_{\text{rad}}$  in a free space is given by [13]

$$R_{\text{rad}} = 80\pi^2 \left(\frac{L}{\lambda}\right)^2. \quad (1)$$

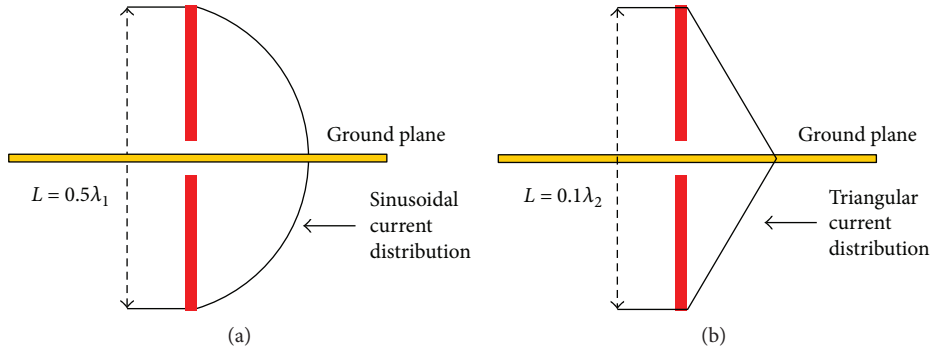


FIGURE 1: (a) Antenna (length =  $0.5\lambda_1$ ) with sinusoidal current distribution. (b) Antenna (length =  $0.1\lambda_2$ ) with triangular current distribution.

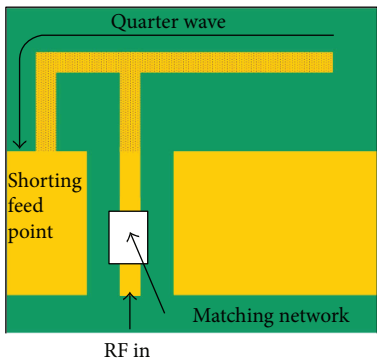


FIGURE 2: Printed inverted-F antenna (PIFA).

TABLE 1: Parameter used in the simulation.

Parameters	Dimension
The width of the strip, $w$	0.6 mm
The space of each turn, $s$	0.4 mm
The length of each turn, $l$	3.5 mm
Distance between shorting feed point and feed point	2.3 mm
Distance to the ground plan	0.8 mm
Area of the antenna ( $W \times L_1$ )	$15 \times 6 \text{ mm}^2$
Ground plane ( $W \times L_2$ )	$15 \times 30 \text{ mm}^2$

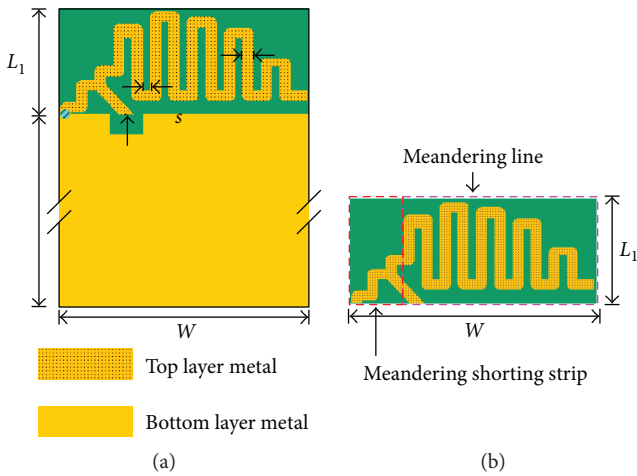


FIGURE 3: (a) Proposed antenna. (b) Antenna with meandering line and meandering shorting strip.

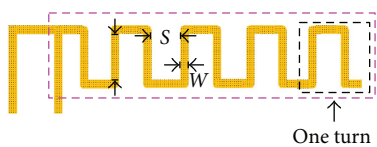


FIGURE 4: Meandering line used in PIFA.

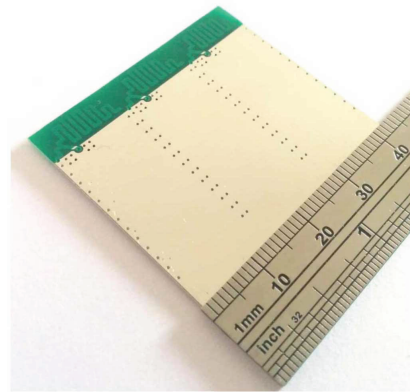


FIGURE 5: Photo of proposed PIFA.

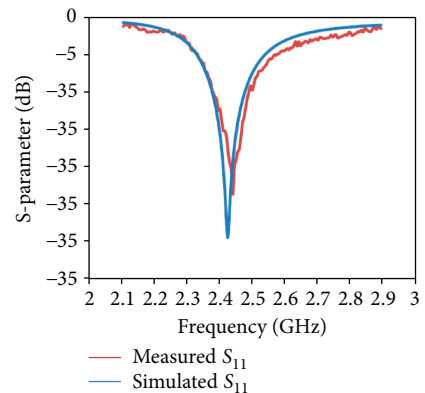


FIGURE 6: Simulated and measured S-parameter,  $S_{11}$ .

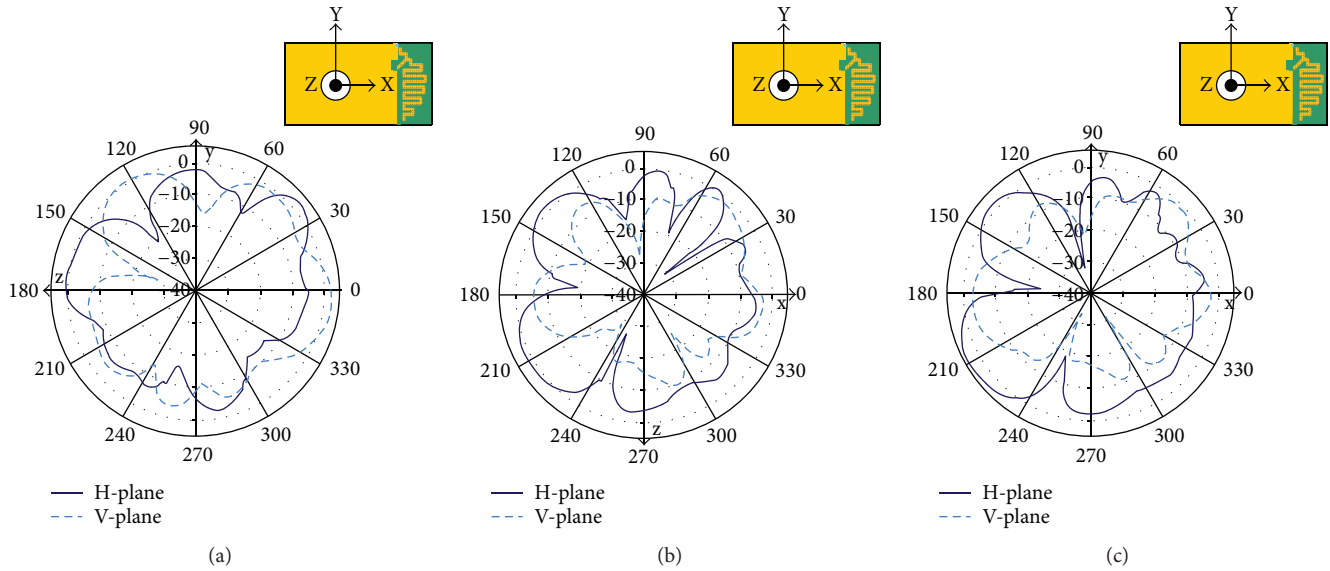


FIGURE 7: Measured radiation patterns in total fields (horizontal plane (H-Plane) and vertical plane (V-Plane)): (a) Y-Z plane, (b) X-Z plane, and (c) X-Y plane.

For triangular current distribution in Figure 1(b), the radiation resistance is smaller than those in Figure 1(a). Small values of radiation resistance indicate that the performance of the antenna is not very efficient. An antenna with a shorter length but not resonant in the correct frequency leads to poor overall performance since its resonant frequency is higher than the operating frequency, and so a matching network is added to tune to the correct resonant frequency. This matching network is used for maximum power transfer from the radio transceiver to the antenna; however, the antenna still gives poor efficiency as well as resulting extra cost and circuit area.

Several designs [14–16] were proposed to reduce the antenna size by loading with capacitance since this lowers the resonant frequency, making it appear electrically longer. However, the performance of the antenna depends on the quality factor  $Q$  of the capacitors used. In general, the components with higher  $Q$  have a higher cost. In this paper, a new implementation of the antenna which has the advantages of low profile, small size, and foldable configuration is presented. No matching network is required, and it can be implemented on standard printed circuit board (PCB).

## 2. Operation of Proposed Printed Inverted-F Antenna (PIFA)

The printed inverted-F antenna (PIFA) is commonly used in the commercial and medical devices compared to other inverted-F antennas (IFAs) [17–20] since it is small, low profile, and low cost. These IFAs [17–20] are in a 3D shape and nonfoldable which occupy a large volume in portable devices. PIFA, therefore, is widely used in small portable devices [21–23]. PIFA is like a monopole printed on the PCB, but it has a shorting feed point along the main resonant structure shown in Figure 2. It has the advantage that the folded part introduces capacitance to the input impedance of the PIFA

TABLE 2: The gain of the proposed PIFA.

Plane	Peak (dBi)		Average (dBi)	
	Horizontal	Vertical	Horizontal	Vertical
Y-Z	2.31	2.75	-4.12	-3.35
X-Z	1.92	-2.00	-3.25	-7.94
X-Y	4.00	-1.12	-2.51	-7.28

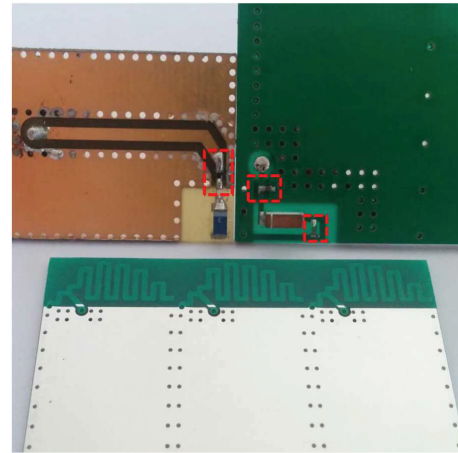


FIGURE 8: Compared result to Walsin (left) and Murata (right) antennas.

which is cancelled by the shorting feed point. This shorting feed point configuration, therefore, reduces the antenna's size. The matching network may be required for maximum power transfer and, hence, efficient radiation.

Figure 3 shows the proposed antenna which contains two parts, meandering line and meandering shorting strip. Since the ground is classified as part of the antenna during the design, the size  $W \times (L_1 + L_2) = 15 \text{ mm} \times (6 + 30) \text{ mm}$  is

TABLE 3: Comparison between proposed PIFA, Walsin [12], and Murata antennas [14].

Antenna	Type	Volume (include the matching network)	Extra components
Proposed PIFA	PCB	$15 \times 6.0 \times 0.035 \text{ mm}^3$	No extra cost required
Walsin	LTCC	$12 \times 5.0 \times 1.2 \text{ mm}^3$	1 antenna and 2 passive components
Murata	LTCC	$12 \times 5.0 \times 1.2 \text{ mm}^3$	1 antenna and 2 passive components

chosen (this is the common size of a wireless part). The antenna is simulated and designed on an FR4 PCB with dielectric constant=4.6, and the PCB thickness used is 0.3 mm. These parameters are used to model the first 2 layers in the multiple-layered PCB structure, and the simulation is obtained by Advanced Design System (ADS).

The resonant frequency of PIFA decreases when the length of the conventional PCB line increases, because of the longer wavelength [13]. This PCB line in the conventional PIFA is replaced by the meandering line in Figure 4. The combination of horizontal and vertical lines forms turns in Figure 4, and the number of turns increases efficiency. The resonant frequency in Figure 4 is much lower than that of the PCB line in the PIFA with equal length [24, 25].

However, one of the disadvantages of the meandering line used is the narrow bandwidth [26, 27] compared to the traditional PIFA in Figure 2. Another disadvantage is a matching network required to be placed at the antenna's input to achieve a good impedance matching for maximum efficiency [28]. The shorting strip of the PIFA becoming a meandering shape increases the bandwidth [29, 30]. Therefore, the meandering shorting strip is then added to increase its bandwidth shown in Figure 3(b). Designing the meandering segment to be a log periodic pattern can improve the antenna's impedance matching [26] shown in Figure 3. Table 1 shows the final dimension used in simulation so that the resonance frequency is close to the operating frequency, 2.45 GHz.

### 3. Experimental Results

A prototype was designed and fabricated on the FR4 PCB based on the dimension in Table 1, and the photo of the prototype is shown in Figure 5. The return loss is measured by a network analyzer, and the radiation patterns are carried out by an antenna measurement system. In Figure 6, the measured return loss is shown as the red line together with the simulated result as the blue line. The return loss is better than 10 dB within the ISM band. Figure 7 shows the measured radiation patterns in total fields of the proposed PIFA at 2.45 GHz as well as the gain of the antenna in Table 2.

Figure 8 shows the photo of the proposed PIFA compared to the Walsin (monopole) antenna [12] and the Murata antenna [14], which are LTCC antennas. Both need the extra components for good impedance matching. An extra capacitive is added in the Murata antenna [14] to achieve the size reduction, and the large ground plane is required to achieve better efficiency as well. Table 3 shows the comparison table of these 3 antennas. It shows that the Walsin and Murata antennas have a little size smaller than the proposed PIFA. However, the proposed PIFA has only

TABLE 4: Gain between proposed PIFA, Murata [13], and Walsin monopole antennas [12].

Antenna	Plane	Total average (dBi)
Proposed	Y-Z	-0.708
	X-Z	-1.980
	X-Y	-1.260
Murata	Y-Z	No data in datasheet
	X-Z	-1.761
	X-Y	-3.318
Walsin	Y-Z	0.891
	X-Z	-1.846
	X-Y	-2.556

the PCB metal trace's thickness (around  $35 \mu\text{m}$ ), which is approximately zero in thickness since it was printed on the PCB; therefore, this can be easily fabricated on the flexible printed circuit (FPC) as well, which is highly foldable for the mechanical housing in portable devices compared to those nonfoldable IFA designs [17–20]. And there is no extra cost required (printed on the PCB) on this proposed PIFA compared to the other two antennas as well as no extra matching network and capacitive load. In Table 4, it shows that the overall gain performance is better than that of the other two antennas.

### 4. Conclusion

This paper proposes a minimized PIFA design suitable for IoT and other ISM band applications. To elaborate on this, the architecture of the PIFA on PCB with meandering line and meandering shorting strip was proposed. The measurement result of return loss and gain performances has shown that it has better performances compared to the LTCC antennas and there are no extra components required for good impedance matching. This proposed PIFA is a paradigm of choice compared to others keeping the portability of devices with low cost and good performance.

### Conflicts of Interest

The authors declare that there is no conflict of interest regarding the publication of this paper.

### Acknowledgments

This work was supported by Innovation Technology Company Limited, Hong Kong.

## References

- [1] B. Ahlgren, M. Hidell, and E. C.-H. Ngai, "Internet of things for smart cities: interoperability and open data," *IEEE Internet Computing*, vol. 20, no. 6, pp. 52–56, 2016.
- [2] Y. Sun, H. Song, A. J. Jara, and R. Bie, "Internet of things and big data analytics for smart and connected communities," *IEEE Access*, vol. 4, pp. 766–773, 2016.
- [3] W. He, G. Yan, and L. Da Xu, "Developing vehicular data cloud services in the IoT environment," *IEEE Transactions on Industrial Informatics*, vol. 10, no. 2, pp. 1587–1595, 2014.
- [4] A. Zanella, N. Bui, A. Castellani, L. Vangelista, and M. Zorzi, "Internet of things for smart cities," *IEEE Internet of Things Journal*, vol. 1, no. 1, pp. 22–32, 2014.
- [5] U. Satija, B. Ramkumar, and M. Sabarimalai Manikandan, "Real-time signal quality-aware ECG telemetry system for IoT-based health care monitoring," *IEEE Internet of Things Journal*, vol. 4, no. 3, pp. 815–823, 2017.
- [6] S. Chen, H. Xu, D. Liu, B. Hu, and H. Wang, "A vision of IoT: applications, challenges, and opportunities with China perspective," *IEEE Internet of Things Journal*, vol. 1, no. 4, pp. 349–359, 2014.
- [7] S. Shinjo, K. Nakatani, K. Tsutsumi, and H. Nakamizo, "Integrating the front end: a highly integrated RF front end for high-SHF wide-band massive MIMO in 5G," *IEEE Microwave Magazine*, vol. 18, no. 5, pp. 31–40, 2017.
- [8] C.-S. Yoo, J.-K. Lee, D. Kim et al., "RF front-end passive circuit implementation including antenna for ZigBee applications," *IEEE Transactions on Microwave Theory and Techniques*, vol. 55, no. 5, pp. 906–915, 2007.
- [9] R. Tabish, A. Ben Mnaouer, F. Touati, and A. M. Ghaleb, "A comparative analysis of BLE and 6LoWPAN for U-HealthCare applications," in *2013 7th IEEE GCC Conference and Exhibition (GCC)*, pp. 286–291, Doha, Qatar, 2013.
- [10] Z. Zhang and X. Hu, "ZigBee based wireless sensor networks and their use in medical and health care domain," in *2013 Seventh International Conference on Sensing Technology (ICST)*, pp. 756–761, Wellington, New Zealand, 2013.
- [11] D. Seo, S. Jeon, N. Kang, J. Ryu, and J.-H. Choi, "Design of a novel compact antenna for a Bluetooth LTCC module," *Microwave and Optical Technology Letters*, vol. 50, no. 1, pp. 180–183, 2008.
- [12] L. K. Yeung, J. Wang, Y. Huang, S.-C. Lee, and K.-L. Wu, "A compact LTCC Bluetooth system module with an integrated antenna," *International Journal of RF and Microwave Computer-Aided Engineering*, vol. 16, no. 3, pp. 238–244, 2006.
- [13] J. D. Kraus and R. J. Marhefka, *Antennas: For All Applications*, McGraw-Hill, Upper Saddle River, NJ, USA, 2002.
- [14] A. Zhao, J. Xue, C. Jing, and A. Salo, "The use of Murata ceramic Bluetooth antenna for wrist device based on flexible printed circuit boards," in *2008 European Conference on Wireless Technology*, pp. 334–337, Amsterdam, Netherlands, 2008.
- [15] P. Tornatta, "A method to design an aperture-tuned antenna using a MEMS digital variable capacitor," *Microwave Journal*, vol. 57, no. 1, pp. 102–114, 2014.
- [16] C. R. Rowell and R. D. Murch, "A capacitively loaded PIFA for compact mobile telephone handsets," *IEEE Transactions on Antennas and Propagation*, vol. 45, no. 5, pp. 837–842, 1997.
- [17] H. D. Hristov, H. Carrasco, and R. Feick, "Bent inverted-F antenna for WLAN units," *Microwave and Optical Technology Letters*, vol. 50, no. 6, pp. 1505–1510, 2008.
- [18] M. J. Ammann and L. E. Doyle, "A loaded inverted-f antenna for mobile handsets," *Microwave and Optical Technology Letters*, vol. 28, no. 4, pp. 226–228, 2001.
- [19] V. K. Palukuru, A. Pekonen, V. Pynttari, R. Mäkinen, J. Hagberg, and H. Jantunen, "An inkjet-printed inverted-F antenna for 2.4-GHz wrist applications," *Microwave and Optical Technology Letters*, vol. 51, no. 12, pp. 2936–2938, 2009.
- [20] S.-W. Su, "Linearly-polarized patch PIFA for GPS/GLONASS operation for tablet-computer applications," *Microwave and Optical Technology Letters*, vol. 57, no. 1, pp. 149–153, 2015.
- [21] C. Soras, M. Karaboikis, G. Tsachtsiris, and V. Makios, "Analysis and design of an inverted-F antenna printed on a PCMCIA card for the 2.4 GHz ISM band," *IEEE Antennas and Propagation Magazine*, vol. 44, no. 1, pp. 37–44, 2002.
- [22] H. Y. D. Yang, "Printed straight F antennas for WLAN and Bluetooth," in *IEEE Antennas and Propagation Society International Symposium. Digest. Held in conjunction with: USNC/CNC/URSI North American Radio Sci. Meeting (Cat. No.03CH37450)*, vol. 2, pp. 918–921, Columbus, OH, USA, 2003.
- [23] M. Ali and G. J. Hayes, "Small printed integrated inverted-F antenna for Bluetooth application," *Microwave and Optical Technology Letters*, vol. 33, no. 5, pp. 347–349, 2002.
- [24] V. B. Ambhore and A. P. Dhande, "An overview on properties, parameter consideration and design of meandering antenna," *International Journal of Smart Sensors and Ad Hoc Networks*, vol. 1, pp. 59–62, 2012.
- [25] S. R. Best and J. D. Morrow, "Limitations of inductive circuit model representations of meander line antennas," in *IEEE Antennas and Propagation Society International Symposium. Digest. Held in conjunction with: USNC/CNC/URSI North American Radio Sci. Meeting (Cat. No.03CH37450)*, vol. 1, pp. 852–855, Columbus, OH, USA, 2003.
- [26] A. Jahanbakhshi, G. Moradi, and R. Sarraf Shirazi, "Design and simulation of different types of meander line antennas with improved efficiency," in *Progress In Electromagnetics Research Symposium Proceeding*, pp. 594–597, Moscow, Russia, 2012.
- [27] D. Misman, "The effect of conductor line to meander line antenna design," in *2007 Asia-Pacific Conference on Applied Electromagnetics*, pp. 1–5, Melaka, Malaysia, 2007.
- [28] T. J. Warnagiris and T. J. Minardo, "Performance of a meandered line as an electrically small transmitting antenna," *IEEE Antennas and Propagation Magazine*, vol. 46, no. 12, pp. 1797–1801, 1998.
- [29] P. W. Chan, H. Wong, and E. K. N. Yung, "Wideband planar inverted-F antenna with meandering shorting strip," *Electronics Letters*, vol. 44, no. 6, p. 395, 2008.
- [30] P. W. Chan, H. Wong, and E. K. N. Yung, "Dual-band printed inverted-F antenna for DCS, 2.4GHz WLAN applications," in *2008 Loughborough Antennas and Propagation Conference*, pp. 185–188, Loughborough, UK, 2008.

## Research Article

# Accurate 3D Mapping Algorithm for Flexible Antennas

Saed Asaly,<sup>1</sup> Boaz Ben-Moshe ,<sup>1</sup> and Nir Shvalb <sup>2</sup>

<sup>1</sup>Department of Computer Science, Aerospace and Nano-Satellite Research Center, K&CG Lab, Ariel University, Ariel, Israel

<sup>2</sup>Department of Industrial Engineering, Aerospace and Nano-Satellite Research Center, K&CG Lab, Ariel University, Ariel, Israel

Correspondence should be addressed to Boaz Ben-Moshe; [benmo@g.ariel.ac.il](mailto:benmo@g.ariel.ac.il)

Received 24 August 2017; Revised 21 December 2017; Accepted 9 January 2018; Published 20 March 2018

Academic Editor: Xuejun Lu

Copyright © 2018 Saed Asaly et al. This is an open access article distributed under the Creative Commons Attribution License, which permits unrestricted use, distribution, and reproduction in any medium, provided the original work is properly cited.

This work addresses the problem of performing an accurate 3D mapping of a flexible antenna surface. Consider a high-gain satellite flexible antenna; even a submillimeter change in the antenna surface may lead to a considerable loss in the antenna gain. Using a robotic subreflector, such changes can be compensated for. Yet, in order to perform such tuning, an accurate 3D mapping of the main antenna is required. This paper presents a general method for performing an accurate 3D mapping of marked surfaces such as satellite dish antennas. Motivated by the novel technology for nanosatellites with flexible high-gain antennas, we propose a new accurate mapping framework which requires a small-sized monocular camera and known patterns on the antenna surface. The experimental result shows that the presented mapping method can detect changes up to 0.1-millimeter accuracy, while the camera is located 1 meter away from the dish, allowing an RF antenna optimization for Ka and Ku frequencies. Such optimization process can improve the gain of the flexible antennas and allow an adaptive beam shaping. The presented method is currently being implemented on a nanosatellite which is scheduled to be launched at the end of 2018.

## 1. Introduction

The vision of having a reliable and affordable global network which can be accessed from any point on the globe at any time is a huge scientific challenge which has attracted many researches during the last few decades. Most proposed solutions are based on a network of hundreds or thousands of LEO nanosatellites which will constitute a global network with the earth via RF communication. These *new-space* projects are of interest to major companies such as Google, Qualcomm, Facebook, and SpaceX. *OneWeb* is an example of such a project involving a large constellation of LEO satellites. Other projects such as Google's *Project Loon* [1] or Facebook's *Aquila Drone* are not directly focused on satellite constellations but generally assume that such global network already exists. The new-space industry includes many small- or medium-size companies which develop

products for the new-space market (e.g., *Planet Labs* and *Spire* are focusing on global imaging [2] and global *IoT*). One of the most famous LEO satellite constellations is the *Iridium* network, developed in the '90s; this global network is still operational, and the second-generation network named *Iridium Next* is currently being deployed. Optimizing a global network in terms of coverage, deployment, and services involves extremely complicated problems from the computational point of view. In order to reduce the cost of deploying such network, many new-space companies are working on miniaturizing their satellites—as launching 100 LEO nanosatellites often costs less than launching a single large satellite into a geosynchronous orbit. In order to allow a long-range, wide-band RF communication between a satellite and a ground station, high-gain directional antennas are being used. Having such a dish antenna on-board of the satellite significantly increases its size and weight, and

therefore, almost all current nanosatellites have a limited bandwidth as they use small low-gain antennas allowing a bandwidth of sub-Mbps. *NSLComm* has developed a concept of nanosatellite with a relatively large expendable antenna, allowing a significantly better link budget from a nanosatellite [3]. Nevertheless, flexible antennas are sensitive to surface distortion especially in space, where significant temperature changes are common. In this paper, we present a generic method to accurately map the surface of a flexible antenna located on a satellite. The presented framework requires very limited space and computing power, allowing it to be implemented even for small nanosatellites.

## 2. Related Works

Mapping a 3D surface is an important problem which is of interest to many researches. Available literature suggests solutions for wide-range mapping techniques including time of flight [4], triangulation [5], structured light [6], RGBD [7], stereo vision [8], and image-based modeling [9].

In this work, we focus on the challenging task of mapping a satellite flexible antenna—which is not suitable for common 3D scanning techniques due to space limitations and the need to perform a 3D scan from a fixed and single angle (i.e., a single image). The ability to infer a 3D model of an object from a single image is necessary for human-level scene understanding. Tatarchenko et al. [10] have presented a convolution network capable of inferring a 3D representation of a previously unseen object given a single image of this object, while in the work of Williams et al. [11], a graph theory and dynamic programming techniques over the shape constraints were presented to compute the anterior and posterior surfaces in individual 2D images. Tanskanen et al. [12] have proposed a complete on-device 3D reconstruction pipeline for mobile monocular hand-held devices, which generates dense 3D models with an absolute scale on-site while simultaneously supplying the user with real-time interactive feedback. Medina et al. [13] suggest a resistor-based 2D shape sensor, and Shvalb et al. [3] show that, using a robotic flexible subreflector, even relatively significant changes in a dish surface can be fixed; naturally, having a 3D model of the current surface of the main dish antenna can improve the accuracy and the run time of such systems.

*2.1. Our Contribution.* In this work, we present a novel method which can robustly recover a surface shape from a single image with known markers (with known shape). The suggested method uses a set of visual markers in order to compute a pointcloud. To the best of our knowledge, this is the first work which presents a framework for performing 3D reconstruction of smooth surfaces with submillimeter accuracy that is applicable for on-board satellite flexible antenna.

## 3. Flexible Antenna for Nanosatellites

The general concept of the flexible antenna with an adjustable robotic subreflector was presented recently [3]. It is

based on a flexible expandable main reflector and an adjustable robotic subreflector which can compensate for minor changes in the main reflector surface. Mechanical mechanisms for manipulating the robotic subreflector may be based on linear servo or piezoelectric motors [3] but can also be based on bioinspired manipulators (see [14]). In order to optimize high-frequency RF communication (e.g., Ka bands), the main antenna should be mapped with an accuracy level which is 25–50 times higher than the communication typical wavelength (about 1 cm in Ka), leading to a challenging mapping accuracy requirement of about 0.2–0.1 mm on average (see [15]). A nanosatellite with such flexible antenna should also be equipped with the following components: (i) a global position receiver (e.g., GPS), (ii) a star tracker in order to determine its orientation, and (iii) an altitude control mechanism (based on both reaction/momentum wheels and a magnetorquer). Using the above components, the satellite on-board computer can aim the antenna to a specific region on earth—in general, this process resembles the task of the imaging satellite that needs to aim its camera to a given region. Denote that for a LEO satellite, such process is a continuous (always on) process, unlike the case of geosynchronous satellites, which only need to maintain a fixed orientation.

The use of flexible antennas for space applications is a relatively new concept. Having an on-board accurate mapping system for the flexible antenna will allow two major benefits:

- (1) A fast and accurate tuning of the robotic subreflector to compensate for the distortion of the main reflector and an adaptive beam-shaping capability of the transmitted pattern.
- (2) A study of the changes in the flexible surface with respect to temperature and time.

Due to space and weight limitations, the on-board 3D mapping system should be as compact as possible. Moreover, the method should use limited computing power for on-board algorithms or limited bandwidth methods for ground-based algorithms. Following these requirements, we shall use a monocular camera and known shape targets for the mapping task.

## 4. Monocular Mapping Algorithm

In order to map the 3-dimensional pointcloud of the satellite antenna, we first embed a set of *targets* (or markers) with a known shape and size. A single camera is assumed to be located near the antenna focal point. We shall now present the general algorithm which analyzes the acquired image to compute the 3D surface of the dish. This process consists of the following stages: (i) camera calibration, (ii) initial pointcloud computation, and (iii) global adjustment.

*4.1. Camera Calibration.* We start by calibrating the camera using an algorithm proposed by Zhang in [16]. Camera calibration is the process of estimating intrinsic and/or extrinsic parameters. Intrinsic parameters deal

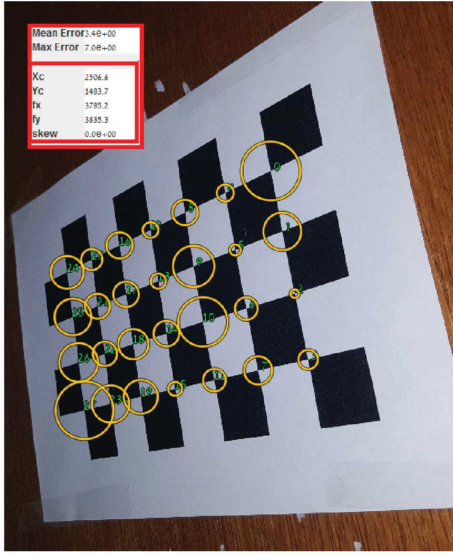


FIGURE 1: An example of an image (after the calibration process). The intrinsic parameters are marked in red, and the expected accuracy (error) is marked in yellow circles (a larger circle implies a larger expected error).

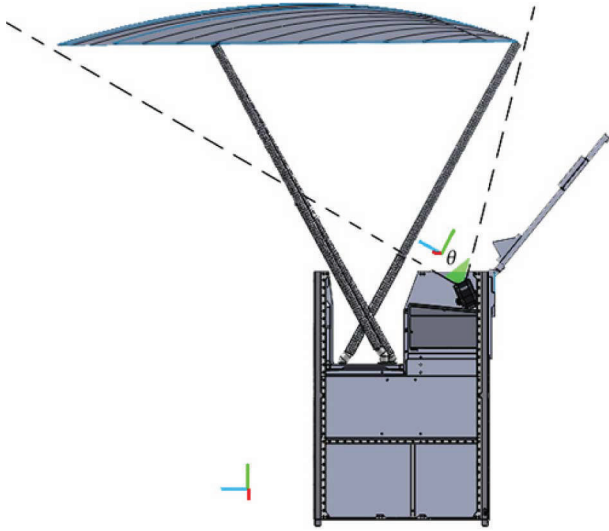


FIGURE 2: The camera location on-board; here,  $\theta$  is the field of view which will be considered as  $\in [60, 90]$ . Note the difference between the coordinate systems of each satellite and camera.

with the camera's internal characteristics, such as its focal length, skewness, distortion, and image center. The camera calibration step is essential for a 3D computer vision, as it allows one to estimate the scene's structure in Euclidean space removing lens distortions, which degrades accuracy. Figure 1 depicts an image taken after a calibration process.

Figure 2 illustrates the position of the camera on the satellite which allows one to view the whole antenna span.

**Input: Undistorted image (frame)  $F$ .**

**Output: 3D pointcloud.**

- 1: Let  $im_i = T(im)$ .
- 2:  $T \leftarrow Segment(F)$
- 3: **for each** triplet  $t_i \in T$  **do** Compute a 3D point:  $p_i \in P$  as follows:
  - (1) The  $x, y$  coordinates of  $p_i$  are the center values of  $t_i$
  - (2)  $\hat{n}_i \leftarrow$  the normal of the target.
  - (3)  $\Delta\alpha_i \leftarrow$  the angular difference between  $\hat{n}_i$  and the vector to  $t_i$ .
  - (4) Let  $p_i.z = \sqrt{t_i.area} \cdot C_{camera} / \cos \Delta\alpha_i$
- 4: **end for**

ALGORITHM 1: Initial 3D mapping using circular targets.

Accordingly, the camera's FoV (field of view) should be chosen to be in the range of  $60^\circ$  and  $90^\circ$ . Such a relatively large FoV imposes a nonnegligible camera distortion. Thus, the calibration process is necessary to allow an accurate angular transformation between the camera coordinate system (i.e., pixel position) and the satellite global coordinate system.

Often, one would also like to express the position of points ( $x$ ,  $y$ , and  $z$ ) given in the camera coordinate system in a world (satellite) coordinate system. This may be done by simply rotating the set of points  $P$  about the angle of inclination of the camera (see Figure 2).

**4.2. Initial Pointcloud Generator Algorithm.** We start our discussion considering circular targets. Algorithm 1 produces the initial pointcloud which we further use in this paper. Here, the function  $T(im)$  uses the information from the calibration step to remove lens distortion from the image.  $C_{camera}$  is the angular resolution (taken from the camera parameters). We mark by  $Segment(F)$  the function that segments the acquired image and detect the targets  $T$  and compute the triplet (center, area, and geometry) for each target. In order to compute  $\Delta\alpha$  for each target  $T$ , consider two of its vertices  $w_1$  and  $w_2$  and do the following:

- (1) Calculate the normal of the surface that the target lies on—for each pattern, the manner in which the normal is calculated is different (we shall discuss this below).
- (2) For each pair  $w_1, w_2 \in T$ , do the following:
  - (a) Consider the plane that passes through the camera point (the origin point) and points  $w_1$  and  $w_2$ . Define line  $l_1$  as the intersection between this plane and the plane that the target lies on.
  - (b) Let  $l_2$  be the line connecting the camera and the midpoint between  $w_1$  and  $w_2$ .
- (3) Set  $\alpha$  to be the angle between  $l_1$  and  $l_2$  (see Figure 3).

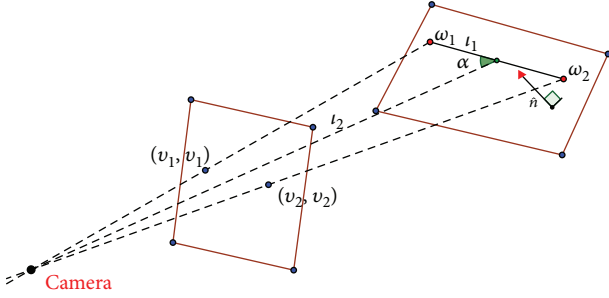


FIGURE 3: An illustration of the information needed to find  $\Delta\alpha$ , where  $\alpha$  is the green angle.

- (4) Define the angular difference as  $90^\circ - \text{avg}(\alpha_i)$ .

We implement the algorithm above for multicircular targets. The use of such targets is motivated by the ability of both preventing the pixel snapping problem—allowing a subpixel resolution accuracy of the center of the target and the accuracy of the normal of the plane the target is lying on. The advantages of using circles therefore contribute to the overall calculated accuracy of the  $Z$  dimension.

Figure 4 depicts the multicircular target cropped from an acquired image; note that each circle is distorted to be an ellipse rather than a circle as a result of the varying orientations and distances. The following explains how one computes the pointcloud using multicircular targets:

- (1) We apply an ellipse detector algorithm which uses a nonlinear pattern (connected component) in the binarized image. Next, the estimation is refined by using a subpixel resolution algorithm in the grayscale image. We detect both outer and inner ellipses; then, for each pair of ellipses, we find the average center, which will be more robust to varying light intensity conditions which could cause a pixel-snapping problem (i.e., a pixel in one image can deviate by a single pixel in another image with the same conditions). In Figure 5, an example of the ellipse detector algorithm result is shown.
- (2) For each target, calculate the center  $C_p$  by running the *K-means clustering* algorithm on its ellipse centers (in Figure 6 shown as an example of the *K-means* result).
- (3) Let the  $x, y$  coordinates of the target in the pointcloud be the  $x, y$  coordinates of  $C_p$ .
- (4) Find the normal of the ellipse as follows: Consider the largest ellipse in the target, find its  $\max(a, b)$ , where  $a$  is the major axis and  $b$  is the minor axis, and its intersections with the ellipse, and let them be  $p_1$  and  $p_2$ , respectively.

Assume that the camera view is on the  $yz$  plane; then,



FIGURE 4: The multicircular targets on a solid main reflector as acquired by the moncamera.

- (a)  $p_1 = (x_1, u_1, v_1)$ , where  $x_1$  is unknown and  $u_1$  and  $v_1$  are the  $x, y$  coordinates for the intersection point; in the same way, let  $p_2 = (x_2, u_2, v_2)$ .
- (b) Then, the center point  $p_c = (0, u_c, v_c)$  (since we have no depth information, we arbitrarily place the  $yz$  plane at the center of the circle).
- (c) Now, we must have  $\|p_1 - p_c\|^2 = r^2 = x_1^2 + (u_1 - u_c)^2 + (v_1 - v_c)^2$  from which we can calculate the absolute value of  $x_1$  and similarly  $\|p_2 - p_c\|^2 = r^2 = x_2^2 + (u_2 - u_c)^2 + (v_2 - v_c)^2$  from which we can calculate the absolute value of  $x_2$ .
- (d) Note that one needs to determine the signs of  $x_1$  and  $x_2$ . If we choose  $p_1, p_2$  so that they are opposite (in the sense that they have inverse coordinates about the center  $u_1 - u_c = u_c - u_2, v_1 - v_c = v_c - v_2$ ), then  $x_1$  and  $x_2$  should have the same absolute value with opposite signs. Since we can correctly determine whether  $x_1$  and  $x_2$  are closer to the camera than the center or further away, this could be easily set.
- (e) Let the vectors  $\mathbf{v}'_1 = (x_1, u_1 - u_c, v_1 - v_c)$  and  $\mathbf{v}'_2 = (x_2, u_2 - u_c, v_2 - v_c)$ ; then,  $\hat{\mathbf{n}} = \mathbf{v}'_1 \times \mathbf{v}'_2$ , with the  $\hat{\mathbf{n}}$  vector is normal to the ellipse.
- (f) Then, compute the angular difference  $\Delta\alpha_i$  and  $Z$ -value as we mentioned above.

As will be exemplified below, using circular targets enables an average accuracy level of below 0.1 mm. Yet, such a method requires high-quality printing of curved lines over a flexible antenna made of Kapton foil. Such printing is hard to perform with space-qualified ink. Therefore, we needed to adjust the algorithm to work with targets which are composed of just straight lines.

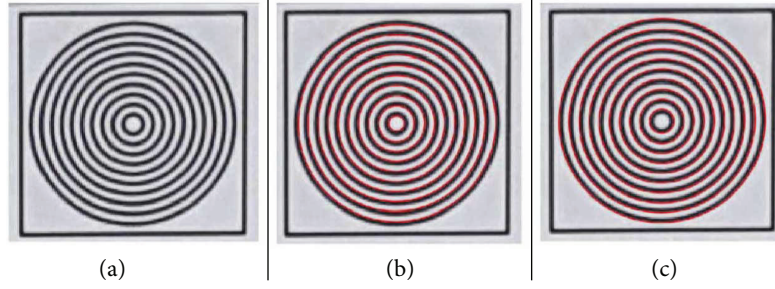


FIGURE 5: The result of the ellipse detector is the target itself (a), shows the inner ellipses detected (b), and shows the outer ellipses detected (c).

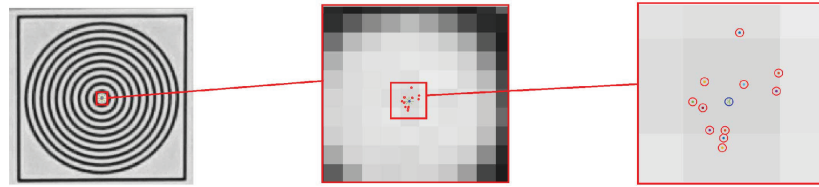


FIGURE 6: An example of the *K*-means clustering (KMC) result; the dotted points on the right are the centers of the ellipses, and the starred ones (blue) are the KMC result.

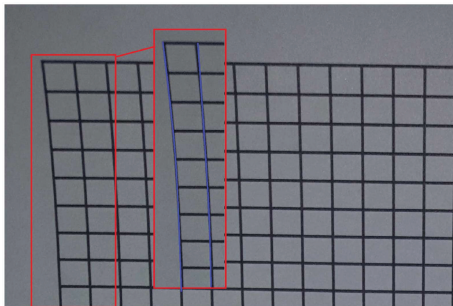


FIGURE 7: The grid pattern printed on a paper. Note that the blue lines are a bit curved.

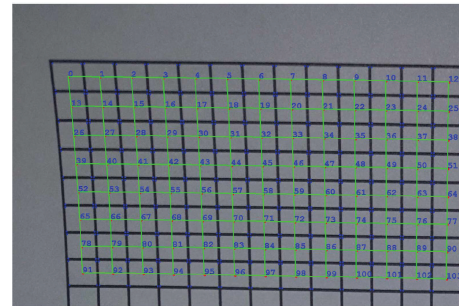


FIGURE 8: Computing  $Level_0$  and  $Level_1$  from a grid-based image:  $Level_0$  is presented as the corners of the green grid.  $Level_1$  is marked as blue dots in the center of each green square.

4.3. *Mapping Using a Uniform Grid.* After testing a wide range of possible straight-line patterns, we conclude that a simple uniform grid (see Figure 7) is the most suitable target available on the actual surface of the flexible antenna. At first, we have tested algorithms for detecting lines using edge detection methods. Such approach leads to relatively poor results as the edges on the antenna as captured by the camera (see Figure 7) are not straight lines but rather complicated curves. Performing regression to such curves introduced significant errors. Thus, we examined an alternative methodology where we first detect all the inner corners of each square (using regression to square). We then define  $Level_0$  to be the set of all center points of each square and  $Level_1$  to be the set of the centers of the unit squares implied by the points in  $Level_0$  (see Figure 8). Algorithm 2 computes a 3D pointcloud from an image of a grid-based target using the notion of the  $Level_1$  point set.

In order to implement the above algorithm, the following properties should be defined:

- (i) Let  $S$  be the set of all small squares in  $L_1$ : including unit squares, two-unit squares, and up to some relatively small number of units—usually smaller than the 10-degree angle.
- (ii) Given a square  $s_p$ , its area, and normal—one can approximate a distance of  $s_i$  from the camera, where the center of  $s_i$  is the angular coordinate of  $p_i$ . This is actually the same method which was used in the circular target of Algorithm 1.
- (iii) In some implementations,  $p_i$  can be generalized to be a weighted point associated with a confidence of the distance approximation based on  $s_p$ ,  $a_p$ , and  $n_i$ . That is, the expected distance accuracy to a two-unit

**Input:** Undistorted image (frame)  $F$ .

**Output:** 3D pointcloud.

- 1: Let  $P^* \leftarrow \emptyset$
- 2: Let  $C_0$  be a set of all points on corners of the grid.
- 3: Compute  $Level_1(L_1)$  from  $F$  and  $C_0$ .
- 4: Let  $S \leftarrow$  be all small squares in  $L_1$
- 5: **for each**  $s_i \in S$  **do**
  - (1) let  $a_i \leftarrow$  be the area of  $s_i$ .
  - (2) let  $n_i \leftarrow$  be the normal of  $s_i$ .
  - (3) let  $p_i \leftarrow$  be a 3D point associated with  $s_i$  w.r.t.  $a_i, n_i$ .
  - (4) add  $p_i$  to  $P^*$
- 6: **end for**
- 7: Return  $P^*$

ALGORITHM 2: Initial 3D mapping using a grid.

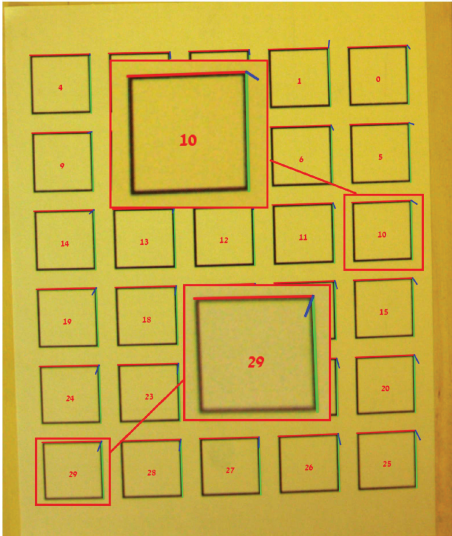


FIGURE 9: An example of normal detection results on some printed squares; note that target 10 and target 29 are oriented differently with different computed normal vectors.

square is usually better than the expected distance accuracy to a single-unit square.

- (iv) Computing the normal of  $s_i$  can be performed using the  $EPnP$  algorithm [17] (see Figure 9).

The grid-based algorithm is relatively robust and simple to implement. Yet, in most cases, the average error level was too large, about 0.3–0.5 mm. Moreover, the manufacturing limitation of the flexible antenna requires us to design an “on-board” algorithm which is both accurate and feasible.

## 5. On-Board Satellite Implementation

In this section, we define the actual “space algorithm” for computing the 3D surface of a flexible antenna. Algorithm 3 compares two images: a reference image ( $P$ ) and a current

**Input:** Undistorted reference image ( $P$ ), and current image ( $I^*$ ).

**Output:** 3D pointcloud.

- 1: Compute  $P^*$  (set of centers) from  $I^*$  (algo 4.3).
- 2: Perform a 2D registration  $P'$  between  $P$  and  $P^*$ .
- 3: **for each** pair  $w_i, w_j \in P'$  **do**
  - (1) Compute it's ratio,  $r = d(p^*)/d(p')/[1 - \epsilon, 1 + \epsilon]$
  - (2) Associate  $r$  with  $RatioMap(RM) \leftarrow mid(P')$ .
- 4: **end for**
- 5: Given  $RM$ , perform a *confidence&normal* analysis (fine tuning).
- 6: Call Minimum  $LAR$  algorithm with an input  $RM$ .

ALGORITHM 3: Computing the difference map between reference image and current image.

image ( $I$ ).  $P$  is the optimal (“perfect”) lab image of the flexible antenna from the satellite camera. This image is taken during an RF test of the complete satellite.  $I$  is the “space” image which is compared with  $P$ . Algorithm 3 computes the 3D difference map between  $P$  and  $I$  instead of the actual 3D pointcloud—as the 3D surface of  $P$  was mapped in high accuracy level during the final testing stage. As the satellite is about to be launched, its flexible antenna is unfolded and the surface of the main (flexible) antenna may suffer from global distortions due to the flexible nature of the antenna. In order to overcome such global distortions, we decided to use two different coordinate systems: satellite coordinate system and antenna coordinate system. For each target center (in the image 2D point), we consider it in the antenna coordinate system and then we consider its relative position in the satellite coordinate system. In order to determine the place of the target in the antenna coordinate system, we detect the contour of the antenna; then, for each point, we consider its relative position to the contour (edge). Figure 10 depicts the contour detection step flowchart. Having the 2D points in the antenna coordinate systems, we use Algorithm 1 to map the antenna surface.

**5.1. 3D Optimized Surface Generation Algorithm.** We define two levels of noise filtering:  $level_0$ , which uses direct position measurements for estimation (e.g., estimation of a target's center) and  $level_1$ , which averages out  $level_0$  estimations (e.g., the center of neighboring target's centers). We define  $level_i$  in the same iterative manner.

**5.1.1. Minimum LAR Algorithm.** After we have found the 3D pointcloud by using the algorithm above, we now find the minimum RMS function which returns a best fitting surface for the 3D points.

Fitting requires a parametric model that relates the response data to the predictor data with one or more coefficients. The result of the fitting process is an estimate of the model coefficients.

The following algorithm returns the best fitting plane for a given 3D pointcloud with a least absolute residual (LAR)

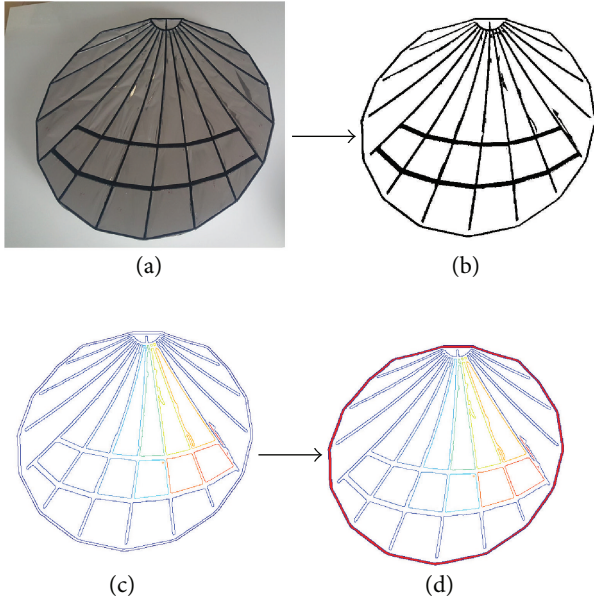


FIGURE 10: An example of the flowchart of the dish edge detection process. (a) The acquired image is binarized. (b) The intersections between the ribs of the dish with the dish are “cleaned.” (c) Detecting the connected components in the binarized image is exemplified. (d) The edge of the dish is then located by finding the resultant convex hull.



FIGURE 11: The camera calibration test setup. Using a calibrated 3D printer with a robotic moving panel, we were able to calibrate the Z approximation up to the 0.4 mm accuracy level.

**Input:** a 3D pointcloud ( $P$ ).

**Output:** A best fitting 3D surface LAR optimized.

1: Fit the model by weighted least squares.

2: **for each**  $p_i \in P$  **do**

(1) Let  $r_{adj} \leftarrow r_i / \sqrt{1 - h_i}$ .

(2) Let  $w_i = \begin{cases} (1 - (u_i)^2)^2, & \text{if } |u_i| < 1, \\ 0, & \text{if } |u_i| \geq 1. \end{cases}$

3: If the fit converges, exit. Otherwise, repeat.

4: **end for**

ALGORITHM 4: Minimum LAR 3D surface algorithm.

surface optimization in order to increase the expected z-accuracy to below 0.1 mm.

Here,  $r_i$  is the usual least-squares residuals and  $h_i$  is the leverage that adjusts the residuals by reducing the weight of high-leverage data points, which have a large effect on the least-squares fit. The standardized adjusted residuals are given by  $u = r_{adj}/K_s$ , where  $K$  is a tuning constant and  $s$  is the robust variance given by  $MAD/c$ , in which  $c$  is the constant and  $MAD$  is the median absolute deviation of the residuals.

## 6. Experimental Results

In this section, we show the experimental results of each step of the proposed algorithm.

**6.1. Camera Calibration Step.** For the setup step, we positioned the calibration targets (chessboard) on a 3D printer plate that has movement accuracy of sub-0.1 mm (up/down). A camera fixed at an 80 cm distance from the plate as shown in Figure 11 was located. Then, the plate was translated up and down in 0.1 mm steps. By comparing the translation with a naive distance calculation for the movement, detection calibration was ratified.

**6.2. Normal Detection Accuracy Test.** In this step, we gave the normal detector Algorithm 4 points with known real normal and ran it. For Figure 12, Table 1 lists some numeric results of the algorithm.

The result above shows an average angular error of  $\sim 0.4^\circ$ . Assuming that the monocular camera is located close to the subreflector, such angular “noise” induces only minor errors which are commonly smaller than the  $10^{-4}$  ratio.

We have built a practical setting that provides an accurate movement of a rigid body (plate) that can obtain a page with printed shapes (targets). In Figure 13, we show the setting with an explanation of its components. Two types of cameras were used: (1) an embedded 14-megapixel sensor with a FoV of about  $75^\circ$  and (2) an Android phone with 16 megapixels (Galaxy S6) with a FoV

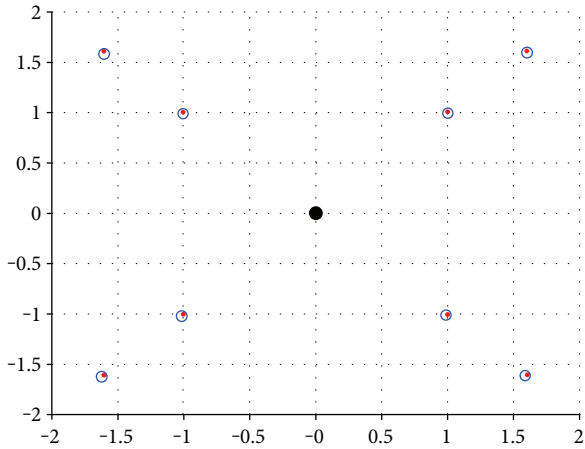


FIGURE 12: The normal detection algorithm tester: shown in blue are the real points of the orthogonal segment corners to the normal and shown in red is the algorithm approximation.

TABLE 1

X	Real normal			Approximated normal		
	Y	Z	X	Y	Z	
0.1808	0.6601	0.7291	0.1716	0.6743	0.7182	
0.0417	0.2682	0.9625	0.0386	0.272	0.9615	
0.0682	0.666	0.7428	0.0695	0.6716	0.7377	
0.0594	0.0738	0.9955	0.0515	0.0694	0.9963	

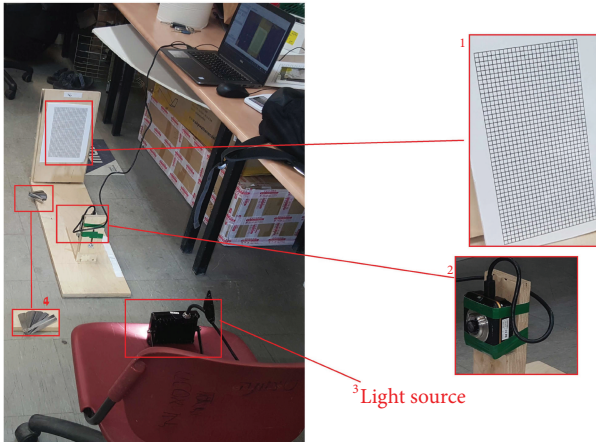


FIGURE 13: The practical setting of the next experiments that proves the accuracy level. The setting is divided into 4 main components: 1 is a dynamic plate that has the surface (plate) to be mapped which can move toward front or back. 2 is a stabilized stand that holds the camera. 3 is a light source to overcome the problem of the pixel snapping. 4 is a submillimeter spacer that we can measure the movement of the plate (1), so we have a reference for the actual movement.

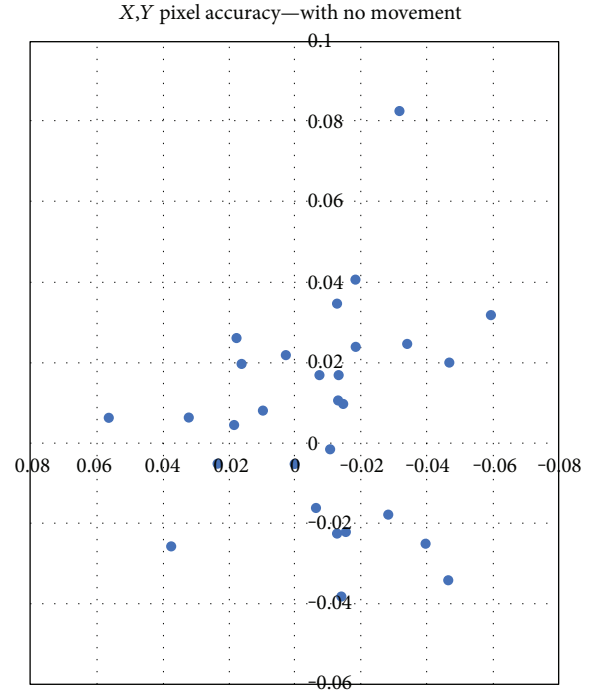


FIGURE 14: The typical noise of level<sub>0</sub> targets. Comparing two images of the same targets, they were shot with the same lighting and camera parameters. The typical noise level is about 0.03–0.04 pixel. In almost all tested cases, the level<sub>0</sub> noise is below 0.1 pixel.

of about 68°. In general, both cameras have reached the same accuracy level.

We have attached various types of paper and Kapton targets on the panel and tested the algorithm’s ability to detect fine changes. Figure 14 shows the expected noise level from comparing two images of the same targets (without moving the panel), which is usually lower than 0.04 pixel. Figure 15 presents the proposed algorithm “in action”; the panel with 30 targets was moved 1 mm on average ((a) almost no movement, (b) 0.2 mm, (c) about 1.8 mm, and (d) about 2 mm) (Figure 16), and the presented graph shows the linearity as well as the accuracy of the level<sub>0</sub> dataset, presenting an accuracy level which is better than 0.2 mm on average.

In Figure 17, we show a test on the Kapton foil which introduced a reflection and lighting problems.

6.3. *Computing the Difference Map and Minimum LAR Surface Algorithm.* In this subsection, we present two typical examples of computing the difference map between two pairs of images. In the first example, we compared two images with no movement—this example is needed in order to test the expected noise level of the suggested method. Figures 18 and 19 show that in general such noise is significantly below the required accuracy. The second pair of images includes a linear movement of 0.3–1.2 mm of the image plate. Figures 20 and 21 show how such

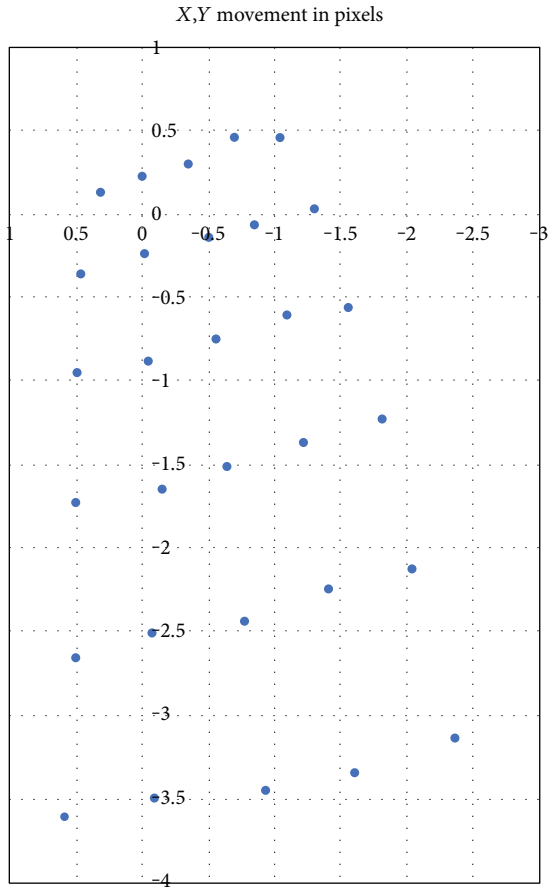


FIGURE 15: An example of a surface movement observed by 30 (5×6) targets (see Figure 16). Comparing two images, with an average tilt change of about 1 mm. A change of 0.1 pixel at targets is detectable (strongly above the noise level), allowing a z-accuracy of about 0.2mm on level<sub>1</sub>.

movement is detected—with an overall accuracy better than 0.1 mm.

### 7. Discussion and Future Work

We introduced a novel methodology for mapping flexible adaptive aerospace antennas. The proposed method can detect submillimeter distortions even on relatively large reflectors. The presented methodology allows autonomous (i.e., on-board) computation of surface, which can be used in order to continuously investigate the unknown nature of Kapton foil flexible antennas in the extreme temperatures of space. Using surface 3D mapping, the robotic subreflector can overcome minor distortions in the main reflector, allowing a typical gain improvement of 3–7 dB [3] and a new capability of dynamic beam shaping. The presented method was implemented and tested on a laboratory prototype of a nanosatellite with a two-foot flexible main reflector. The presented method reached an accuracy level of 0.1 millimeter on circular targets and a 0.3–0.5-millimeter accuracy on grid-based targets (with low-quality printed grid-based targets).

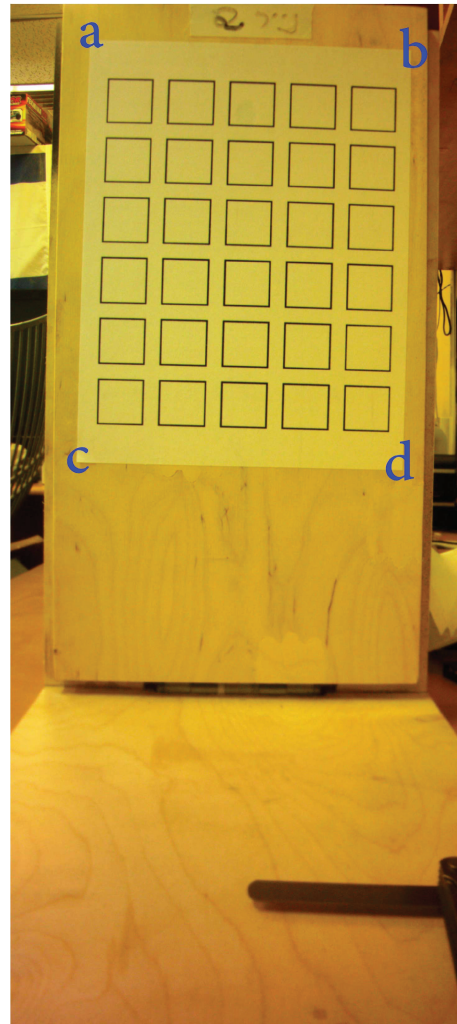


FIGURE 16: A testing setup: a paper with 30 (5×6) targets was attached to a flat panel. This panel can be moved using a set of accurate spacers (at a, b, c, and d), allowing us to test global movements with a high level of accuracy.

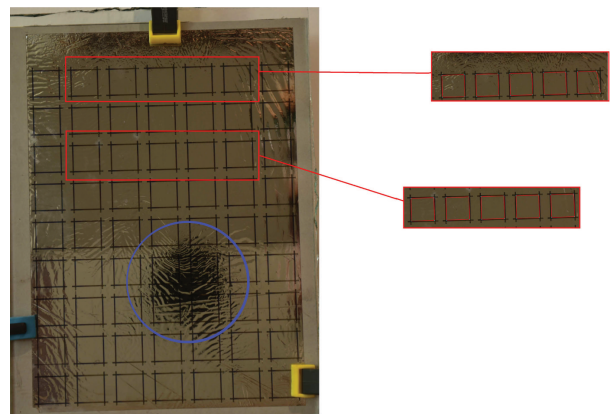


FIGURE 17: Kapton foil test. Denote the black reflection (marked by a blue circle) at the lower part—such reflection issues can be solved with a controlled lighting. Yet, any real implementation should be able to overcome reflection problems by detecting them and addressing them as outliers.

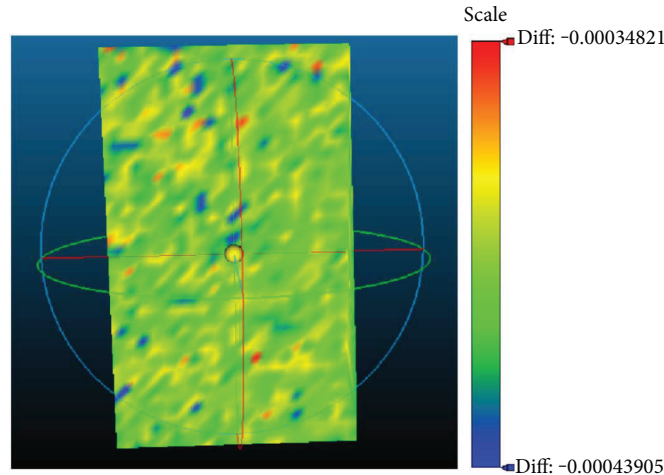


FIGURE 18: A difference map between two images taken continuously with no movement. In the scale of the difference, we can see that the maximum difference between the two images is 0.00035 pixel, which is significantly below 0.1 millimeter; this result demonstrates the algorithm’s accuracy.

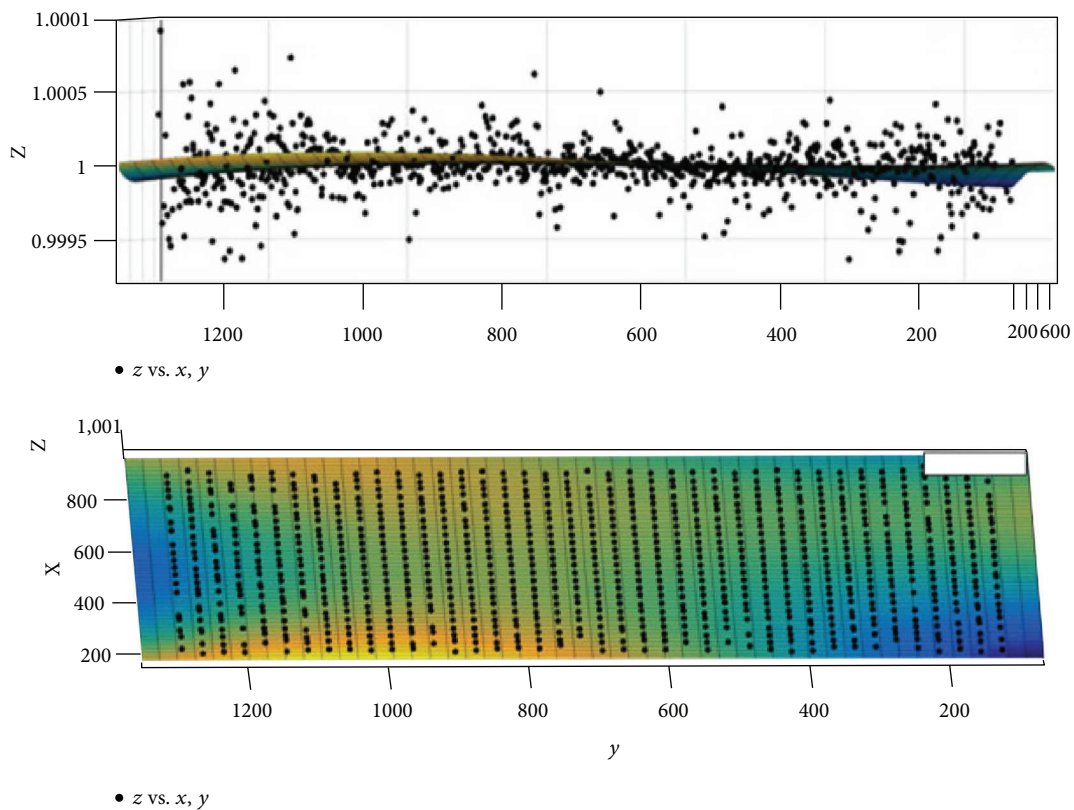


FIGURE 19: The minimum LAR surface optimization algorithm on the setting, running on two images taken continuously with no movement. The upper part of the figure shows the surface from the ZY plane viewpoint, and the lower part shows the XY plane viewpoint.

Using the “on-board” algorithm which uses a reference image, the expected accuracy reached the required level of 0.1 millimeter.

We plan to implement the current method on a real nanosatellite with a flexible antenna, which is scheduled

to be launched at the end of 2018. We hope that using the presented framework, the vision of having a large-scale LEO satellite constellation which is both affordable and globally accessible can get one step closer to reality.

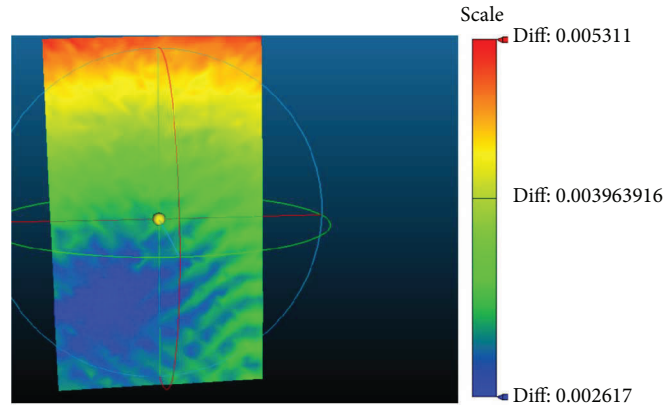


FIGURE 20: The result of the difference map with a 1.2 mm movement of the top of the plate (and a movement of about 0.3 mm of the lower part of the plate). This result demonstrates the ability of the algorithm to compute a smooth and continuance difference map.

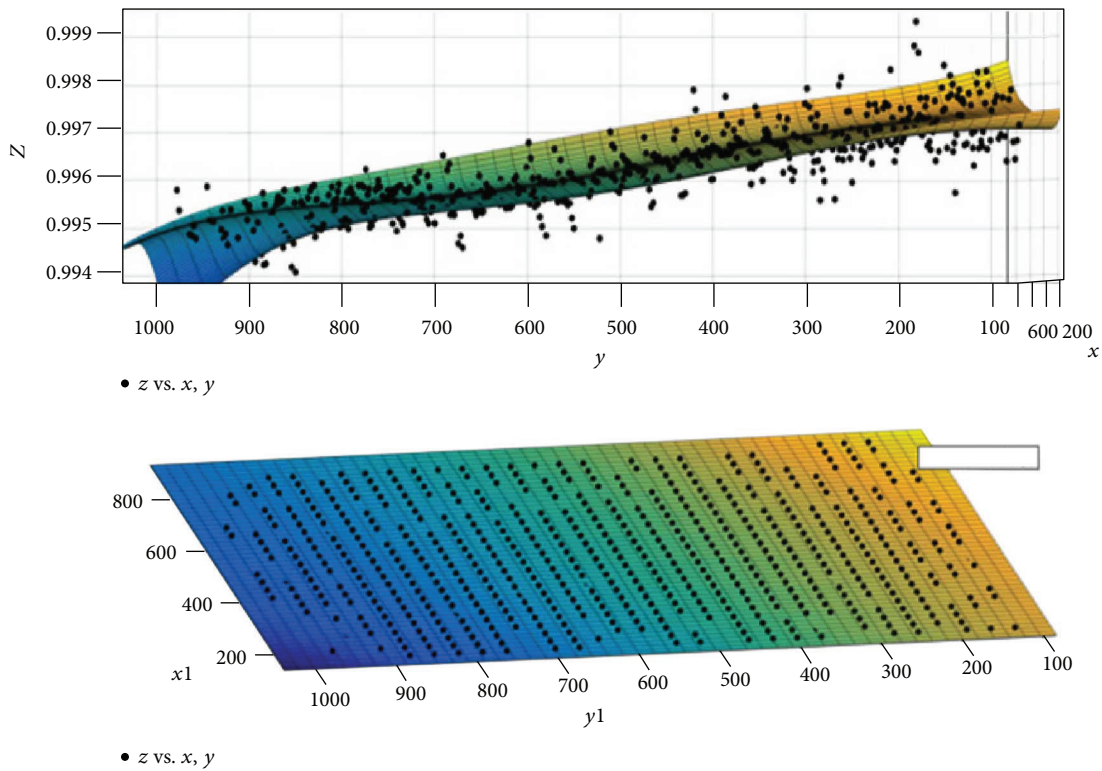


FIGURE 21: In this figure, we show the result of the minimum LAR surface optimization algorithm with a 1.2 mm movement of the top of the plate (and a movement of about 0.3 mm of the lower part of the plate). The upper part of the figure shows the surface from the ZY plane viewpoint, and the lower part shows the XY plane viewpoint.

**Conflicts of Interest**

The authors declare that they have no conflicts of interest.

**Acknowledgments**

This research was partially supported by NSLComm. NSLComm (<http://nslcomm.com>) provides satellite manufacturers with unprecedented expandable antennas for satellite telecommunications. The authors would like to

thank Peter Abeles for his amazing open source named *BoofCV* [18]—by far the most advanced geometric computer vision software.

**References**

[1] K. Kamnani and C. Suratkar, “A review paper on Google Loon technique,” *International Journal of Research In Science & Engineering*, vol. 1, no. 1, pp. 167–171, 2015.

- [2] R. Houborg and M. McCabe, "High-resolution NDVI from planets constellation of earth observing nanosatellites: a new data source for precision agriculture," *Remote Sensing*, vol. 8, no. 9, p. 768, 2016.
- [3] N. Shvalb, B. Ben-Moshe, O. Medina, and R. I. Tamir, "Flexible-robotic reflector for aerospace applications," *International Journal of Antennas and Propagation*, vol. 2015, Article ID 252371, 8 pages, 2015.
- [4] S. Schuon, C. Theobalt, J. Davis, and S. Thrun, "High-quality scanning using time-of-flight depth superresolution," in *2008 IEEE Computer Society Conference on Computer Vision and Pattern Recognition Workshops*, pp. 1–7, Anchorage, AK, USA, June 2008.
- [5] D. Acosta, O. Garcia, and J. Aponte, "Laser triangulation for shape acquisition in a 3D scanner plus scan," in *Electronics, Robotics and Automotive Mechanics Conference (CERMA'06)*, vol. 2, pp. 14–19, Cuernavaca, Mexico, September 2006.
- [6] R. A. Newcombe, S. Izadi, O. Hilliges et al., "KinectFusion: real-time dense surface mapping and tracking," in *2011 10th IEEE International Symposium on Mixed and Augmented Reality*, pp. 127–136, Basel, Switzerland, 2011.
- [7] E. E. Hitomi, J. V. L. Silva, and G. C. S. Ruppert, "3D scanning using RGBD imaging devices: a survey," in *Developments in Medical Image Processing and Computational Vision*, Lecture Notes in Computational Vision and Biomechanics, pp. 379–395, Springer, Cham, 2015.
- [8] S. M. Seitz, B. Curless, J. Diebel, D. Scharstein, and R. Szeliski, "A comparison and evaluation of multi-view stereo reconstruction algorithms," in *2006 IEEE Computer Society Conference on Computer Vision and Pattern Recognition (CVPR'06)*, vol. 1, pp. 519–528, New York, NY, USA, 2006.
- [9] F. Remondino and S. El-Hakim, "Image-based 3D modelling: a review," *The Photogrammetric Record*, vol. 21, no. 115, pp. 269–291, 2006.
- [10] M. Tatarchenko, A. Dosovitskiy, and T. Brox, "Multi-view 3D models from single images with a convolutional network," in *Computer Vision – ECCV 2016. ECCV 2016*, Lecture Notes in Computer Science, pp. 322–337, Springer, Cham, 2016.
- [11] D. Williams, Y. Zheng, P. G. Davey, F. Bao, M. Shen, and A. Elsheikh, "Reconstruction of 3D surface maps from anterior segment optical coherence tomography images using graph theory and genetic algorithms," *Biomedical Signal Processing and Control*, vol. 25, pp. 91–98, 2016.
- [12] P. Tanskanen, K. Kolev, L. Meier, F. Camposeco, O. Saurer, and M. Pollefeys, "Live metric 3D reconstruction on mobile phones," in *2013 IEEE International Conference on Computer Vision*, pp. 65–72, Sydney, NSW, Australia, 2013.
- [13] O. Medina, A. Shapiro, and N. Shvalb, "Resistor-based shape sensor for a spatial flexible manifold," *IEEE Sensors Journal*, vol. 17, no. 1, pp. 46–50, 2017.
- [14] O. Medina, A. Shapiro, and N. Shvalb, "Kinematics for an actuated flexible  $n$ -manifold," *Journal of Mechanisms and Robotics*, vol. 8, no. 2, article 021009, 2016.
- [15] Y. Demers, A. Liang, E. Amyotte, E. Keay, and G. Marks, "Very large reflectors for multibeam antenna missions," in *Fifteenth KA and Broadband Communications, Navigation and Earth Observation Conference*, pp. 23–25, Cagliari, Italy, 2009.
- [16] Z. Zhang, "A flexible new technique for camera calibration," *IEEE Transactions on Pattern Analysis and Machine Intelligence*, vol. 22, no. 11, pp. 1330–1334, 2000.
- [17] V. Lepetit, F. Moreno-Noguer, and P. Fua, "EPnP: an accurate  $o(n)$  solution to the PnP problem," *International Journal of Computer Vision*, vol. 81, no. 2, p. 155, 2009.
- [18] P. Abeles, "Boofcv v0.27," 2017, <http://boofcv.org/>.

## Research Article

# A Ring-Focus Antenna with Splash Plate in Ka-Band

Laiding Zhao <sup>1,2</sup>, Xiaodong Bai,<sup>1,2</sup> Rui Li,<sup>1,3</sup> and Jidong Xie<sup>1,2</sup>

<sup>1</sup>College of Telecommunications and Information Engineering, Nanjing University of Posts and Telecommunications, Nanjing 210003, China

<sup>2</sup>Satellite Communication and Navigation Collaborative Innovation Center, Nanjing 210003, China

<sup>3</sup>Electronic and Optical Engineering & College of Microelectronics and Information Engineering, Nanjing University of Posts and Telecommunications, Nanjing 210003, China

Correspondence should be addressed to Laiding Zhao; zhaold@njupt.edu.cn

Received 5 September 2017; Revised 27 November 2017; Accepted 21 December 2017; Published 18 March 2018

Academic Editor: Xuejun Lu

Copyright © 2018 Laiding Zhao et al. This is an open access article distributed under the Creative Commons Attribution License, which permits unrestricted use, distribution, and reproduction in any medium, provided the original work is properly cited.

A design for Ka-band satellite communication antenna in earth station is introduced. This kind of antenna uses splash plate feed based on ring-focus antenna. The theory of the new splash plate feed design is presented and the relative equations are derived. The measured antenna parameters, VSWR, and patterns are highly consistent with the simulated results, which demonstrates the success of the design for such kind of antenna that can be effectively used in Ka-band applications.

## 1. Introduction

There are many kinds of Ka-band antenna, as reported in documents, including microstrip array antenna [1–3], waveguide array antenna [4–6], waveguide slot antenna [7], horn antenna [8–10], dielectric spherical lens feed antenna [11–13], and reflector antenna [14, 15]. The efficiency of Ka-band antenna is usually in the range of 50% to 60% [16].

The antenna designers always pursue high gain while using low sidelobes for the design of Ka-band antenna [17–27].

Ring-focus parabolic antenna overcomes feed shelter to realize low sidelobes and VSWR in a broad bandwidth and has been applied widely in VSAT. The antenna can enhance its efficiency by changing the shape of hat feed [28], reducing its size by using a spline-profiled smooth horn [29], and improving its performance on VSWR and cross-polarization via a small ring-shaped aperture [30]. But all the schemes above have low efficiency due to the support for subreflector.

Splash plate feed, which traces back to World War II, has not been used widely for the high VSWR [31]. Since the 1980s, antenna with splash plate feed has been researched

by few papers, which present the power distribution control and equiphase on the main reflector aperture through dielectric materials and subreflector forming, while the main attention is paid on subreflector forming to improve performance [32–36]. Since the antenna with splash plate feed does not need the support for subreflector, it can gain higher efficiency. However, the problem caused by feed shelter [32–36] still exists.

In this paper, the design of a new antenna in Ka-band is introduced. This antenna adopts splash plate feed, whose main reflector is ring focus without strut and feed shelter.

In this paper, the principle of ring-focus reflector antenna with splash plate feed is introduced firstly. A group of differential equations are derived and the geometry of the antenna's subreflector and dielectric surface is obtained by solving these differential equations. The simulated results indicate that this antenna can achieve high gain with low sidelobes. This kind of antenna has been produced based on the proposed design in this paper. The measured far-field patterns are highly consistent with the simulated results.

This product can be applied widely in Ka-band satellite communications considering its novel structure, low cost, good electrical performance, and high efficiency.

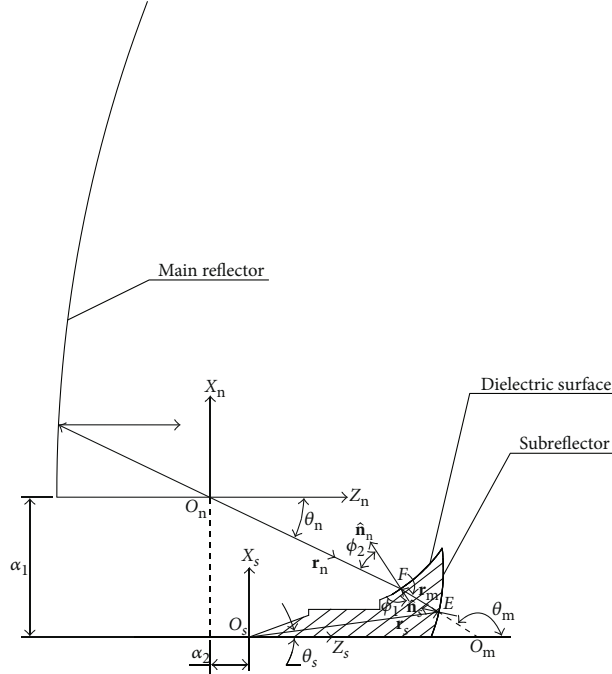


FIGURE 1: Principle of ring-focus antenna with splash plate feed.

## 2. Theoretical Analysis

The method based on geometric optics is adopted to design the ring-focus antenna with splash plate feed. This antenna consists of four parts including the main reflector, splash plate feed, media, and subreflector.

This antenna is rotational symmetric, and the principle of such design is simply described through XZ 2D section in Figure 1.

The main reflector of such antenna is ring focus. It is produced by rotation of a parabola, whose focal length is  $F$ , away from symmetry axis  $a_1$ . The main reflector equation of this antenna, whose focus is the origin, can be expressed as follows:

$$Z = \frac{(|X| - a_1)^2}{4F} - F. \quad (1)$$

The principle of designed antenna is shown in Figure 1. The feed phase center is  $O_s$ . The optics ray is from  $O_s$  to  $E$ , then reflects to  $F$ , and then refracts to  $O_n$ , where  $O_n$  is the ring focal of the main reflector.  $O_m$  is a point of intersection by reflect line extension line and  $Z_s$  axis. The vector  $\mathbf{r}_s$  is pointing from  $O_s$  to  $E$ . The vector  $\mathbf{r}_m$  is pointing from  $E$  to  $F$ . The vector  $\mathbf{r}_n$  is pointing from  $O_n$  to  $F$ .

*2.1. Design of Subreflector.* 3D description equations are required in theory derivation while 2D section is shown Figure 1. Thus, assuming that  $\phi_s$  is the included angle of vector  $\mathbf{r}_s$  in  $O_s X_s Z_s$  plane and  $O_s X_s$  axis, if  $f_s(\theta_s, \phi_s)$  is the equation of subreflector, the vector  $\mathbf{r}_s$  can be expressed as

$$\mathbf{r}_s = f_s(\theta_s, \phi_s) \hat{\mathbf{r}}_s, \quad (2)$$

where  $\hat{\mathbf{r}}_s$  is the unit vector. In rectangular coordinate system,  $\hat{\mathbf{r}}_s$  and  $\hat{\mathbf{r}}_m$  can be expressed as

$$\hat{\mathbf{r}}_s = \sin \theta_s (\cos \phi_s \hat{\mathbf{x}}_s + \sin \phi_s \hat{\mathbf{y}}_s) + \cos \theta_s \hat{\mathbf{z}}_s, \quad (3)$$

$$\hat{\mathbf{r}}_m = \sin \theta_m (\cos \phi_s \hat{\mathbf{x}}_s + \sin \phi_s \hat{\mathbf{y}}_s) + \cos \theta_m \hat{\mathbf{z}}_s.$$

To express simply, let  $f_s(\theta_s, \phi_s) = f_s$ . Then the differential coefficient is

$$\begin{aligned} \frac{d\hat{\mathbf{r}}_s}{d\phi_s} &= \left( \frac{df_s}{d\phi_s} \sin \theta_s \cos \phi_s - f_s \sin \theta_s \sin \phi_s \right) \hat{\mathbf{x}}_s \\ &+ \left( \frac{df_s}{d\phi_s} \sin \theta_s \sin \phi_s + f_s \sin \theta_s \cos \phi_s \right) \hat{\mathbf{y}}_s \\ &+ \frac{df_s}{d\phi_s} \cos \theta_s \hat{\mathbf{z}}_s, \end{aligned} \quad (4)$$

$$\begin{aligned} \frac{d\hat{\mathbf{r}}_s}{d\theta_s} &= \left( \frac{df_s}{d\theta_s} \sin \theta_s \cos \phi_s + f_s \cos \theta_s \cos \phi_s \right) \hat{\mathbf{x}}_s \\ &+ \left( \frac{df_s}{d\theta_s} \sin \theta_s \sin \phi_s + f_s \cos \theta_s \sin \phi_s \right) \hat{\mathbf{y}}_s \\ &+ \left( \frac{df_s}{d\theta_s} \cos \theta_s - f_s \sin \theta_s \right) \hat{\mathbf{z}}_s. \end{aligned}$$

The unit normal vector of subreflector is

$$\hat{\mathbf{n}}_s = \frac{(d\mathbf{r}_s/d\phi_s) \times (d\mathbf{r}_s/d\theta_s)}{|(d\mathbf{r}_s/d\phi_s) \times (d\mathbf{r}_s/d\theta_s)|}, \quad (5)$$

where “ $\times$ ” represents vector cross product. It can be derived from (5) that

$$\begin{aligned}\hat{\mathbf{n}}_s &= \frac{1}{\Delta} \left( \frac{df_s}{d\theta_s} \cos \theta_s - f_s \sin \theta_s \right) \cos \phi_s \hat{\mathbf{x}}_s \\ &+ \left( \frac{df_s}{d\theta_s} \cos \theta_s - f_s \sin \theta_s \right) \sin \phi_s \hat{\mathbf{y}}_s \\ &- \left( \frac{df_s}{d\theta_s} \sin \theta_s + f_s \cos \theta_s \right) \hat{\mathbf{z}}_s,\end{aligned}\quad (6)$$

where

$$\Delta = \sqrt{\left( \frac{df_s}{d\theta_s} \right)^2 + f_s^2}.\quad (7)$$

The inner product of incident wave  $\mathbf{r}_s$ 's unit vector and subreflector's unit normal vector is

$$-\hat{\mathbf{r}}_s \cdot \hat{\mathbf{n}}_s = \frac{f_s}{\sqrt{(df_s/d\theta_s)^2 + f_s^2}}.\quad (8)$$

The inner product of reflected wave  $\mathbf{r}_m$  from subreflector and subreflector's unit normal vector is

$$\hat{\mathbf{r}}_m \cdot \hat{\mathbf{n}}_s = \frac{(df_s/d\theta_s) \sin(\theta_m - \theta_s) - f_s \cos(\theta_m - \theta_s)}{\sqrt{(df_s/d\theta_s)^2 + f_s^2}}.\quad (9)$$

According to Snell's law,

$$-\hat{\mathbf{r}}_s \cdot \hat{\mathbf{n}}_s = \hat{\mathbf{r}}_m \cdot \hat{\mathbf{n}}_s.\quad (10)$$

It can be derived from (8), (9), and (10) that

$$\frac{d\mathbf{r}_s}{d\theta_s} = \mathbf{r}_s(\theta_s) \cot\left(\frac{\theta_m - \theta_s}{2}\right).\quad (11)$$

**2.2. Design of Dielectric Surface Forming.** For simple derivation, assuming a coordinate system  $O_n X_n Z_n$ , the dielectric surface equation is

$$\mathbf{r}_n = f_n(-\theta_n, \phi_s) \hat{\mathbf{r}}_n,\quad (12)$$

where  $\hat{\mathbf{r}}_n$  is the unit vector and can be expressed as

$$\hat{\mathbf{r}}_n = -\sin \theta_n (\cos \phi_s \hat{\mathbf{x}}_n + \sin \phi_s \hat{\mathbf{y}}_n) + \cos \theta_n \hat{\mathbf{z}}_n\quad (13)$$

in a rectangular coordinate system. For simple description, let  $f_n(-\theta_n, \phi_s)$  be  $f_n$ ; the unit normal vector of the dielectric surface is

$$\hat{\mathbf{n}}_n = \frac{(d\mathbf{r}_n/d\phi_n) \times (d\mathbf{r}_n/d\theta_n)}{|(d\mathbf{r}_n/d\phi_n) \times (d\mathbf{r}_n/d\theta_n)|}.\quad (14)$$

So it can be derived that

$$\begin{aligned}\hat{\mathbf{n}}_n &= \frac{1}{\Delta'} \left( \frac{df_n}{d\theta_n} \cos \theta_n + f_n \sin \theta_n \right) \cos \phi_s \hat{\mathbf{x}}_n \\ &+ \left( \frac{df_n}{d\theta_n} \cos \theta_n - f_n \sin \theta_n \right) \sin \phi_s \hat{\mathbf{y}}_n \\ &+ \left( \frac{df_n}{d\theta_n} \sin \theta_n - f_n \cos \theta_n \right) \hat{\mathbf{z}}_n,\end{aligned}\quad (15)$$

where

$$\Delta' = \sqrt{\left( \frac{df_n}{d\theta_n} \right)^2 + f_n^2}.\quad (16)$$

The inner product of incident wave  $\mathbf{r}_m$ 's unit vector and dielectric surface's unit normal vector is

$$\hat{\mathbf{r}}_m \cdot \hat{\mathbf{n}}_n = \frac{(df_n/d\theta_n) \sin(\theta_m + \theta_n) - f_n \cos(\theta_m + \theta_n)}{\sqrt{(df_n/d\theta_n)^2 + f_n^2}} = \cos \phi_1.\quad (17)$$

The inner product of refracted wave  $\mathbf{r}_n$  and dielectric surface's unit normal vector is

$$(-\hat{\mathbf{r}}_n) \cdot \hat{\mathbf{n}}_n = \frac{f_n}{\sqrt{(df_n/d\theta_n)^2 + f_n^2}} = \cos \phi_2.\quad (18)$$

According to Snell's law,

$$\frac{\sin \phi_1}{\sin \phi_2} = \frac{1}{n},\quad (19)$$

where

$$n = \sqrt{\epsilon_r}.\quad (20)$$

It is derived from (17), (18), and (19) that

$$\frac{df_n}{d\theta_n} = \frac{nf_n \sin(\theta_m + \theta_n)}{1 - n \cos(\theta_m + \theta_n)}.\quad (21)$$

**2.3. Energy Conservation Equation.** According to the law of energy conservation,

$$P(\theta_s) \sin \theta_s d\theta_s = \frac{-I(X_m) X_m dX_m}{A},\quad (22)$$

where  $P(\theta_s)$  is the spatial angle distribution function of feed axisymmetric radiation power,  $I(X_m)$  is the aperture power distribution function of the antenna main paraboloid,  $X_m$  is the radius variable of the antenna aperture, and  $A$  is the proportionality coefficient.

The main reflector equation of ring-focus reflector antenna is

$$X_m = 2F \tan \frac{\theta_n}{2} + a_1.\quad (23)$$

In logs, it can be obtained as

$$\frac{dX_m}{d\theta_n} = F \sec^2 \frac{\theta_n}{2}. \quad (24)$$

According to (23) and (24), then

$$\frac{d\theta_n}{d\theta_s} = -\frac{AP(\theta_s)\sin\theta_s \cos^2(\theta_n/2)}{FI(X_m)X_m}. \quad (25)$$

**2.4. Equiphase Equation.** In definition,  $\theta_{s\max}$  is the maximum of  $\theta_s$ ,  $f_{s\max}$  is the maximum of  $f_s$ ,  $\theta_{n\min}$  is the minimum of  $\theta_n$ , and  $f_{n\max}$  is the maximum of  $f_n$ . According to the qualification requirement,  $P(\theta_s)$ ,  $I(X_m)$ ,  $a_1$ ,  $a_2$ ,  $\theta_{s\max}$ ,  $f_{s\max}$ , and  $F$  can be certain firstly.

When  $\theta_s = \theta_{s\max}$  and  $f_s = f_{s\max}$ , boundary condition can be obtained according to the following geometrical relationship:

$$\theta_{n\min} = \arctan \frac{f_{s\max} \cos \theta_{s\max} + a_2}{a_1 - f_{s\max} \sin \theta_{s\max}},$$

$$f_{n\max} = \sqrt{(f_{s\max} \cos \theta_{s\max} + a_2)^2 + (f_{s\max} \sin \theta_{s\max} - a_1)^2}. \quad (26)$$

In a dielectric material, the optical length that an electromagnetic wave radiates from primary feed  $O_s$  and refract to the air after being reflected by subreflector to the main reflector's focus is equal. Namely,

$$\begin{aligned} nf_s + nf_m + f_n &= K, \\ f_{s\max} + f_{n\max} &= K. \end{aligned} \quad (27)$$

**2.5. Calculation of Subreflector Equation and Dielectric Surface 2D Equation.** According to the geometric relationship in Figure 1, it can be obtained that

$$\begin{aligned} f_s \sin \theta_s + f_m \sin(\pi - \theta_m) + f_n \sin \theta_n &= a_1, \\ f_s \cos \theta_s + a_2 &= f_m \cos(\pi - \theta_m) + f_n \cos \theta_n. \end{aligned} \quad (28)$$

When  $\theta_s$  is certain,  $\theta_m$ ,  $\theta_n$ ,  $f_s$ ,  $f_m$ , and  $f_n$  can be solved according to (11), (21), (23), (25), and (28).

In  $O_s X_s Z_s$  plane, subreflector equations are

$$\begin{aligned} X &= f_s \sin \theta_s, \\ Z &= f_s \cos \theta_s. \end{aligned} \quad (29)$$

Dielectric surface equations are

$$\begin{aligned} X &= \alpha_1 - f_n \sin \theta_n, \\ Z &= f_n \cos \theta_n - \alpha_2. \end{aligned} \quad (30)$$

Thus, the shapes of subsurface and dielectric surface can be obtained.

### 3. Structure of Antenna

The main reflector, whose material is carbon fiber, is a rotationally symmetric paraboloid. The surface of the reflector should be processed by metallization, and the accuracy

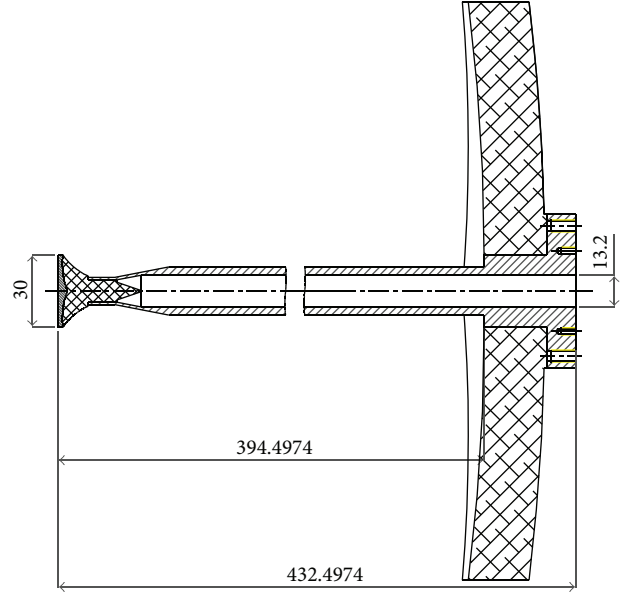


FIGURE 2: Structure of the main and side reflector.

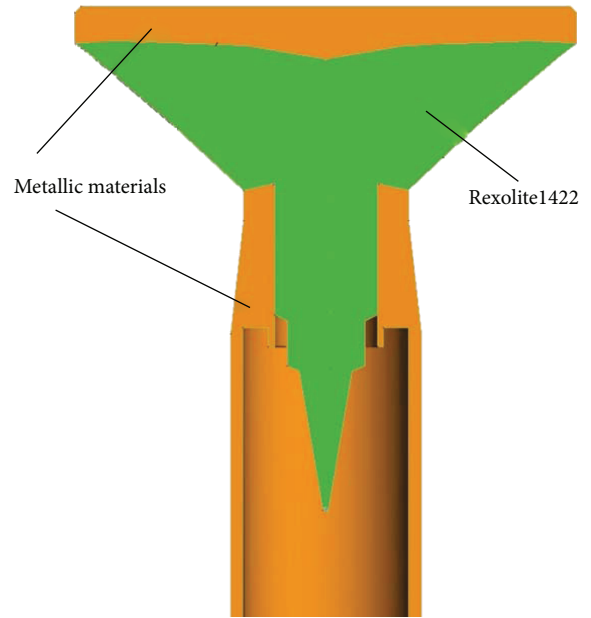


FIGURE 3: Exploded view of the feed structure.

should be controlled within 0.3 mm (r.m.s.). In the processing, a carbon fiber reflector and a copper sheet are made out of molds. Then they are bonded together with glue. The accuracy of the molds ensures the accuracy of the reflector. The structures of the main reflector and subreflector and dielectric are shown in Figure 2.

The exploded view of the feed structure is shown in Figure 3, where the green and yellow parts are dielectric material REXOLITE1422 and aluminum material, respectively. After programming according to the designed data, the subreflector and dielectric can be processed by high



FIGURE 4: Antenna front view.



FIGURE 5: Antenna lateral view.

precision CNC (computer numerical control) machines. Ultraviolet (UV) glue is adopted here to bond the subreflector and the dielectric. Since the dielectric is transparent, the glue between subreflector and dielectric will cure after UV radiates for a period of time.

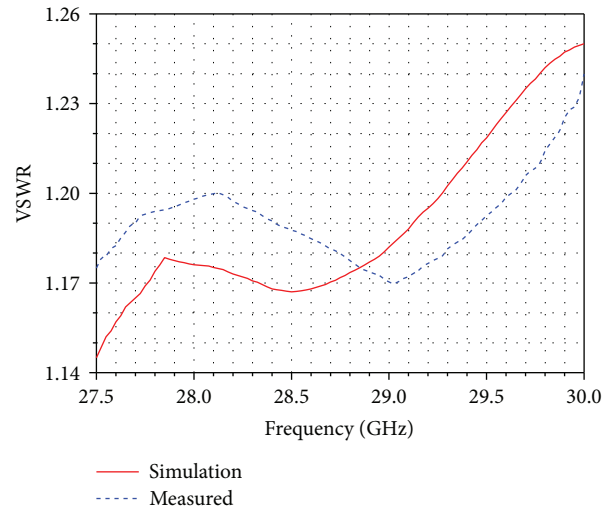


FIGURE 6: Curves of transmitting VSWR.

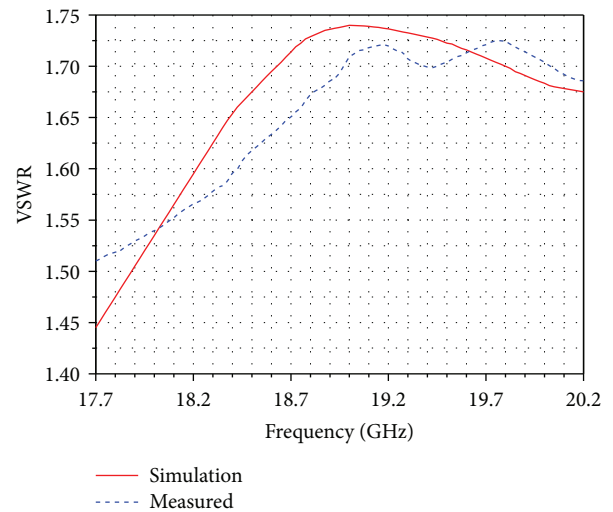


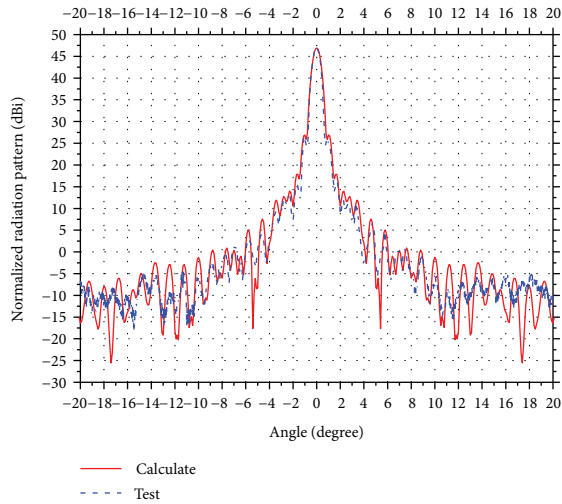
FIGURE 7: Curve of receiving VSWR.

Let  $15 \text{ mm} \leq |X| \leq 525 \text{ mm}$ ,  $F = 420 \text{ mm}$ ,  $a_1 = 15 \text{ mm}$ . After fabrication of the subreflector and dielectric materials, the assembled antenna is shown in Figures 4 and 5.

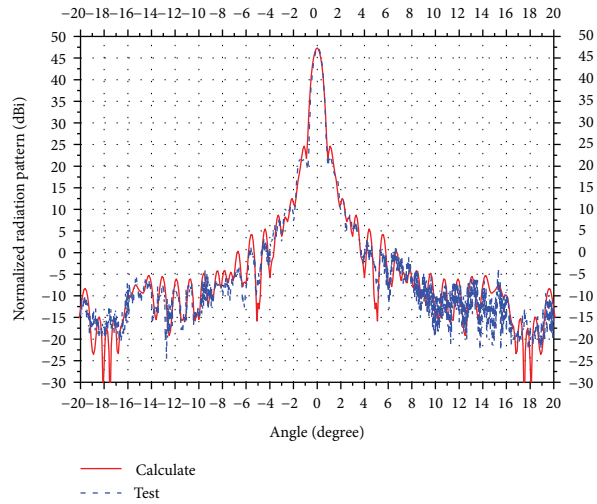
#### 4. Simulation and Measurement on VSWR

This antenna adopts circular polarization. It uses 27.5~30.0 GHz as transmitting frequency and 17.7~20.2 GHz as receiving frequency. Physical optics (PO) method and finite element method (FEM) are combined in the simulation by FEKO, where PO method is used for the main reflector and FEM for the feed (subreflector and dielectric). The simulation defines “mesh” as 1/6 wavelength. The computer has an 8-core CPU and 128 GB RAM.

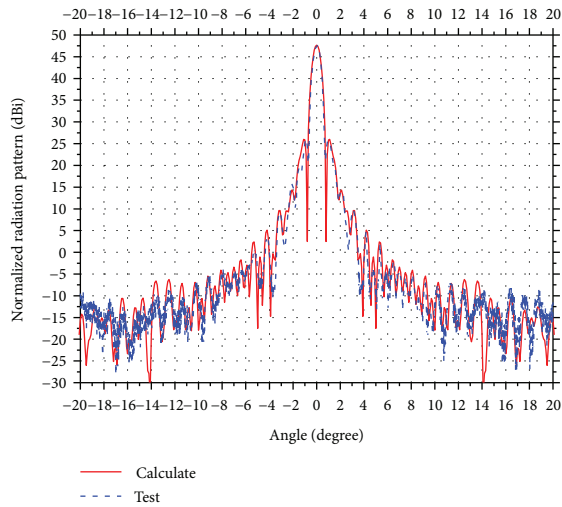
The curves of VSWR are obtained through the simulation of FEKO, and the simulated results are shown as red continuous lines in Figures 6 and 7.



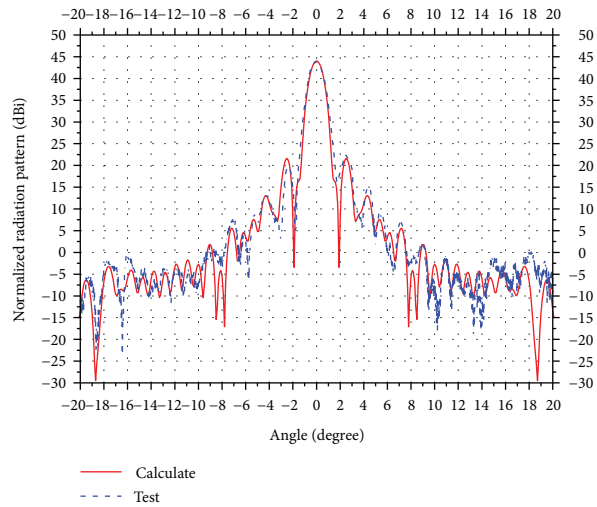
(a) 27.5 GHz



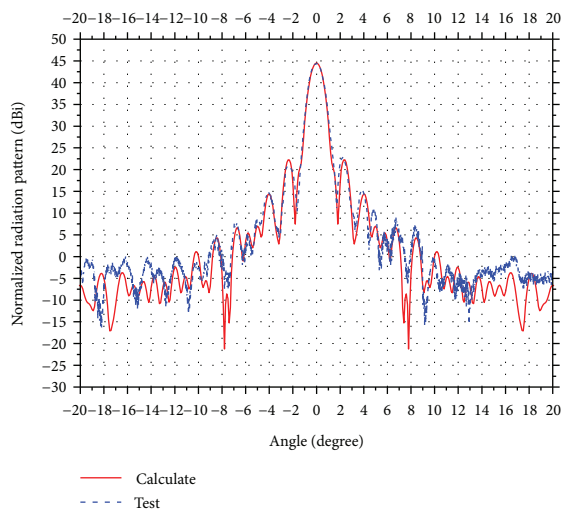
(b) 28.75 GHz



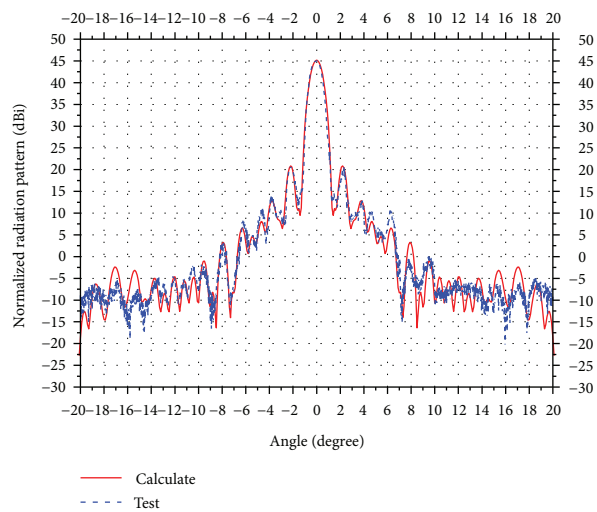
(c) 30.0 GHz



(d) 17.7 GHz



(e) 18.95 GHz



(f) 20.2 GHz

FIGURE 8: Antenna pattern.

TABLE 1: Measured data of antenna transmitting patterns.

	27.5 GHz	28.75 GHz	30 GHz
Gain (dBi)	47.57	47.92	48.63
First sidelobe (dB)	-20.04	-22.65	-21.66

TABLE 2: Measured data of antenna receiving patterns.

	17.7 GHz	18.95 GHz	20.2 GHz
Gain (dBi)	43.79	44.27	44.89
First sidelobe (dB)	-22.4	-22.28	-24.31

The VSWR is measured with Agilent Vector Network Analyzer N5230C in microwave anechoic chamber. After the measurement on antenna transmitting and receiving VSWR, the relative results are shown as blue chain lines in Figures 6 and 7.

As shown in Figure 6, antenna transmitting VSWR is below 1.24. As shown in Figure 7, antenna receiving VSWR is below 1.73.

## 5. Simulation and Measurement on Antenna Patterns

This design adopts arbitrary phase and amplitude feed power pattern  $P(\theta_s)$  as the feed model. Antenna patterns are simulated and analyzed by FEKO, and the curves obtained are shown with red continuous lines in Figure 8.

The far-field patterns are then measured, and the measured patterns obtained from data are shown as blue chain lines in Figure 8.

The distance between the transmitting and receiving antennas should satisfy the far-field test distance condition, namely,

$$R \geq \frac{2D^2}{\lambda}, \quad (31)$$

where  $R$  is the distance between the source antenna and the antenna under test.  $D$  is the aperture of the antenna under test, and  $\lambda$  is the wavelength. According to (31), it is possible to calculate the minimum distance between the transmitting and receiving antennas in the far-field test. The highest frequency of the Ka-band antenna is 30 GHz, and  $D = 1020$  mm, so  $R \geq 200$  m. The actual distance is about 282 m.

The sidelobes meet the envelope of 29–25log $\theta$  dBi. The measurement and related calculation of the antenna gain adopt comparison method. Acquired gain and first sidelobe are listed in Tables 1 and 2.

As shown in Figure 8, considering dielectric loss, splash plate scattering, cross-polarization efficiency, main reflector toleration, and other efficiency, simulated results of the antenna are highly consistent with the measured results, which demonstrates the success of such design. The measured antenna efficiency is about 65.6%, while the efficiency of the existing antenna in Ka-band is below 60% [16].

## 6. Conclusion

This paper introduces a ring-focus antenna based on splash plate feed. The prototype of this antenna has been produced based on the proposed design. The measured results verify that this antenna can achieve efficiency of over 65% and can satisfy the regulations of Rec. ITU-R S.580-6 in receiving band on antenna sidelobe. The measured results of the antenna are highly consistent with the simulated results, which proves the high engineering value of the proposed method.

## Conflicts of Interest

The authors declare that there is no conflicts of interest regarding the publication of this paper.

## Acknowledgments

This work was jointly sponsored by scientific research foundation NUPTSF (Grant nos. NY-214144 and NY-215073) and NSFC (Grant no. 61701260).

## References

- [1] T. Varum, J. N. Matos, V. Duarte, and P. Pinho, "Circularly polarized microstrip antenna array for the Ka-band," in *2015 IEEE International Symposium on Antennas and Propagation & USNC/URSI National Radio Science Meeting*, pp. 1864–1865, Vancouver, BC, Canada, 2015.
- [2] A. Chen, Y. Zhang, Z. Chen, and C. Yang, "Development of a Ka-band wideband circularly polarized 64-element microstrip antenna array with double application of the sequential rotation feeding technique," *IEEE Antennas and Wireless Propagation Letters*, vol. 10, pp. 1270–1273, 2011.
- [3] A. Chen, Y. Zhang, Z. Chen, and S. Cao, "A Ka-band high-gain circularly polarized microstrip antenna array," *IEEE Antennas and Wireless Propagation Letters*, vol. 9, pp. 1115–1118, 2010.
- [4] R. Glogowski, C. Peixeiro, J.-F. Zurcher, and J. R. Mosig, "Design and optimization of a shaped-beam ka-band substrate integrated waveguide antenna array," in *2015 Global Symposium on Millimeter Waves (GSMW)*, pp. 1–3, Montreal, QC, Canada, 2015.
- [5] S. Chatterjee and A. Majumder, "Design of circularly polarized waveguide crossed slotted array antenna at Ka band," in *2015 International Conference on Microwave and Photonics (ICMAP)*, pp. 1–2, Dhanbad, India, 2015.
- [6] A. Valero-Nogueira, J. I. Herranz-Herruzo, M. Ferrando-Rocher, R. Lenormand, A. Hirsch, and J.-L. Almeida, "Switchable RHCP/LHCP slotted waveguide array antenna for SATCOM on-the-move applications in Ka-band," in *The 8th European Conference on Antennas and Propagation (EuCAP 2014)*, pp. 2047–2051, The Hague, Netherlands, April 2014.
- [7] Y. Wang and A. M. Abbosh, "Software-defined reconfigurable antenna using slotted substrate integrated waveguide for Ka-band satellite-on-the-move communication," in *2015 International Symposium on Antennas and Propagation (ISAP)*, pp. 1–3, Hobart, TAS, Australia, 2015.

- [8] Y. Z. Liu, S. Xiao, and B. Z. Wang, "Analysis of a novel Ka horn antenna with low cross-polarization," *Applied Computational Electromagnetics Society Journal*, vol. 28, pp. 1061–1067, 2013.
- [9] A. Rolland, N. T. Nguyen, R. Sauleau, C. Person, and L. Le Coq, "Smooth-walled light-weight Ka-band shaped horn antennas in metallized foam," *IEEE Transactions on Antennas and Propagation*, vol. 60, no. 3, pp. 1245–1251, 2012.
- [10] D.-J. Lee, J.-Y. Kwon, N.-W. Kang, and J. F. Whitaker, "Reactive-to-radiating near-field propagation behavior measured on a Ka-band horn antenna," *IEEE Antennas and Wireless Propagation Letters*, vol. 10, pp. 1085–1087, 2011.
- [11] Q. Lai, G. Almpanis, C. Fumeaux, H. Benedickter, and R. Vahldieck, "Comparison of the radiation efficiency for the dielectric resonator antenna and the microstrip antenna at Ka band," *IEEE Transactions on Antennas and Propagation*, vol. 56, no. 11, pp. 3589–3592, 2008.
- [12] W. Fang, P. Fei, F. Nian, Y. Yang, and K. Feng, "Ka-band dielectric waveguide antenna array for millimeter wave active imaging system," *Journal of Infrared, Millimeter, and Terahertz Waves*, vol. 35, no. 11, pp. 962–973, 2014.
- [13] Y. S. Kim, B. S. Kang, and B. J. Ku, "Design and measurements of Ka-band waveguide dielectric rod antenna for 7 channel digital beamformer for HAPS," in *SympoTIC '04. Joint 1st Workshop on Mobile Future & Symposium on Trends In Communications (IEEE Cat. No.04EX877)*, pp. 25–28, Bratislava, Slovakia, 2004.
- [14] T. Gabriel, H. Kozilek, C. Hartwanger, M. Gerhard, and M. Schneider, "Steerable Ka-band dual reflector antenna," in *2016 German Microwave Conference (GeMiC)*, pp. 329–332, Bochum, Germany, March 2016.
- [15] K. Kagoshima, S. Takeda, K. Ikeda et al., "A X/Ka bands feeder antenna for a planetary exploration high gain reflector antenna," in *2012 IEEE Antennas and Propagation Society International Symposium (APSURSI)*, pp. 1–2, Chicago, IL, USA, 2012.
- [16] E. Curuk, K. Yegin, and C. Ozdemir, "A novel ultra-wide band design for feeding structure of Ka band VSAT parabolic reflector antenna," in *2016 21st International Conference on Microwave, Radar and Wireless Communications (MIKON)*, pp. 1–4, Krakow, Poland, 2016.
- [17] R. Glogowski, J.-F. Zurcher, C. Peixeiro, and J. R. Mosig, "A low-loss planar Ka-band antenna subarray for space applications," *IEEE Transactions on Antennas and Propagation*, vol. 61, no. 9, pp. 4549–4557, 2013.
- [18] Q. Luo, S. Gao, C. Zhang et al., "Design and analysis of a reflectarray using slot antenna elements for Ka-band SatCom," *IEEE Transactions on Antennas and Propagation*, vol. 63, no. 4, pp. 1365–1374, 2015.
- [19] J. C. Guo, X. Q. Liu, W. Zhang, and B. Q. He, "Design of the Ka-band satellite antenna by parallel differential evolution," *Applied Mechanics and Materials*, vol. 556–562, pp. 2194–2197, 2014.
- [20] S. Yun, M. Uhm, J. Choi, and I. Yom, "Multibeam reflector antenna fed by few elements for Ka-band communication satellite," in *2012 IEEE Antennas and Propagation Society International Symposium (APSURSI)*, pp. 1–2, Chicago, IL, USA, 2012.
- [21] M. R. Chaharmir and J. Shaker, "Design of an FSS-backed 20/30 GHz circularly polarized reflectarray for shared aperture X/Ka-band satellite applications," in *2014 16th International Symposium on Antenna Technology and Applied Electromagnetics (Antem)*, p. 1, Victoria, BC, Canada, 2014.
- [22] R. Wilke, S. Hamid, K. Schraml, R. Khunti, and D. Herberling, "Multi-layer patch antenna array design for Ka-band satellite communication," in *2013 SBMO/IEEE MTT-S International Microwave & Optoelectronics Conference (IMOC)*, pp. 1–4, Rio de Janeiro, Brazil, 2013.
- [23] A. Hoehn, P. B. Hager, and J. T. Harder, "Design characterization of an electronic steerable Ka-band antenna using liquid crystal phase shifters," in *IEEE Aerospace Conference*, pp. 1–14, Big Sky, MT, USA, March 2013.
- [24] T. Smith, U. Gothelf, O. S. Kim, and O. Breinbjerg, "An FSS-backed 20/30 GHz circularly polarized reflect array for a shared aperture L- and Ka-band satellite communication antenna," *IEEE Transactions on Antennas and Propagation*, vol. 62, no. 2, pp. 661–668, 2014.
- [25] A. I. Sandhu, E. Arneri, G. Amendola, L. Boccia, E. Meniconi, and V. Ziegler, "Radiating elements for shared aperture Tx/Rx phased arrays at K/Ka band," *IEEE Transactions on Antennas and Propagation*, vol. 64, no. 6, pp. 2270–2282, 2016.
- [26] H. Bayer, A. Krauss, T. Zaiczek, R. Stephan, O. Enger-Rosenblatt, and M. A. Hein, "Ka-band user terminal antennas for satellite communications [antenna applications corner]," *IEEE Antennas and Propagation Magazine*, vol. 58, no. 1, pp. 76–88, 2016.
- [27] J.-M. Baracco, P. Ratajczak, P. Brachat, and G. Toso, "A dual frequency Ka-band printed Fresnel reflector for ground terminal applications," *IEEE Transactions on Antennas and Propagation*, vol. 63, no. 10, pp. 4352–4366, 2015.
- [28] J. Yang and P.-S. Kildal, "Calculation of ring-shaped phase centers of feeds for ring-focus paraboloids," *IEEE Transactions on Antennas and Propagation*, vol. 48, no. 4, pp. 524–528, 2000.
- [29] M. Van der Vorst and J. Gumpinger, "Applicability of 3D printing techniques for compact Ku-band medium/high-gain antennas," in *2016 10th European Conference on Antennas and Propagation (EuCAP)*, pp. 1–4, Davos, Switzerland, April 2016.
- [30] T. Xiao-rong and S. Gao, "Design of low-cross-polarization wideband spaceborne ring focus reflector antenna," in *2014 Loughborough Antennas and Propagation Conference (LAPC)*, pp. 469–472, Loughborough, UK, November 2014.
- [31] M. K. Kasraian, A. A. Kishk, and M. Tew, "Radiation characteristics of loaded shaped splash plate antennas," in *Proceedings IEEE Southeastcon '92*, vol. 1, pp. 306–309, Birmingham, AL, USA, April 1992.
- [32] P. S. Kildal and A. Nyseth, "The hat feed: a new class of splashplate antenna having low cross-polarization," in *1986 Antennas and Propagation Society International Symposium*, vol. 24, pp. 75–78, Philadelphia, PA, USA, June 1986.
- [33] G. L. James and D. P. S. Malik, "Towards the theoretical design of splash-plate feeds," *Electronics Letters*, vol. 11, no. 24, pp. 593–594, 1975.
- [34] C. Liu, S. Yang, and Z. Nie, "Design of a parabolic reflector antenna with a compact splash-plate feed," in *2013 Cross Strait Quad-Regional Radio Science and Wireless Technology Conference (CSQRWC)*, pp. 241–244, Chengdu, China, 2013.
- [35] T. Inamura, "Upwash formation on splash plate atomization," *International Journal of Multiphase Flow*, vol. 85, pp. 67–75, 2016.
- [36] Y. Ascı, E. Curuk, K. Yegin, and C. Ozdemir, "Improved splash-plate feed parabolic reflector antenna for Ka-Band VSAT applications," in *2016 46th European Microwave Conference (EuMC)*, pp. 1283–1286, London, UK, October 2016.

## Research Article

# Low-Cost Printed Flexible Antenna by Using an Office Printer for Conformal Applications

Kashif Nisar Paracha,<sup>1</sup> Sharul Kamal Abdul Rahim,<sup>1</sup> Hassan Tariq Chattha ,<sup>2</sup>  
Saqr Saleh Aljaafreh,<sup>3</sup> Sabih ur Rehman ,<sup>4</sup> and Yew Chiong Lo<sup>5</sup>

<sup>1</sup>Wireless Communication Centre, Universiti Teknologi Malaysia, Johor Bahru, Malaysia

<sup>2</sup>Department of Electrical Engineering, Faculty of Engineering, Islamic University of Madinah, Al-Madinah, Saudi Arabia

<sup>3</sup>Department of Electrical Engineering, Mu'tah University, Mu'tah, Jordan

<sup>4</sup>Charles Sturt University, Bathurst, NSW, Australia

<sup>5</sup>Faculty of Engineering, Multimedia University, Cyberjaya, Malaysia

Correspondence should be addressed to Hassan Tariq Chattha; chattha43@hotmail.com

Received 24 August 2017; Revised 17 November 2017; Accepted 6 December 2017; Published 14 February 2018

Academic Editor: Xuejun Lu

Copyright © 2018 Kashif Nisar Paracha et al. This is an open access article distributed under the Creative Commons Attribution License, which permits unrestricted use, distribution, and reproduction in any medium, provided the original work is properly cited.

A low-cost inkjet printing method for antenna fabrication on a polyethylene terephthalate (PET) substrate is presented in this paper. An office inkjet printer is used to have desired patterns of silver nanoparticle ink on the PET substrate without any postprocessing. Silver nanoparticle ink cures instantly as soon as it is ejected from the printer on a chemically treated PET substrate. The thickness of the silver nanoparticle layer was measured to be 300 nm with a sheet resistance of as low as  $0.3 \Omega/\text{sq}$  and a conductivity around  $1.11 \times 10^7 \text{ S/m}$  with single layer deposition. A coplanar waveguide- (CPW-) fed Z-shape planar antenna on the PET substrate achieved the measured radiation efficiency of 62% and the IEEE gain of 1.44 dBi at 2.45 GHz. The printed antenna is also tested in bending conditions to ascertain its performance for the Internet of things (IoT) conformal applications for the future 5G network.

## 1. Introduction

As per the vision of IMT-2020 for the future 5G network, the cost of Internet of things (IoT) devices needs to be reduced to as low as 5 dollars per unit [1]. To reduce the cost of these IoT devices, there is a dire need of a low-cost fabrication process. The production of low-cost devices is being revolutionized by the invention of inkjet printing of functional materials like polymers/nanocomposites, carbon nanotubes, graphene, and most recently molybdenum disulfide ( $\text{MoS}_2$ ) nanosheets [2]. These materials are being used to fabricate transistors, antennas, sensors, light-emitting diodes, and many other printable devices [3]. Out of these, silver nanoparticle (AgNP) ink has been extensively used to deposit a thin metallic film on various substrates due to its well-known high conductivity and being relatively low cost

compared to other noble metals such as gold and platinum [4]. However, the printing of the antenna using the commonly used Dimatix printer 2800 series requires a subsequent thermal sintering (annealing) process which not only makes the usage of many polymeric substrates like polyethylene terephthalate (PET) or polycarbonate impractical due to their low glass transition temperature ( $100^\circ\text{C}$ – $200^\circ\text{C}$ ) but also makes the fabrication process become complex and time consuming [5]. Instead of heating the complete sample during the sintering process, more selective sintering techniques were also used by various researchers, including laser sintering, low-pressure argon plasma exposure, microwave radiation, and electrical and photonic sintering [6]. However, the fabrication process using these techniques requires expensive equipment and proper parameter control to avoid the damage to the substrate. Moreover, the commonly used

TABLE 1: Comparison between the office inkjet printer and commercially Dimatix 2800 series.

Properties	Dimatix printer 2800 series	Office inkjet printer with AgNP ink.
Cost of the printer	Very expensive > 30,000\$	Very cheap < 600\$
Cost of the ink	Expensive > 1000\$	Cheap < 400\$
Postprocessing	Annealing processes for 4 hrs in an expensive industrial oven	Instantly cured ink
Preheating	Heating vacuumed platen up to 60°C	Not required
Conductivity	$1.6 \times 10^6$ S/m (single layers, at 200°C)	$1.11 \times 10^7$ S/m (single layer, at room temperature)
Annealing temperature	Up to 120°C for 10 hours	Instantly cured
Low-cost glossy paper and PET substrate	Not possible	Possible
Layer thickness	450 nm	300 nm
Sheet resistance of a single layer	9 $\Omega$ /sq at 100°C after 1 hour	0.3 $\Omega$ /sq at room temperature after 10 min

inkjet printer (e.g., DMP 2800 series) is too expensive to make this type of the fabrication process commercially viable. In [6–10], antennas for wearable and conformal applications are fabricated using an inkjet printer on flexible substrates like Kapton, resin-coated paper, and glossy paper achieving reasonable conductivity up to  $1e10^7$  S/m, but, unfortunately, it involves a long sintering process at higher temperature, that is, 150°C for several hours. Although the conventional office printer has also been used for printing the radiating part of the antenna on glossy paper by using AgNP ink to reduce the fabrication cost of the antenna, it requires long annealing time to exhibit reasonable conductivity for the antenna applications [11]. Some commercially available instantly chemically cured paints and markers are also available to avoid the thermal sintering process, but the large silver nanoparticle size (1  $\mu$ m) with uneven and high sheet resistance of up to 55  $\Omega$ /sq limits their implementation as an instant prototyping technique [12–14]. Hence, the formation of an AgNP ink layer by an office inkjet printer is one of the viable additive fabrication techniques which offers the advantage of being compatible with low-cost roll-to-roll processing [15].

In this letter, we are using an instantly cured silver nanoparticle ink using an office inkjet printer for antenna application. A coplanar waveguide- (CPW-) fed Z-shape antenna on a chemically treated PET substrate is printed using an office printer. The ink is compatible with conventional Brother's printers, and its conductivity for a single printed layer reaches to a value of  $1.11 \times 10^7$  S/m with 300 nm layer thickness. The electrical conductivity and morphology analyses are done to ascertain the effectiveness of our used technique for a low-cost antenna fabrication method. Moreover, antenna performance is evaluated by measuring the reflection coefficients, gain, and radiation pattern of the antenna.

## 2. Characterizing the Printed Silver Ink Layer

**2.1. Instantly Chemically Cured AgNP Layer.** The silver nanoparticle ink is a special ink to work on a chemically treated PET substrate. This special AgNP ink has been successfully implemented to make electric circuits on a flexible PET

substrate [16]. After inkjet printing, the polymer-confined silver nanoparticles used in the Dimatix printer series need several hours of the heating process, called sintering, to exhibit reasonable conductivity. The invention of chemically cured conductive inks has opened a new era of inkjet printing technology enabling the use of office inkjet printers without any postprocessing of printed conductive layers [17]. Chemical curing of the AgNP ink in printed antenna fabrication requires special treatment of the surface of the substrate so that a conduction path could be formed instantly at room temperature [18]. The comparison between our low-cost printed technique and the commercially available Dimatix printer technique is done in Table 1.

**2.2. Morphological Analysis.** The morphological analysis is very crucial for the complete study of the newly proposed technique for antenna fabrication. An SEM image was used to evaluate the surface morphology of the printed silver nanoparticle layer and the distribution of the silver particles by using a field emission scanning electron microscope (FESEM) (Hitachi, SU8020) operating at 2 kV.

EDS spectrum, as shown in Figure 1, reveals strong signal in the silver region and confirms the formation of AgNPs along with some traces of chemicals like chloride (Cl), carbon (C), and aluminium (Al).

As shown in the images in Figure 2, the silver nanoparticles are agglomerated just by using a chemical sintering method which eliminates the development of "hot spots" due to differences in the conductivity within the printed layer. The white spots appearing in Figure 2(b) are believed to be the impurities present in the ink.

The cross-sectional SEM image of the printed layer, as shown in Figure 3, taken on a 200 nm scale with 5 kV ETH, shows the thickness of the AgNPs and PET substrate to be 300 nm and 125  $\mu$ m, respectively.

One of the important factors for performance of the printed antenna is its roughness. As we know that the AC current does not flow in the whole conductor, it remains near the surface of the conductor, resulting in higher current density. Especially, when the roughness dimensions are comparable to the skin depth of the EM waves at the operating frequency, these losses are prominent [17]. The roughness

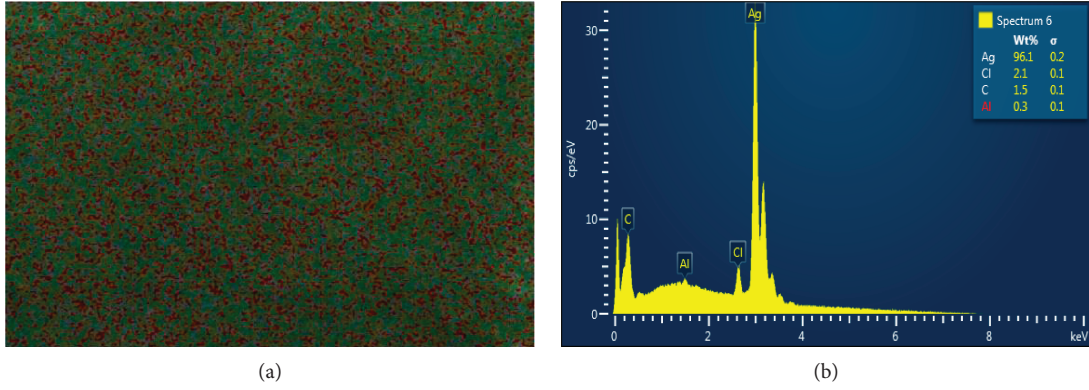


FIGURE 1: (a) SEM images of a nanoparticle layer for EDS analysis. (b) Quantitative spectrum of the contents of the particles in %age.

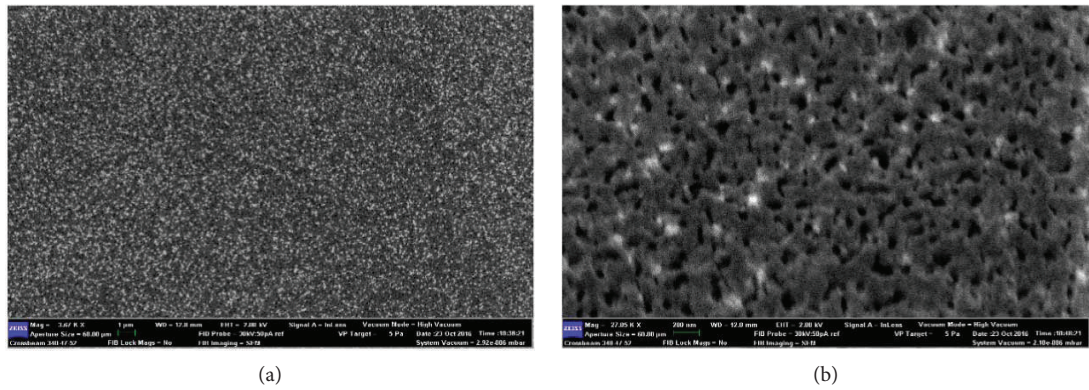


FIGURE 2: SEM image of the printed AgNP sample through FESEM with a voltage potential of 2 kV. (a) Scale bar = 1 μm. (b) Scale bar = 200 nm.

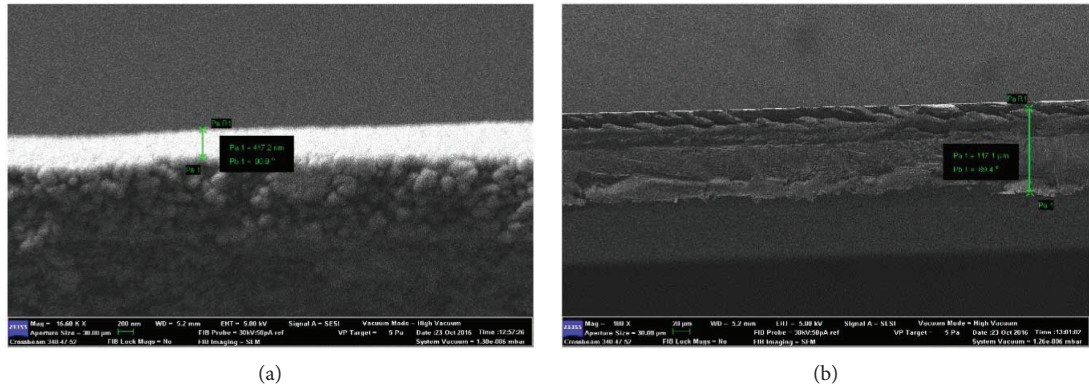


FIGURE 3: Cross-sectional SEM images of the printed layer. (a) Scale bar = 200 nm. (b) Scale bar = 20 μm.

of the printed layer has a direct impact on the AC resistance of the antenna which can be described by the following equations [19]:

$$R = \frac{1}{w} \sqrt{\frac{\pi \mu f}{\sigma}},$$

$$c = \left[ 1 + \frac{2}{\pi} \tan^{-1} \left\{ 1.4 \left( \frac{\Delta}{\delta} \right)^2 \right\} \right], \quad (1)$$

$$R_s = c \cdot R,$$

where  $\delta$  means the surface roughness,  $c$  is the correction factor, and  $R_s$  is the surface resistance per unit length of the printed layer. To know the roughness of the printed AgNP layer, the height profile of the sample has been taken using the latest noncontact 3D surface profiler (Sensofar, SneaX) along the edge of the AgNP layer. As shown in Figure 4, the mean roughness ( $S_a = 0.299 \mu\text{m}$ ) and the root mean square roughness ( $S_q = 0.368 \mu\text{m}$ ) of the printed layer are quite reasonable to be used for antenna application since they are quite small as compared to the skin depth of the silver layer at 2.45 GHz, that is,  $\delta = 1.29 \mu\text{m}$ .

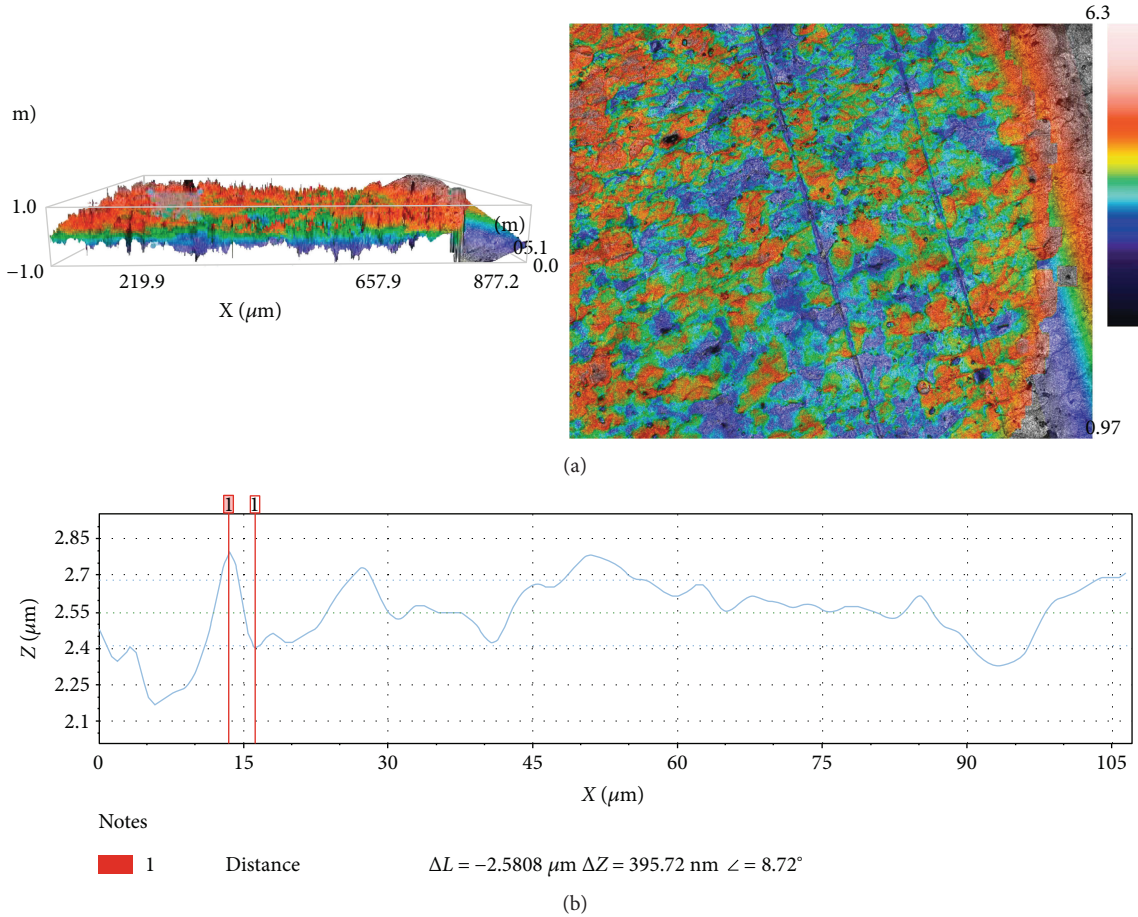


FIGURE 4: (a) Colored SEM image of the sample layer and 3D height profile. (b) 2D surface roughness graph.

By using (1), for the surface roughness of  $0.299 \mu\text{m}$  and the skin depth of  $1.29 \mu\text{m}$ , the correction factor ( $c$ ) is calculated to be 1.045. Hence, the increase in the AC resistance per unit length is only 4.5% with respect to a perfectly smooth surface (ideal). As we go towards higher frequency, for example, 6 GHz, the skin depth reduces, which results in surface roughness losses of only 11% (still acceptable). In addition, the average thickness observed from this profiler is well matched with FESEM measurements as shown in Figure 4.

### 3. Fabrication and Results of a CPW-Fed Z-Shaped Antenna

A CPW-fed Z-shaped antenna at 2.45 GHz ISM band has been fabricated to ascertain the functionality of our new low-cost inkjet antenna fabrication technology as per the dimensions given in Figure 5. The dielectric characteristics of the substrate are measured using a dielectric probe. DAK-3.5 and the measured relative permittivity  $\epsilon_r$  of the dielectric are found to be equal to 2.7, and the loss tangent  $\tan \delta$  is 0.135. The gap between the ground and the feed line is 0.3 mm, and rectangular slots in the Z-shape antenna are of equal size. Antenna design parameters are first optimized for the PET substrate based on simulations carried out using the CST microwave studio, and fabrication is done using

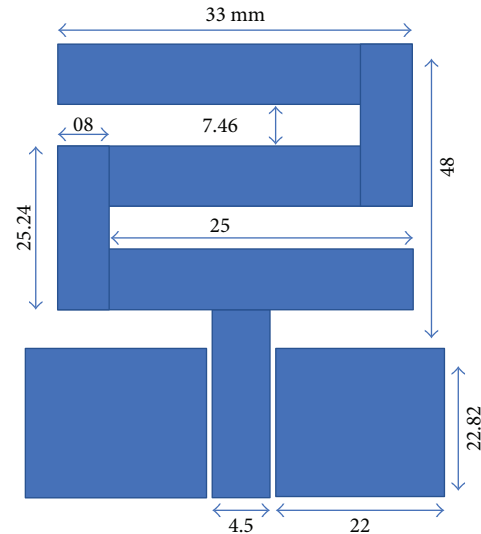


FIGURE 5: The dimensions of the CPW-fed Z-shaped antenna.

commercial low-cost piezoelectric inkjet Brother's printer. To validate its functionality as a bent antenna for conformal application, we also performed a bending test by placing the antenna on a curved sample of foam with 30 mm and 40 mm bending radius as depicted in Figure 6(b). The coplanar

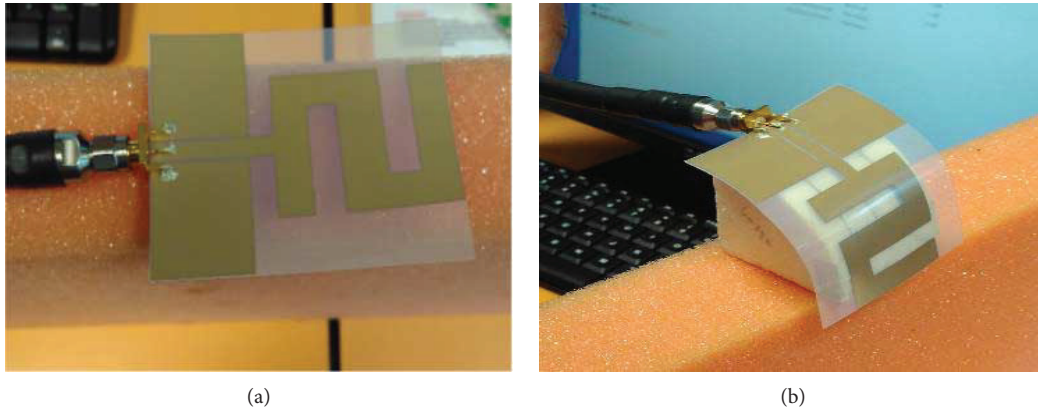


FIGURE 6: Fabricated Z-shape antenna by the proposed inkjet printer technique on the PET substrate. (a) Flat condition. (b) Bending condition (radius: 40 mm).

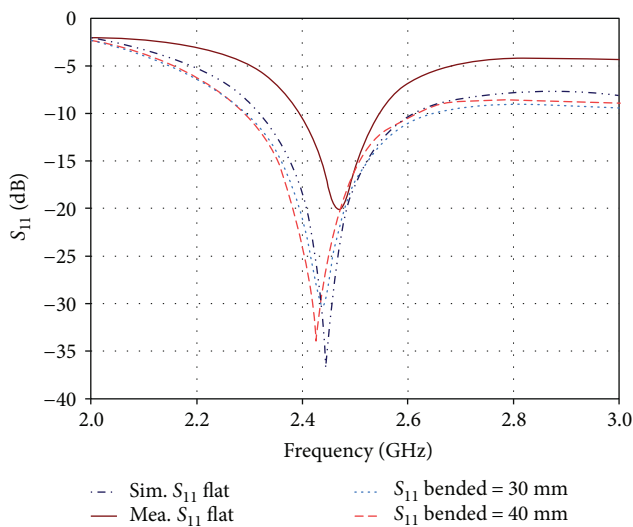


FIGURE 7: The reflection coefficient  $S_{11}$  in dB of the Z-shaped antenna with and without bending conditions.

waveguide (CPW) configuration, where the radiator and the ground plane are printed on the same side of the substrate, is chosen for its simplicity and ease of fabrication in a roll-to-roll production process. The printed CPW-fed Z-shape antenna is first printed by the office printer, and then the SMA connector was connected to the feed line. Due to higher soldering temperature ( $150^{\circ}\text{C}$ ), the thermal soldering method cannot be used; hence, silver nanoparticle paint from PELCO<sup>®</sup> has been used to connect the SMA connector with the feed line of the antenna, as shown in Figure 6.

The conventional Brother printer MFC-J430W with AgIC ink cartridge model number 1000 has been used to print this antenna. A cartridge from AgIC Company comes with three containers filled with AgNP ink to be inserted in three holders of the inkjet printer. The size of the silver nanoparticle is around 20 nm in diameter. Due to its very small particle size, the dissolution of AgNPs is made possible in the chemical solution used for chemical sintering of the deposited layer and makes the ejection of the ink from the printer nozzle easy.



FIGURE 8: Simulated current distribution of the antenna at 2.45 GHz.

To verify our proposed technique, we evaluated the reflection coefficient of the antenna at flat and bending radii of 30 and 40 mm by attaching it on a foam. As shown in Figure 7, the antenna is performing quite well for both radius positions. These radius values are taken considering the normal radii of the human arms and legs. The measurements are performed using a 4-port Vector Network Analyzer (VNA) model N5242A PNA-X from Agilent Technologies. The results show that a good match of measured reflection coefficient is found not only with the simulated results in the ISM band (2.45 GHz) in the flat shape but also after bending conditions. Since there is no heating process involved, the cracks cannot be observed in the printed layer after bending the antenna as reported in [8]. The measured conductivity of the printed layer is found to be around  $1.11 \times 10^7$  S/m (14.7% of the conductivity of the bulk silver) with single 300 nm layer thickness and  $0.3 \Omega/\text{sq}$  sheet resistance. The conductivity of the double printed layer is reported to be twofold with misalignment error

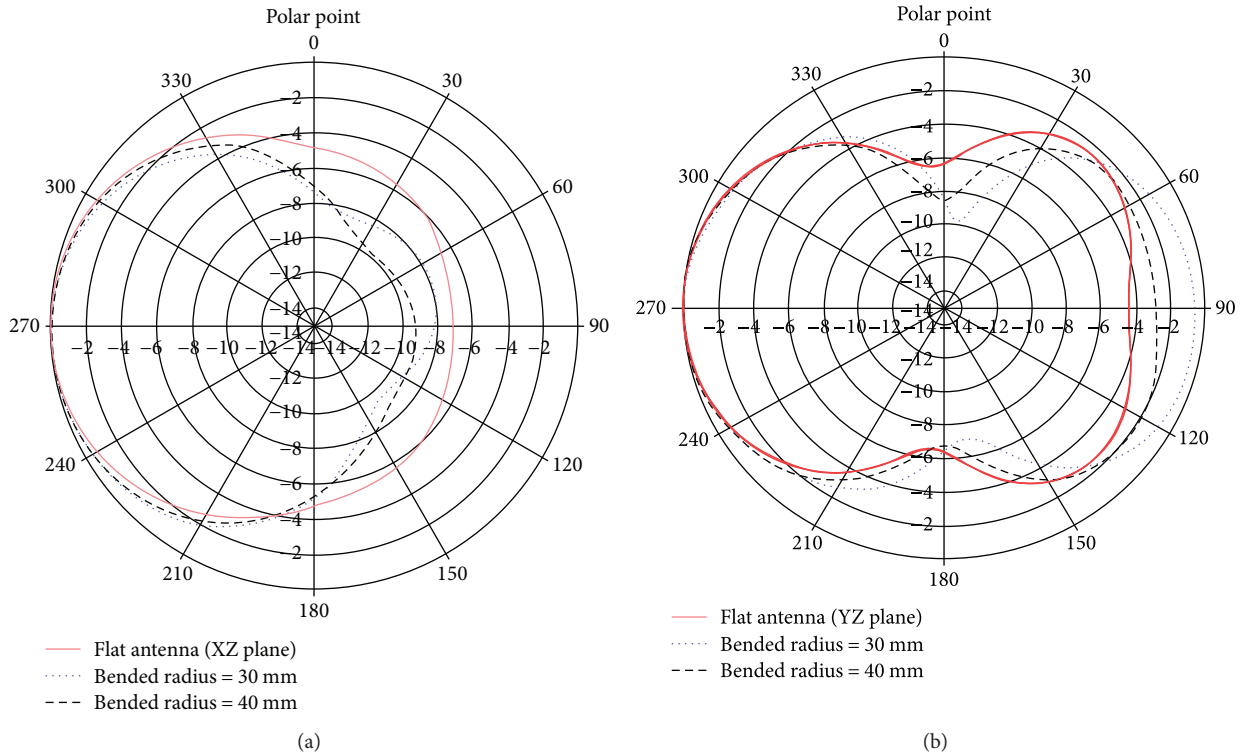


FIGURE 9: Radiation patterns of the antenna with different bending radii of 30 and 40 mm: (a) XZ plane ( $\phi = 0^\circ$ ) and (b) YZ plane ( $\phi = 90^\circ$ ).

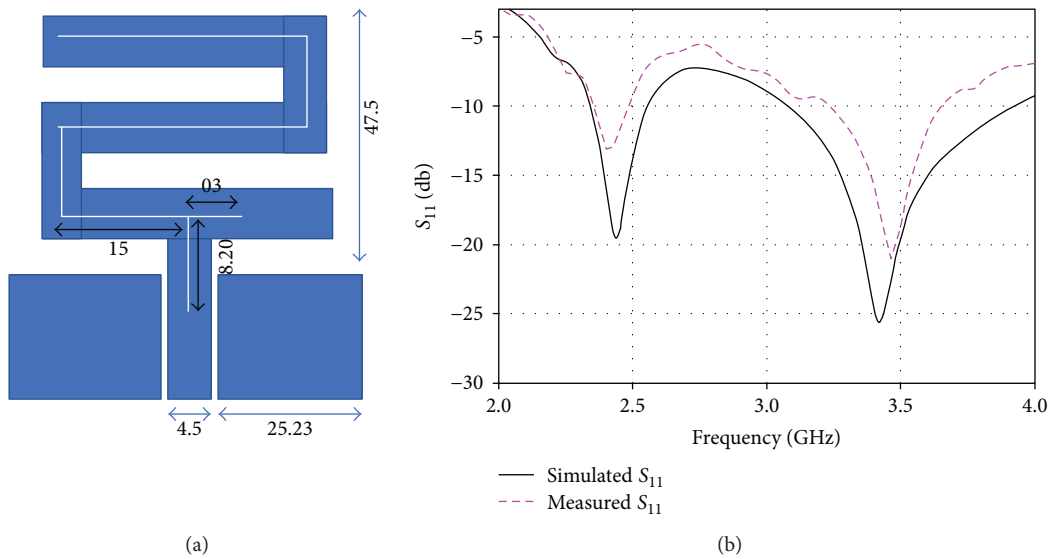


FIGURE 10: (a) The layout of the slotted Z-shaped antenna. (b) The reflection coefficient  $S_{11}$  in dB of the slotted Z-shaped antenna.

up to 0.5 mm while using an off-the-shelf printer [16]. The behavior of the antenna is also studied through its current distribution at 2.45 GHz, as shown in Figure 8, where it is shown that good current density distribution exists along the edges as normally happening in the case of the patch antenna.

To see the performance of this antenna for different antenna parameters, the gain of this fabricated antenna is also measured. The maximum measured gain of the

antenna is found to be 1.44 dBi with more than 60% radiation efficiency.

To see the radiation performance of the antenna, the radiation patterns of this antenna in the flat and curved shapes at a frequency of 2.45 GHz are plotted in Figure 9. The bending of the antenna results in slight widening of the radiation pattern for both XZ and YZ planes. Hence, our inkjet printed antenna can be used for both flexible and conformal applications.

#### 4. Modified CPW-Fed Z-Shaped Antenna

To check the validity of our printing technology for higher frequencies specially 5G, the CPW-fed Z-shaped antenna, presented above, is modified to cover a future expected 5G band, that is, 3.5 GHz. A slot of 0.5 mm thickness is etched in the middle of the zigzag path of the Z-shaped antenna, and then it is slightly optimized to work at our required frequency bands. The remaining dimensions of the etched slot are shown in Figure 10(a). The other dimensions of the proposed antenna are the same as those of the Z-shaped antenna shown in Figure 5 unless, otherwise, mentioned. The other parameters of the modified Z-shaped antenna are the same as shown in Figure 5. This designed antenna is fabricated, and the simulated and measured results of reflection coefficient  $S_{11}$  (dB) in the flat shape are shown in Figure 10(b). The measured results match reasonably well with the simulated ones.

#### 5. Conclusion

A CPW-fed Z-shaped antenna is fabricated using low-cost printed fabrication techniques. An office inkjet printer using a special cartridge from AgIC, Japan, has been used during printing the antenna. The most prominent feature of this silver ink is that it dries out instantly at the room temperature. This chemically cured formation of the conduction path of the silver nanoparticles not only facilitates the usage of substrates of low glass transition temperature ( $T_g$ ) but also eliminates the need of a prevalent expensive inkjet printer which employs expensive equipment and long postheating process. Moreover, the bending test has been performed to validate its functionality for conformal antenna applications. The surface morphology and height profile analyses of the printed layer are also executed. This proposed technique using an office inkjet printer should pave the path for easy and low-cost printing of the antennas for conformal applications.

#### Conflicts of Interest

The authors declare that they have no conflicts of interest.

#### References

- [1] A. Osseiran, F. Boccardi, V. Braun et al., "Scenarios for 5G mobile and wireless communications: the vision of the METIS project," *IEEE Communications Magazine*, vol. 52, no. 5, pp. 26–35, 2014.
- [2] D. J. Finn, M. Lotya, and J. N. Coleman, "Inkjet printing of silver nanowire networks," *ACS Applied Materials & Interfaces*, vol. 7, no. 17, pp. 9254–9261, 2015.
- [3] J. Hu, "Overview of flexible electronics from ITRI's viewpoint," in *2010 28th VLSI Test Symposium (VTS)*, pp. 84–84, Santa Cruz, CA, USA, 2010.
- [4] J. Kim and W. S. Kim, "Stretching silver: printed metallic nano inks in stretchable conductor applications," *IEEE Nanotechnology Magazine*, vol. 8, no. 4, pp. 6–13, 2014.
- [5] Y. Al-Naiemy, T. A. Elwi, H. R. Khaleel, and H. Al-Rizzo, "A systematic approach for the design, fabrication, and testing of microstrip antennas using inkjet printing technology," *ISRN Communications and Networking*, vol. 2012, Article ID 132465, 11 pages, 2012.
- [6] S. Ahmed, F. A. Tahir, A. Shamim, and H. M. Cheema, "A compact Kapton-based inkjet-printed multiband antenna for flexible wireless devices," *IEEE Antennas and Wireless Propagation Letters*, vol. 14, pp. 1802–1805, 2015.
- [7] H. R. Khaleel, "Design and fabrication of compact inkjet printed antennas for integration within flexible and wearable electronics," *IEEE Transactions on Components, Packaging and Manufacturing Technology*, vol. 4, no. 10, pp. 1722–1728, 2014.
- [8] H. F. Abutarboush, M. F. Farooqui, and A. Shamim, "Inkjet-printed wideband antenna on resin-coated paper substrate for curved wireless devices," *IEEE Antennas and Wireless Propagation Letters*, vol. 15, pp. 20–23, 2016.
- [9] B. S. Cook and A. Shamim, "Inkjet printing of novel wideband and high gain antennas on low-cost paper substrate," *IEEE Transactions on Antennas and Propagation*, vol. 60, no. 9, pp. 4148–4156, 2012.
- [10] H.-L. Kao, C.-L. Cho, X. Y. Zhang et al., "Bending effect of an inkjet-printed series-fed two-dipole antenna on a liquid crystal polymer substrate," *IEEE Antennas and Wireless Propagation Letters*, vol. 13, pp. 1172–1175, 2014.
- [11] A. M. Mansour, N. Shehata, B. M. Hamza, and M. R. M. Rizk, "Efficient design of flexible and low cost paper-based inkjet-printed antenna," *International Journal of Antennas and Propagation*, vol. 2015, Article ID 845042, 6 pages, 2015.
- [12] P. Bare, <http://www.bareconductive.com/>.
- [13] C. C. Pen, October, <https://www.chemtronics.com/p-693-circuitworks-conductive-pen.aspx>.
- [14] Z. Li, H. Liu, C. Ouyang et al., "Recent advances in pen-based writing electronics and their emerging applications," *Advanced Functional Materials*, vol. 26, no. 2, pp. 165–180, 2016.
- [15] Z. Cui, C. Ma, Z. Chen et al., *Printed Electronics: Materials, Technologies and Applications*, John Wiley & Sons, Singapore Pte. Ltd., 2016.
- [16] Y. Kawahara, S. Hodges, B. S. Cook, C. Zhang, and G. D. Abowd, "Instant inkjet circuits: lab-based inkjet printing to support rapid prototyping of UbiComp devices," in *Presented of the Proceedings of the 2013 ACM International Joint Conference on Pervasive and Ubiquitous Computing*, pp. 363–372, Zurich, Switzerland, 2013.
- [17] C. R. Garcia, H. H. Tsang, J. H. Barton, and R. C. Rumpf, "Effects of extreme surface roughness on 3D printed horn antenna," *Electronics Letters*, vol. 49, no. 12, pp. 734–736, 2013.
- [18] K. Black, J. Singh, D. Mehta, S. Sung, C. J. Sutcliffe, and P. R. Chalker, "Silver ink formulations for sinter-free printing of conductive films," *Scientific Reports*, vol. 6, article 20814, 2016.
- [19] D.-Y. Shin, Y. Lee, and C. H. Kim, "Performance characterization of screen printed radio frequency identification antennas with silver nanopaste," *Thin Solid Films*, vol. 517, no. 21, pp. 6112–6118, 2009.

## Review Article

# Printable Materials for the Realization of High Performance RF Components: Challenges and Opportunities

Eva S. Rosker,<sup>1,2</sup> Rajinder Sandhu,<sup>1</sup> Jimmy Hester,<sup>1</sup> Mark S. Goorsky,<sup>2</sup> and Jesse Tice <sup>1</sup>

<sup>1</sup>NG Next, Northrop Grumman Corporation, 1 Space Park, Redondo Beach, CA 90278, USA

<sup>2</sup>Department of Materials Science and Engineering, University of California, Los Angeles, CA 90095, USA

Correspondence should be addressed to Jesse Tice; [jesse.tice@northropgrummannext.com](mailto:jesse.tice@northropgrummannext.com)

Received 7 September 2017; Accepted 28 November 2017; Published 28 January 2018

Academic Editor: Félix A. Miranda

Copyright © 2018 Eva S. Rosker et al. This is an open access article distributed under the Creative Commons Attribution License, which permits unrestricted use, distribution, and reproduction in any medium, provided the original work is properly cited.

Printing methods such as additive manufacturing (AM) and direct writing (DW) for radio frequency (RF) components including antennas, filters, transmission lines, and interconnects have recently garnered much attention due to the ease of use, efficiency, and low-cost benefits of the AM/DW tools readily available. The quality and performance of these printed components often do not align with their simulated counterparts due to losses associated with the base materials, surface roughness, and print resolution. These drawbacks preclude the community from realizing printed low loss RF components comparable to those fabricated with traditional subtractive manufacturing techniques. This review discusses the challenges facing low loss RF components, which has mostly been material limited by the robustness of the metal and the availability of AM-compatible dielectrics. We summarize the effective printing methods, review ink formulation, and the postprint processing steps necessary for targeted RF properties. We then detail the structure-property relationships critical to obtaining enhanced conductivities necessary for printed RF passive components. Finally, we give examples of demonstrations for various types of printed RF components and provide an outlook on future areas of research that will require multidisciplinary teams from chemists to RF system designers to fully realize the potential for printed RF components.

## 1. Introduction

Additive manufacturing (AM) and direct write (DW) printing have seen an explosion of tooling within the past decade, which has gone from large prototyping houses to consumer friendly benchtop models and engineering grade tool sets. This has enabled greater ease of access to produce interesting functional components [1, 2]. Here, we define AM as tools that fabricate in a layer-by-layer fashion, while DW is a selective deposition of materials with high resolution on any flat, conformal, or flexible surface. These printing methods are highly attractive because traditional fabrication required for radio frequency (RF) circuitry and electronics can be eliminated, while allowing for direct digital manufacturing of arbitrarily complex objects [3–6]. RF component design simulations reduced to fabrication can be an iterative process to refine, thus making printing methods ideal because they enable rapid prototyping and testing cycles. A large number of publications to date have demonstrated low-cost, low

performance-printed RF passive components fabricated by AM and/or DW processes that may impact the consumer market [7–10]. However, a considerable amount of research is still required to unlock the technological potential for printing, especially on high performance components including lumped elements (inductors and capacitors), antennas, transmission lines, and interconnects, which are based on all dielectric or metal-dielectric building blocks, especially for conformal and flexible surfaces. Reliable and high performing printed RF passives are within reach; however, printed counterparts for active RF electronic circuits including inorganic transistors are still very much in their infancy [11]. Active components such as transistors are still very much limited by the available material performance and printing resolution [12]. Passive components can now be partially or fully fabricated with a number of different AM techniques (FDM, SLA, DLP, inkjet, and aerosol jet) and manufacturable at scale with roll-to-roll, Gravure, and screen printing. With the recent advent of multimaterial

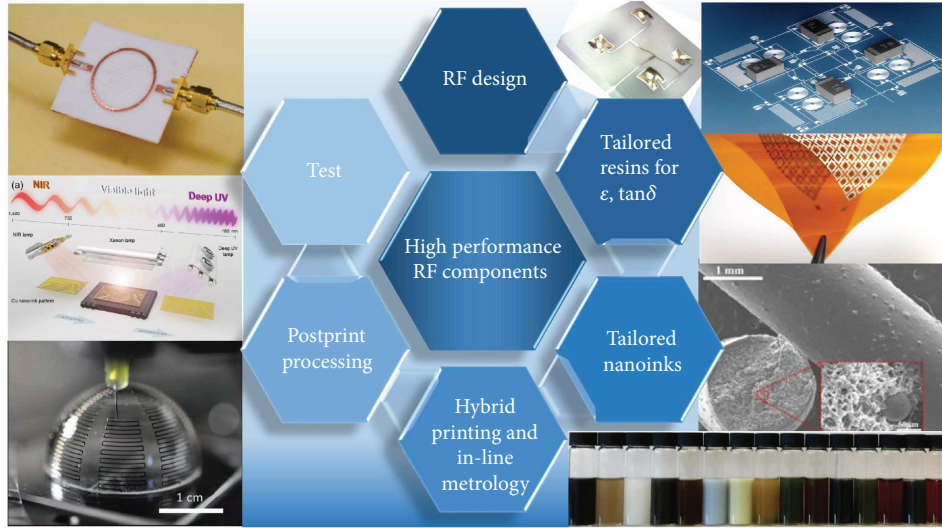


FIGURE 1: Methodology to obtain desired high performing RF components. Beginning with the initial RF component design, tailor the ink and resin chemistry around the required performance. Next, determine printing method(s) that would ideally have in-line metrology for surface profiles. The postprint processing is the key and needs to be compatible with materials chosen and end properties desired. Testing or characterization validates the initial design. Adapted with permission from [9, 14–20].

DW tooling, both metals and dielectrics may be printed concomitantly while previously these processes were decoupled to AM dielectric and then subsequently metallized with a separate technique. Advancements in printing technologies and processes will enable an entirely new class of fully 3D printed components on conformal surfaces that are not constrained to 2- or 2.5-D.

For many researchers, the overarching goal is to create printed, highly functional components with DC and RF properties near their bulk or non-AM counterparts while adding a degree of functionality that cannot be obtained with their planar counterparts. Achieving these bulk-like material properties will enable a wide application space, but at present, unfortunately there are several limits on which precursor materials are available to print and how well these functionally printed materials perform. Reliability is also a concern as these printed parts could potentially see extreme environments such as aerospace [13]. To this end, it becomes increasingly critical to understand the systemic effects of and controlling both the nano- and microstructures and topology of printed materials while expanding the “toolbox” of materials to print. Additionally, as conformal printing is near realization, flexible antennas and electronics require nanomaterials with high mobilities and on/off ratios such as carbon nanotubes (CNTs) and 2D materials. While the problem statement is simply defined, the execution is complex and rigorous. If successful, a new arena in high performing antenna materials and processes with disruptively fast turnaround times will be unlocked impacting the aerospace, medical, and communications industries.

Figure 1 depicts an approach to understand the initial component designs and simulated performance design trades (such as S-parameters) and then work towards achieving this by tailoring material properties. This could include nanoinks with nanoparticle size tuned to have compatible sintering

temperatures with the substrate. If near-bulk metal conductivity is required, the choice of solvents, ligand chemistry, and surfactants to prevent agglomeration needs to be chosen accordingly. Dielectric properties such as  $\epsilon$  and  $\tan\delta$  affect loss. If the design requires, utilize one or more printing methods with in line metrology to understand surface profiles and roughness, then perform postprocess sintering, curing, and characterization of the final component. Until techniques, materials, and design parameters are well enough established, this top down approach, while not as efficient, is an effective process to obtain high performance.

In this review, we will discuss the main challenges to the realization of high performance-printed RF antennas and components, the materials currently used for printing in highly functional RF components, including ink and polymer formulation, and overview of AM methods for printing with high precision. Also, we will offer perspective on the opportunities available to make major impacts to high-quality RF components that will offer similar performance to their simulated counterparts. In order to understand the contribution of losses and mitigate them, we will analyze structure-property relationships that will enable a path to optimal print and postprocessing properties. Since the opportunities outlined for improvement are universal to all printed parts, the authors note that there are likely other applications that will take advantage of these techniques outside of the RF community. Finally, we will review key demonstrations of conformally printed antennas and their performance factors and provide outlook on promising new paths in the arena of printed RF components.

## 2. Challenges Ahead

Currently, printing functional antennas, RF passives, and actives do not compete with more traditional manufacturing

approaches. AM and DW methods do enable innovative designs that cannot be obtained with traditional manufacturing, but several parameter spaces still need to be addressed in order for the components to match simulated performance. One of the main challenges for RF passives and an area ripe for material chemists is the development of new materials compatible with existing print processes that are tailored for their electromagnetic properties. Specific parameters include the electric permittivity ( $\epsilon$ ), metal conductivity ( $\sigma$ ), and loss tangent ( $\tan\delta$ ), each as a function of frequency. As miniaturization of circuitry and antennas becomes a driver, the permeability ( $\mu$ ) becomes the relevant variable to consider. These new materials could be printable inks and resin systems that are designed to be on the extreme ends of the spectrum for  $\epsilon$  and  $\mu$ , while making  $\sigma$  as high and  $\tan\delta$  as low as possible. Dielectric polymers that intrinsically have  $\tan\delta$  less than 0.06 and either very low ( $<2.5$ ) or very high ( $>10$ )  $\epsilon$  are very challenging to print as they are either short-chain or ceramic-filled polymers, respectively. The rheology of these materials is incompatible with current AM tooling. Conversely, for conductors, near-bulk metal  $\sigma$  has not been readily achieved. For RF, bulk  $\sigma$  is extremely important because of skin-depth effects, which unlike DC components cannot be compensated for by simply printing thicker with lower  $\sigma$  metals. With tailored silver (Ag) chemistries, researchers have been able to obtain near-bulk  $\sigma$  of Ag with DW methods [21, 22]. Since Ag is relatively inexpensive and the chemistry is very well understood, Ag-based inks have become ubiquitous in DW processes. Those well versed in print-compatible materials know that both Ag and copper (Cu) tend to degrade in  $\sigma$  over time as they are reactive even under modest ambient conditions being susceptible to sulfurization and oxidation, respectively. More robust inks such as gold have been developed; however, they are costly. The commercially available ones typically have short shelf lives and require handling under inert atmospheres. Since the palette of print-compatible materials has not been well developed for RF, this often leads researchers to develop their own inks and resins.

Due to coefficient of thermal expansion (CTE) and surface energy mismatches, printing metals onto printed dielectric substrates is challenging. In order to achieve high  $\sigma$ , a sintering step is necessary, which typically requires temperatures above that of the dielectric glass transition temperature ( $T_g$ ) of the dielectric substrate. Surface-sensitive sintering techniques based on photonics have recently become popular in order to circumvent this challenge [23]. Since this type of sintering evolves under nonequilibrium conditions across multiple scales there are not well known, process-structure-property relationships must be developed. Additionally, the adhesion of DW materials on AM surfaces postsintering is also not well understood and warrants further research [24]. As buried metal on dielectric applications, such as through lines and 3D vias in multilayer/multimaterial printing, becomes more relevant, then nonthermal curing methods will also need to be further developed such as electrical sintering to obtain near-bulk  $\sigma$  [25].

Surface roughnesses of both the printed metal and dielectrics are currently much higher than is desired when

compared to bulk manufacturing processes. Lithography and wafer-based antenna components can reach low nanometer (nm) resolution in root-mean squared (RMS) surface roughness values, while machined parts and circuit boards can be in the hundreds of nm RMS resolution. Stereolithography (SLA) and fused deposition modeling (FDM) processes are in the few micrometers ( $\mu\text{m}$ ) and tens of  $\mu\text{m}$  RMS surface roughness regimes, while inkjet and aerosol jet metal line profiles are quite variable. While this may not be an issue for low frequency (i.e., MHz) applications, the roughness can seriously degrade S-parameter loss at GHz frequencies. To mitigate the roughness limitations, a postprocess polishing step is currently necessary, which unequivocally reduces the utility of printing; however, if the desired structure is nonplanar, then polishing may even be precluded. New surface planarization techniques or software-based topology optimizations need to be developed to achieve RMS surface roughness comparable to at least machined surfaces on both printed metals and dielectrics. The development of roughness models also will play a dominant role in the optimization of antenna performance as both the dielectric and metal surface profiles are nonuniform [26].

As frequency increases, the size of the components drastically decreases, which limits the AM techniques that can be employed due to their resolution. While high-resolution techniques such as two-photon lithography and electrohydrodynamic printing are available with nm resolution, there becomes a trade space between resolution, total area, and throughput. These processes may be amenable to high-frequency antennas (EHF), but they do not scale well to low-frequency antennas that require much larger size features. Additionally, as antenna systems become more functional and complex, it will become necessary to traverse the different size regimes (nm to cm) seamlessly, which would require either incorporating more robotics to go in between printing tools with different resolution or further integration of multimaterial printing beyond what is currently available [27–29]. Ideally, in situ or in-line monitoring of critical process parameters that have been outlined above can be implemented into the print process steps similar to practices employed in the more mature semiconductor industry. To date, little research in this area has been demonstrated [30].

### 3. Methods and Materials for Printing RF Components

In this section, we will discuss the common methods for DW and AM techniques and review the materials that have been developed for printing RF components. For each method, there are specific requirements for the inks and resin systems to be compatible with the tool parameters. As new inks and resins are designed for the electromagnetic properties, these constraints will need to be well understood in order to optimize RF performance. Additionally, we focus on the methods for realization of high performance including scalability. While there are many emerging technologies for both DW and AM, we focus on those most well understood that will enable true micro- and macromanufacturing of complex RF assemblies. Laser sintering and electron beam

melt approaches will not be covered in this review; while they have recently gained interest in microwave horns, research to date has almost entirely focused on structural-mechanical properties.

**3.1. Methods for Direct Write.** Compared to traditional photolithography methods, DW approaches are faster, lower cost, and more environmentally friendly because they rely on additive rather than subtractive processes. AM of metallic lines encompasses a broad range of technologies, including Gravure printing and screen printing, but these techniques tend to be low quality and low-precision processes. The most common routes to printing high-precision metals to date are inkjet printing (IJP), aerosol jet printing (AJP), and direct ink writing (DIW). These methods use a computer-aided design (CAD) file input to dispense inks containing colloidal suspensions of metal nanoparticles (NPs) or other materials of interest (such as 2D materials and dielectrics) and may be used to print patterns of varying thicknesses by increasing the number of overprints. However, there are significant differences in print resolution, design flexibility, and process scalability arising from the respective mechanisms of deposition, so each method has advantages depending on the desired application. In this section, we will discuss the mechanism of printing, the effect on the morphology and properties, and finally, we will present a comparison of the three methods.

**3.1.1. Inkjet Printing (IJP).** IJP has been the most ubiquitous DW process used to date, which utilizes a low viscosity ink expelled through a nozzle in a dropwise fashion. A pattern is created by overlapping the droplets so that a continuous line is formed. The characteristics of the print may be altered by changing the overlap percentage or the print direction [31]. The spacing must be less than 65% overlap [32] in order to prevent bulging of the printed line, and the ultimate resolution is a function of the droplet diameter as well as the spreading upon contact with the substrate surface [19, 31, 33]. Currently, the smallest achievable feature sizes of 25–50  $\mu\text{m}$  are comparable to or even better than processes such as screen printing and photolithography [33]. Still, AJP or electrohydrodynamic (EHD) printing may be necessary for further miniaturization.

A significant challenge is the lack of uniformity in printed lines. A “coffee-ring” height distribution has been well documented, in which the height of the line is depressed in the center as compared to the outside edges. The printed drop is thinner at the outside, resulting in an increased rate of evaporation at the edges. This creates an outward current, which can be minimized by the addition of solvents with a higher boiling point and a lower surface tension than the primary ink solvent. This will induce the Marangoni effect [34], in which a surface tension gradient produces an inward current to balance the natural outward current. The simultaneous currents circulate the ink as it dries, thereby creating a more even height. Dimethylformamide (DMF) when mixed with water as a solvent for Ag NPs has been shown to be effective in reducing the coffee-ring phenomenon [35]. Furthermore, printing lines counter to the nozzle direction have

been shown to reduce the coffee-ring effect and create a more uniform lateral profile [31].

**3.1.2. Aerosol Jet Printing.** Similar to IJP, AJP is also a DW method, but the print head continuously sprays ink that has been either pneumatically or ultrasonically aerosolized into 2–5  $\mu\text{m}$  droplets [36]. A sheath gas flowing along the outside of the atomized ink droplets focuses the beam and prevents nozzle clogging. As a result, inks with much higher viscosities than IJP, which is limited to less than 30 cP, may be used. The desired pattern is produced by closing an electromagnetic shutter to halt the flow of the ink mist until the nozzle is in the correct position. Due to the small size of the aerosol droplets, the printed path begins to dry during deposition [37] which can affect the smoothness of the final print.

Like IJP, AJP also shows the coffee-ring effect [31], indicating that similar evaporation processes take place for both printing methods. However, no work has shown successful mitigation of this effect to date for AJP. Despite the difference in nozzle sizes between IJP and AJP, both methods achieve decreased feature sizes with a decrease in nozzle diameter [31, 36]. AJP demonstrates a splatter effect [31] rather than cleanly defined droplets due to the mist of particles, and this can be detrimental to achieving finer patterns and tighter print spacing.

**3.1.3. Direct Ink Writing.** DIW operates by using a combination of precision pump and variable size syringes to extrude highly viscous inks. Due to the shear-thinning rheological properties of the ink, it flows while in the nozzle tube but becomes solidified once deposited. This acts as an “instant-cure” process and allows for rapid 3D architecturing [38].

Some of the highest printed conductivities to date have been demonstrated with DIW by Lewis and Walker, who report Ag electrodes with conductivity of  $6.25 \times 10^7 \text{ S/m}$ , which is as close to bulk Ag conductivity ( $6.25 \times 10^7 \text{ S/m}$ ) as anyone has demonstrated [21]. However, this may be a result of the ink properties rather than the printing mechanism. Adding 2,3-butanediol dilutes the viscosity so that this ink may be used with IJP [21]; however, there have been no widely circulated reports regarding the conductivities using this ink and printing method.

Uniquely, this method is also very versatile as sol-gels, ceramics, waxes, and even silk have been printed. Since DIW affixes to a multiaxis stage, omnidirectional printing is achieved to enable true conformal printing on any surface. Additionally, since the print heads are analogous to IJP printers, multiple heads can be utilized at once at very high printing rates. While this technique is relatively new, it has emerged as a versatile method that will likely play a critical role in high performance antennas and components.

**3.1.4. Comparison of Direct Write Methods.** While there are a multitude of publications about IJP, however AJP and DIW are relatively newer technologies. Table 1 gives an overview of the different DW printing including their key benefits. A schematic representation of the three DW methods highlighted in this review is shown in Figure 2. AJP is more versatile than IJP for the following reasons. First, AJP

TABLE 1: Comparison of direct write printing techniques.

Print method	Ink viscosity (cP)	Nozzle diameter ( $\mu\text{m}$ )	Feature size ( $\mu\text{m}$ )	Min. line thickness ( $\mu\text{m}$ )	Key benefits
IJP	1–30 [34]	20–60 [31, 39]	20–100 [34]	0.6 [31]	Low cost, multiple heads
AJP	1–1000 [36]	150–300 [40]	10–200 [40]	0.1 [40]	High throughput, thin layers, fine features
DIW	1–1000000 [21, 41]	0.1–1 [21, 42]	1–1000 [42]	0.5 [41]	Most precise, best resolution

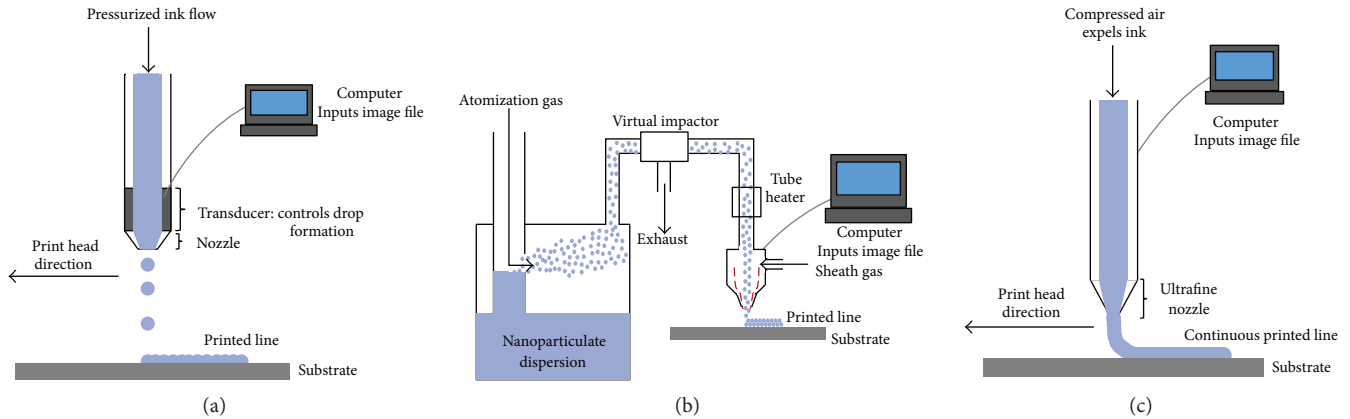


FIGURE 2: Schematic representation of direct write (DW) printing methods. (a) Inkjet printing (IJP); (b) aerosol jet printing (AJP). Reproduced with permission from [37]. (c) Direct ink writing (DIW).

produces much finer resolution. Mahajan et al. defined the “focusing ratio” as the flow rate ratio of sheath gas flow rate to carrier gas flow rate [43]; they found that the printed line width decreases as the focusing ratio increases, while the standard deviation from run to run decreases, thus enabling a highly repeatable reduction in feature size. However, DIW with its submicron nozzle diameter enables even finer printing than AJP. Second, because of the vector-based printing approach as opposed to the line-by-line pixel rastering of IJP, a higher level of manufacturing flexibility is afforded to AJP systems. For example, a square may be printed using either a serpentine or a perimeter-fill pattern [31]. The drying rate of the ink affects the smoothness of the final printed structure. Third, the large distance between the nozzle and the substrate allows for printing on nonplanar, conformal substrates. This is especially useful for applications such as 3D RF antennas. Fourth, AJP may be able to produce higher conductivity structures than IJP. Because of the large range of acceptable viscosities, the ink can contain a higher weight percentage of metal, thereby increasing the probability of contact between the metal NPs. Finally, AJP can print much thinner single passes than IJP, therefore leading to increased design flexibility for device manufacturing.

The notable disadvantage of AJP is the resultant morphology of the printed line. Werner et al. found that higher sintering temperatures were needed to achieve the same resistivity within AJP structures versus IJP structures [37]. This is because the contact area with the substrate is increased for IJP, leading to more thermal dissipation and thus more progressed sintering. Also, the AJP structures are more porous, thus leading to a decreased effective cross-

section [37]. However, some interesting methods to combat this increase in resistivity have been proposed, such as the inclusion of carbon nanotubes [44] to enhance conductivity. Electrical sintering, rather than furnace sintering, has also been shown to produce conductivities as high as half that of bulk silver with AJP [37].

The advantage of DIW in comparison to IJP and AJP is that it can produce much finer resolution prints. However, it is a less mature technology and the intricate process parameters are not as well researched.

**3.2. Methods for Additive Manufacturing.** Three-dimensional printing of dielectrics is also of interest. Stereolithography (SLA), fused deposition modeling (FDM), and digital light processing (DLP) produce polymers with properties favorable for flexible electronics and RF devices. These methods are all layer-by-layer manufacturing processes which utilize a curing process to turn resins into solid structures via treatment with heat or light. A schematic representation of the three AM methods highlighted in this review is shown in Figure 3.

**3.2.1. Fused Deposition Modeling.** FDM is the most mature technology in AM of dielectric materials. In this technique, filaments are heated and extruded from the print head and deposited onto the print bed in a shape defined by the CAD file in a continuous flow. As the print progresses, newly extruded polymer fuses with the already printed layer to form the solid structure. Reducing the layer thickness increases the smoothness of the final structure, but it also increases the amount of time needed to form the sample. Since this is a bottom-up approach, structures with overhanging segments

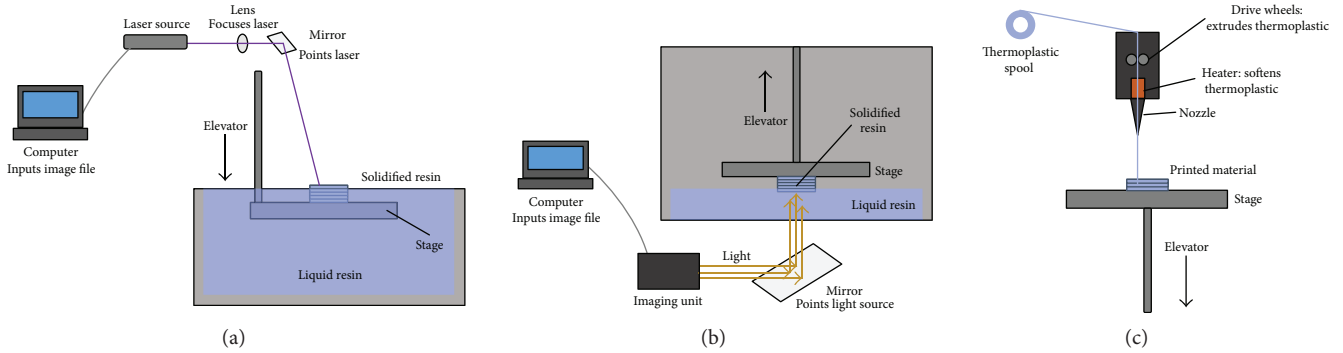


FIGURE 3: Schematic representation of additive manufacturing (AM) printing methods. (a) Stereolithography (SLA), (b) digital light processing (DLP), and (c) fused deposition modeling (FDM).

may require the addition of a support piece, which can either be mechanically broken off, or it can be made with a different resin that dissolves in a chosen solvent [45]. Thus, a significant disadvantage is that FDM-manufactured structures may require some level of postprocessing depending on their complexity, which may include organic acid etching to reduce surface roughness. Also, since there can be voiding between the printed layers, additional postprocessing or annealing to minimize these features is necessary.

For RF applications, low loss within the substrate is desired. Deffenbaugh et al. found that FDM structures exhibit lower loss  $\tan\delta$  than SLA [46]. Furthermore, embedding cyclo-olefin polymer (COP) resin with  $\text{TiO}_2$  demonstrates low loss  $\tan\delta$  of 0.0014 up to frequencies of 17 GHz [18]. However, FDM structures also have lower print resolution ( $>200\ \mu\text{m}$ ) and a rougher surface finish than SLA structures.

### 3.2.2. Vat Photopolymerization

(1) *Stereolithography*. SLA printing works by exposing a photosensitive liquid polymer resin to a light source, typically a hundred of mW UV laser, since the high-power output is desirable, to solidify the resin. The light source rasters across the surface of the sample in point-by-point or line-by-line fashion and introduces enough energy into the resin to induce photopolymerization resulting in the cross-linking of resin polymer chains to form a cohesive solid structure. Some SLA printers employ a top-down approach, in which the build plate is above the vat of resin and increases in height after each layer is cured [45], while others employ a bottom-up approach in which the build plate is in the resin and moves down after each layer is cured to expose the next layer of resin. The structure is generated from a 3D mesh of triangular elements [47]; the tolerances are specific to the printer used, but the layers are generally 0.05–0.15 mm thick in the z-direction, with accuracies of 0.01–0.02 mm in the xy-plane [48]. Because of the layer-by-layer addition and specific laser raster pattern, smooth surfaces with highly detailed features may be obtained.

SLA-printed substrates demonstrate promising capability to be used for RF and microwave circuits. Some prints show material properties comparable to FR-4 circuit boards [46], with the advantage of being flexible or of arbitrary shape

(FR-4 is planar); however, FR-4 is not the industry standard due to high loss. In applications where a high dielectric constant is desired, such as for waveguides and increasingly miniaturized devices, SLA-printed materials may be better suited than FDM materials [46].

(2) *Digital Light Processing*. DLP is similar to SLA as it uses a projection light source to solidify a liquid resin layer by layer. However, rather than rastering a laser, DLP flashes a digital image of each layer onto the exposed resin; thus, each layer is created at once rather than in a point or line process profile. The build plate then moves down, and the next layer is cured. DLP is a relatively new technology compared to SLA and FDM, but the all-at-once approach means that print time is drastically reduced [49]. Total print resolution depends on the pixel size, which is affected by the projector. Since the projector is limited by a maximum number of pixels, prints approaching the size of a pixel will be increasingly lower resolution. Thus, there is a trade-off between size of print and resolution obtained. This approach also creates striations known as voxel lines along the z-axis of the print and therefore may necessitate some level of postprocessing to obtain a smoother print. To date, there have been few studies on the RF characteristics of DLP-printed dielectrics, although they are anticipated to be comparable to SLA.

Controlled oxygen inhibition enables simpler and faster DLP printing [4]. Printers equipped with an oxygen-permeable membrane below the print window obtain an “oxygen dead zone,” a thin layer of uncured liquid resin between the print window that supplies the digital image and the already-solidified resin. Polymerization begins at the point where oxygen no longer exists but free radicals (produced by photons from the DLP projector) are present. Suction forces result in the continuous renewal of resin as the part is pulled upwards from the vat so the process is continuous rather than stepwise like in SLA and standard DLP processes. Thus, the viscosity and cure rate of the resin are the process-limiting factors, allowing for vastly reduced printing times.

3.2.3. *Emerging Methods*. The ultrasonic wire mesh embedding printing method developed by UTEP researchers combines FDM and ultrasonic thermal embedding to employ

wires and wire meshes into the printed thermoplastic surfaces, which enables nonplanar printed circuit boards and antennas [28, 50]. This method also circumvents sintering; however, it would likely still require some form of printed interconnect. While vat photopolymerization, FDM, and IJP are the most widely used and understood processes to date, we do want to highlight emerging additive manufacturing methods that may play a role in the future for realization of difficult to fabricate RF components. As printed components become increasingly smaller, some higher-resolution techniques such as 2-photon polymerization (2PP) have emerged. 2PP has been popularized by the mechanical engineering community by demonstrating extremely high-yield strength to density ratio, but the authors envision that this technique could meet the high-resolution needs for RF systems [51, 52]. Electrohydrodynamic printing is the high-resolution printing analog to IJP. With this method, researchers have achieved nm-scale resolution and achieve this by changes in voltage potentials between the printer nozzle and the surface to be printed on [53, 54]. While these methods have shown that they can impact future RF systems, there has not been widespread adoption of these techniques to date making a path towards realization of high performance RF components difficult. However, we envision a path towards hybrid additive manufacturing approaches in the future.

**3.3. Ink and Resin Formulation.** Inks containing conductive materials must be printed in order to fabricate a conductive path within the RF circuit. Resins are the dielectric that acts as the structural and capacitive medium for RF components. Nanoinks based on van der Waals (vdW), materials and CNTs have been successfully printed, showing promise for the field of conformal and, more specifically, flexible RF electronics based on their propensity to perform under flexing.

**3.3.1. Direct Write Metallic Nanoparticle Inks.** Metal-containing inks are of great importance as the conductive path in DC circuits and RF devices. The high surface to volume ratio of NPs reduces the necessary thermal cure temperature by up to 90% relative to their bulk counterpart [55]. This is important for use with flexible substrates that are sensitive to high temperatures and also for overall process efficiency. Most metal NPs are fabricated using a bottom-up approach [42], in which crystallization is induced via the addition of a surfactant. The distribution of size and shape results in inks with varying properties, so growth must be carefully controlled. The smaller the NP diameter, the lower the required annealing temperature [56]; therefore, for flexible electronics and other substrates that are incompatible with long heat treatments, achieving smaller NP inks is important. For use with AJP, the NPs must be less than  $1\ \mu\text{m}$  or  $0.1\ \mu\text{m}$  for pneumatic and ultrasonic atomizers, respectively. To develop an ink for DW, the metal NPs are dispersed within a solution of cosolvents with different vapor pressures. The high vapor pressure solvent ensures that the viscosity of the ink is lowered enough to achieve high rates of atomization. It evaporates out of the ink upon deposition, increasing the effective weight percentage of metal in the printed ink. The low vapor

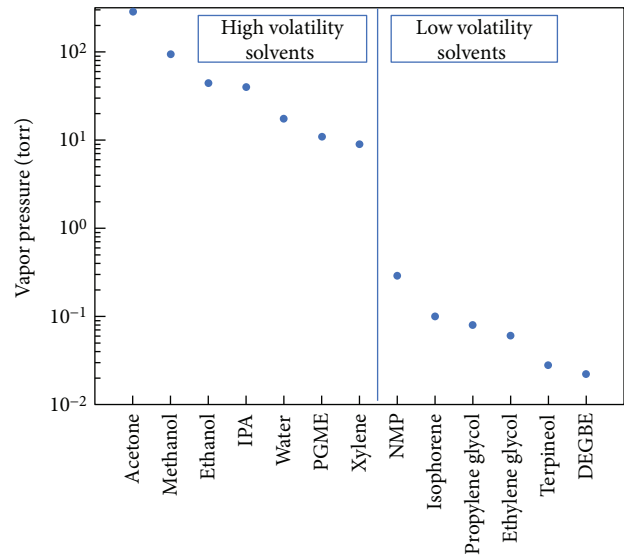


FIGURE 4: Common high and low vapor pressure solvents for AJP.

pressure solvent ensures that the ink retains its droplet shape, thereby minimizing the amount of overspray. The vapor pressures of some commonly used solvents are shown in Figure 4. Spherical or flake-like NPs have the highest chance of successful printing, since long or rod-like NPs may be damaged by the atomizer or nozzle. An adhesion promoter may need to be added to the ink in order to achieve good adhesion on all types of substrates. This also helps to mitigate the coffee-ring effect.

For IJP, controlling viscosity between 1 and 30 cP will generally prevent nozzle clogging. The viscosity window to obtain good resolution and line profile is typically much narrower at 8–13 cP. NP loading in the IJP-based ink is one example how viscosity may be tuned. For DIW, rheology and high particle loading are most important to control. The viscoelastic properties of the ink can be tailored to allow continuous flow through the nozzle and then “fixing” or setting upon deposition, while the high loading maintains the line shape and profile upon drying.

**3.3.2. 2D Material Inks.** In addition to metal NPs, 2D vdW materials such as graphene and transition metal dichalcogenides have successfully been implemented as inks [19, 42]. These rely upon a top-down fabrication approach, in which exfoliation of the bulk crystal via ball milling, ultrasonication, or liquid-phase exfoliation is necessary to break the interlayer van der Waals forces [42] and form 2D sheets. Surfactants are added to the ink to stabilize these sheets, as they will preferentially bond or create linkers on the surfaces, thus preventing aggregation. Like metal inks however, it is difficult to control the size and thickness of the sheets during exfoliation [19]. While the performance in RF is orders of magnitude worse than traditional III–V RF electronics, these vdW flextronics are a very promising printable alternative to surpass organic thin film flexible transistors because of their excellent electrical and mechanical properties such as strain to failure ratios [57–59]. These vdW inks will not enable realization of extremely high performance RF actives in the near future;

TABLE 2: Comparison of RF parameters for printed dielectrics [46].

Material	Print method	Characterization frequency range	$\tan\delta$	$\epsilon$
COP w/ 30% TiO <sub>2</sub> [18]	FDM (then 1100°C)	17 GHz	0.0014	4.56
PC-ABS	FDM	1 MHz–1 GHz	0.0076–0.0055	2.74–2.77
Polycarbonate	FDM	1 MHz–11 GHz	0.0076–0.0066	2.74–2.59
ABS-M30	FDM	1 MHz–11 GHz	0.0069–0.0098	2.63–2.60
Ultem 9085™ [18]	FDM	N/A	0.0040	3.00
DMX-SL 100	SLA	8.2 GHz–11 GHz	0.0115–0.0130	2.97–3.09
Prototherm 12120, thermal-cured	SLA	1 MHz–11 GHz	0.0171–0.0170	3.45–2.71
NanoForm	SLA	1 MHz–11 GHz	0.0131–0.0286	3.75–2.88
Prototherm 12120, UV-cured	SLA	1 MHz–11 GHz	0.0148–0.0368	3.68–2.93

however, they fill a niche to enable completely foldable and deployable RF active circuits that are currently only comparable to CNT-based inks, but with a broader range of properties. These vdW inks can also be utilized to create heterostructures with quite a few materials available including dielectrics, conductors, and semiconductors as more layered materials are being discovered at a near exponential rate [60, 61].

**3.3.3. Additive Manufacturing Resin Formulation for Printed Dielectrics.** Since FDM relies on polymer extrusion while SLA and DLP rely on resin solidification, the formation of the precursors affords different material properties. For RF applications, a low  $\tan\delta$  is ideal, as well as either very high or very low  $\epsilon$ . Both these properties are correlated to molecular structure by polarity or dipole moments. Since  $\epsilon$  is the tendency of the material to polarize in an applied electric field, and loss tangent is minimized by how fast the polymer relaxes back to equilibrium after the electric field is turned off, then the more symmetric and smaller chain length a polymer is, that is, cyclic polyolefin, the lower its  $\epsilon$  and  $\tan\delta$ . High  $\epsilon$  may be obtained by choosing the polymer matrix base and adjusting the amount of additive agents to be within the desired  $\epsilon$  range.

These mixtures or composite resins represent a large and promising class of materials, as the mechanical characteristics of the resin may be chosen to fit the specifications of the printer by altering the polymer matrix base [62]. The effective permittivity of a composite is dependent on the permittivity of the interfaces within the mixture as well as on the DC conductivity of the composite, expressed in

$$k_{\text{eff}}^* = k^*(\omega) + \sum_i k_{\text{MW},i}^*(\omega) + j \left( \frac{\sigma_{\text{DC}}}{\omega k_0} \right), \quad (1)$$

where  $k^*(\omega)$  is the permittivity of all composite components,  $k_{\text{MW}}^*(\omega)$  is the permittivity of the composite interfaces,  $\sigma_{\text{DC}}$  is the DC current, and  $k_0$  is the permittivity of free space. Ceramic fillers afford naturally high  $\epsilon$  and low  $\tan\delta$ , but they may alter the mechanical or electrical properties of the printed part, which needs to be considered in advance. At high ceramic loading concentrations, a postprint high temperature firing step may need to occur causing densification or shrinkage of the printed component. A summary of key

printed dielectric materials properties for RF can be found in Table 2.

Environmental stability is also required for a high performance printed dielectric. Materials such as polylactic acid (PLA) are commonplace in printing and satisfy many of the parameters previously listed. However, PLA absorbs moisture readily at ambient conditions causing unwanted warpage, thus rendering it an impractical material for high performance RF components.

#### 4. Structure-Property Relationships

In this section, we will review the postprint sintering and curing approaches for DW and AM methods, respectively. We will also discuss the methods used to characterize DC and RF properties that are critical to obtaining high performance printed RF materials. The material properties such as  $\epsilon$ , metal  $\sigma$ ,  $\tan\delta$ , and  $\mu$  will also be covered. It should be noted that bulk conductor conductivity acquires a major importance as the operation frequency is increased. Indeed, due to the skin-depth effect, the electromagnetic field can only penetrate inside the conductor by a thickness on the order of a few skin depths, expressed in

$$\delta = \sqrt{\frac{\rho}{\pi f \mu}}, \quad (2)$$

where  $\delta$  is the skin depth,  $\rho$  the bulk resistivity of the conductor,  $\mu$  is the permeability of the conductor, and  $f$  is the operating frequency. As a consequence, the effective thickness of a printed conductor cannot exceed the skin depth ( $2 \mu\text{m}$  in bulk silver at 10 GHz). Therefore, a low bulk conductivity cannot be compensated by printing thicker, as it could for DC.

RF microstrip and stripline test structure fabricated with DW and AM methods can be used to determine the RF properties of printed metal lines and dielectric substrate materials [63]. S-parameter measurements obtained from the RF test structures over the desired frequency range combined with modeling can be used to extract  $\epsilon$ ,  $\sigma$ ,  $\tan\delta$ , and  $\mu$  [64]. Correlating the electrical parameters from both DC and RF measurements with microstructural characteristics of the printed thin film materials is essential to provide a more complete and in depth understanding of key parameters

optimization in the thin film printing and sintering process for more optimal DC and RF performance as a path forward to obtain high performance RF components.

*4.1. Postprint Sintering of Metal NP Inks.* Sintering processes play a key role in microstructure formation of printed metal thin film lines. Correlations in electrical, mechanical, and thermal properties of the printed thin film lines relate directly to microstructure. In the following sections, we will discuss the sintering of NP printed inks; however, similar mechanisms and characterization methods are applicable to the study of non-NP reactive inks. These reactive inks either require mixing within deposition or a two-step printing process of depositing metal precursors followed by reducing reactants to create the thin film metal line [65].

In order to create a conductive path, metal NPs must be in contact with each other in the printed metal line. Since nanoinks require a liquid carrier such as organic or aqueous solvents with surfactants to prevent agglomeration, these must be removed to have optimal contact of the metal NPs. Furthermore, NPs may be understood as many distinct grains, of varying sizes. Growth of large grains by the consumption and coalescence of smaller ones will occur during the sintering process as predicted by the Gibbs-Thompson effect [66]. Optimizing the thermal coalescence process to completion during sintering to overcome the activation barrier to diffusion without introducing large thermal gradients within the growing film plays a critical role in forming fully dense and conductive metal film microstructures [67, 68]. The phenomenon of necking, in which NPs come into contact with each other, is also important to facilitate a more conductive path. Necking has been observed to initiate at various sintering temperatures and scales nonlinearly with particle size. This has been more thoroughly discussed in the Ag system by Seifert et al. at 200°C and above for >30-minute intervals [31]. Numerous publications [31, 55, 69–71] have shown that increased annealing temperature or time leads to increased densification of the metal film, which is consistent with well-known ripening phenomena in crystal grain growth.

High performing electrical conductivity values have been achieved by printed Ag films at 50–70% of bulk Ag [72]. Zhao et al. have seen conductivity 57% of bulk Ag by including 0.15 weight percent carbon nanotubes [44]. These highly conductive structures are reported to act as bridges across defects and grain boundaries. Similarly, Li et al. have recorded thermal conductivity 65% of bulk Ag by utilizing ink with a 2:1 ratio of 10 nm Ag NPs to 50 nm Ag NPs to decrease the porosity [73]. Separately, for Au, half of the bulk conductivity has been demonstrated on carefully tailored ligand chemistry and particle sizes at 150°C; however, this was in a thin film ink and not printed [22]. There have been a number of mechanistic explanations proposed for the decrease in DC resistivity observed during sintering. First, increasing sintering time leads to grain agglomeration via Ostwald ripening, thereby decreasing the amount of grain boundaries in the structure. Furthermore, the dislocation density decreases with annealing [74]. Finally, decreases in porosity have been observed with increased sintering time,

which increases the effective cross-sectional area. All of these phenomena decrease the hindrance to the conductive path of electrons, thereby increasing conductivity.

There are many different methods to achieve the sintering of metals after they have been printed with DW techniques. The sintering method will highly depend upon the glass transition temperature ( $T_g$ ) of the dielectrics or substrate present, the temperature required for sintering the metal (dependent upon particle size), and the form factor of the component. Environmentally controlled oven treatments are commonly utilized for sintering NP-based inks to rid the metal of solvents, binders, and surfactants if they exist in the native ink. The smaller the particle size the lower the sintering temperature can be; however, care has to be taken to design the ink sintering not to exceed temperatures of the other materials printed to. Photonic sintering is an approach that can circumvent this issue by flooding quick flashes of light at high powers so there is only surface effect [75]. Under the right conditions, the energy is absorbed by the surface and quickly dissipates as a function of depth so the materials below the surface are selectively cooler. This enables printed high  $\sigma$  metals with sintering temperatures > 150°C to be sintered on substrates with  $T_g < 100^\circ\text{C}$ . The mechanism of this local heating effect is due to the surface plasmon resonances within the range of the light source, with the main variables to consider being the layer thickness and specific heat capacity. This method also allows for rapid sintering and in-process sintering at potentially large areal domains since the timescales are on the order of ms or less. The drawback to photonic sintering approaches is that because they are surface mediated, it may cause nonuniform sintering or even preclude applications with nonplanar surfaces. Another interesting sintering approach is electrical. Current (DC or AC) is applied to the printed metals, and local resistive heating can rapidly increase enough to sinter NP printed inks [76]. With this approach, there needs to be some initial treatment of the printed metal to go from insulator to resistor in order for current flow to cause heating. This method can be contact (DC) or contactless (AC) and can achieve reasonably high conductivity values; however, further work in this area is required. Both microwave and plasma sintering approaches are emerging but have only been demonstrated at small scales to date.

*4.2. Postprint Curing of Dielectrics.* Curing of printed dielectric materials may not be compatible with methods and annealing conditions used to sinter printed metal lines due to the lower glass transition temperatures of the printed dielectric materials. Therefore, multiple steps may be required to obtain optimal dielectric properties in conjunction with high conductivity metal lines for RF structures [77]. Polymeric dielectrics can be cured using several methods. UV irradiation is one of the most common methods. UV curable dielectrics consist of chemical mixtures of oligomers (long molecules), monomers (short molecules), photoinitiators, and other fillers. Upon exposure to UV light, the photoinitiators break apart reacting with the oligomers and monomers to form a thermoset that cannot be returned to a liquid state. Optimization of dielectric curing conditions

TABLE 3: Summary of prior work on metallic nanoparticle conductive inks.

Metal	Particle size (nm)	Solvent	Conc. (wt%)	Curing	Print method	Width ( $\mu\text{m}$ )	Thickness (nm)	$\rho$ ( $\Omega \text{ cm}$ )	Ref
Ag	N/A	$\text{NH}_4\text{OH}$ , formic acid	22	15 min at $90^\circ\text{C}$	DIW	5	—	$1.6 \times 10^{-8}$	[21]
Ag/CNT	—	Alcohol-based	—	30 min at $350^\circ\text{C}$	AJP	13.5	700	$2.8 \times 10^{-6}$	[44]
Ag	5–7	Alpha-terpineol	10	$100\text{--}300^\circ\text{C}$	IJP	80	100	$3 \times 10^{-6}$	[80]
Ag	10–50	Water-DEG	25	$150\text{--}260^\circ\text{C}$	IJP	130	532	$1.6 \times 10^{-5}$	[81]
Ag	1–10	Toluene	30–35	$300^\circ\text{C}$	IJP	120	1000	$3.5 \times 10^{-5}$	[82]
Au	2–4	Toluene	30	$300\text{--}400^\circ\text{C}$ (laser)	IJP	20	50	$1.4 \times 10^{-5}$	[83]
Au	2–4	Toluene	30–35	200–500 mW (laser)	IJP	123	250	$4.5 \times 10^{-6}$	[84]
Au	2–5	Toluene	30	200–1000 mW (laser)	IJP	17	20–200	$1.4 \times 10^{-5}$	[85]
Au	5–20	Toluene	30	$300^\circ\text{C}$	IJP	1000	600	$1 \times 10^{-5}$	[86]

such as power, wavelength, temperature, and time is essential to minimize the occurrence of pinholes in the post cured dielectric materials. In addition to pinholes, contaminants must be eliminated as they will also affect the film quality and electrical/mechanical integrity.

Roughness of printed dielectric materials after curing can be the order of several micrometers, which is much greater than the typical printed metal lines thickness of a micron per layer. Printed dielectric substrates with roughness of several microns will attenuate the RF signal to degrade circuit performance. One approach to reduce roughness of printed dielectric substrates is to follow with printing a more conformal dielectric material, which spreads over the rough substrate surface before UV cure. After UV curing, the conformal dielectric material substrate surface roughness can be reduced to a few submicron RMS roughness [78].

**4.3. Materials for DC and RF: Structure-Property Relationships.** The baseline metal deposition focuses on electrical and structural properties. While the electrical resistivity is an important operational parameter, it is the microstructural features of the lines that determine the resistivity. The electrical resistivity of a metal line is determined by measuring the resistance [79]. The resistivity then can be calculated if the cross-sectional area of the line and length of the line is known. The resistivity is expressed in 3 for 3D and 4 for 2D below.

$$\rho = R * \frac{A}{l}, \quad (3)$$

$$\rho = R_{\text{sq}} * h, \quad (4)$$

where  $A$  is the cross-sectional area of the sample,  $l$  is the length of the structure, and  $h$  is the height of the stripline. For AJP- or IJP-deposited metal lines, the lines are highly resistive after deposition. The AJP deposit consists of nano-sized particles. After annealing, the NPs agglomerate into larger grains and become more conductive after postdeposition annealing. Table 3 summarizes measured resistivity values for Ag and Au NPs with varying particle sizes, solvents, concentrations, and curing conditions. Upon annealing, the deposited thin film resistivity values remain a factor

of 2x–10x greater than the bulk values, showing that a better understanding of the annealing process is necessary.

For metal lines, the cross-sectional area is determined by two key factors. First, the spray deposition process does not typically produce a circular or rectangular cross section. Instead, the cross section depends on deposition parameters [31]. Second, the deposited metal lines are not fully dense. The agglomeration of the metal NPs after deposition and annealing determines the final density. Focused ion beam (FIB) techniques can be used to determine that the actual cross section is the porosity of the deposited metal lines. Determining the cross-sectional area using FIB of the irregular shape provides a more accurate determination of the resistivity. However, this difference does not account for the 2x or greater difference is the deposited line resistivity and bulk resistivity.

A second important issue relates to the porosity and microstructure of the metal line. Figure 5 shows SEM images of Ag-printed lines after different annealing temperatures from  $70$  to  $260^\circ\text{C}$  [81]. Several features stand out in the SEM images in Figure 5(a). The dark regions represent pores, confirming that the layers are not fully dense after the  $70^\circ\text{C}$ -curing condition. The small, spherical particles are those originally deposited in the AJP process and are on the order of  $10\text{--}50 \text{ nm}$ . NP coalescence and grain formation occurs at the  $150^\circ\text{C}$ -annealing conditions (Figure 5(b)). Observations of grains on the order of  $0.2\text{--}0.4 \mu\text{m}$  can be seen in Figures 5(c) and 5(d) at  $200^\circ\text{C}$ - and  $260^\circ\text{C}$ -annealing temperatures. These are the results of the fusion of many of the original  $10\text{--}50 \text{ nm}$  particles. Cross sections of the microstructure taken at different curing conditions are the key to understanding the sintering process of the metal (and other NP-deposited materials). As seen in Figure 5, higher annealing temperatures after deposition would be expected to produce larger grains and consume the remainder of the small NPs into the larger grains.

Work by Werner et al. investigated microstructural changes in AJP Ag lines upon annealing temperatures of  $150$  and  $250^\circ\text{C}$  and times for  $30\text{--}120$  minutes [37]. As seen in Figure 6,  $150^\circ\text{C}$ -annealing temperature did not lead to significant changes in the microstructure structure, even for extended annealing times up to  $120 \text{ min}$  (Figures 6(a)–6(c)). The  $50 \text{ nm}$  Ag NPs are still visible and are in contact, and

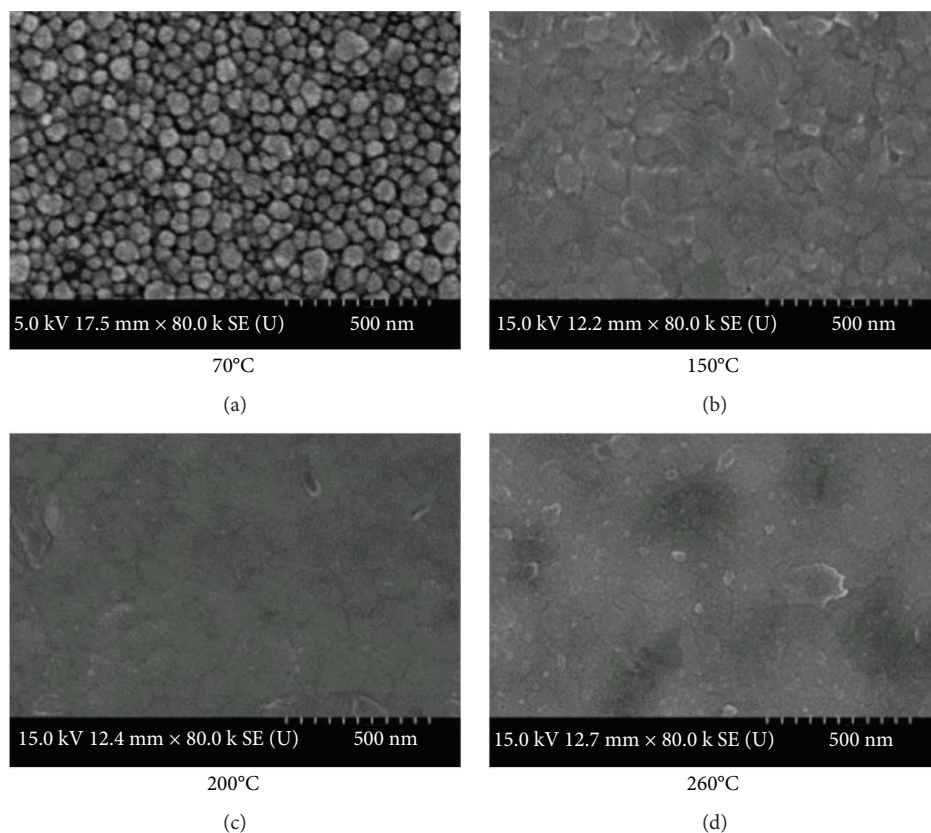


FIGURE 5: SEM images of IJP-printed Ag lines after different curing temperatures. Reproduced with permission [81].

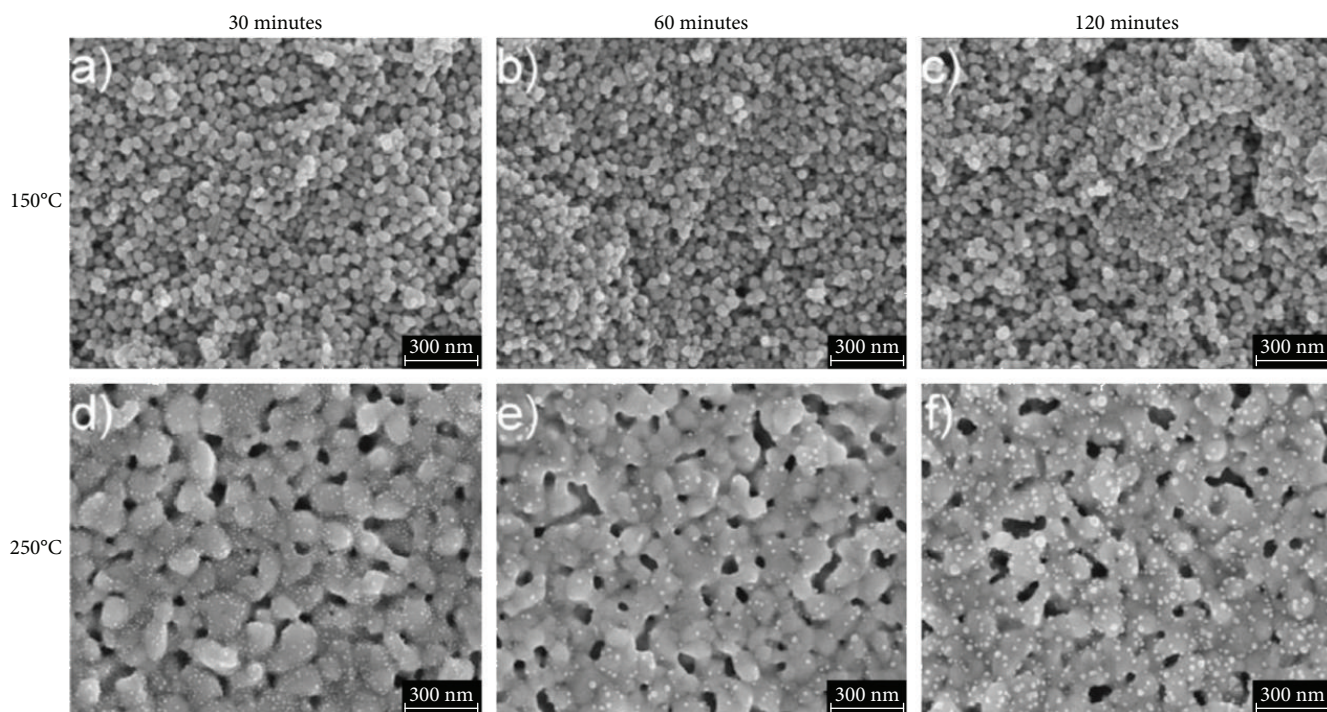


FIGURE 6: SEM images of AJP printed Ag lines taken at different temperature and time sintering conditions. Reproduced with permission [37].

sintering neck formation between these particles is only partially observable after 60 and 120 min. However, as sintering temperature is increased to 250°C, they observe coalescence

of the particles for 30 min-annealing times (Figure 6(d)). With the coalescence occurring at 250°C, there is no observation of 50 nm Ag NPs. 250°C-annealing temperatures allow for NPs

TABLE 4: Thin film microstructure analysis.

Characterization methods	AFM	XRD	Optical profilometer	SEM & TEM	Nanoindentation
Figures of merit	Surface roughness, line shape	Lattice parameter, crystal structure, phase analysis, residual stress, preferred orientation	Line shape, line widths, line thickness	Grain size, grain orientation, crystal defects, voids	Hardness, fracture toughness

TABLE 5: Thin film electrical characterization.

Characterization methods	DC van der Pauw	RF through line
Figures of merit	Sheet resistance, conductivity	Impedance, RF loss tangent, dielectric constant, permeability

to neck and form grain boundaries (Figures 6(e) and 6(f)). Pores in the sintered Ag films can be observed with each of the annealing conditions. The authors noted that small spherical structures containing both Si and O are observed on the Ag surfaces sintered at 250°C. It was mentioned that the probable cause for the Si and O was from thermal decomposition of silanes in the ink.

Studies by Rahman et al. correlated microstructural-electrical properties of AJP Ag NP thin films at high temperatures [87]. They determined that optimization of sintering conditions could provide efficient means to control the temperature stability and oxidation resistance of the Ag NP thin films up to a temperature of 500°C.

**4.4. Characterization Methods and Figures of Merit.** Studies to date have leveraged a limited set of characterization methods to correlate printed thin film electrical performance with microstructure [72, 74, 87–89]. A more comprehensive set of characterization methods shown in Tables 4 and 5 must be employed to establish a better understanding of the kinetics and growth mechanisms during sintering to achieve thin film conductivities near-bulk values for AM-printed metal film lines.

Optical profilometry and atomic force microscopy (AFM) are essential characterization methods to provide valuable insights on the printed metal line shape, width, thickness, and dielectric substrate surface roughness as discussed in Sections 3.2 and 3.3 to further optimize printed electronic circuit RF performance. X-ray diffraction (XRD) can be leveraged for nondestructive quick turnaround analysis of the printed thin film metal lattice parameter, crystal structure, phase analysis, texturing, and evidence of residual stress in the thin film [90]. XRD analysis can be used to tune and guide annealing conditions in a design of experiments to better understand microstructure evolution during the various stages of thin film sintering as outlined in Section 4.1. SEM measurements combined with transmission electron microscopy (TEM) for higher-resolution analysis of the printed metal thin film enable more critical insights on the stages of NP ink necking, grain growth kinetics, and microstructure evolution during the sintering. SEM and TEM will also provide more insights on the metal defects, voiding, and overall assessment of printed metal film density as these parameters will be important in achieving near-bulk conductivity values. Nanoindentation provides an assessment of

printed film microhardness and fracture toughness properties as these parameters will be important to understand the overall mechanical integrity of the printed thin films for various RF circuit applications.

Table 5 summarizes electrical characterization methods and test structures for printed dielectric substrates and metal thin films. DC van der Pauw measurements can be used to study the printed metal sheet resistance and conductivity as samples are annealed at different conditions. Stripline and microstrip RF test structures can be used, preferably after obtain desired conductivities, to further analyze the impedance, loss tangents, permeability, and dielectric constant of the printed substrate and metal line structures.

Integrating the information obtained from microstructural analysis with electrical characterization of printed substrates and metal thin films provides a more complete study to further drive experiments and process optimization to fully realize the potential of printed electronic circuit performance at the desired frequencies.

## 5. Demonstrations of Printed RF Passive and Active Components

There have been a number of printed RF components produced to date using different techniques, as indicated in Figure 7; however, the most common AM method is FDM and the most common DW method is IJP. While active RF components such as transistors, tunnel diodes, integrated circuits, and thyristors are beginning to be demonstrated via printing methods, these printed actives are still in their infancy as far as realization for high performance RF demonstrations. Indeed, printed semiconducting films only display carrier mobilities of up to a mere  $10 \text{ cm}^2 \text{ V}^{-1} \text{ s}^{-1}$  [97, 98] compared to the  $8500 \text{ cm}^2 \text{ V}^{-1} \text{ s}^{-1}$  of a III-V semiconductor like GaAs. Conversely, RF passives may be printed with good performance compared to their subtractively manufactured counterparts; however, as previously described, control over the electromagnetic properties in the raw materials along with the feature size, resolution, and surface topology requires further innovations. In this section, we will review unique RF structures that have been demonstrated via printing and the different types of passive components that are enablers to the realization of printed RF systems.

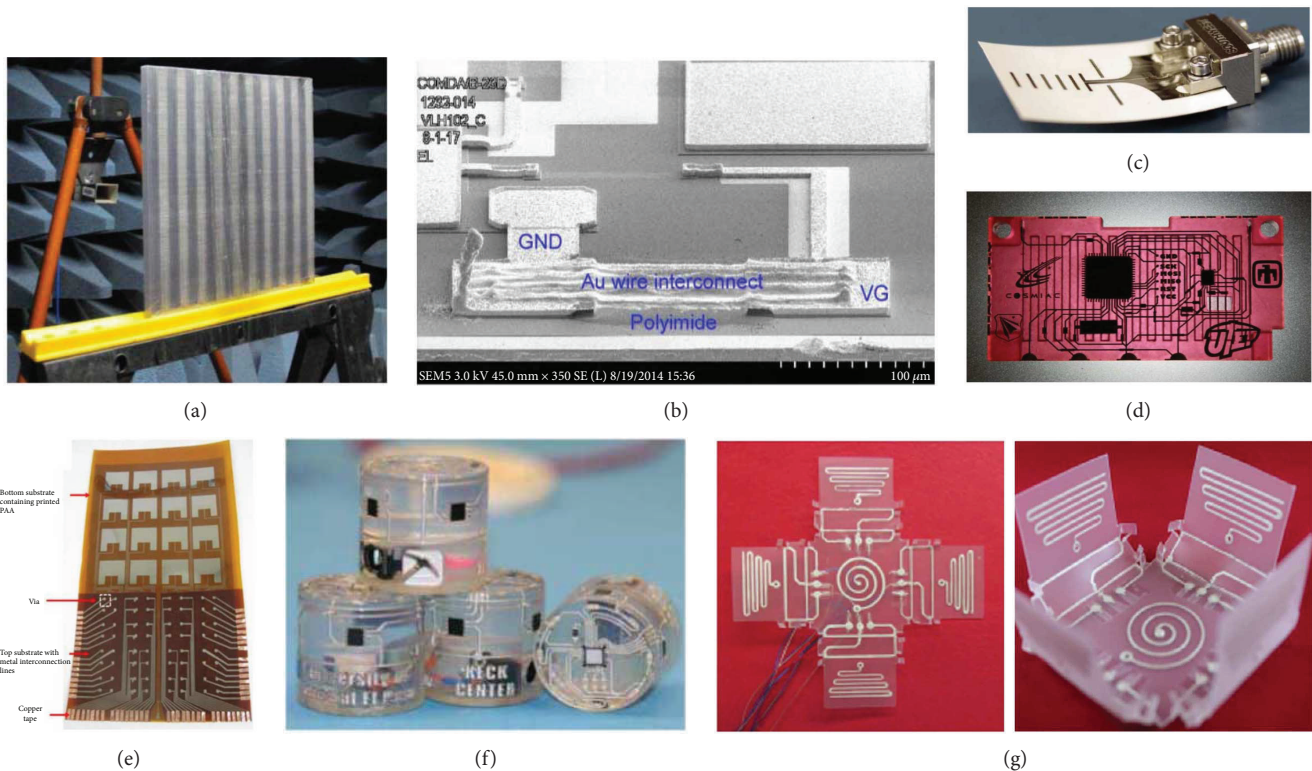


FIGURE 7: Demonstrations of 3D printed RF components. (a) All-dielectric frequency selective surface under C-band testing. Reproduced with permission from [91]. (b) SEM image of postreliability tested printed gold wire interconnect. Reproduced with permission from [13]. (c) IJP-printed mm-wave Yagi-Uda antenna on flexible substrate. Reproduced with permission from [92]. (d) Multifunctional embedded electronics for a cubesat demonstration. Reproduced with permission from [93]. (e) IJP-printed phased array on a flexible substrate. Reproduced with permission from [94]. (f) Hybrid AM and DW demonstration of 3D-embedded structural electronics. Reproduced with permission from [95]. (g) A controllably folded inverted F antenna smart structure. Reproduced with permission from [96].

### 5.1. Printed Metamaterials and Frequency Selective Surfaces.

RF metamaterials are a relatively new arena in electromagnetics that are typically composed of subwavelength unit cells that get their unique properties by a careful design of dielectric or metal-dielectric building blocks which are not exhibited in their bulk counterparts (i.e., negative index of refraction). There have been recent demonstrations of complex printed metamaterials that have been enabled by advancements in printing techniques which would otherwise be impossible to fabricate with conventional techniques [99, 100]. Additionally, frequency selective surfaces are periodic structures with elements that can act as band stops or band passes. These structures can be complicated to design and often require multiple design/fabricate/test loops in order to tune to the desired frequency. The fabrication piece of this cycle has been demonstrated with a printed all-dielectric frequency selective surface, which shows the utility and expediency of these techniques [91].

**5.2. Printed Transmission Lines and Interconnects.** Reports in the recent literature have shown that transmission lines can be fabricated by printing with competitive performance to standard copper lithographic-based processes in impedance,  $\epsilon$ , and  $\tan\delta$  in the microwave regime, which enables flexibility in the design parameter space [64, 95, 101, 102]. Further improvements in these RF parameters will increase the

overall system efficiency, as indicated by the use of AJP, and the transmission lines showed an order of magnitude reduction in insertion losses when compared against IJP.

RF interconnects are abundant, in high density (analogous to the body's nervous system), and can become incredibly complex within RF systems as evidenced by the different types of vias that exist. Interconnect parasitic losses can quickly add up to degrade the overall system performance. Therefore, it is critical to have near-bulk metal conductivity, while maintaining reliable conductivity over temperature and environmental excursions [13, 93, 103, 104]. While there are many different techniques that have been investigated for interconnects in DW processes, the current best performers are AJP and wire mesh embedding. RF waveguides, such as a metal pipe rectangular waveguide, direct the electromagnetic waves in one direction to prevent inverse square law losses. Interestingly, these waveguides have been printed using FDM for use in the microwave regime, and SLA in the mm-wave regime and subsequently Cu plated [105]. By these methods, similar attenuation values and return losses were obtained when compared to traditional manufacturing approaches. Surface roughness scattering tends to dominate the losses, and a chemical polishing step is needed to reduce the roughness below 300 nm RMS. RF filters are necessary to select desired frequency bands and eliminate others similar to the aforementioned

frequency selective surfaces; however, these can also include low-pass or high-pass cutoffs. Using Polyjet printing, a few types of RF filters have been demonstrated with very high performance including return loss and unloaded quality factor [106, 107].

**5.3. Printed Antennas.** There have also been many different types of demonstrations of printed antennas in the recent literature. Liang et al. fabricated a microwave patch antenna with a  $50\ \Omega$  microstrip line on a printed polyethylene substrate 2.4 mm thick ( $\epsilon=2.4$ ) via FDM and ultrasonic wire mesh embedding with a 5.5 dB gain at 7.5 GHz [50]. MSU researchers demonstrated a rectangular patch antenna using a multijet printer loaded with Vero White ( $\epsilon=2.4$ ,  $\tan\delta=0.02$ ) with  $-20\ \text{dB } S_{11}$  reflection coefficient at 5.5 GHz and a simulated 6.94 dB gain [108]. The first demonstration of a fully printed patch antenna at 2.4 GHz also using Vero White with a measured  $\epsilon=3.13$  and a tailored resistivity as a function of Ag layers printed to compensate for losses was shown by Nate et al [109]. Ghazali et al. have demonstrated an ultrawide band (4–18 GHz) Vivaldi notch antennas with a measured 12 dB gain; however, this was fabricated with 3D printed ABS plastic and sputtered Cu metal [110]. Georgia Tech researchers were the first to demonstrate a printed log-periodic Koch-Dipole array antenna that has a much reduced areal footprint owing to its design [111]. An interesting dipole antenna was printed with a carbon nanotube (CNT) ink with a resonance at 2 GHz; however, a  $10\ \Omega/\square$  sheet resistance was required to give a  $-10\ \text{dB } S_{11}$  [112]. A Yagi-Uda antenna was aerosol jet printed using Ag ( $5.13 \times 10^6\ \text{S/m}$ ) on a printed Vero White Plus ( $\epsilon=2.8$ ,  $\tan\delta=0.04$ ) by He and coworkers which shows a low profile at 24 GHz with a 26.4 dB return loss with a 3.3 dBi [113]. These authors also showed a 14.6 dB return loss at 25.8 GHz. The first demonstration of a Yagi-Uda antenna was done a year earlier using IJP Ag ( $1.1 \times 10^7\ \text{S/m}$ ) and SU-8 dielectric ( $\epsilon=3.2$ ,  $\tan\delta=0.04$ ) on a liquid crystalline polymer laminate substrate that has a high 8 dBi gain at 24.5 GHz with a  $>33\ \text{dB } S_{11}$  [92]. Several horn-type antennas have also been demonstrated with the best performance going to a hybrid printing and plating process [114, 115]. An SLA process based on epoxy was used to generate the structure, and then a Cu-plating step was added. While the return loss was not verified in [114], the authors reported  $>25\ \text{dBi}$  peak directivity at 12 GHz. In [115], a  $2 \times 2$  horn antenna array utilized the design freedom of SLA to minimize insertion losses to 34 dB along the main radiation axis, while demonstrating a 24 dBi directivity from 26 to 40 GHz.

When an area becomes a constraint, researchers have typically turned to printing fractal-based antennas [116, 117]. These fractals also tend to have growing popularity for wireless sensing and communications in commonly used commercial bands and have been demonstrated via AJP Ag with a conductivity of  $1.1 \times 10^7\ \text{S/m}$ . Inverted F antennas that have been aerosol jet printed using Ag have also recently demonstrated by several groups [96, 118]. Deng et al. have shown that by tailoring the Ag ink trace resistivity and using electrical bias as external stimuli that self-folding inverted F antennas can be generating, which

can be discretely delivered and subsequently deployed based on the usage requirements; however, no antenna measurements were taken. Harle et al. demonstrated return losses of 17.8 and 20.4 dB and gain of 2 dBi and 0 dBi at 36.5 and 74.5 GHz, respectively.

Printed, flexible, and conformal-phased array antennas have also emerged, which are becoming increasingly popular for radar communications [94, 119, 120]. These antennas utilize printed CNT thin film transistors and multilayer interconnects to generate a fully packaged system that allows nonmechanical beam steering with an 8.2 dB insertion loss and 11.2 mW power consumption operating at 5 GHz. Finally, Adams et al. have shown that concepts generated in planar structures can also be considered in full 3D by utilizing DIW techniques to print an electrically small antenna on a hemispherical dielectric, which shows much potential and promise for designing in 3D for future antenna systems [16].

## 6. Opportunities and Conclusion

There is much to look forward to within the arena of printed RF components and their realization as the community moves from rapid prototyping towards manufacturing. Additionally, there are a number of fascinating new fully 3D RF component concepts in the recent literature that can only be fabricated using AM techniques [121–124]. These RF components in full 3D outperform their planar counterparts and give an extra degree of freedom for designing new structures that additionally have function or could potentially be embedded into structures. Hester et al. have demonstrated that by cleverly designing in the 3rd dimension, a 43 dB increase in maximum rejection of the  $S$ -parameters can occur over a much broader range (5–14 GHz) than its planar counterpart.

There is a need to establish an upper bound on what can reproducibly be achieved for environmentally robust DW metals, but first, a baseline understanding of the process-structure-property relationship must be achieved. This will become more evident as fully 3D printed RF systems are necessary, which require near-bulk printed metal conductivity on printed dielectrics. A systematic experimental approach is necessary, in which the conductivity of the prints is compared against their morphology, aspect ratio, and processing conditions. Since these structures differ from their bulk counterparts in terms of porosity and grain size, it will be necessary to determine the maximum possible conductivity for different printed metal inks and subsequently work towards achieving such a threshold. Understanding these material effects will allow for dramatically improved material engineering.

For dielectrics, there is a large window of process space to take advantage of the low loss ( $<0.005$ ) and permittivity ( $<2.5$  or  $>10$ ) regime. Short-chain polymers are an exciting class of materials due to their small dielectric constant. Tuning their permittivity with small, low-loss additives may be a means to decrease the overall loss of the final RF component. The crucial step here is to ensure that these polymer composites are indeed printable.

Here, we have focused on the main RF building blocks including metals and dielectrics. If DW is to impact RF circuits, then switches will need to be developed, such as MEMS or phase change materials that can act as reconfigurable electronics for phased array applications [125, 126]. Moreover, some new works are coming out on printed magnetic materials that could be viable for use as inductors or circulators that will enable further miniaturization of printed microelectronics since these have been difficult to fabricate with traditional thin film growth techniques with high permeability ( $\mu$ ) over high frequencies [127]. Additionally, there have been some good advancements in printed barium strontium titanate (BST) for tunable capacitors; however, their turn on voltages is currently considerably high [128, 129]. The tunability offers another degree of freedom for design and operation; however, a drastic reduction in voltage will be necessary for realization in many applications.

Looking ahead even further for realization, we anticipate that smart structures, or 3D printed structures that can be actuated via an external mechanism over time, will become increasingly important in applications where compaction is critical. These printed smart components have small form factor for storage, but during usage or deployment, the structure is able to unfold into a fully functioning and truly 3D product [130]. Some antenna examples using this type of “4D” printing have been demonstrated and show an interesting future path [96]. We also wish to highlight that rapid advancements are needed in the design of experiments necessary to address the challenges we have outlined. Here, machine learning and autonomous experimentation could be integrated into the current research field as they have shown great promise for carbon nanotube synthesis [131]. Ultimately, we envision processes associated with AM to be highly automated during the full-scale production workflow with robotics, especially when needed to go between instruments to print at different scales (nm to cm) and final system assembly. Again, borrowing from the semiconductor manufacturing industry, this would reduce unknown variables and increase speed of production once the challenges in this field have been addressed.

In this review, we have identified the major material’s challenges facing realization of AM and DW for RF antennas and components. We have also suggested how to approach solutions to reduce the loss correlated with current materials and processes pertaining to printing that preclude wide usage in the current state-of-the-art. We also envision that additional inks and resins still need to be developed that have tailorable properties for RF applications, so this is an exciting arena to be in moving forward. The realization of high performance RF antennas and components will take a multi-disciplinary effort moving forward in order to result in demonstrations of conformally printed antennas that could be considered robust and reliable.

## Conflicts of Interest

The authors declare that there is no conflict of interest regarding the publication of this paper.

## References

- [1] M. Vaezi, H. Seitz, and S. Yang, “A review on 3D micro-additive manufacturing technologies,” *International Journal of Advanced Manufacturing Technology*, vol. 67, no. 5-8, pp. 1721–1754, 2013.
- [2] I. Gibson, D. Rosen, and B. Stucker, *Additive Manufacturing Technologies*, 2015.
- [3] T. P. Ketterl, Y. Vega, N. C. Arnal et al., “A 2.45 GHz phased array antenna unit cell fabricated using 3-D multi-layer direct digital manufacturing,” *IEEE Transactions on Microwave Theory and Techniques*, vol. 63, no. 12, pp. 4382–4394, 2015.
- [4] J. R. Tumbleston, D. Shirvanyants, N. Ermoshkin et al., “Continuous liquid interface production of 3D objects,” *Science*, vol. 347, no. 6228, pp. 1349–1352, 2015.
- [5] P. C. Joshi, R. R. Dehoff, C. E. Duty et al., “Direct digital additive manufacturing technologies: path towards hybrid integration,” in *2012 Future of Instrumentation International Workshop (FIW) Proceedings*, pp. 1–4, Gatlinburg, TN, USA, October 2012.
- [6] M. Vaezi, S. Chianrabutra, B. Mellor, and S. Yang, “Multiple material additive manufacturing – part 1: a review,” *Virtual and Physical Prototyping*, vol. 8, no. 1, pp. 19–50, 2013.
- [7] M. Ahmadloo and P. Mousavi, “A novel integrated dielectric-and-conductive ink 3D printing technique for fabrication of microwave devices,” in *2013 IEEE MTT-S International Microwave Symposium Digest (MTT)*, pp. 1–3, Seattle, WA, USA, June 2013.
- [8] J. J. Casanova, J. A. Taylor, and J. Lin, “Design of a 3-D fractal heatsink antenna,” *IEEE Antennas and Wireless Propagation Letters*, vol. 9, pp. 1061–1064, 2010.
- [9] N. Zhou, C. Liu, J. A. Lewis, and D. Ham, “Gigahertz electromagnetic structures via direct ink writing for radio-frequency oscillator and transmitter applications,” *Advanced Materials*, vol. 29, no. 15, article 1605198, 2017.
- [10] P. Deffenbaugh, K. Church, J. Goldfarb, and X. Chen, “Fully 3D printed 2.4 GHz Bluetooth/Wi-Fi antenna,” *International Symposium on Microelectronics*, vol. 1, pp. 914–920, 2013.
- [11] A. G. Kelly, T. Hallam, C. Backes et al., “All-printed thin-film transistors from networks of liquid-exfoliated nanosheets,” *Science*, vol. 356, no. 6333, pp. 69–73, 2017.
- [12] Y. Cao, Y. Che, H. Gui, X. Cao, and C. Zhou, “Radio frequency transistors based on ultra-high purity semiconducting carbon nanotubes with superior extrinsic maximum oscillation frequency,” *Nano Research*, vol. 9, no. 2, pp. 363–371, 2016.
- [13] X. Lan, X. Lu, M. Y. Chen et al., “Direct on-chip 3-D aerosol jet printing with high reliability,” *IEEE Transactions on Components, Packaging and Manufacturing Technology*, vol. 7, no. 8, pp. 1369–1376, 2017.
- [14] R. Bahr, T. Le, M. M. Tentzeris et al., “RF characterization of 3D printed flexible materials-NinjaFlex filaments,” in *2015 European Microwave Conference (EuMC)*, pp. 742–745, Paris, France, September 2015.
- [15] H. Hwang, K. Oh, and H. Kim, “All-photonic drying and sintering process via flash white light combined with deep-UV and near-infrared irradiation for highly conductive copper nano-ink,” *Scientific Reports*, vol. 6, no. 1, article 19696, 2016.
- [16] J. J. Adams, E. B. Duoss, T. F. Malkowski et al., “Conformal printing of electrically small antennas on three-dimensional

- surfaces," *Advanced Materials*, vol. 23, no. 11, pp. 1335–1340, 2011.
- [17] B. I. Wu and I. Ehrenberg, "Ultra conformal patch antenna array on a doubly curved surface," in *2013 IEEE International Symposium on Phased Array Systems and Technology*, pp. 792–798, Waltham, MA, USA, October 2013.
- [18] J. Castro, E. Rojas, A. Ross, T. Weller, and J. Wang, "High-k and low-loss thermoplastic composites for fused deposition modeling and their application to 3D-printed Ku-band antennas," in *2016 IEEE MTT-S International Microwave Symposium (IMS)*, pp. 16–19, San Francisco, CA, USA, May 2016.
- [19] F. Bonaccorso, A. Bartolotta, J. N. Coleman, and C. Backes, "2D-crystal-based functional inks," *Advanced Materials*, vol. 28, no. 29, pp. 6136–6166, 2016.
- [20] M. Haghzadeh and A. Akyurtlu, "All-printed, flexible, reconfigurable frequency selective surfaces," *Journal of Applied Physics*, vol. 120, no. 18, p. 184901, 2016.
- [21] S. B. Walker and J. A. Lewis, "Reactive silver inks for patterning high-conductivity features at mild temperatures," *Journal of the American Chemical Society*, vol. 134, no. 3, pp. 1419–1421, 2012.
- [22] B. T. Anto, S. Sivaramkrishnan, L. L. Chua, and P. K. H. Ho, "Hydrophilic sparse ionic monolayer-protected metal nanoparticles: highly concentrated nano-Au and nano-Ag 'inks' that can be sintered to near-bulk conductivity at 150°C," *Advanced Functional Materials*, vol. 20, no. 2, pp. 296–303, 2010.
- [23] E. B. Secor, B. Y. Ahn, T. Z. Gao, J. A. Lewis, and M. C. Hersam, "Rapid and versatile photonic annealing of graphene inks for flexible printed electronics," *Advanced Materials*, vol. 27, no. 42, pp. 6683–6688, 2015.
- [24] K. Arapov, G. Bex, R. Hendriks et al., "Conductivity enhancement of binder-based graphene inks by photonic annealing and subsequent compression rolling," *Advanced Engineering Materials*, vol. 18, no. 7, pp. 1234–1239, 2016.
- [25] D. A. Roberson, R. B. Wicker, and E. MacDonald, "Ohmic curing of three-dimensional printed silver interconnects for structural electronics," *Journal of Electronic Packaging*, vol. 137, no. 3, article 31004, 2015.
- [26] H. H. Tsang, J. H. Barton, R. C. Rumpf, and C. R. Garcia, "Effects of extreme surface roughness on 3D printed horn antenna," *Electronics Letters*, vol. 49, no. 12, pp. 734–736, 2013.
- [27] F. Medina, A. Lopes, A. Inamdar et al., "Hybrid manufacturing: integrating direct write and stereolithography," *Journal of Electronic Packaging*, vol. 137, no. 3, pp. 129–143, 2005.
- [28] C. Kim, D. Espalin, A. Cuaron et al., "Cooperative tool path planning for wire embedding on additively manufactured curved surfaces using robot kinematics," *Journal of Mechanisms and Robotics*, vol. 7, no. 2, article 21003, 2015.
- [29] E. MacDonald and R. Wicker, "Multiprocess 3D printing for increasing component functionality," *Science*, vol. 353, no. 6307, article aaf2093, 2016.
- [30] R. Salary, J. P. Lombardi, R. K. Prahalad, and M. D. Poliks, "Additive manufacturing (AM) of flexible electronics devices: online monitoring of 3D line topology in aerosol jet printing process using shape-from-shading (SFS) image analysis," in *ASME 2017 12th International Manufacturing Science and Engineering Conference*, pp. 1–11, Los Angeles, CA, USA, 2017.
- [31] T. Seifert, E. Sowade, F. Roscher, M. Wiemer, T. Gessner, and R. R. Baumann, "Additive manufacturing technologies compared: morphology of deposits of silver ink using inkjet and aerosol jet printing," *Industrial and Engineering Chemistry Research*, vol. 54, no. 2, pp. 769–779, 2015.
- [32] J. Vaithilingam, M. Simonelli, E. Saleh et al., "Combined inkjet printing and infrared sintering of silver nanoparticles using a swathe-by-swathe and layer-by-layer approach for 3-dimensional structures," *ACS Applied Materials & Interfaces*, vol. 9, no. 7, pp. 6560–6570, 2017.
- [33] S. H. Ko, "Low temperature thermal engineering of nanoparticle ink for flexible electronics applications," *Semiconductor Science and Technology*, vol. 31, no. 7, article 73003, 2016.
- [34] Z. Zhan, J. An, Y. Wei, V. T. Tran, and H. Du, "Inkjet-printed optoelectronics," *Nanoscale*, vol. 9, no. 3, pp. 965–993, 2017.
- [35] Y. Oh, J. Kim, Y. J. Yoon et al., "Inkjet printing of Al<sub>2</sub>O<sub>3</sub> dots, lines, and films: from uniform dots to uniform films," *Current Applied Physics*, vol. 11, no. 3, Supplement 3, pp. S359–S363, 2011.
- [36] S. Agarwala, G. L. Goh, and W. Y. Yeong, "Optimizing aerosol jet printing process of silver ink for printed electronics," *IOP Conference Series: Materials Science and Engineering*, vol. 191, article 12027, 2017.
- [37] C. Werner, D. Godlinski, V. Zöllmer, and M. Busse, "Morphological influences on the electrical sintering process of aerosol jet and ink jet printed silver microstructures," *Journal of Materials Science: Materials in Electronics*, vol. 24, no. 11, pp. 4367–4377, 2013.
- [38] J. A. Lewis, "Direct ink writing of 3D functional materials," *Advanced Functional Materials*, vol. 16, no. 17, pp. 2193–2204, 2006.
- [39] A. Chiolerio, M. Cotto, P. Pandolfi et al., "Ag nanoparticle-based inkjet printed planar transmission lines for RF and microwave applications: considerations on ink composition, nanoparticle size distribution and sintering time," *Microelectronic Engineering*, vol. 97, pp. 8–15, 2012.
- [40] Optomec Inc., *Aerosol Jet 300 Series Systems*, 2015, [https://www.optomec.com/wp-content/uploads/2014/04/AJ-300-Datasheet\\_Web.pdf](https://www.optomec.com/wp-content/uploads/2014/04/AJ-300-Datasheet_Web.pdf).
- [41] nScript Inc., *Specification Sheet: SmartPump*, 2016, <https://www.nscript.com/wp-content/uploads/2017/02/2016-SmartPump-Gen2.pdf>.
- [42] J. Zhu and M. C. Hersam, "Assembly and electronic applications of colloidal nanomaterials," *Advanced Materials*, vol. 29, no. 4, 2017.
- [43] A. Mahajan, C. D. Frisbie, and L. F. Francis, "Optimization of aerosol jet printing for high-resolution, high-aspect ratio silver lines," *ACS Applied Materials & Interfaces*, vol. 5, no. 11, pp. 4856–4864, 2013.
- [44] D. Zhao, T. Liu, J. G. Park, M. Zhang, J. M. Chen, and B. Wang, "Conductivity enhancement of aerosol-jet printed electronics by using silver nanoparticles ink with carbon nanotubes," *Microelectronic Engineering*, vol. 96, pp. 71–75, 2012.
- [45] J. Griffey, "Chapter 2: the types of 3-D printing," *Library Technology Reports*, vol. 50, no. 5, 2014.
- [46] P. I. Deffenbaugh, R. C. Rumpf, and K. H. Church, "Broad-band microwave frequency characterization of 3-D printed materials," *IEEE Transactions on Components, Packaging and Manufacturing Technology*, vol. 3, no. 12, pp. 2147–2155, 2013.

- [47] P. J. Bartolo, "Stereolithographic processes," in *Stereolithography: Materials, Processes, and Applications*, P. J. Bartolo, Ed., pp. 1–36, Springer, New York, 2011.
- [48] E. G. Geterud, P. Bergmark, and J. Yang, "Lightweight waveguide and antenna components using plating on plastics," in *2013 7th European Conference on Antennas and Propagation (EuCAP)*, pp. 1812–1815, Gothenburg, Sweden, April 2013.
- [49] FormLabs, *3D Printing Technology Comparison: SLA vs. DLP*, 2016, <https://formlabs.com/blog/3d-printing-technology-comparison-sla-dlp/>.
- [50] M. Liang, C. Shemelya, E. MacDonald, R. Wicker, and H. Xin, "3-D printed microwave patch antenna via fused deposition method and ultrasonic wire mesh embedding technique," *IEEE Antennas and Wireless Propagation Letters*, vol. 14, pp. 1346–1349, 2015.
- [51] L. R. Meza, S. Das, and J. R. Greer, "Strong, lightweight, and recoverable three-dimensional ceramic nanolattices," *Science*, vol. 345, no. 6202, pp. 1322–1326, 2014.
- [52] X. Zheng, H. Lee, T. H. Weisgraber et al., "Ultralight, ultrastiff mechanical metamaterials," *Science*, vol. 344, no. 6190, pp. 1373–1377, 2014.
- [53] M. S. Onses, C. Song, L. Williamson et al., "Hierarchical patterns of three-dimensional block-copolymer films formed by electrohydrodynamic jet printing and self-assembly," *Nature Nanotechnology*, vol. 8, no. 9, pp. 667–675, 2013.
- [54] K. Barton, S. Mishra, K. A. Shorter, A. Alleyne, P. Ferreira, and J. Rogers, "A desktop electrohydrodynamic jet printing system," *Mechatronics*, vol. 20, no. 5, pp. 611–616, 2010.
- [55] J. R. Greer and R. A. Street, "Thermal cure effects on electrical performance of nanoparticle silver inks," *Acta Materialia*, vol. 55, no. 18, pp. 6345–6349, 2007.
- [56] P. Buffat and J.-P. Borel, "Size effect on the melting temperature of gold particles," *Physical Review A*, vol. 13, no. 6, pp. 2287–2298, 1976.
- [57] D. Akinwande, "Two-dimensional materials: printing functional atomic layers," *Nature Nanotechnology*, vol. 12, no. 4, pp. 287–288, 2017.
- [58] F. Torrisi, T. Hasan, W. P. Wu et al., "Inkjet-printed graphene electronics," *ACS Nano*, vol. 6, no. 4, pp. 2992–3006, 2012.
- [59] V. Fiore, P. Battiato, S. Abdinia et al., "An integrated 13.56-MHz RFID tag in a printed organic complementary TFT technology on flexible substrate," *IEEE Transactions on Circuits and Systems I: Regular Papers*, vol. 62, no. 6, pp. 1668–1677, 2015.
- [60] C. Casiraghi, "Water-based 2D-crystal inks: from formulation engineering to printed devices," in *2017 75th Annual Device Research Conference (DRC)*, South Bend, IN, USA, June 2017.
- [61] F. Withers, H. Yang, L. Britnell et al., "Heterostructures produced from nanosheet-based inks," *Nano Letters*, vol. 14, no. 7, pp. 3987–3992, 2014.
- [62] C. Gray, A. Roach, S. Rappaport, A. Dineen, and R. Irion, *High Dielectric Constant, Low Loss Additive Manufacturing Materials for RF/Microwave Applications*, IMAPS, New England, 2016.
- [63] D. C. Thompson, O. Tantot, H. Jallageas, G. E. Ponchak, M. M. Tentzeris, and J. Papapolymerou, "Characterization of liquid crystal polymer (LCP) material and transmission lines on LCP substrates from 30 to 110 GHz," *IEEE Transactions on Microwave Theory and Techniques*, vol. 52, no. 4, pp. 1343–1352, 2004.
- [64] P. I. Deffenbaugh, T. M. Weller, and K. H. Church, "Fabrication and microwave characterization of 3-D printed transmission lines," *IEEE Microwave and Wireless Components Letters*, vol. 25, no. 12, pp. 823–825, 2015.
- [65] W. Wu, "Inorganic nanomaterials for printed electronics: a review," *Nanoscale*, vol. 9, no. 22, pp. 7342–7372, 2017.
- [66] S. Das, "Physical aspects of process control in selective laser sintering of metals," *Advanced Engineering Materials*, vol. 5, no. 10, pp. 701–711, 2003.
- [67] H. C. Kim, T. L. Alford, and D. R. Allee, "Thickness dependence on the thermal stability of silver thin films," *Applied Physics Letters*, vol. 81, no. 22, pp. 4287–4289, 2002.
- [68] S. K. Sharma and J. Spitz, "Hillock formation, hole growth and agglomeration in thin silver films," *Thin Solid Films*, vol. 65, no. 3, pp. 339–350, 1980.
- [69] A. L. Dearden, P. J. Smith, D. Y. Shin, N. Reis, B. Derby, and P. O'Brien, "A low curing temperature silver ink for use in ink-jet printing and subsequent production of conductive tracks," *Macromolecular Rapid Communications*, vol. 26, no. 4, pp. 315–318, 2005.
- [70] M. Maiwald, C. Werner, V. Zöllmer, and M. Busse, "INKteligent printing<sup>®</sup> for sensorial applications," *Sensor Review*, vol. 30, no. 1, pp. 19–23, 2010.
- [71] S. K. Volkman, S. Yin, T. Bakhishev, K. Puntambekar, V. Subramanian, and M. F. Toney, "Mechanistic studies on sintering of silver nanoparticles," *Chemistry of Materials*, vol. 23, no. 20, pp. 4634–4640, 2011.
- [72] A. Simchi, "Direct laser sintering of metal powders: mechanism, kinetics and microstructural features," *Materials Science and Engineering A*, vol. 428, no. 1–2, pp. 148–158, 2006.
- [73] M. Li, Y. Xiao, Z. Zhang, and J. Yu, "Bimodal sintered silver nanoparticle paste with ultrahigh thermal conductivity and shear strength for high temperature thermal interface material applications," *ACS Applied Materials & Interfaces*, vol. 7, no. 17, pp. 9157–9168, 2015.
- [74] P. Peng, A. Hu, and Y. Zhou, "Laser sintering of silver nanoparticle thin films: microstructure and optical properties," *Applied Physics A: Materials Science & Processing*, vol. 108, no. 3, pp. 685–691, 2012.
- [75] J. Perelaer, R. Abbel, S. Wünscher, R. Jani, T. Van Lammeren, and U. S. Schubert, "Roll-to-roll compatible sintering of inkjet printed features by photonic and microwave exposure: from non-conductive ink to 40% bulk silver conductivity in less than 15 seconds," *Advanced Materials*, vol. 24, no. 19, pp. 2620–2625, 2012.
- [76] S. Sivaramkrishnan, P.-J. Chia, Y.-C. Yeo, L.-L. Chua, and P. K.-H. Ho, "Controlled insulator-to-metal transformation in printable polymer composites with nanometal clusters," *Nature Materials*, vol. 6, no. 2, pp. 149–155, 2007.
- [77] E. Saleh, P. Woolliams, B. Clarke et al., "3D inkjet-printed UV-curable inks for multi-functional electromagnetic applications," *Additive Manufacturing*, vol. 13, pp. 143–148, 2017.
- [78] G. McKerricher, M. Vaseem, and A. Shamim, "Fully inkjet-printed microwave passive electronics," *Microsystems & Nanoengineering*, vol. 3, p. 16075, 2017.
- [79] C. Wargo, "Characterization of Conductors for Printed Electronics," Technical report, PChem Associates, Bensalem, PA, 2014.

- [80] S. B. Fuller, E. J. Wilhelm, and J. M. Jacobson, "Ink-jet printed nanoparticle microelectromechanical systems," *Journal of Microelectromechanical Systems*, vol. 11, no. 1, pp. 54–60, 2002.
- [81] H.-H. Lee, K.-S. Chou, and K.-C. Huang, "Inkjet printing of nanosized silver colloids," *Nanotechnology*, vol. 16, no. 10, pp. 2436–2441, 2005.
- [82] J. B. Szczech, C. M. Megaridis, D. R. Gamota, and J. Zhang, "Fine-line conductor manufacturing using drop-on-demand PZT printing technology," *IEEE Transactions on Electronics Packaging Manufacturing*, vol. 25, no. 1, pp. 26–33, 2002.
- [83] N. R. Bieri, J. Chung, S. E. Haferl, D. Poulikakos, and C. P. Grigoropoulos, "Microstructuring by printing and laser curing of nanoparticle solutions microstructuring by printing and laser curing of nanoparticle solutions," *Applied Physics Letters*, vol. 82, no. 20, pp. 3529–3531, 2003.
- [84] J. Chung, S. Ko, N. R. Bieri et al., "Conductor microstructures by laser curing of printed gold nanoparticle ink," *Applied Physics Letters*, vol. 84, no. 5, pp. 801–803, 2004.
- [85] N. R. Bieri, J. Chung, D. Poulikakos, and C. P. Grigoropoulos, "Manufacturing of nanoscale thickness gold lines by laser curing of a discretely deposited nanoparticle suspension," *Superlattices and Microstructures*, vol. 35, no. 3-6, pp. 437–444, 2004.
- [86] J. Szczech, C. Megaridis, J. Zhang, and D. Gamota, "Ink jet processing of metallic nanoparticle suspensions for electronic circuitry fabrication," *Microscale Thermophysical Engineering*, vol. 8, no. 4, pp. 327–339, 2004.
- [87] M. T. Rahman, J. McCloy, C. V. Ramana, and R. Panat, "Structure, electrical characteristics, and high-temperature stability of aerosol jet printed silver nanoparticle films," *Journal of Applied Physics*, vol. 120, no. 7, p. 075305, 2016.
- [88] D. J. Lee and J. H. Oh, "Inkjet printing of conductive Ag lines and their electrical and mechanical characterization," *Thin Solid Films*, vol. 518, no. 22, pp. 6352–6356, 2010.
- [89] M. A. H. Khondoker, S. C. Mun, and J. Kim, "Synthesis and characterization of conductive silver ink for electrode printing on cellulose film," *Applied Physics A: Materials Science & Processing*, vol. 112, no. 2, pp. 411–418, 2013.
- [90] B. D. Cullity and S. R. Stock, *Elements of X-Ray Diffraction*, Prentice Hall, New Jersey, USA, 3rd edition, 2001.
- [91] J. H. Barton, C. R. Garcia, E. A. Berry, R. Salas, and R. C. Rumpf, "3-D printed all-dielectric frequency selective surface with large bandwidth and field of view," *IEEE Transactions on Antennas and Propagation*, vol. 63, no. 3, pp. 1032–1039, 2015.
- [92] B. K. Tehrani, B. S. Cook, and M. M. Tentzeris, "Inkjet printing of multilayer millimeter-wave Yagi-Uda antennas on flexible substrates," *IEEE Antennas and Wireless Propagation Letters*, vol. 15, pp. 143–146, 2016.
- [93] D. Espalin, D. W. Muse, E. Macdonald, and R. B. Wicker, "3D printing multifunctionality: structures with electronics," *International Journal of Advanced Manufacturing Technology*, vol. 72, no. 5-8, pp. 963–978, 2014.
- [94] H. Subbaraman, D. T. Pham, X. Xu et al., "Inkjet-printed two-dimensional phased-array antenna on a flexible substrate," *IEEE Antennas and Wireless Propagation Letters*, vol. 12, pp. 170–173, 2013.
- [95] A. J. Lopes, E. Macdonald, and R. B. Wicker, "Integrating stereolithography and direct print technologies for 3D structural electronics fabrication," *Rapid Prototyping Journal*, vol. 18, no. 2, pp. 129–143, 2012.
- [96] D. Deng, Y. Yang, Y. Chen, X. Lan, and J. Tice, "Accurately controlled sequential self-folding structures by polystyrene film," *Smart Materials and Structures*, vol. 26, no. 8, article 85040, 2017.
- [97] J. Li, Y. Zhao, H. S. Tan et al., "A stable solution-processed polymer semiconductor with record high-mobility for printed transistors," *Scientific Reports*, vol. 2, pp. 1–9, 2012.
- [98] P. H. Lau, K. Takei, C. Wang et al., "Fully printed, high performance carbon nanotube thin-film transistors on flexible substrates," *Nano Letters*, vol. 13, no. 8, pp. 3864–3869, 2013.
- [99] M. W. Elsallal, J. Hood, I. Mcmichael, and T. Busbee, "3D printed material characterization for complex phased arrays and metamaterials," *Microwave Journal*, vol. 59, no. 10, pp. 20–34, 2016.
- [100] C. R. Garcia, J. Correa, D. Espalin et al., "3D printing of anisotropic metamaterials," *Progress in Electromagnetics Research Letters*, vol. 34, pp. 75–82, 2012.
- [101] F. Cai, Y. H. Chang, K. Wang, W. T. Khan, S. Pavlidis, and J. Papapolymerou, "High resolution aerosol jet printing of D-band printed transmission lines on flexible LCP substrate," in *2014 IEEE MTT-S International Microwave Symposium (IMS2014)*, Tampa, FL, USA, June 2014.
- [102] M. Liang, X. Yu, C. Shemelya, E. Macdonald, and H. Xin, "3D printed multilayer microstrip line structure with vertical transition toward integrated systems," *IEEE Antennas and Wireless Propagation Letters*, vol. 14, pp. 1346–1349, 2015.
- [103] F. Cai, S. Pavlidis, J. Papapolymerou et al., "Aerosol jet printing for 3-D multilayer passive microwave circuitry," in *2014 44th European Microwave Conference*, pp. 512–515, Rome, Italy, October 2014.
- [104] B. Y. Ahn, E. B. Duoss, M. J. Motala et al., "Omnidirectional printing of flexible, stretchable, and spanning silver microelectrodes," *Science*, vol. 323, no. 5921, pp. 1590–1593, 2009.
- [105] M. D'Auria, W. J. Otter, J. Hazell et al., "3-D printed metal-pipe rectangular waveguides," *IEEE Transactions on Components, Packaging and Manufacturing Technology*, vol. 5, no. 9, pp. 1339–1349, 2015.
- [106] F. Cai, W. T. Khan, and J. Papapolymerou, "A low loss X-band filter using 3-D polyjet technology," in *2015 IEEE MTT-S International Microwave Symposium*, Phoenix, AZ, USA, May 2015.
- [107] L. Hernandez, Y. He, A. Kaur, J. Papapolymerou, and P. Chahal, "Low-loss RF filter through a combination of additive manufacturing and thin-film process," in *2017 IEEE Radio and Wireless Symposium (RWS)*, pp. 114–116, Phoenix, AZ, USA, January 2017.
- [108] M. Ghazali, E. Gutierrez, J. C. Myers, A. Kaur, B. Wright, and P. Chahal, "Affordable 3D printed microwave antennas," in *2015 IEEE 65th Electronic Components and Technology Conference (ECTC)*, pp. 240–246, San Diego, CA, USA, May 2015.
- [109] K. A. Nate, J. Hester, M. Isakov, R. Bahr, and M. M. Tentzeris, "A fully printed multilayer aperture-coupled patch antenna using hybrid 3D/inkjet additive manufacturing technique," in *2015 European Microwave Conference (EuMC)*, pp. 610–613, Paris, France, September 2015.
- [110] M. Ghazali, K. Y. Park, J. A. Byford, J. Papapolymerou, and P. Chahal, "3D printed metalized-polymer UWB high-gain

- Vivaldi antennas,” in *2016 IEEE MTT-S International Microwave Symposium (IMS)*, San Francisco, CA, USA, May 2016.
- [111] D. E. Anagnostou, J. Papapolymerou, M. M. Tentzeris, and C. G. Christodoulou, “A printed log-periodic Koch-dipole array (LPKDA),” *IEEE Antennas and Wireless Propagation Letters*, vol. 7, pp. 456–460, 2008.
- [112] I. Puchades, J. E. Rossi, C. D. Cress, E. Naglich, and B. J. Landi, “Carbon nanotube thin-film antennas,” *Applied Materials & Interfaces*, vol. 8, no. 32, pp. 20986–20992, 2016.
- [113] Y. He, C. Oakley, P. Chahal, J. Albrecht, and J. Papapolymerou, “Aerosol jet printed 24 GHz end-fire quasi-Yagi-Uda antenna on a 3-D printed cavity substrate,” in *2017 International Workshop on Antenna Technology: Small Antennas, Innovative Structures, and Applications (iWAT)*, Athens, Greece, March 2017.
- [114] M. Van Der Vorst and J. Gumpinger, “Applicability of 3D printing techniques for compact Ku-band medium/high-gain antennas,” in *2016 10th European Conference on Antennas and Propagation (EuCAP)*, Davos, Switzerland, April 2016.
- [115] A. I. Dimitriadis, M. Favre, M. Billod, J. Ansermet, and E. De Rijk, “Design and fabrication of a lightweight additive-manufactured Ka-band horn antenna array,” in *2016 10th European Conference on Antennas and Propagation (EuCAP)*, Davos, Switzerland, April 2016.
- [116] B. S. Cook and A. Shamim, “An inkjet-printed UWB antenna on paper substrate utilizing a novel fractal matching network,” in *Proceedings of the 2012 IEEE International Symposium on Antennas and Propagation*, Chicago, IL, USA, July 2012.
- [117] A. R. Maza, B. S. Cook, G. Jabbar, and A. Shamim, “Paper-based inkjet-printed ultra-wideband fractal antennas,” *IET Microwaves, Antennas & Propagation*, vol. 6, no. 12, pp. 1366–1373, 2012.
- [118] L. Harle, C. Oakley, and J. Papapolymerou, “3D-printed dual band planar inverted F antenna,” in *2016 IEEE International Symposium on Antennas and Propagation (APSURSI)*, pp. 817–818, Fajardo, Puerto Rico, July 2016.
- [119] M. Y. Chen, X. Lu, H. Subbaraman, and R. T. Chen, “Fully printed phased-array antenna for space communications,” *Proceeding of SPIE*, vol. 7318, article 731814, 2017.
- [120] M. Y. Chen, D. Pham, H. Subbaraman, X. Lu, and R. T. Chen, “Conformal ink-jet printed C-band phased-array antenna incorporating carbon nanotube field-effect transistor based reconfigurable true-time delay lines,” *IEEE Transactions on Microwave Theory and Techniques*, vol. 60, no. 1, pp. 179–184, 2012.
- [121] J. Hester, E. Nguyen, J. Tice, and V. Radisic, “A novel 3D printing enabled ‘roller coaster’ transmission line,” in *2017 IEEE International Symposium on Antennas and Propagation & USNC/URSI National Radio Science Meeting*, San Diego, CA, USA, July 2017.
- [122] Y. Xie, S. Ye, C. Reyes et al., “Microwave metamaterials made by fused deposition 3D printing of a highly conductive copper-based filament,” *Applied Physics Letters*, vol. 110, article 181903, 2017.
- [123] I. M. Ehrenberg, S. E. Sarma, and B. Wu, “A three-dimensional self-supporting low loss microwave lens with a negative refractive index,” *Journal of Applied Physics*, vol. 112, no. 7, article 73114, 2012.
- [124] J. W. Allen and B. Wu, “Design and fabrication of an RF GRIN lens using 3D printing technology,” *Proceedings of SPIE*, vol. 8624, article 86240V, 2017.
- [125] N. El-hinnawy, P. Borodulin, E. B. Jones et al., “Improvements in GeTe-based inline phase-change switch technology for RF switching applications,” in *CS MANTECH Conference*, pp. 401–404, Denver, CO, USA, May 2014.
- [126] L. Chau, J. G. Ho, X. Lan, G. Altwater, R. M. Young, and N. El-hinnawy, “Optically controlled GeTe phase change switch and its applications in reconfigurable antenna arrays,” *Proceeding of SPIE*, vol. 9479, article 947905, 2017.
- [127] F. A. Ghaffar, M. Vaseem, M. F. Farooqui, and A. Shamim, “A ferrite nano-particles based fully printed process for tunable microwave components,” in *2016 IEEE MTT-S International Microwave Symposium (IMS)*, pp. 4–6, San Francisco, CA, USA, May 2016.
- [128] M. Haghzadeh, C. Armiento, and A. Akyurtlu, “Fully printed varactors and phase shifters based on a BST/polymer ink for tunable microwave applications,” in *2016 IEEE MTT-S International Microwave Symposium (IMS)*, San Francisco, CA, USA, 2016.
- [129] A. Friederich, C. Kohler, M. Nikfalazar et al., “Microstructure and microwave properties of inkjet printed barium strontium titanate thick-films for tunable microwave devices,” *Journal of the European Ceramic Society*, vol. 34, no. 12, pp. 2925–2932, 2014.
- [130] Z. X. Khoo, J. Ee, M. Teoh, Y. Liu, and C. K. Chua, “3D printing of smart materials: a review on recent progresses in 4D printing,” *Virtual and Physical Prototyping*, vol. 10, no. 3, pp. 103–122, 2015.
- [131] P. Nikolaev, D. Hooper, F. Webber et al., “Autonomy in materials research: a case study in carbon nanotube growth,” *npj Computational Materials*, vol. 2, no. 1, article 16031, 2016.

## Research Article

# Design, Fabrication, and Testing of Active Skin Antenna with 3D Printing Array Framework

Jinzu Zhou,<sup>1,2</sup> Haitao Li,<sup>1</sup> Le Kang,<sup>3</sup> Baofu Tang,<sup>4</sup> Jin Huang,<sup>1</sup> and Zhiheng Cai<sup>1</sup>

<sup>1</sup>Key Laboratory of Electronic Equipment Structure Design, Ministry of Education, Xidian University, Xi'an 710071, China

<sup>2</sup>State Key Laboratory of Structural Analysis for Industrial Equipment, Dalian University of Technology, Dalian 116024, China

<sup>3</sup>National Key Laboratory of Antennas and Microwave Technology, Xidian University, Xi'an 710071, China

<sup>4</sup>Nanjing Research Institute of Electronic Technology, Nanjing 210039, China

Correspondence should be addressed to Jinzu Zhou; [xidian\\_jzzhou@126.com](mailto:xidian_jzzhou@126.com)

Received 25 August 2017; Accepted 17 October 2017; Published 23 November 2017

Academic Editor: Maggie Y. Chen

Copyright © 2017 Jinzu Zhou et al. This is an open access article distributed under the Creative Commons Attribution License, which permits unrestricted use, distribution, and reproduction in any medium, provided the original work is properly cited.

An active skin antenna with structural load-bearing and electromagnetic functions is usually installed in the structural surface of mobile vehicles such as aircrafts, warships, and high-speed train. This paper presents the design, fabrication, and testing of a novel active skin antenna which consists of an encapsulation shell, antenna skin, and RF and beam control circuits. The antenna skin which consists of the facesheet, honeycomb, array framework, and microstrip antenna elements was designed by using Bayesian optimization, in order to improve the design efficiency. An active skin antenna prototype with 32 microstrip antenna elements was fabricated by using a hybrid manufacturing method. In this method, 3D printing technology was applied to fabricate the array framework, and the different layers were bonded to form the final antenna skin by using traditional composite process. Some experimental testing was conducted, and the testing results validate the feasibility the proposed antenna skin structure. The proposed design and fabrication technique is suitable for the development of conformal load-bearing antenna or smart skin antenna installed in the structural surface of aircraft, warships, and armored vehicles.

## 1. Introduction

Over the last decade, structural, material, and antenna designers have collaborated to integrate the microstrip antennas (or planar spiral antennas) and microwave circuits into the structural surfaces of the aircraft, warship, and armored vehicles. This multidisciplinary effort has developed a new high payoff technique known as the skin antenna [1–3]. The skin antenna provides a new paradigm where the structural surface becomes an antenna, and it is not only a microwave device receiving or sending electromagnetic waves but also a load-bearing structure [2]. Compared with the antennas mounted on the structural surface, the skin antenna could have several advantages such as reducing the weight and improving the structural efficiency and the electromagnetic performance, and it will play increasingly a key role in future radar and wireless communications of mobile vehicles such as aircraft, high-speed train, car, and ship.

Many researchers have dedicated to the investigation of the skin antenna and proposed different concepts such as a conformal load-bearing antenna [4–6], structurally integrated antenna [7, 8], structurally embedded vascular antenna [9, 10], three-dimensionally integrated microstrip antenna [11–14], and composite antenna [15–17]. Almost all the investigations have been dedicated to the design and fabrication of the passive skin antenna. The basic structure of the passive skin antenna is a sandwich construction consisting of facesheets, honeycomb core, microstrip or spiral antenna elements, and feeding networks. The antenna elements and feeding networks are inserted into the facesheets and honeycomb, and the epoxy adhesive is applied to bond the different components. However, in practice, the active skin antenna is usually required for radar and wireless communication applications. Different from the passive skin antennas, the active skin antenna has a steerable beam pointing capability, and its structure is more complicated. Generally, the low temperature co-fired ceramics (LTCC)

and printing circuit board (PCB) are utilized to fabricate the active skin antenna. For example, in [3], LTCC was applied to fabricate the RF layer (containing antenna elements, feeding networks, low-noise amplifiers, phase shifters, and power amplifiers) of the active skin antenna. In [2], the substrate Rogers 5880 was applied to fabricate the antenna array embedded in the skin structure. However, for a large skin antenna, it is costly and different to fabricate the antenna array using the LTCC and PCB. In addition, the conventional fabrication of the skin antenna is the lack of the flexible use and reuse of the antenna elements, due to the fixedness of the antenna elements in the antenna array.

In recent years, 3D printing (also called additive manufacturing) was applied to fabricate the antenna and microwave devices [18]. Compared to conventional manufacturing techniques, 3D printing offers several advantages, including the capability of a more flexible design, less prototyping time, cost reduction, much less human interaction, and a faster product development cycle [19]. 3D printing technology has been investigated to realize advanced wireless devices, such as antennas, from GHz to THz frequency range. Antennas with different structures such as horn antennas [20], patch antennas [21], conformal antennas [22], gradient index lens antennas [23], and reflect array antennas [24] have been realized using 3D printing techniques. The 3D printed passive circuits and components for higher frequencies have also been demonstrated. In [25], dielectric ridge waveguides, a photonic crystal filter, and a power splitter were all printed on a commercially available 3D printer. Almost all the investigations above have been dedicated to the design and fabrication of the 3D printed passive antenna and microwave devices. As for the active antenna array, Chen and her teams have firstly demonstrated an inkjet-printed flexible phased-array antenna without any lithography process [26–28]. Passive and active components, such as microstrip transmission lines, phase shifters, and RF power distribution networks, are all developed adopting a room temperature 3D printing process. The electronics, such as switch and amplifiers, are printed with ultrapure CNT solution. Their proposed design and fabrication technology show great advantages for developing the smart skin antenna, electronic paper, epidermal electron, and so on.

In this paper, 3D printing techniques were applied to fabricate the array framework into which microstrip antenna elements were embedded for radiating electromagnetic waves. Subsequently, composite process was applied to bond the array framework, the facesheet, honeycomb, and the antenna elements to form the final antenna skin which can provide the structural load-bearing and electromagnetic receiving sending functions simultaneously. The motivation of this investigation is to provide the design and fabrication technology of a new active skin antenna structure for wireless communications of mobile vehicles such as aircraft, high-speed train, car, and ship. Compared with the active skin antenna in [2, 3], the proposed antenna has the following advantages such as low cost, easy maintenance, and flexible use and reuse of antenna elements. In addition, the

active skin antenna prototype with 32 microstrip antenna elements was fabricated by using a hybrid manufacturing method. In this method, 3D printing technology was applied to fabricate the array framework, which can simplify the manufacturing process and reduce the cost of the antenna skin, especially for the complex conformal array framework. Subsequently, the different layers were bonded to form the final antenna skin by using traditional composite process.

This paper presents the design, fabrication, and testing of a new active skin antenna with 3D printing array framework. This proposed antenna consists of an encapsulation shell, an antenna skin, and RF and beam control circuits. Bayesian optimization was applied to design the antenna skin, in order to improve the design efficiency. The active skin antenna prototype with 32 microstrip antenna elements was fabricated, and some experiments were conducted to evaluate the fabricated antenna prototype. The remainder of this paper is organized as follows. The overall structure of the active skin antenna is presented in Section 2. Section 3 describes the design of an active skin antenna prototype, and Bayesian optimization is applied to obtain an optimal design of the antenna skin. The fabrication of the active skin antenna prototype is succinctly described in Section 4. Section 5 presents the testing results of the skin antenna prototype. Finally, Section 6 concludes the paper.

## 2. Overall Structure of Active Skin Antenna

An active skin antenna can provide the structural load-bearing and electromagnetic receiving sending functions simultaneously. In the following, we present a novel active skin antenna structure. Figure 1(a) shows an application of the distributed active skin antenna installed in the wing of an aircraft, and the overall structural configuration of the active skin antenna is shown in Figure 1(b).

From Figure 1(b), it is observed that the proposed antenna consists of an encapsulation shell, an antenna skin, and RF (i.e., transmitting and receiving circuits) and beam control circuits. The encapsulation shell is filled with the RF and beam control circuits. Bolt connections are applied to connect the encapsulation shell and load-bearing framework which is a part of the wing. The encapsulation shell can protect the internal circuits against the external loads such as impact loads and aerodynamic loads. The antenna skin can provide the structural load-bearing and electromagnetic receiving functions, and it is composed of an antenna layer and a protective layer which contains the facesheet and honeycomb/foam. The antenna skin is embedded into the load-bearing framework using adhesive bonding or bolt connection technology. The RF circuits comprise feeding networks, low-noise amplifiers, phase shifters, and power amplifiers, and so on. The beam control circuits consist of direct current (DC) power and control circuits, and it generates the beamforming signal and supplies the power required by the RF circuits. Every antenna element in the antenna skin is fed by a SMA which connects the RF circuits by a flexible RF cable.

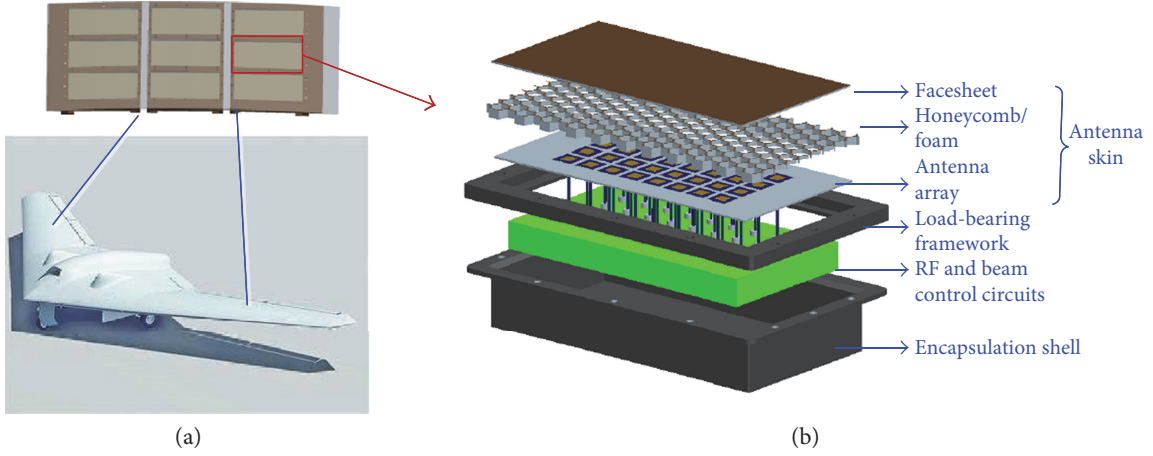


FIGURE 1: Schematic diagram of active skin antenna. (a) Application of active skin antenna. (b) Structural configuration of active skin antenna.

### 3. Design of Active Skin Antenna Prototype

According to the antenna structure in Figure 1, this section presents the design of an active skin antenna prototype with only the RF receiving function. The desired performance requirements are listed in Table 1. In this table, the desired deformation displacement and structural stress mean the maximum allowable structural stiffness and strength, when a 50N load is applied to the central point of the antenna structure. In the following, the antenna skin is designed using Bayesian optimization, and then the RF receiving and beam control circuits are described concisely.

**3.1. Bayesian Optimal Design of Antenna Skin.** Figure 2 shows the structural configuration of the proposed antenna skin. From Figure 2, it is observed that the antenna skin comprises the facsheet, honeycomb, and antenna array. The facsheet, honeycomb, and antenna array are bonded to form the final antenna skin. In the antenna skin, the antenna array consists of 32 microstrip antenna elements and an array framework fabricated by using 3D printing technology, and every antenna element is embedded into the array framework using the adhesive bonding technology. Table 2 shows the materials which every layer needs and the electrical properties of these materials.

Figure 3 presents the flowchart of the antenna skin design. As shown in Figure 3, the antenna skin design consists of two steps. The first step is to design the length, width of the antenna element, and the position of the feed port. The second step is to optimize the thickness of facsheet and honeycomb in this skin antenna, and an electromechanical codesign optimization is proposed to balance the mechanical and electrical requirements.

**3.1.1. Formulation of Optimizing Antenna Elements.** The first stage is to specify the substrate materials, antenna element type, and the dimensions of the antenna element substrate, according to some predefined performances. In the antenna skin prototype, the length  $L_g$  and width  $W_g$  of the antenna element substrate were 28 mm, as shown in Figure 4.

TABLE 1: Performance requirements of the skin antenna.

Layer	Performance specifications	Value
Electrical performance	Central frequency	5.8 GHz
	$S_{11}$ of element	$\leq -20$ dB
	Antenna array gain	$\geq 18$ dB
Mechanical performance	Structural stress	$\leq 240$ MPa
	Deformation displacement	$\leq 12$ mm

Utilizing the initial design determined by some empirical formulas, the simulation model of the microstrip antenna element was developed using HFSS VBScript. In order to obtain an optimal design, the paper constructed the following optimization model:

$$\begin{aligned}
 &\text{Find } \mathbf{x} = [x_1, x_2, Dx, Dy], \\
 &\text{Min } S_{11} = S_0 - \max[0, S_0 - S], \\
 &\text{s.t. } |f - f_0| < \varepsilon, \\
 &\quad \mathbf{x}_l < \mathbf{x} < \mathbf{x}_u,
 \end{aligned} \tag{1}$$

where the design variables  $x_1$  and  $x_2$  represent the length and width of the microstrip antenna elements, respectively.  $Dx$  and  $Dy$  represent the  $x$ -axis and  $y$ -axis coordinates of the feed port, respectively;  $S_{11}$  is the return loss;  $S$  is the return loss under the current design size;  $S_0$  is upper bound of the return loss;  $f_0$  is the center frequency of antenna element;  $\varepsilon$  is the resonant frequency deviation from the allowable value; and  $\mathbf{x}_l$  and  $\mathbf{x}_u$  denote the lower bound and upper bounds of the design variable  $\mathbf{x}$ , respectively.

As for the antenna element design used in the antenna skin prototype, the parameters  $S_0$ ,  $\varepsilon$ , and  $f_0$  were chosen as  $-20$  dB,  $0.05$  GHz, and  $5.8$  GHz, respectively. The lower bound  $\mathbf{x}_l$  and upper bounds  $\mathbf{x}_u$  are  $[10, 10, -3.2, -3.2]$  and  $[15, 15, 3.2, 3.2]$ , respectively.

**3.1.2. Electromechanical Codesign Formulation.** The aim in the second stage is to obtain optimal dimensions of the

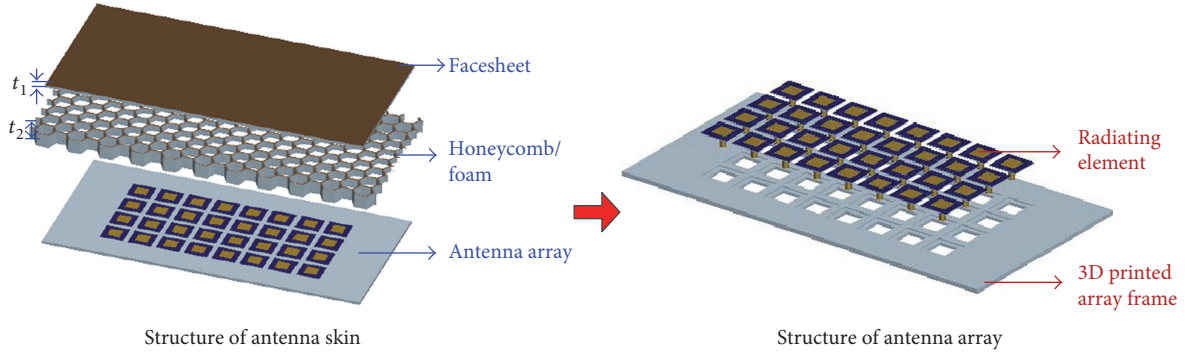


FIGURE 2: Structural configuration of antenna skin.

TABLE 2: Electrical properties of every layer.

Layer	Material	Dielectric constant
Upper facesheet	Glass/epoxy	4
Honeycomb core	Nomex honeycomb	1.1
Array framework	Photosensitive resin	2.4
Antenna element	RO4350B	3.66

facesheet and honeycomb core, which influence the mechanical and electrical performance. The mechanical performance consists of the structural weight, stiffness, and strength, which can be calculated by the mechanical model of the antenna structure. The electrical performance such as the radiation pattern can be obtained from an electromagnetic simulation model.

In this stage, the antenna array was firstly constructed by utilizing the optimal antenna element. Subsequently, the electromagnetic model of the antenna skin was developed using HFSS VBScript, and the mechanical model of the skin antenna structure was developed using ANSYS parametric design language. Finally, the following electromechanical codesign formulation was proposed to determine the thickness of the facesheet and honeycomb which can simultaneously meet the mechanical and electrical requirements.

$$\begin{aligned}
 &\text{Find } \mathbf{d} = [t_1, t_2]^T; \\
 &\text{Min } G = -\text{Gain}(\mathbf{d}); \\
 &\quad |f_i - f_0| < e, \quad i = 1, 2, \dots, 32; \\
 &\quad S_i < S_1, \quad i = 1, 2, \dots, 32; \\
 &\text{s.t. } \delta_{\max}(\mathbf{d}) \leq [\delta]; \\
 &\quad \sigma_{\max}(\mathbf{d}) \leq [\sigma]; \\
 &\quad \mathbf{d}_l \leq \mathbf{d} \leq \mathbf{d}_h,
 \end{aligned} \tag{2}$$

where the design variable  $\mathbf{d} = [t_1, t_2]^T$  will be solved by the optimization;  $t_1$  and  $t_2$  represent the thickness of facesheet and honeycomb, as shown in Figure 2. The antenna gain  $G$   $\text{ain}(\mathbf{d})$  of the antenna skin is used as the optimization objective, and  $[\delta]$  and  $[\sigma]$  are the allowable deformation

displacement and structural stress, respectively.  $\delta_{\max}(\mathbf{d})$  and  $\sigma_{\max}(\mathbf{d})$  are the maximum deformation displacement and maximum structural stress under the current design variable  $\mathbf{d}$ , respectively. In this paper, the allowable maximum deformation displacement  $\delta_{\max}(\mathbf{d})$  and maximum structural stress  $\sigma_{\max}(\mathbf{d})$  are 12 mm and 240 MPa, respectively.  $\mathbf{d}_l$  and  $\mathbf{d}_h$  are the predefined lower bound and upper bound, respectively.

The mechanical performances  $\delta_{\max}(\mathbf{d})$  and  $\sigma_{\max}(\mathbf{d})$  are determined using the following mechanical model of the antenna skin structure:

$$\mathbf{K}(\mathbf{d})\boldsymbol{\delta} = \mathbf{F}, \tag{3}$$

where  $\mathbf{K}(\mathbf{d})$  is the stiffness matrix and it is a function of the design variable  $\mathbf{d}$ .  $\mathbf{F}$  is the vector of the load.  $\boldsymbol{\delta}$  is the displacement vector of the node deformation.

In this paper, the maximum deformation displacement  $\delta_{\max}(\mathbf{d})$  and maximum structural stress  $\sigma_{\max}(\mathbf{d})$  are used to evaluate the mechanical stiffness and strength before the antenna structure is destroyed. The maximum displacement  $\delta_{\max}(\mathbf{d})$  is defined as the deflection at the central point of the antenna skin, when a predefined load is applied to the antenna structure.

**3.1.3. Solution Based on Bayesian Optimization.** Bayesian optimization is a statistical framework that uses information gained from past experiments to model and minimize an arbitrary objective function, and it works by building and querying cheap surrogate models which estimate the behavior of real objective functions which are expensive to evaluate [29]. Surrogate models are typically built using Gaussian process regression (GPR). GPR is to fit previously observed data and used to make predictions about the objective values in areas not yet explored. These predictions are easy to compute and can intelligently choose the next set of parameters such that solutions are found with a minimal number of expensive objective function.

In this subsection, the objective function in (1) and (2) was built by GPR model with given training data  $(\mathbf{X}, \mathbf{Y}) = \{\mathbf{x}_i, \mathbf{y}_i\}_{i=1}^N$ . According to the research in [29–31], the new point  $\mathbf{x}_{N+1}$  is obtained by a search algorithm, and the new

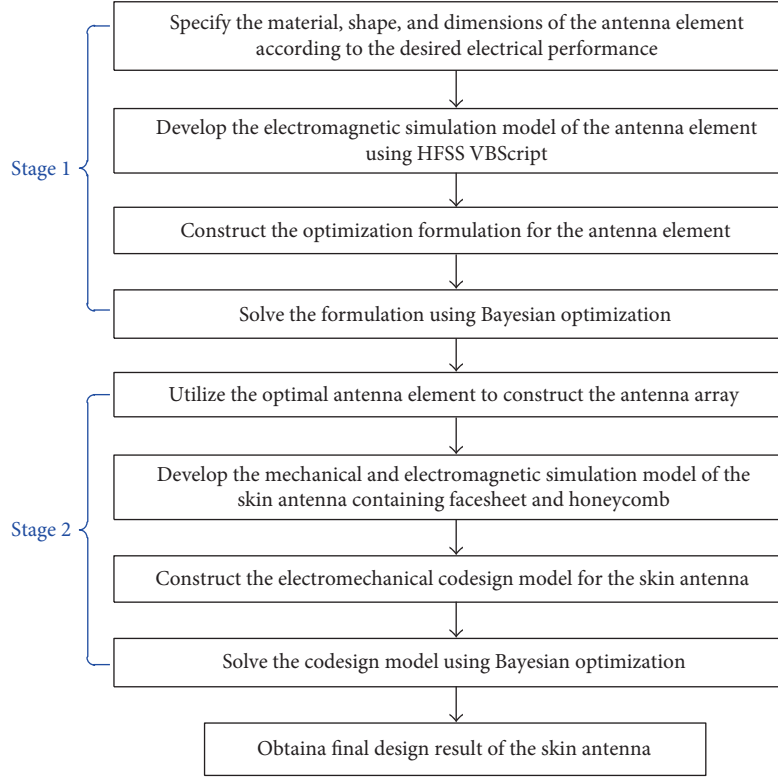


FIGURE 3: Flowchart of the antenna skin design.

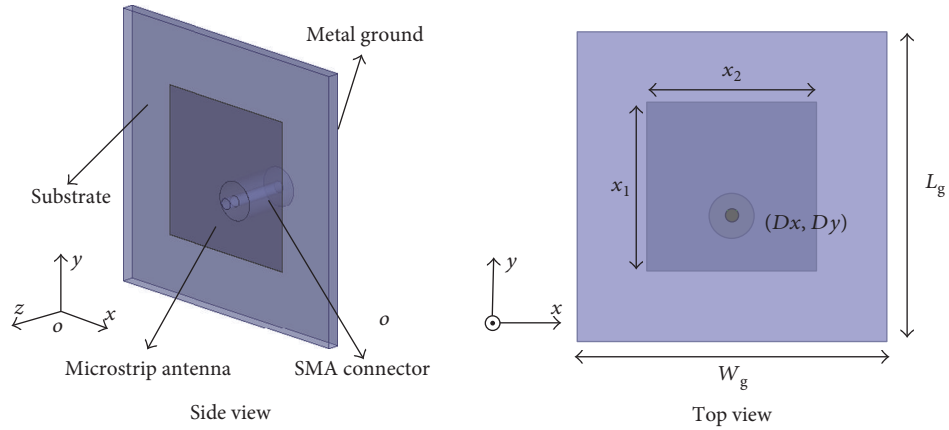


FIGURE 4: Geometry of microstrip antenna element.

output,  $\mathbf{y}_{N+1}$ , can be expressed with the predicted mean  $m(\mathbf{x}_{N+1})$  and the standard deviation  $\sigma(\mathbf{x}_{N+1})$  as

$$\mu(\mathbf{x}_{N+1}) = \mathbf{k}^T [\mathbf{K} + \sigma_N^2 \mathbf{I}]^{-1} \mathbf{Y}, \quad (4)$$

$$\sigma^2(\mathbf{x}_{N+1}) = \mathbf{k}(\mathbf{x}_{N+1}, \mathbf{x}_{N+1}) - \mathbf{k}^T [\mathbf{K} + \sigma_N^2 \mathbf{I}]^{-1} \mathbf{k}, \quad (5)$$

$$\mathbf{y}_{N+1} = \mu(\mathbf{x}_{N+1}) \pm \sigma(\mathbf{x}_{N+1}), \quad (6)$$

where  $N$  is the number of training data,  $\mathbf{I}$  is the identity matrix,  $\mathbf{K}$  denotes the kernel matrix for the training data  $(\mathbf{X}, \mathbf{Y})$ ,  $\mathbf{k}$  represents the covariance matrix between  $\mathbf{x}_{N+1}$

and  $\mathbf{X} = (\mathbf{x}_1, \mathbf{x}_2, \dots, \mathbf{x}_N)$ ,  $\mathbf{k}(\mathbf{x}_{N+1}, \mathbf{x}_{N+1})$  signifies the self-covariance matrix, and  $\sigma_N$  is the noise deviation and the coefficient.

This GPR model provides a posterior distribution of the unknown function. We can choose the next value of the function representing the targeted values by minimizing an acquisition function. In this paper, the lower confidence bound (LCB) is used as the acquisition function to find the optimal value of the design variables [29], and it is expressed as follows:

$$\mathbf{x}_{N+1} = \arg \min_i [\mu(x_i) - \kappa \sigma(x_i)], \quad (7)$$

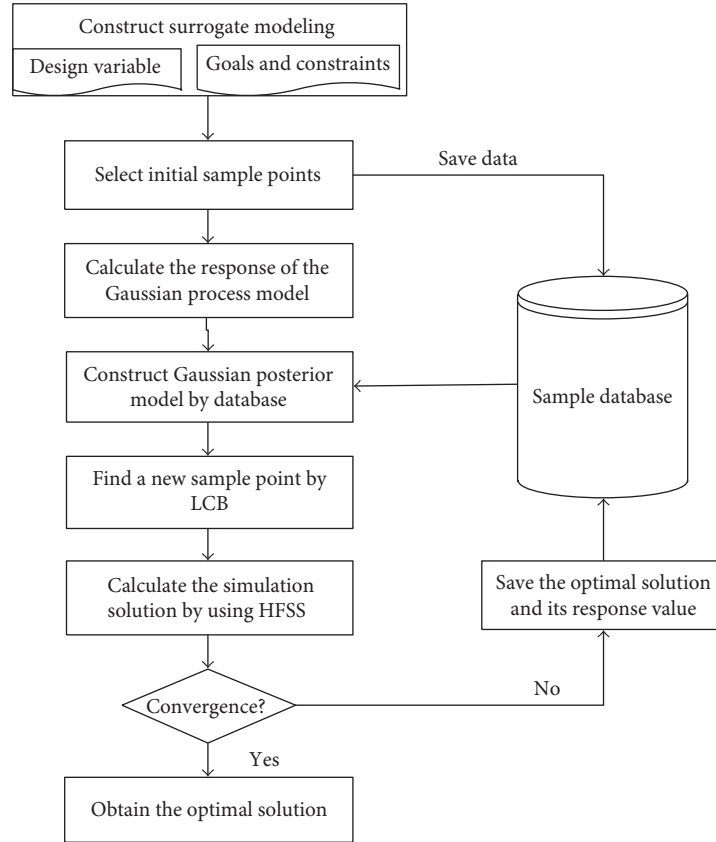


FIGURE 5: Flowchart of Bayesian optimization solution.

where  $\kappa > 0$  and  $\kappa = (2\log \pi^2 x^2 / 12\nu)^{0.5}$  (where  $\nu = 0.05$ );  $\mu(x_i)$  and  $\sigma(x_i)$  are determined from (4) and (5).

The Bayesian optimization above was applied to solve the optimization model in (1) and (2). The objective functions were built using GPR. Figure 5 presents the flowchart of Bayesian optimization solution, and the optimal value of the design variable is obtained by using the following procedure.

- (1) Determine design variables and design space and build the target model which is to be optimized. The initial sample points are selected by the Latin hypercube sampling method in the whole design space. Let  $K = 1$ , which represents the number of iteration.
- (2) Fit a Gaussian distribution model by calculating the response of the Gaussian process model based on the multivariate normal distribution at sampling points.
- (3) Optimize LCB acquisition function to find out the next design point  $x_t$ .
- (4) Perform an electromagnetic simulation at  $x_t$  by using HFSS to get the actual response value.
- (5) If the response obtained in the previous step meets the convergence, stop the procedure; otherwise, go to the step 6.

- (6) Add the point sampled in step 3 to the database and return to step 2.

It is important to note that the selection of the next sample does not require the computation of electromagnetic model developed by HFSS, since (7) is computed only based on the previous simulation results, which minimizes computational time. Unlike most optimization techniques, this approach provides a posterior distribution of the unknown function and hence the search involves determining the function (rather than the output itself) that is closer to the targeted goal.

#### 3.1.4. Design Results

##### (1) Optimization Results of Antenna Element

In this part, the antenna element was optimized according to the optimization model in (1) by using the Bayesian optimization algorithm and genetic algorithm. Figures 6(a) and 6(b) show the optimization iterative process of the Bayesian algorithm and genetic algorithm, respectively. Compared with the two figures, it is found that Bayesian optimization needs 16 iterations to obtain the target solution which satisfies the design requirement. However, the genetic algorithm needs 50 iterations to achieve the target solution. The comparison of iteration numbers shows that the genetic algorithm is more likely to fall into the local optimal solution than the Bayesian algorithm. Table 3 shows the

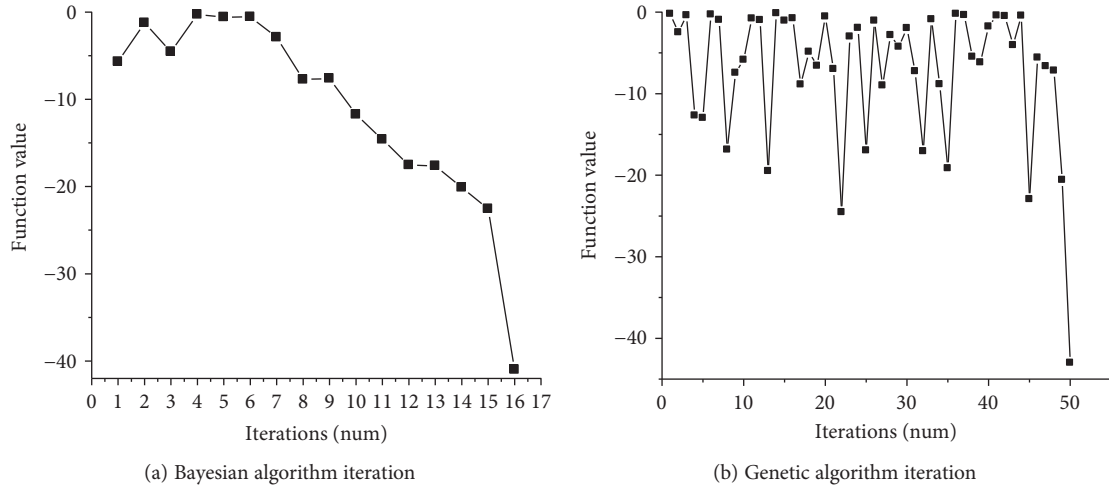


FIGURE 6: Iteration process of the Bayesian algorithm and genetic algorithm.

TABLE 3: Comparison of the antenna element optimization results.

	Function valuation numbers	Time consuming (s)	Function value (dB)	Center frequency (GHz)	Target solution (mm)
Bayesian algorithm	17	1521	-41	5.808	[12.9,12.9,0,0]
Genetic algorithm	50	3209	-43	5.763	[13,13,-0.09,0]

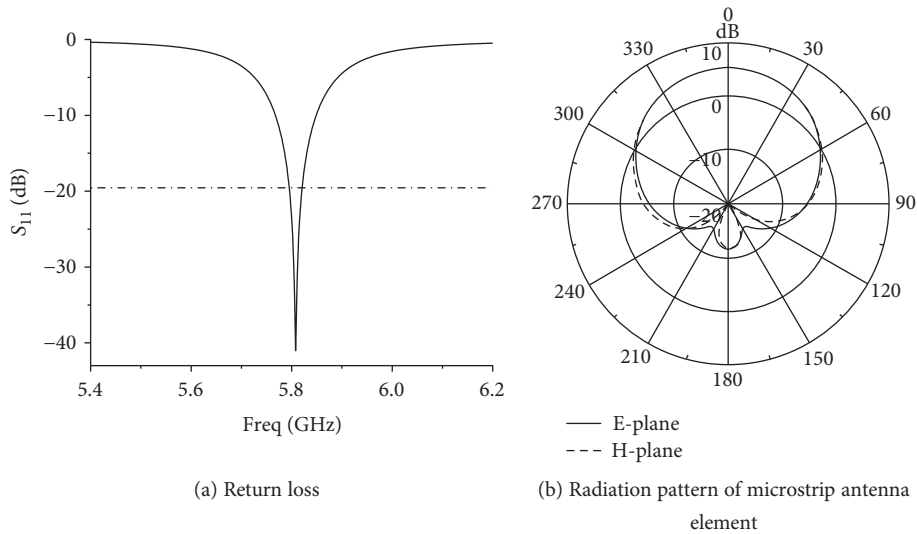


FIGURE 7: Simulated return loss and radiation pattern of the radiating element.

comparing results of the two algorithms for optimizing the antenna element. As seen from these results, the target solutions obtained by the Bayesian optimization algorithm and genetic algorithm are similar. However, the center frequency obtained by the Bayesian algorithm is much closer to 5.8 GHz. Besides, the time required by the Bayesian algorithm is less than half the time required by the genetic algorithm. Figure 7 shows the optimal return loss and the gain pattern of the antenna element obtained by Bayesian

optimization. From Figure 7(b), it is observed that the gain of the antenna element is about 6.23 dBi.

(2) Optimization Results of Antenna Skin

In this investigation, the antenna array was firstly constructed by utilizing the optimal antenna element from the previous section. Subsequently, according to (2), the thickness of facesheet and honeycomb was optimized by the Bayesian algorithm and genetic algorithm, respectively.

TABLE 4: Comparison of the antenna skin optimization results.

	Time consuming (min)	Function value (dB)	Target solution (mm)
Bayesian algorithm	191.4	21.4	[0.27,2]
Genetic algorithm	429	21.5	[0.26,4.25]

Table 4 provides some comparisons of the two algorithms. As shown in Table 4, the calculating time required by the two algorithms is different. The time required by the genetic algorithm is more than twice time required by the Bayesian algorithm. Therefore, it is clear that the Bayesian algorithm is much faster than the genetic algorithm. Utilizing the optimization results from the Bayesian algorithm, Figure 8 shows the simulation results of the antenna skin gain, and its gain is 21.4 dB. When a 50 N load is applied to the central point of the antenna skin structure, the mechanical performance of the antenna skin is shown in Figure 9. The maximum deformation displacement is 11.9 mm, and the maximum structural stress is 225 MPa. These results can meet the desired performance requirements in Table 1.

**3.2. Design of RF Receiving and Beam Control Circuits.** The RF receiving and beam control circuits are responsible for the reception of electromagnetic waves, amplitude, and phase control of antenna elements. Figure 10 presents the block diagram of the circuit in the active skin antenna prototype. The circuit consists of the same four RF receiver modules and a beam control circuit.

From Figure 10, it is observed that each RF receiver module connects eight microstrip antenna elements by using RF cables. Each RF receiver module consists of an active receiving circuit and two-stage feed networks. Figure 11 shows the internal circuits in every RF receiver module. Each active receiving circuit has eight channels which realize the connection between the antenna element and the first-stage feed network. Each receiving channel consists of a low-noise amplifier (LNA), a 6-bit digital phase shifter, a variable attenuator, and a gain amplifier. In this prototype, the LNA and gain amplifier utilize the same chip PMA3-83LN+ manufactured by Mini-Circuits. The voltage-controlled variable attenuator HMC712LP3C is manufactured by ADI, and the 6-bit digital phase shifter MAPS-011008 is from MACOM. The attenuator and phase shifter are used to control the amplitude and phase, respectively, of incoming signal on each individual channel, and the control commands of the attenuator and phase shifter are from the beam control circuits, as shown in Figure 10.

In this paper, two-stage feed networks are used to combine each channel signal received by the antenna element to the RF terminal. The feed networks were designed by using integrated circuit combiners and distributed microstrip transmission line. The integrated circuit combiner WP4A+ and SCN-2-65+ from Mini-Circuits Corporation were used to realize the combination of four or two equal amplitude and phase power signals, respectively. The Wilkinson feed networks realized by distributed transmission line were designed to connect the output channel and the integrated

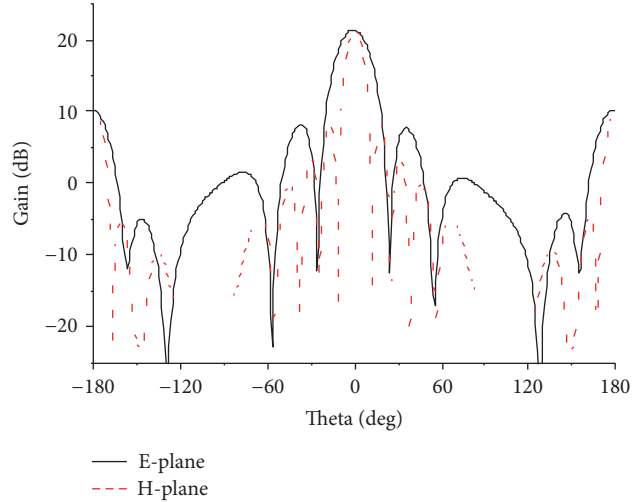


FIGURE 8: Simulation result of antenna skin gain.

circuit combiner chip. Figure 12 presents the design of the first-stage feed networks (i.e., 4:1 combining networks), due to the limitation of the length of the paper. From the simulation results in Figure 12(b), it is found that the network can obtain approximately equal insertion loss and equal phase characteristics in the 5.4–6.2 GHz frequency range.

#### 4. Fabrication of Active Skin Antenna

This section presents the fabrication of an active skin antenna prototype, and the fabrication process is succinctly described in the following.

The antenna skin was fabricated by using a hybrid manufacturing approach. In this paper, the hybrid manufacturing approach refers to the combination of 3D printing manufacturing and traditional manufacturing process. The 3D printing manufacturing was applied to fabricate the antenna array framework, and the remainder was fabricated by using traditional manufacturing process. The hybrid manufacturing approach can simplify the manufacturing process and reduce the cost of the antenna skin, especially for the complex conformal array framework.

First, every layer in the antenna skin was manufactured separately, according to the design results above. During the course of the fabrication, the antenna array framework was fabricated by using the 3D printing technology, and 32 microstrip antenna elements were fabricated by screen printing methods. Figure 13(a) presents the fabricated microstrip antenna elements and array framework. Subsequently, the microstrip antenna elements were embedded into the array framework using the adhesive bonding technology, as shown in Figure 13(b). The designed facesheet and honeycomb were prepared by confirming their mechanical and electrical performances. For the facesheet, two-ply glass/epoxy prepregs were symmetrically laid up, and each layer was bonded on the top or bottom of another one in the design sequence by using the epoxy film adhesive. Subsequently, the layers were aligned and laminated according to the assembly sequence of each layer. After being covered

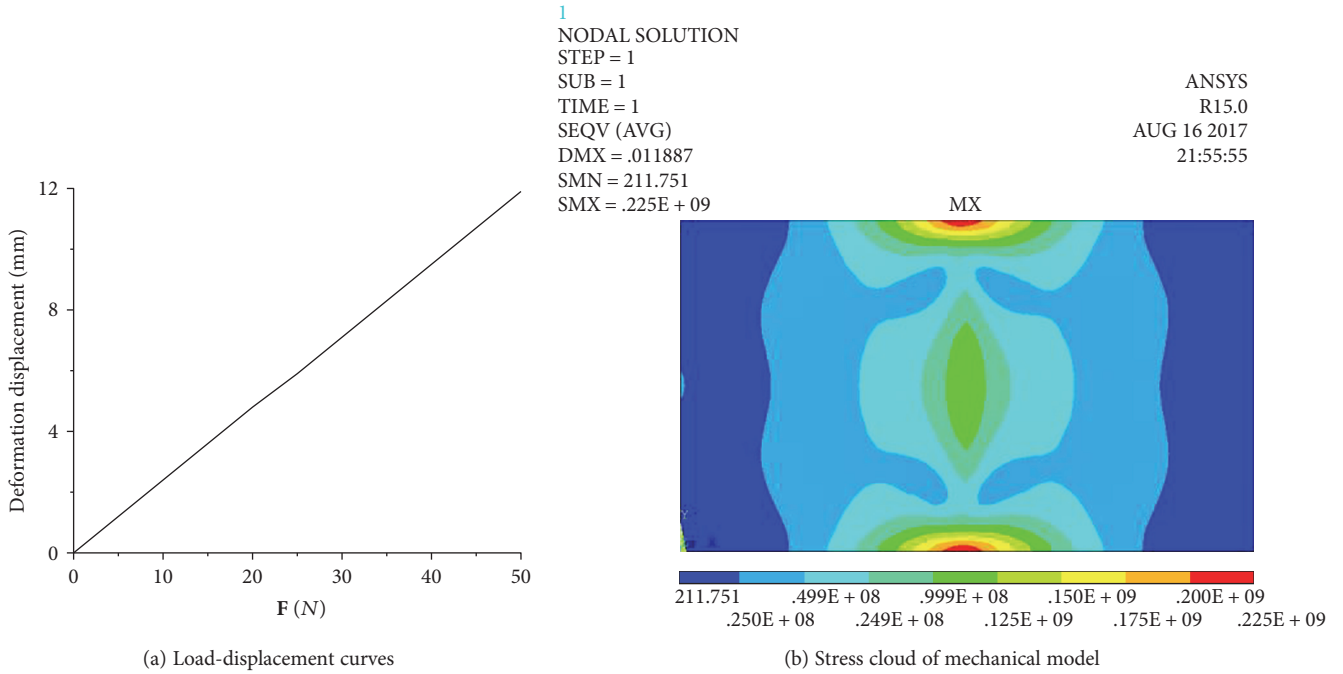


FIGURE 9: Analysis results of mechanical performance.

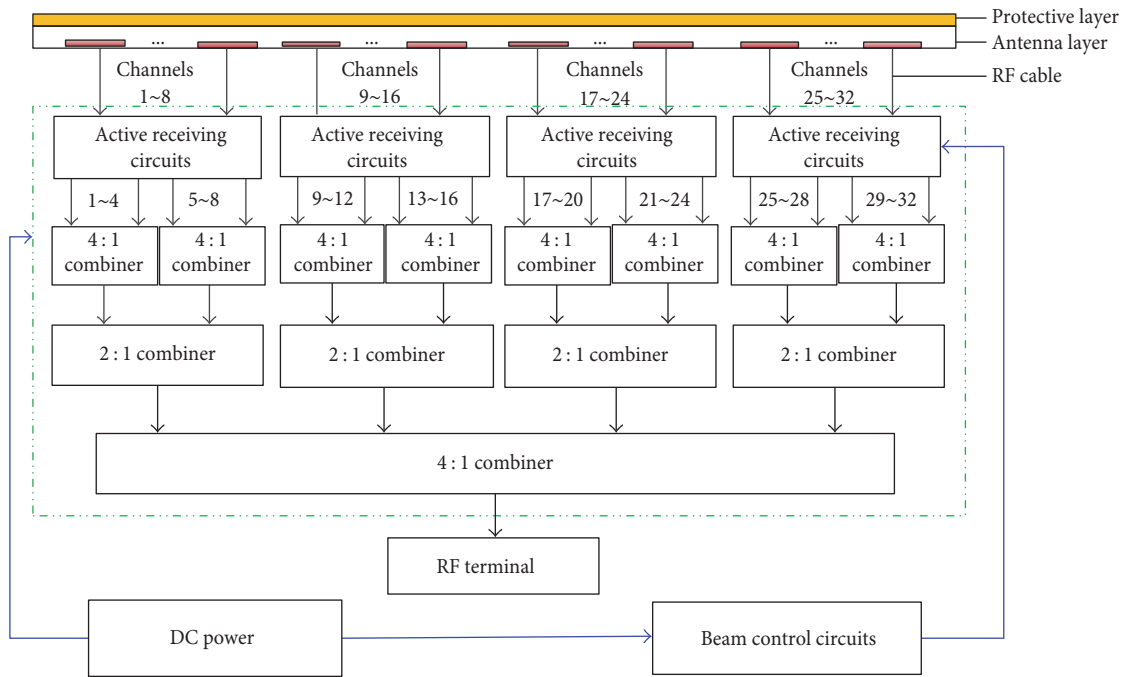


FIGURE 10: Block diagram of information transmission of smart skin antenna prototype.

by a vacuum bag, the assembly was cocured in an autoclave, according to the recommended curing cycle for this adhesive (125°C for 180 min at a pressure of 0.45 MPa). Figure 13(f) shows the final skin antenna sample. The RF receiving and beam control circuits were fabricated by printing circuit board technology. Figure 14 shows the fabricated active skin antenna prototype. The soft RF label was utilized to connect the antenna skin with the RF receiving and beam control circuits.

### 5. Testing Results

Utilizing the fabricated antenna prototype, we have conducted some experiments to validate the proposed design and fabricating method. Figure 15 presents the experimental system which consists of a test fixture, active skin antenna, and near-field measuring system. Moreover, the absorbing wave materials cover the metal surface of the test fixture to avoid the reflection and scattering of electromagnetic wave.

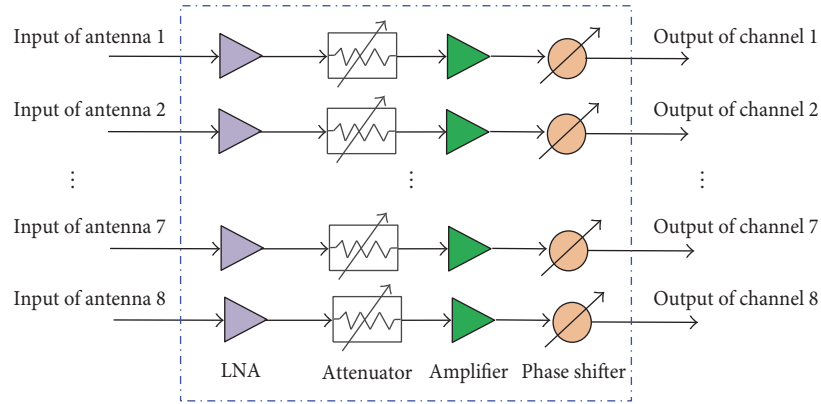
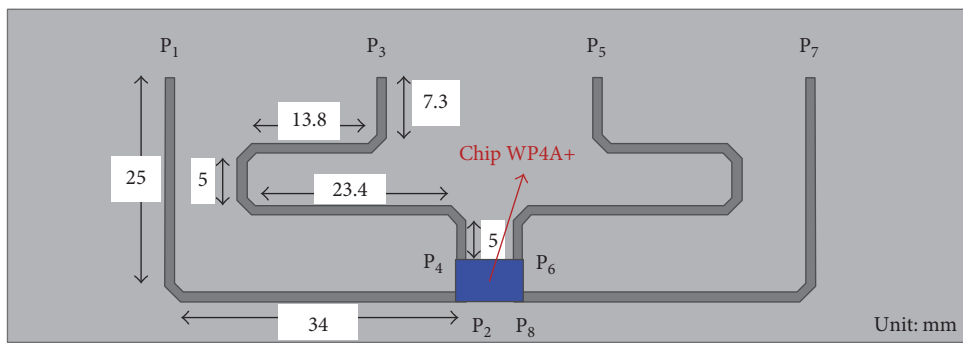
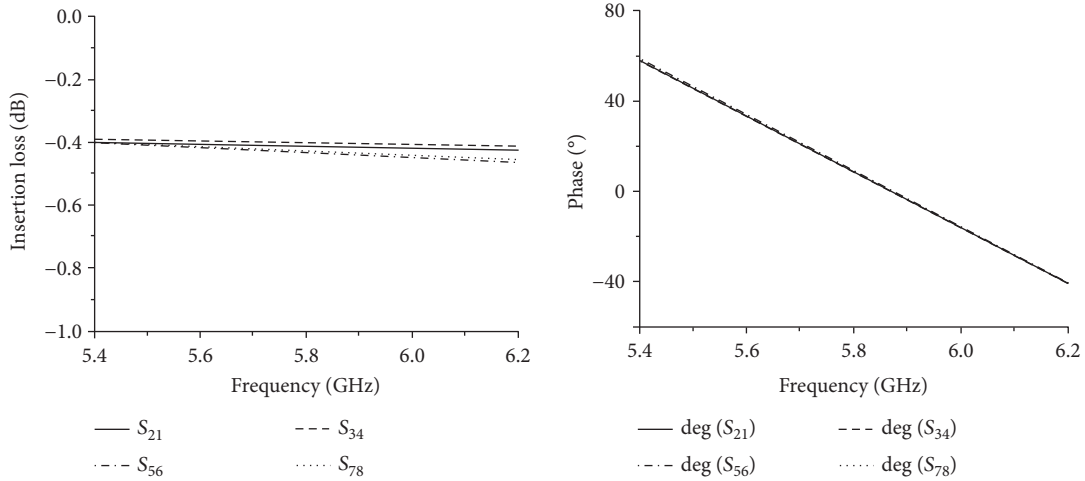


FIGURE 11: Active receiving circuits in a RF receiver module.



(a) 4:1 combining network



(b) Insertion loss and phase of microstrip line

FIGURE 12: Design results of 4:1 combining networks.

The experimental results and discussions were presented in the following.

**5.1. Comparisons of Simulation and Measured Results.** In order to validate the Bayesian optimal design, this paper firstly presents the measured return loss of microstrip antenna element and then presents the comparisons of measured and simulation radiation patterns of the antenna prototype at 5.8GHz. Figure 16 gives the measured return

loss of the 32 fabricated antenna elements. It is found that the measured return loss satisfies the design specification in Table 1. The maximum error between the simulation and measured center frequency is 0.03 GHz. Figure 17 presents the comparisons between the measured and simulation radiation patterns of the antenna prototype at 5.8 GHz. The maximum gain of the active skin antenna is about 21.2 dBi.

From Figure 17, it is also found that the measured radiation patterns are closed to the simulation ones. However,

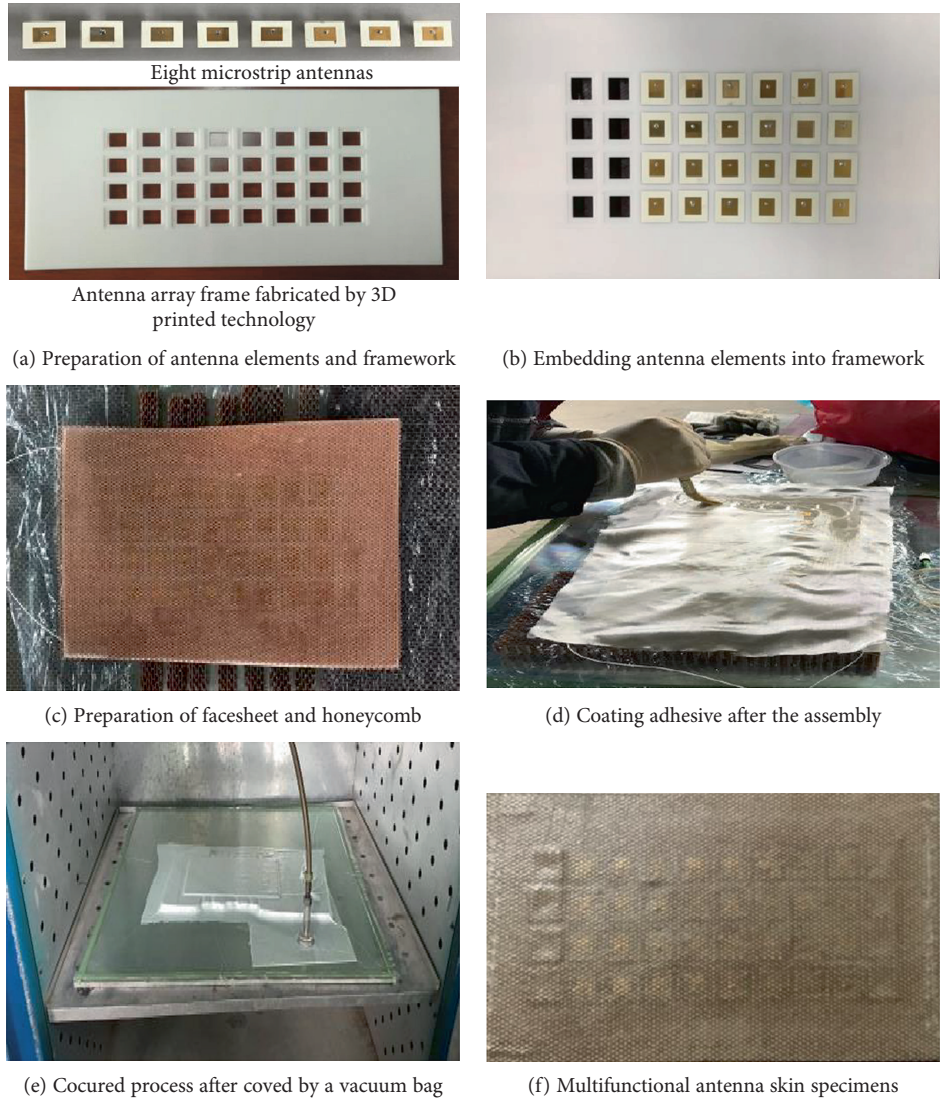


FIGURE 13: Fabrication process of antenna skin.

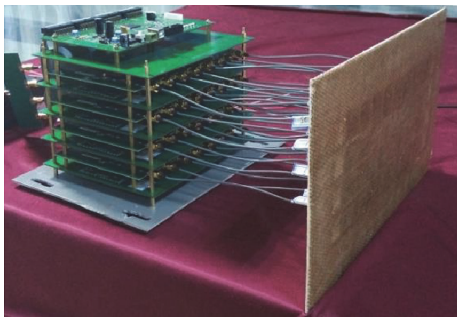


FIGURE 14: Active skin antenna prototype.

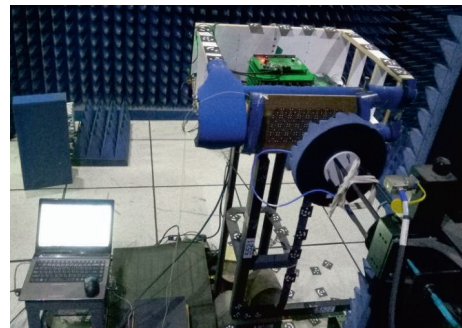


FIGURE 15: Measurements of active skin antenna prototype.

there is a little difference between the measured and simulation side lobe. One of the reasons for this is the effect of the adhesive in the skin antenna. The adhesive that bonds the different layers to provide mechanical strength also influences the electrical performance of the skin antenna. The adhesive influences the effective dielectric constant in the

antenna structure. The change of the effective dielectric constant leads to inaccurate simulation results and makes the central frequency have a drift. In addition, the manufacturing errors in RF receiving circuits and microstrip antenna elements, which mean the structural dimension deviations

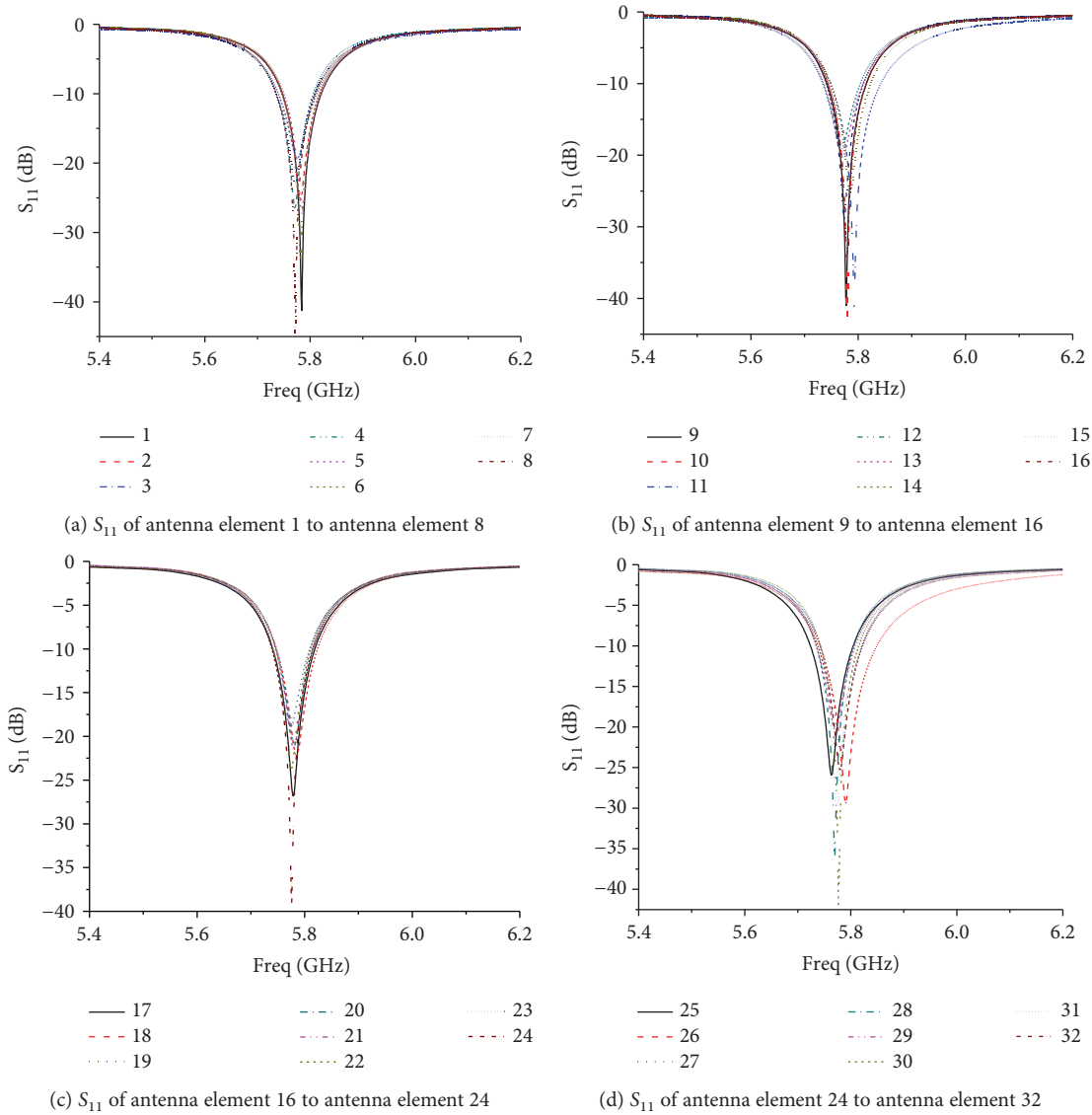


FIGURE 16: Measured return loss.

relative to the optimal design dimensions, also lead to the differences between the simulation and measured results of the radiation patterns and return loss.

**5.2. Measured Scanning Patterns.** To demonstrate the electromagnetic performance, the scanning radiation characteristics of the fabricated antenna prototype were also measured in an anechoic chamber. Figure 18 presents the measured scanning patterns in  $xoz$ -plane and  $yoz$ -plane of the active skin antenna operating at 5.8 GHz. It is observed that the active skin antenna has a peak gain of 21.2 dBi and the side lobe levels (SLL) in  $xoz$ -plane and  $yoz$ -plane are about  $-14.1$  and  $-13.7$  dB, respectively. In addition, it is observed that the scanning range in  $xoz$ -plane is from  $-29.0^\circ$  to  $29.3^\circ$  and that the scanning range in  $yoz$ -plane is from  $-14.2^\circ$  to  $14.9^\circ$ . Table 5 gives some electrical performance indexes extracted from the measured scanning patterns in Figure 18. From the table, it is found that there is some difference between the desired beam direction

and actual beam direction. This difference may be due to the imperfections of the measurement system such as the phase error caused by the manufacturing errors in RF receiving circuits.

## 6. Conclusions

This paper presents a novel active skin antenna structure which consists of an encapsulation shell, an antenna skin, and RF and beam control circuits. The antenna skin comprises facesheet, honeycomb, microstrip antenna elements and an array framework fabricated by 3D Printing technology. The different layers were bonded to form the final antenna skin. In addition, Bayesian optimization method was applied to design the microstrip antenna element and the thickness of facesheet and honeycomb of the skin antenna, in order to obtain an optimal design and improve the design efficiency. The active skin antenna prototype with 32 microstrip antenna elements was fabricated and some

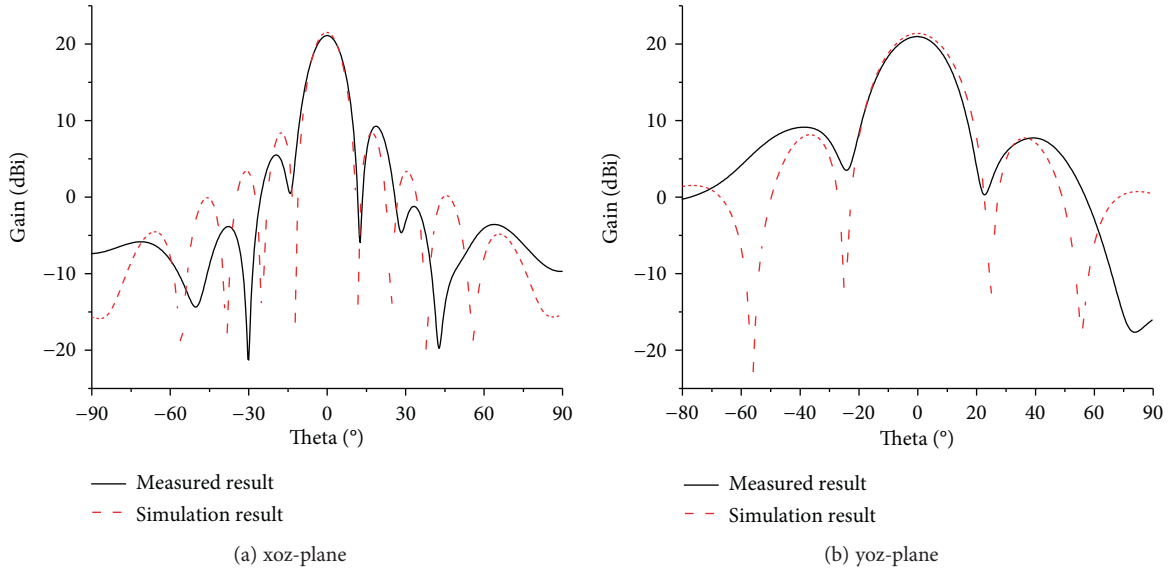


FIGURE 17: Comparisons of the measured and simulation radiation patterns of the prototype at 5.8 GHz.

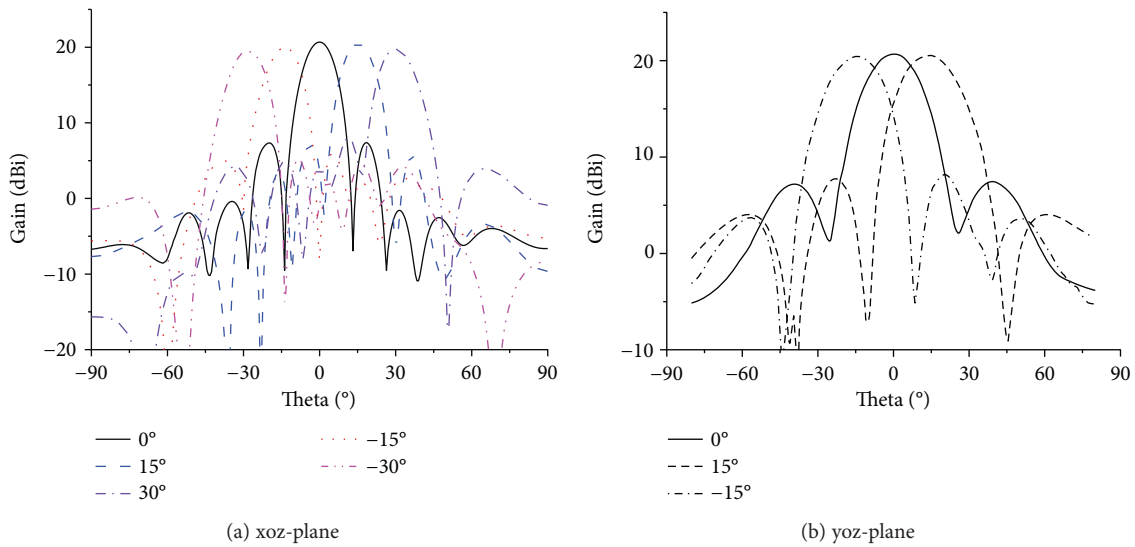


FIGURE 18: Measured scanning patterns of the active skin antenna prototype at 5.8 GHz.

TABLE 5: Electrical performance indexes of active skin antenna under undeformed conditions.

Plane	Desired beam direction (°)	Actual beam direction (°)	Gain (dB)	Beam width (°)	Maximum side lobe level (dB)
xoz-plane	0°	0.2	21.2	11.6	-14.1
xoz-plane	15°	14.7	20.9	12.2	-13.5
xoz-plane	30°	29.3	20.2	13	-12.1
xoz-plane	-15°	-14.3	20.8	12.5	-13.8
xoz-plane	-30°	-29.0	19.9	13.8	-11.3
yoz-plane	0°	0.4	21.2	21.2	-13.7
yoz-plane	15°	14.9	21.0	23	-12.5
yoz-plane	-15°	-14.2	20.9	23.8	-12.6

experiments were conducted to evaluate the fabricated antenna prototype. The comparisons between the simulation and measured results show that Bayesian optimization

method can obtain accurate design results under the less computing time. The measured scanning radiation patterns validate the feasibility the proposed antenna skin structure.

Our design and fabrication technique is suitable for the development of conformal load-bearing antenna or smart skin antenna installed in the structural surface of aircraft, warships, and armored vehicles. Furthermore, Bayesian optimization method provides an alternative approach to realize the fast and accurate optimal design of antenna and microwave circuits.

## Conflicts of Interest

The authors declare that they have no conflicts of interest.

## Acknowledgments

This project is supported by the National Natural Science Foundation of China (Program no. 51775405, no. 51490664, no. 51575419, and no. 51305323), Natural Science Basic Research Plan in Shaanxi Province of China (Program no. 2016JM5002), Opening Foundation of State Key Laboratory of Structural Analysis for Industrial Equipment (Program no. GZ15110), the Fundamental Research Funds for the Central Universities (Grant no. JB160420), and Defense Basic Research Program (Program no. JCKY2016210B002). Zhaoxi Liu and Haiyang Li from Xidian University provided experimental help during the project. Their efforts were crucial to the completion of the research.

## References

- [1] J. Kim, J. Y. Jang, G. H. Ryu, J. H. Choi, and M. S. Kim, "Structural design and development of multiband aero-vehicle smart skin antenna," *Journal of Intelligent Material Systems and Structures*, vol. 25, pp. 631–639, 2014.
- [2] S. H. Son, S. Y. Eom, and W. B. Hwang, "Development of a smart-skin phased array system with a honeycomb sandwich microstrip antenna," *Smart Materials and Structures*, vol. 17, article 035012, 2008.
- [3] J. Zhou, J. Huang, Q. He, B. Tang, and L. Song, "Development and coupling analysis of active skin antenna," *Smart Materials and Structures*, vol. 26, article 025011, 2017.
- [4] C. K. Kim, L. M. Lee, H. C. Park, W. Hwang, and W. S. Park, "Impact damage and antenna performance of conformal load-bearing antenna structures," *Smart Materials and Structures*, vol. 12, pp. 672–679, 2003.
- [5] C. S. You and W. B. Hwang, "Design of load-bearing antenna structures by embedding technology of microstrip antenna in composite sandwich structure," *Composite Structures*, vol. 71, pp. 378–382, 2005.
- [6] S. E. Morris, Y. Bayram, L. Zhang, Z. Wang, M. Shtein, and J. L. Volakis, "High-strength, metalized fibers for conformal load bearing antenna applications," *IEEE Transactions on Antennas and Propagation*, vol. 59, pp. 3458–3462, 2011.
- [7] J. Zhou, J. Huang, L. Song, D. Zhang, and Y. Ma, "Electromechanical co-design and experiment of structurally integrated antenna," *Smart Materials and Structures*, vol. 24, article 037004, 2015.
- [8] J. Zhou, L. Song, J. Huang, and C. Wang, "Performance of structurally integrated antennas subjected to dynamical loads," *International Journal of Applied Electromagnetics and Mechanics*, vol. 48, pp. 409–422, 2015.
- [9] D. J. Hartl, G. J. Frank, G. H. Huff, and J. W. Baur, "A liquid metal-based structurally embedded vascular antenna: I. Concept and multiphysical modeling," *Smart Materials and Structures*, vol. 26, article 025001, 2017.
- [10] D. J. Hartl, G. J. Frank, R. J. Malak, and J. W. Baur, "A liquid metal-based structurally embedded vascular antenna: II. Multiobjective and parameterized design exploration," *Smart Materials and Structures*, vol. 26, article 025002, 2017.
- [11] L. Yao, X. Wang, F. J. Xu, D. Zhao, M. W. Jiang, and Y. P. Qiu, "Fabrication and impact performance of three-dimensionally integrated microstrip antennas with microstrip and coaxial feeding," *Smart Materials and Structures*, vol. 18, article 095034, 2009.
- [12] L. Yao and Y. P. Qiu, "Design and fabrication of microstrip antennas integrated in three dimensional orthogonal woven composites," *Composites Science and Technology*, vol. 69, pp. 1004–1008, 2009.
- [13] F. J. Xu, L. Yao, X. Wang, and Y. P. Qiu, "Effect of conductive yarn crimp in radiation patch on electromagnetic performance of 3D integrated microstrip antenna," *Composites Part B-Engineering*, vol. 43, pp. 465–470, 2012.
- [14] F. Xu, L. Yao, D. Zhao, L. Zhao, M. Jiang, and Y. Qiu, "Performance and impact damage of a three dimensionally integrated microstrip feeding antenna structure," *Composite Structures*, vol. 93, pp. 193–197, 2010.
- [15] C. You, D. Kim, S. Cho, and W. Hwang, "Impact behavior of composite antenna array that is conformed around cylindrical bodies," *Composites Science and Technology*, vol. 70, pp. 627–632, 2010.
- [16] D. Kim, C. You, and W. Hwang, "Effect of adhesive bonds on electrical performance in multi-layer composite antenna," *Composite Structures*, vol. 90, pp. 413–417, 2009.
- [17] D. Kim, J. Kim, J. Kim et al., "Design and fabrication of a composite-antenna-structure for broadband frequency with microwave absorber," *Journal of Composite Materials*, vol. 46, pp. 1851–1858, 2012.
- [18] W. C. Bing Zhang, W. Yanjie, K. Ding, and R. Li, "Review of 3D printed millimeter-wave and terahertz passive devices," *International Journal of Antennas and Propagation*, vol. 2017, Article ID 1297931, 10 pages, 2017.
- [19] H. Xin and M. Liang, "3-D-printed microwave and THz devices using polymer jetting techniques," *Proceedings of the IEEE*, vol. 105, pp. 737–755, 2017.
- [20] W. J. Otter and S. Lucyszyn, "Hybrid 3-D-printing technology for tunable THz applications," *Proceedings of the IEEE*, vol. 105, pp. 756–767, 2017.
- [21] M. Liang, C. Shemelya, E. MacDonald, R. Wicker, and H. Xin, "3-D printed microwave patch antenna via fused deposition method and ultrasonic wire mesh embedding technique," *IEEE Antennas and Wireless Propagation Letters*, vol. 14, pp. 1346–1349, 2015.
- [22] J. J. Adams, E. B. Duoss, T. F. Malkowski et al., "Conformal printing of electrically small antennas on three-dimensional surfaces," *Advanced Materials*, vol. 23, pp. 1335–1340, 2011.
- [23] M. Liang, W. R. Ng, K. H. Chang, K. Gbele, M. E. Gehm, and H. Xin, "A 3-D Luneburg lens antenna fabricated by polymer jetting rapid prototyping," *IEEE Transactions on Antennas and Propagation*, vol. 62, pp. 1799–1807, 2014.
- [24] P. Nayeri, M. Liang, R. A. Sabory-Garcia et al., "3D printed dielectric reflectarrays: low-cost high-gain antennas at sub-

- millimeter waves,” *IEEE Transactions on Antennas and Propagation*, vol. 62, pp. 2000–2008, 2014.
- [25] J. A. Byford, M. I. M. Ghazali, S. Karuppuswami, B. L. Wright, and P. Chahal, “Demonstration of RF and microwave passive circuits through 3-D printing and selective metalization,” *IEEE Transactions on Components Packaging and Manufacturing Technology*, vol. 7, pp. 463–471, 2017.
- [26] M. Y. Chen, D. Pham, H. Subbaraman, X. J. Lu, and R. T. Chen, “Conformal ink-jet printed C-band phased-array antenna incorporating carbon nanotube field-effect transistor based reconfigurable true-time delay lines,” *IEEE Transactions on Microwave Theory and Techniques*, vol. 60, pp. 179–184, 2012.
- [27] H. Subbaraman, D. T. Pham, X. C. Xu et al., “Inkjet-printed two-dimensional phased-array antenna on a flexible substrate,” *IEEE Antennas and Wireless Propagation Letters*, vol. 12, pp. 170–173, 2013.
- [28] X. Lan, X. Lu, M. Y. Chen et al., “Direct on-Chip 3-D aerosol jet printing with high reliability,” *IEEE Transactions on Components, Packaging and Manufacturing Technology*, vol. 7, no. 8, pp. 1369–1376, 2017.
- [29] B. Shahriari, K. Swersky, Z. Y. Wang, R. P. Adams, and N. de Freitas, “Taking the human out of the loop: a review of Bayesian optimization,” *Proceedings of the IEEE*, vol. 104, pp. 148–175, 2016.
- [30] P. Chen, B. M. Merrick, and T. J. Brazil, “Bayesian optimization for broadband high-efficiency power amplifier designs,” *IEEE Transactions on Microwave Theory and Techniques*, vol. 63, pp. 4263–4272, 2015.
- [31] P. Chen, J. Xia, B. M. Merrick, and T. J. Brazil, “Multiobjective Bayesian optimization for active load modulation in a broadband 20-W GaN Doherty power amplifier design,” *IEEE Transactions on Microwave Theory and Techniques*, vol. 65, pp. 860–871, 2017.